PRECIPITATION STUDIES ON ALLOYS FROM THE SYSTEM COPPER-CHROMIUM-ZIRCONIUM

by

BRIAN LYNCH, B.Sc.

A thesis submitted for the degree of Doctor of Philosophy of the University of Aston in Birmingham.

August 1968.

SUMMARY

The precipitation reactions occurring in a series of copper-based alloys selected from the system copper-chromium-zirconium have been studied by resistometric and metallographic techniques.

A survey of the factors influencing the development of copper-based alloys for high strength, high conductivity applications is followed by a more general review of contemporary materials, and illustrates that the most promising alloys are those containing chromium and zirconium. The few systematic attempts to study alloys from this system have been collated, discussed, and used as a basis for the selection of four alloy compositions viz:-

Cu - 0.4% Cr

Cu - 0.24. Zr

Cu - 0.3% Cr - 0.1% Zr

Cu - 0.2% Cr - 0.2% Zr

A description of the experimental techniques used to study the precipitation behaviour of these materials is preceeded by a discussion of the currently accepted theories relating to precipitate nucleation and growth.

The experimental results are presented and discussed for each of the alloys independently, and are then treated jointly to obtain an overall assessment of

the way in which the precipitation kinetics, metallography and mechanical properties vary with alloy composition and heat treatment.

The metastable solid solution of copper-chromium is found to decompose by the rejection of chromium particles which maintain a coherent interface and a Kurdjumov-Sachs type crystallographic orientation relationship with the copper matrix. The addition of 0.1% zirconium to the alloy retards the rate of transformation by a factor of ten and modifies the dispersion characteristics of the precipitate without markedly altering the morphology.

Further additions of zirconium lead to the growth of stacking faults during ageing, which provide favourable nucleation sites for the chromium precipitate. The partial dislocations bounding such stacking faults are also found to provide mobile heterogeneous nucleation sources for the precipitation reactions occurring in copper-zirconium.

TABLE OF CONTENTS

CHAPTER 1.

LITERATURE SURVEY

LITERATURE SURVEY

1.0 Introduction

A survey of the development of high conductivity, high strength copper alloys must be preceeded by a discussion of the underlying principles governing any attempt to vary mechanical properties without adversly affecting conductivity.

1.1 The Conductivity of Copper

The simplest model used to account for the conduction of electrons by metals is one in which the positive ions are arranged in a geometrically perfect array, and are surrounded by a diffuse cloud of loosely bound electrons which, under the influence of an applied potential, will drift through the lattice. From this model it follows that the resistance to the flow of electrons can result from collisions between positive ions and electrons, or from the inability of the electrons to escape from the field around the positive ion. The latter condition gives an indication of the inherent conductivity of metals, and using this criterion alone, the elements possessing the highest conductivity are the monovalent metals Lithium, Potassium and Sodium. However, the mean free path of electrons in the metallic state controls the velocity of electrons moving under an applied potential and it is this parameter which controls the total conductivity attainable. Copper, Silver and Gold have the highest total conductivity

when these two factors are considered together. Fig.1.1

Fig.1.1 Conductivity v Period Number

A more realistic model takes into account the vibrational amplitude of metal atoms about their crystal lattice points which occurs at temperatures above $0^{o}K$. However, over a wide temperature range, the incoherent scattering produced by thermal vibrations in the copper lattice is small in comparison to that of other metals and explains the efficiency of copper as an electrical conductor.

As well as effects due to temperature, the lattice periodicity in metals is disturbed by point and planar defects. Vacant lattice sites, interstitial and

substitutional impurity atoms, dislocations, grain boundaries and stacking faults all affect the periodicity of the metallic lattice and their presence causes an increase in resistance to the passage of electrons. It has long been realized that other defects play an insignificant role in reducing the electrical conductivity compared with the presence of substitutional impurity atoms, and indeed, the past difficulties in preparing pure copper samples have led to the curious position whereby a present day material can possess a conductivity of 103% of the International Annealed Pure Copper Standard (I.A.C.S.)*. A conductivity of 100% I.A.C.S. corresponds to a resistivity of 1.7241×10^{-6} ohm.cm^{-3} at $20^{\circ}C$ whereas O.F.H.C. copper is supplied today with an electrical conductivity of 101.7% I.A.C.S.

Gregory, Bangay and Bird[1] have reviewed the position regarding the ultimate conductivity attained to date and report a value of 103.06% I.A.C.S. which was obtained using copper with a stated impurity level of less than 8 p.p.m.

---

* In 1913, the International Electrotechnical Commission laid down a standard for the measurement of conductivity which states that copper wire of density 8.89 gms/c.c., 1 metre long, weighing 1 gramme and having a resistance of 0.15328 ohms has a conductivity of 100% I.A.C.S., all measurements being made at $20^{\circ}C$.

1.1.1 Effect of Impurities

Many workers[2,3,4] have devoted their efforts to making additions of single elements to copper and assessing their effect on electrical conductivity. The combined results are presented graphically in Fig.1.2 and as a table(Table I) and are based on a copper containing less than 10 p.p.m. impurity prior to alloying. A linear relationship exists between the presence of substitutional impurity atoms in solid solution and electrical resistivity. This is in agreement with the earlier concept which predicts that disturbances of the lattice periodicity on an atomic scale, as produced by solute in solid solution, are more effective in increasing electrical resistance than second phase particles which are generally too far apart to influence the mean free path of the electrons. The contribution of second phase particles to the resistivity

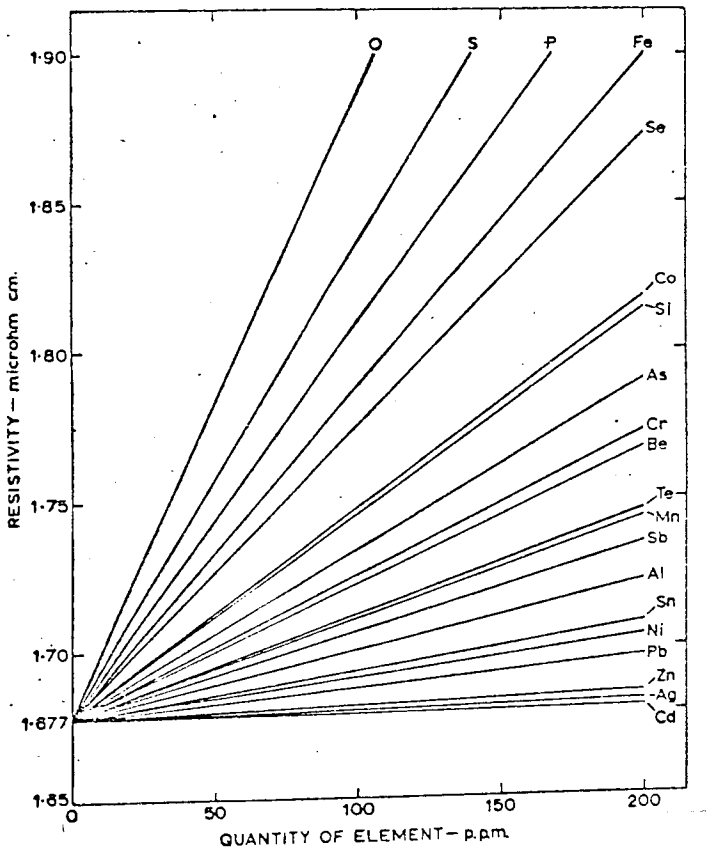

Fig.1.2 Effect on electrical resistivity of elements present singly in solid solution in copper.

of copper is therefore slight, i.e. that due to the atomic volume of copper it displaces, whereas impurity atoms in solid solution markedly increase the resistance of copper.

Impurity Element	Increase in Resistivity (microhm cm.) per 10 Parts per Million Increase of Impurity Element			
	Pawlek and Reichel[7]	Smart and Smith [13, 14, 15]	Hess and Pawlek[11]	Mean Value
Oxygen	—	—	0·02105	0·02105
Sulphur	—	0·01375	0·01824	0·01600
Phosphorus	0·01460	0·01185	—	0·01323
Iron	0·01023	0·01219	—	0·01121
Selenium	—	0·01100	0·00845	0·00973
Cobalt	0·00727	0·00684	—	0·00706
Silicon	0·00687	—	—	0·00687
Arsenic	0·00560	0·00568	—	0·00564
Chromium	0·00481	—	—	0·00481
Beryllium	0·00451	—	—	0·00451
Tellurium	—	0·00267	0·00418	0·00343
Manganese	0·00325	—	—	0·00329
Antimony	0·00285	0·00290	—	0·00288
Aluminium	0·00225	—	—	0·00225
Tin	0·00155	0·00154	—	0·00155
Nickel	0·00118	0·00152	—	0·00135
Lead	0·00093	—	—	0·00093
Zinc	0·00034	—	—	0·00034
Silver	0·00040	0·00009	—	0·00020
Cadmium	0·000 8	0·00014	—	0·00016

Table I. Increase in resistivity produced by impurity elements present singly in solid solution in copper.

1.2 Mechanical Properties of Copper

The mechanical strenth of polycrystalline copper may be increased by (i) Deformation or (ii) Alloying.

1.2.1. Deformation

This is probably the most potent way of increasing the strength of copper without adversly affecting the electrical conductivity. In the annealed condition, the dislocation density is likely to be approximately 10^6 lines/cm^2, whereas after deformation, dislocations densities ranging from 10^{11} - 10^{13} lines/cm^2 are found, producing an increase in the flow stress from 2.8 kg/mm^2 to 19 kg/mm^2, with a corresponding reduction in conductivity of 3% I.A.C.S.

The structure of cold worked copper is typical of that expected from a material of medium/high stacking fault energy (70 ergs/cm^2) in that a cell structure is produced

bounded by tangled dislocation lines Fig.1.3. The mean diameter of the underformed cells in the electron micrograph is 1 micron, which is in agreement with a value obtained by Warrington[5] for copper deformed at room temperature.

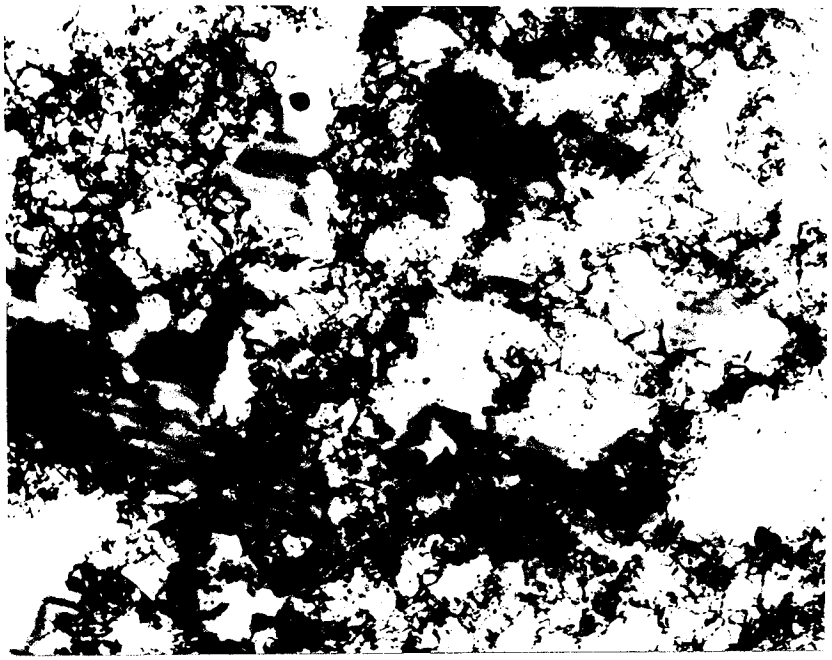

Fig.1.3 Cell structure developed in 10% cold rolled copper.

1.2.2 Alloying

In the preceding section 1.1.1, it was shown that alloying elements in solid solution invariably lower the electrical conductivity. Similarly, such small additions also increase the flow stress markedly. Seeger[6], and more recently honeycombe[7] have independently reviewed the effect of solid solution strengthening in single crystals where the effect is much more apparent than in polycrystals, especially at low temperatures. The effect of solute elements on the critical resolved shear stress of single crystals can be three times as great at $0^{\circ}K$ as it is at room temperature. An account of the theoretical situation involved in solid solution strengthening is given in

Seeger's[6] article.

A more startling increase in yield strength can accompany the precipitation of a second phase from a super-saturated solid solution. In most metals exhibiting age-hardening, the yield stress increases from a value of approximately $10^{-3}G$ in the solution treated condition, to values approaching $10^{-2}G$ when fully aged, where G is the shear modulus of the material.

For example, polycrystalline copper has a yield strength of 2.8 kg/mm^2 in the solution annealed condition which is approximately $10^{-3}G$ since $G = 4.6 \times 10^3 kg/mm^2$. Therefore, the maximum yield stress to be expected from a precipitation hardenable copper alloy is:-

$10^{-2}G = 46$ kg/mm^2 or 29 tons/sq.ins.

Copper - 2% Cobalt - 0.5% Beryllium represents the strongest age-hardening copper based alloy developed and typical values of yield stress are 60 - 65 kg/mm^2, which corresponds to $G/75$. Unfortunately the room temperature solubility of Beryllium in copper is high, and the maximum values of conductivity that can be achieved in the fully aged alloy are 45 - 50% I.A.C.S.

Having outlined the principles governing the development of copper based alloys for high strength, high conductivity applications it is instructive to trace the history of such developments in the copper industry.

1.3 Contemporary Materials

The most striking fact to emerge from such a study is the reluctance on the part of electrical engineers to depart from the use of heavily wrought tough pitch copper or O.F.H.C. copper for appliances operating at room temperature. However, it is common, in the fabrication of components requiring high strength and conductivity to include either soldering or brazing operations. In such instances, heavily wrought copper is found unsuitable and small additions of silver or cadmium have been introduced to increase the temperature at which recrystallization of the heavily wrought components occurs. Comparative properties of two such commercial materials are shown in (Table II). Additions of silver exert little effect on the electrical or mechanical properties of pure copper, whereas cadmium gives rise to a slight increase in mechanical properties with a corresponding decrease in conductivity.

Alloy	Added Elements %	0·1% Proof Strength ton/in.²		Tensile Strength ton/in.²		Elongation† %		Hardness HV		Shear Strength ton/in.²		Conductivity % IACS	
		A	H	A	H	A	H	A	H	A	H	A	H
Copper	—	4	21	14	25	50	4	45	115	10	14	100	97
Copper-silver	0·02–0·15 Ag	4	21	14	25	50	4	45	115	10	14	100	97
Copper-cadmium	0·2–1 Cd	4	30	18	35	45	3	60	140	12	20	90	80

Table II. Comparative properties of high conductivity materials in the annealed (A), and the cold worked (H) condition.

Brazing cycles involving transient peak temperatures of 500 - 600°C, together with the need for conductors to operate continously at temperatures in the range 150 - 200°C introduced precipitation-hardenable alloys into the range of materials used in the copper industry. An alloy containing up to 1% chromium was found to give an adequate combination of properties, and since maximum properties are developed by a heat-treatment cycle, then the system is more stable than one involving heavily wrought products. Several workers[8] have reported that copper chromium alloys become notch-sensitive at temperatures in the range 100 - 250°C, but have advanced no explanation for this unusual behaviour. However, such reports have led to the investigation of alloys containing zirconium as suitable alternatives. Fig.1.4 shows the resistance to softening of both copper chromium and copper zirconium during isochronal annealing experiments with reference to copper and a copper silver alloy (all cold worked), indicating the superiority of precipitation hardening systems where stability of mechanical properties is required at elevated temperatures. Based on empirical approaches, additions of both chromium and zirconium have been made to copper in the hope that alloys combining the desirable properties of both binary systems could be developed. A review of such attempts, together with a survey of work performed on the binary systems copper chromium, and

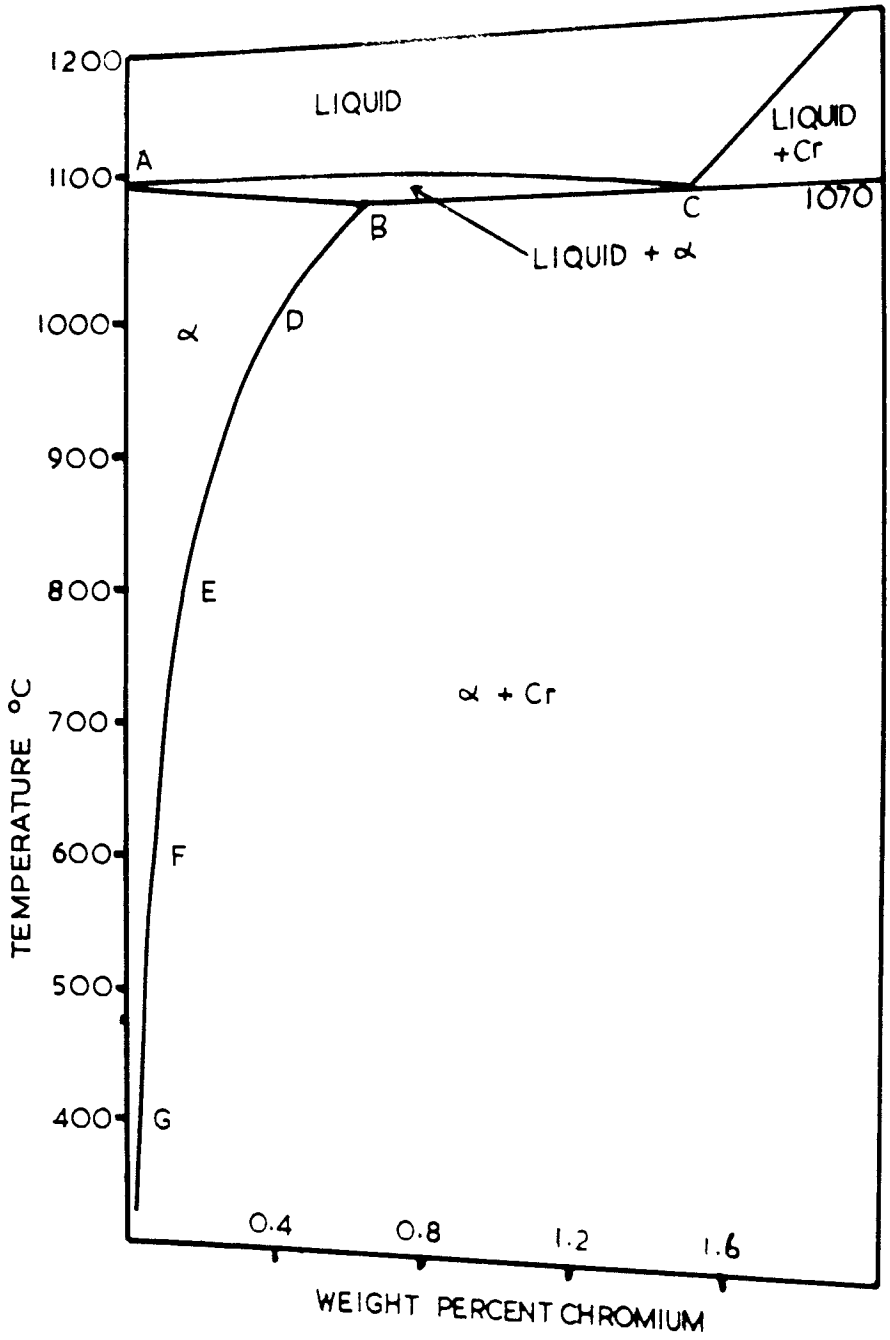

Point	A	B	C	D	E	F	G
°C	1083	1070	1070	1000	800	600	400
%Cr	0	0.65	1.5	0.4	0.15	0.07	<0.03

Fig.1.5 Relevant Section of the Copper Chromium Equilibrium Diagram (Hansen)

copper zirconium follows.

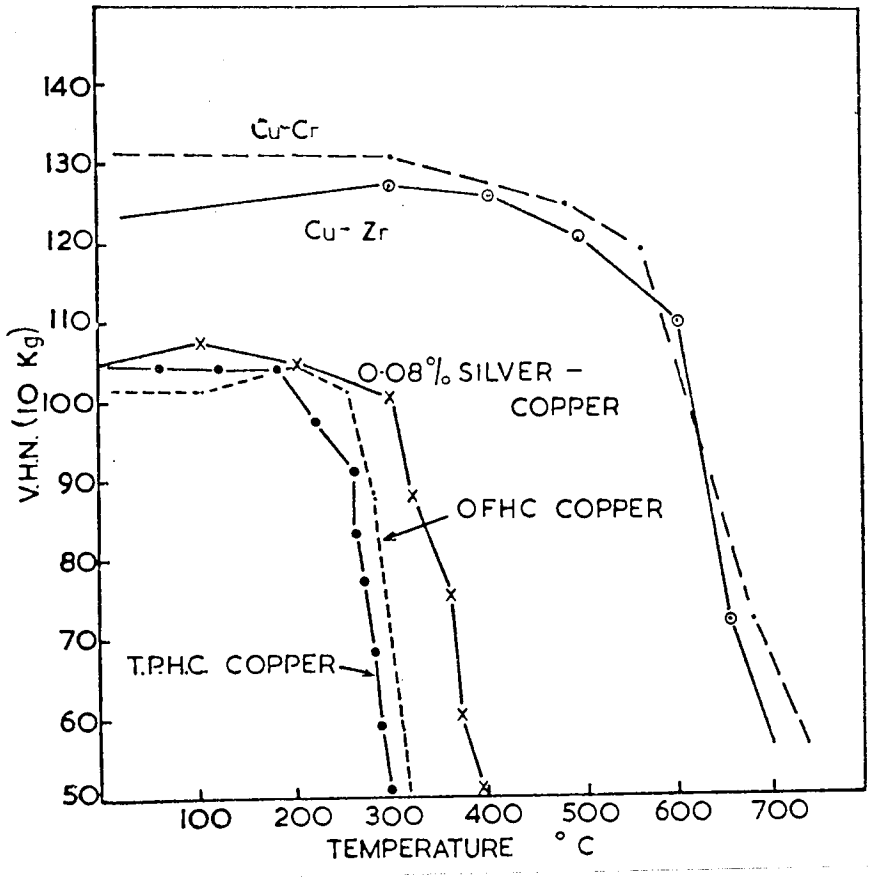

Fig.1.4 Resistance to softening of five high-conductivity materials. Test specimens cold worked then heated for 30 mins. at temperature, air cooled and tested.

1.4 The System Copper-Chromium-Zirconium

1.4.1 Phase Diagrams

1.4.1.1 Copper Chromium

The system copper chromium is a simple eutectic one in which no intermetallic compounds are formed, and in which each element has a very limited solubility in the other. The section of the equilibrium phase diagram concerning this study is that shown in Fig.1.5 i.e. the copper rich end. According to Hansen[9], this part of the diagram has received the attention of many workers, and its accuracy is well established. The diagram illustrates the very restricted temperature range in which alloys

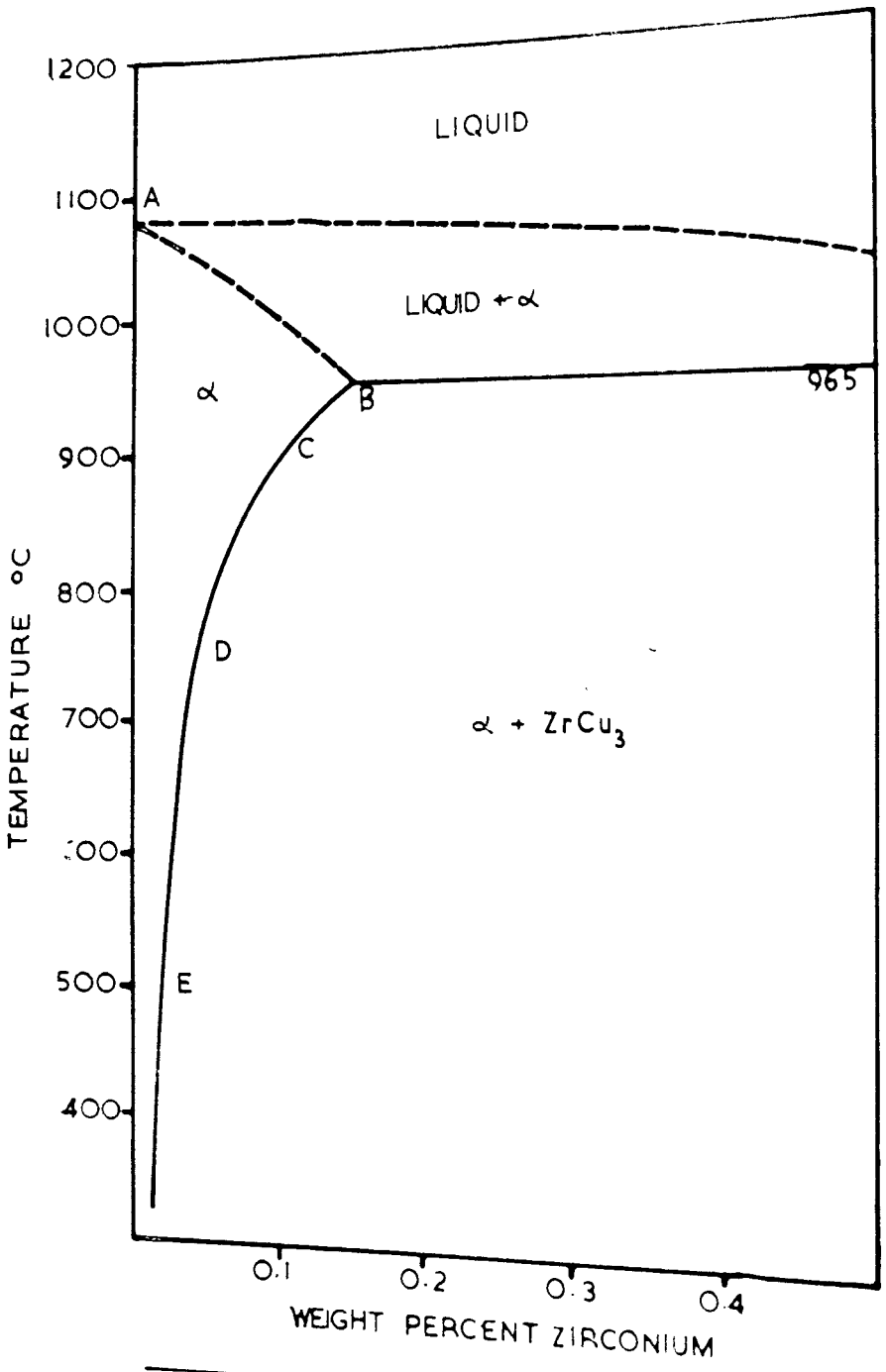

Point	A	B	C	D	E
°C	1083	965	900	750	500
% Zr	0	0.15	0.08	0.03	0.01

Fig.1.6 Relevant Section of the Copper Zirconium Equilibrium Diagram (Saarivirta[10])

containing more than 0.5% chromium may be heat treated to obtain a single phase solid solution. The system can be made to precipitation harden by the rejection of chromium from a super saturated solid solution.

1.4.1.2 Copper Zirconium

The majority of investigations in this system have been concerned with an assessment of the solubility of zirconium in copper and its variation with temperature.

Early publications reported a maximum solubility of 1.0 wt.% at the eutectic temperature of 965°C. Recently, Saarivirta[10], Zwicker[11], and Showak[12] have reported the maximum limit of solubility of zirconium in copper as 0.15, 0.11 and 0.24% by weight repectively with room temperature solubility between 0.01 and 0.02%. Fig.1.6 shows the copper rich portion of the copper zirconium phase diagram, after Saarivirta, based on microstructural examination.

The first intermediate phase has been reported as Cu_2Zr (32.37% Zr), however, little data is available to substantiate this conclusion, and Hansen[9] has suggested that Cu_4Zr (20.41% Zr) might be more appropriate. Donachie[13], using microprobe analysis supplemented by metallographic and thermal analysis indicated that the first intermediate phase was Cu_4Zr and reported the maximum limit of solubility of zirconium in copper as 0.17% by weight at 970°C, which

COPPER-RICH END
OF THE COPPER-CHROMIUM-ZIRCONIUM
EQUILIBRIUM DIAGRAM

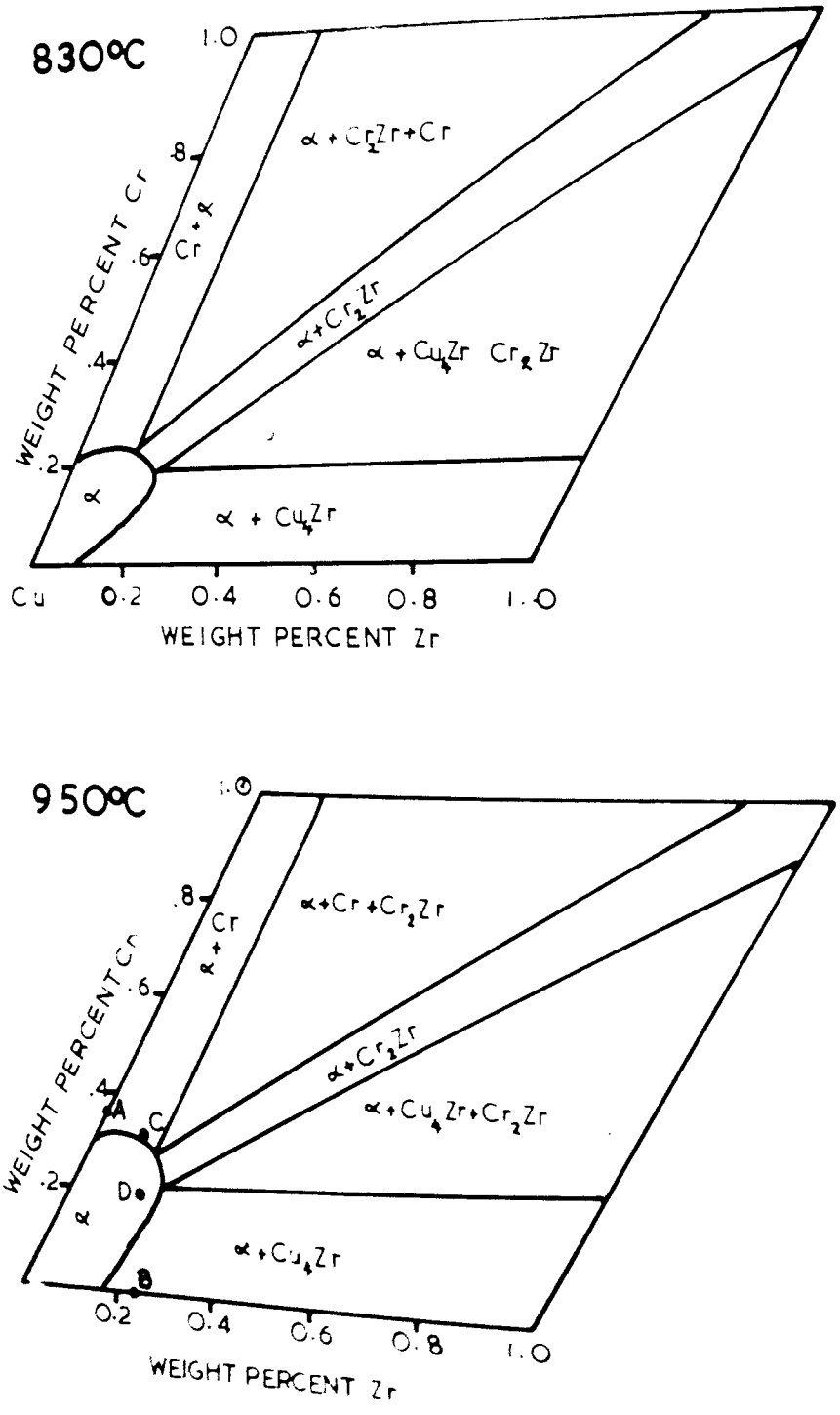

Fig.1.7 Ternary Isotherms for Cu-Cr-Zr (Harris[15])

is close to the value of 965°C chosen by Hansen[9] and 980°C reported by Showak[12].

1.4.1.3 Copper Chromium Zirconium

The ternary system within the range 3.5 wt.% Zr - 3.5 wt.% Cr has been investigated by Zakharov, Stepanova and Glazov[14], and more recently by Harris[15]. The techniques employed were microhardness testing and electron probe microanalysis respectively. The results of the two investigations are markedly different, although both show that the equilibrium solubility of each element increases in the presence of the other. A pseudo binary is formed between the α solid solution and Cr_2Zr, a laves phase with a hexagonal crystal structure, $c/a = 1.63$, and which is stable below 990°C.

Two isotherms have been determined by Harris[15], one at 950°C and another at 830°C Fig.1.7, which illustrate that the α solvus line of the ternary diagram follows closely that predicted from the behaviour of the constituent binary diagrams, and it is therefore likely to be a more accurate determination of the solid solution phase boundary than the work of Zakharov[14] et.al. Furthermore, it is suggested from the work of Zakharov et.al. that the solubility of zirconium in copper at 970°C exceeds 1.0 wt.% and that of chromium in copper at 1070°C 1.0 wt.%. From these figures it appears that microhardness measurements are unsuitable for the determination of phase boundari

1.4.2 Precipitation Behaviour

1.4.2.1 Copper Chromium

The first systematic study of the precipitation of substantially pure chromium from copper is due to Köster and Knorr[16]. Using an alloy containing 0.6% Cr and 0.015% Fe, they measured changes in hardness, conductivity, magnetic susceptibility and thermo-electric power during isothermal ageing experiments. The hardness results are reproduced, Fig.1.8, for the alloy quenched from 1030°C since they outline the general form of all the property changes measured. Isothermal ageing treatments performed at temperatures above 600°C yielded little information regarding the rate of separation of chromium because of a tendency for the solid solution to re-form, thus not giving a rate solely due to the precipitation reactions occurring at that temperature.

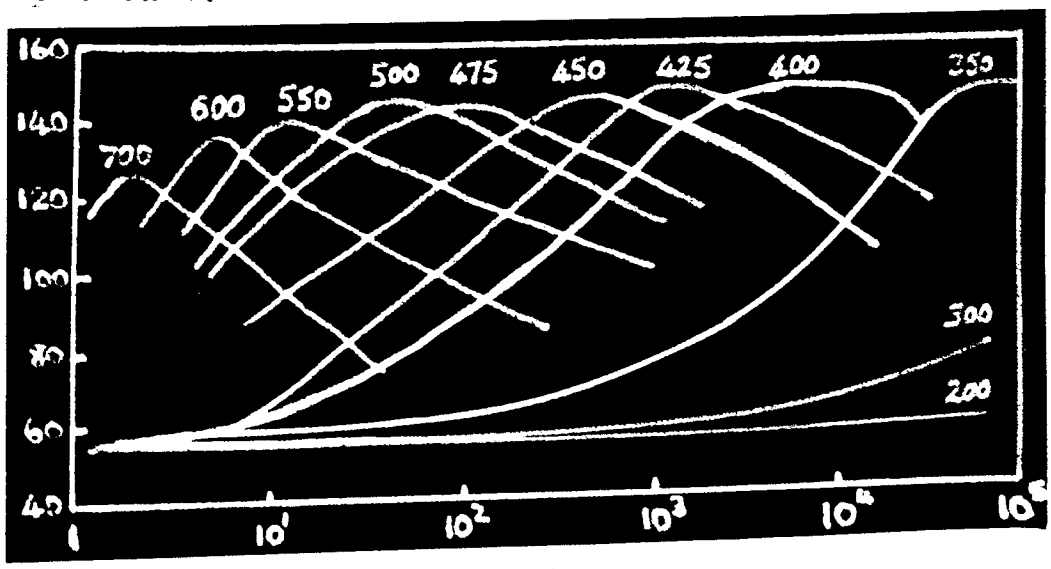

D.P.N.

Ageing Time (minutes)

Fig.1.8 Isothermal ageing behaviour of Cu - Cr after Köster and Knorr

A value of 2.1 eV for the activation energy of separation of chromium from copper is quoted using data collected from experiments following changes in hardness and conductivity whereas a lower value of 1.4eV is obtained by measuring susceptibility and thermo-electric power changes during ageing. Although, in their paper Köster and Knorr[16] do not state over what range of ageing temperatures these values of activation energy apply, it is assumed to be from 550°C - 700°C. Moreover, no attempt is made to analyse exactly what such a value means in terms of the nucleation or growth stages of the transformation. The structural changes occurring during hardening were investigated using X-ray techniques, but it was not possible to detect the separation of the chromium from the solid solution. Using a single crystal rotation X-ray method on large grain size samples, Köster and Knorr[16] deduced that no orientation relationship existed between the precipitated chromium and the matrix.

Williams[17] also experienced considerable difficulty in obtaining meaningful data from X-ray analysis of a super-saturated alloy, precipitation treated at 400°C and 500°C. Williams[17] claims that no precipitation could be detected by electron microscopy after ageing at 400°C for 70 days - contrary to Köster and Knorr's results which suggest that precipitation is completed after 6 days at this temperature (see Fig.1.8). When precipitation was

observed by Williams[17], it was said to proceed via two stages, first by precipitation of very thin plates coherent with the {111} planes of the copper matrix followed by competitive growth of these particles to give maximum strength and eventual loss of coherency. Based on observations that chromium precipitate particles tended to lie in four predominant directions in overaged material, Hibbard[18] also suggested that the habit planes of the precipitate were the close packed planes of the copper matrix. An investigation recently carried out by Nishikawa, Kobayashi and Nagata[19] on a series of alloys containing from 0.05% to 0.91wt.% chromium utilising electrical resistivity and hardness measurements, and supplemented by transmission electron microscopy observations has not led to any clearer understanding of the precipitation behaviour in such alloys. Their resistivity and hardness measurements confirm the much earlier results of Köster and Knorr[16] whilst their electron micrographs are presented without comment.

Further studies made on the precipitation behaviour of chromium from solid solution, notably by Saarivirta[20], Hibbard and Hart,[21] and Hodge[22] are confined to mechanical property measurements obtained from isothermal ageing experiments and no indication is given of possible mechanisms giving rise to these properties. It is noteworthy that results published after Köster and Knorr[16] add

little to the knowledge of hardness changes during ageing. Hibbard and Hart[21], by viewing the system as a dispersion of hard particles in a soft matrix concluded that above 15% strain the increment in the flow stress due to the precipitate is essentially constant and is a function of the amount of precipitate present. Their mechanical test results should be treated cautiously since the experimental procedure adopted in the production of tensile test pieces was to give a 90% reduction cold rolling treatment to 0.2" thick strip followed by a high temperature annealing treatment (800°C). Although no mention is made of testing direction with respect to rolling direction it should be appreciated that this pattern of mechanical and thermal treatments is bound to produce a highly developed "cube-texture" in the test specimen which, in turn, will exhibit highly anisotropic mechanical properties.

1.4.2.2 Copper Zirconium

Copper zirconium alloys were originally developed to eliminate the disadvantages exhibited by copper chromium e.g. notch sensitivity and consequently all of the work published, to date, is of a direct comparison of the properties that can be developed in each material. Unfortunately, the majority of exercises which purport to being comparitive are not. The main reason for this is that copper zirconium, unlike copper chromium, is thought not to age harden in the conventional sense and so

comparisons are often made on materials which have been solution treated, cold rolled and then aged. These comparisons are then wrongly taken to show that copper zirconium alloys containing greater than 0.13% Zr are superior to copper chromium on many counts. Saarivirta[10], Rutherford, Hooley and Hewitt[23], and Lynch[24] have reported such mechanical property data for alloys containing from 0.0% - 1.10% Zr, although Saarivirta[10] shows that optimum mechanical and physical properties are obtained when the zirconium content is sufficient to completely saturate the solid solution i.e. 0.15%. Fig.1.9.

Therefore, whilst a large volume of literature has accumulated concerning the electrical and mechanical properties of heat treated and wrought copper zirconium alloys, no data is available in the literature for the kinetics of or mechanism of the precipitation of zironium from the solid solution formed at the copper rich end of the equilibrium diagram.

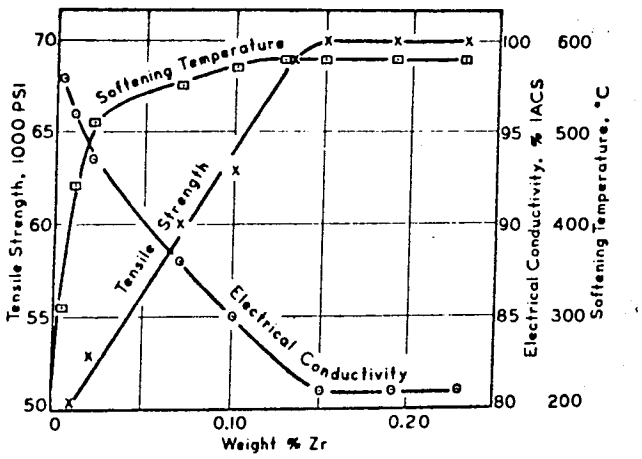

Fig.1.9 Effect of zirconium content on mechanical and physical properties of copper zirconium alloys.[10]

1.4.2.3 Copper Chromium Zirconium

Rutherford, Dooley and Hewitt[23] first pointed out that by the addition of chromium and zirconium to copper creep properties considerably in excess of those exhibited by either binary alloy could be attained but no details of alloy composition were supplied in their report. Mizuno[25] in a review of precipitation hardenable copper alloys concluded that an alloy containing 0.5% Cr and 0.2 - 0.6% Zr showed the greatest precipitation response - again after using an intermediate cold working operation. No investigation to date has specifically set out to elucidate the precipitation reactions in any ternary alloy containing chromium and zirconium.

Table III is reproduced in part from a paper by Richards and Stamford[26] published in May 1968 which may be said to represent, fairly, the state of knowledge concerning

Alloy	Added Elements %	0·1% Proof Stress ton/in.²		Tensile Strength ton/in.²		Elongation† %		Hardness HV		Conductivity % IACS
		Fully Heat Treated	Fully Heat Treated and cold worked*	Fully Heat Treated	Fully Heat Treated and cold worked*	Fully Heat Treated	Fully Heat Treated and cold worked*	Fully Heat Treated	Fully Heat Treated and cold worked*	
Copper-chromium	0·4–1 Cr	17	23–28	24	27–34	25	25–15	125	130–160	80–85
Copper-zirconium	0·1–0·2 Zr	6	18–26	16	20–30	35	25–12	70	100–135	85–90
Copper-chromium-zirconium	0·4–1 Cr 0·1–0·2 Zr	17	23–28	24	27–34	25	25–15	125	130–160	80–85

Table III. Typical properties of alloys from the system copper chromium zirconium.

the optimum mechanical strength levels which have been attained in copper alloys containing chromium and/or zirconium with or without intermediate cold working operations.

1.5 Concluding Summary

The main points which arise from a study of the literature describing the development of copper alloys containing chromium and/or zirconium are as follows:-

1. Kinetic data regarding the precipitation reactions in an alloy of Cu - 0.6% Cr - 0.015% Fe has been obtained[16], but not interpreted in detail.
2. No electron metallographic studies of the precipitation behaviour of alloys from this system have been reported other than a series of micrographs illustrating the structure of the solid solution for a Cu-Cr alloy[19].
3. Mechanical property measurements for cold worked binary and ternary materials are available, but do not relate to the true ageing response of the alloys. Very few publications quote mechanical test data for solution treated and aged materials.

4. It is agreed that chromium and zirconium alloying additions, when precipitated from solid solution, allow an electrical conductivity of greater than 85% I.A.C.S. to be retained with improved mechanical properties and are consequently the most promising alloying elements to have been used to copper for high strength, high conductivity applications.

1.4 Research Programme

A research programme was initiated to quantitatively assess the precipitation behaviour of alloys from the copper chromium zirconium system. Originally four alloys were chosen from the system such that on solution treating at 950°C, they would exist almost completely as a single phase solid solution. The alloys were:-

(a) Copper - 0.4% Chromium

(b) Copper - 0.3% Chromium - 0.1% Zirconium

(c) Copper - 0.2% Chromium - 0.2% Zirconium

(d) Copper - 0.15% Zirconium

It was found necessary to increase the zirconium content of the copper zirconium binary alloy during the investigation to combat segregation effects. The replacement alloy contained 0.24% zirconium.

Alloy (c) was chosen expressly to investigate the

α + Cr_2Zr psuedo-binary region of the phase diagram (see Fig.1.7) and alloy (b) to assess the effect of trace additions of zirconium on the precipitation behaviour of copper chromium.

The techniques used to execute the programme are described in Chapter 3, and are preceeded by a discussion of the theories relating to precipitation from super-saturated solid solutions.

CHAPTER 2.

PRECIPITATION FROM SUPER-SATURATED SOLID-SOLUTIONS

PRECIPITATION FROM SUPER-SATURATED SOLID-SOLUTIONS

2.0 Introduction

The mechanism by which the nucleation and subsequent growth of precipitates occurs on ageing super-saturated solid solutions has been the subject of much theoretical speculation since the phenomenon of age hardening was first discovered. The most characteristic feature of "nucleation and growth" transformations is that it is invariably a final product which is nucleated and grows. However, this does not preclude the formation of a series of metastable products, each of which eventually gives way to a more stable product until the final equilibrium state is reached. In such cases the overall transformation is made up of a succession of discrete transformations, and it is always possible to determine whether or not a particular point has transformed because the material at that point will either be in the initial or final condition at any instant.

Nucleation in such transformations may be either homogeneous or heterogeneous. Homogeneous nucleation occurs at random throughout the parent phase and may be regarded therefore as a natural property of the phase concerned. One condition for homogeneous nucleation is that any small volume element in the parent phase must be identical in terms of structure, composition and thermodynamic characteristics with every other volume element. Under these conditions the location

of each nucleus is determined by chance as a result of a statistical fluctuation which might have occurred anywhere throughout the phase. In practice the above condition is rarely satisfied since the presence of imperfections, grain boundaries, surfaces, and impurities produces local energy peaks which increase the probability of nucleation at such points. Nucleation under these circumstances is spoken of as heterogeneous nucleation.

In considering the nucleation stage in the phase changes typical of most precipitation-hardening systems it has become customary to apply the simpler thermodynamic treatments of classical homogeneous nucleation and then to modify the theories to take into account the factors producing heterogeneity in nucleation.

The study of nucleation is only one part of the study of transformations in general. In a phase transformation two aspects must be considered. Firstly, the transformation will only occur, under a given set of conditions, if a thermodynamic driving force exists. The driving force may always be related to the free energies of the initial and final states, since the criterion for transformation is that a reduction in free energy occurs. The existence of a finite driving force is a necessary but not sufficient condition for transformation. In order that the transformation shall proceed, a reaction path must be available and this usually involves a necessity to surmount

some sort of activation barrier. Thus the rate of transformation will always depend on the rate at which an activation energy can be supplied. Where the activation energy is derived from the thermal vibrations of the atoms, the rate of reaction will be determined by the magnitude of the activation energy and the temperature

i.e. Rate $\propto \exp(-Q/kT)$

where Q is the activation energy, k is Boltzmann's constant and T is the temperature (^{o}K).

The aim in studying the kinetics of nucleation and growth processes is to derive expressions for the rate of transformation and its dependence on temperature and other variables, assuming particular transformation models. These theoretical results are compared with observed kinetics in an effort to elucidate the mechanisms involved. The major difficulty which arises in this work is associated with the dual nature of the transformation process. Different thermodynamic and kinectic considerations are operative in the processes of nucleation and growth, and thus separate rate equations must be derived for each. Experimental difficulties are also considerable - in the first place it is difficult to study nucleation experimentally, because of the size of the initial nuclei expected in precipitation hardening systems, although thin-foil electron microscopy is beginning to contribute to such studies.[27] Secondly, it is found to be almost impossible to

separate the contributions of the nucleation rate and the growth rate to the observed rate of transformation.

2.1 Thermodynamic Treatment of Nucleation Processes

2.1.1 Homogeneous Nucleation

The simplest theory of nucleation was that proposed by Volmer and Weber[28] in 1925 which was derived from observations of droplet formation in super-saturated vapours. In its revised form by Becker and Doring[29] in 1935 the theory led to the concept of a "critical nucleus size" being required before transformation could begin. Equating the change in free energy ΔG associated with the homogeneous nucleation of an embryo of the new phase with the sum of the change in volume free energy ΔG_v and the interfacial energy γ required to form the new surface, gives rise to a critical particle size, above which the embryo will remain stable and grow, and below which it will re-dissolve. viz:-

$$\Delta G = \Delta G_v + \gamma$$

With condensed systems there is an immediate complication arising from the rigidity of the atomic lattice, and a strain energy term must be introduced ΔG_ϵ. Then for a cubic nucleus of edge r at a given temperature and pressure,

$$\Delta G = r^3 \Delta G_v + 6r^2 \gamma + \Delta G_\epsilon$$

The relationship of ΔG with r is considered to have the form shown in Fig.2.1. The condition for continued growth of an embryo is that the radius should exceed a critical value r_c where:-

$$r_c = - \frac{4\gamma}{(\Delta G_v + \Delta G_\epsilon)} \qquad \ldots\ldots (1)$$

The energy required to grow to this radius is known as the activation energy for nucleation ΔG^* and is given by:

$$\Delta G^* = r_c^3 \left(\frac{-4\gamma}{r_c}\right) + 6r_c^2\gamma = 2r_c^2\gamma \qquad \ldots\ldots (2)$$

Substituting the value for r_c obtained in (1)

$$\Delta G^* = \frac{32\gamma^3}{(\Delta G_v + \Delta G_\epsilon)^2} \qquad \ldots\ldots (3)$$

Thus, if an embryo of size less than r_c is formed by fluctuation, ΔG is positive, and an activation barrier exists for the continued growth of the embryo and therefore the embryo can lower its free energy by dispersing.

The most significant result of this analysis is the controlling influence which the interfacial energy exerts on the nucleation process since this term is cubed in the expression for activation energy.

Subsequent developments of the classical nucleation theory by Becker, Borelieus, Hobstelter, Cahn and Hilliard provide very little information concerning nucleation from super-saturated solid solutions primarily because they do

not take into account strain energy effects. Only the theory proposed by Cahn and Hilliard[30] suggests that a sharp interface need not necessarily exist between the nucleus and matrix, so that calculations based on a unique value of the interfacial energy, independent of surface curvature, may not be accurate. A discussion of the above theories dealing with homogeneous nucleation has been presented by Burke[31], and illustrates the very limited nature of such theories when applied to condensed systems.

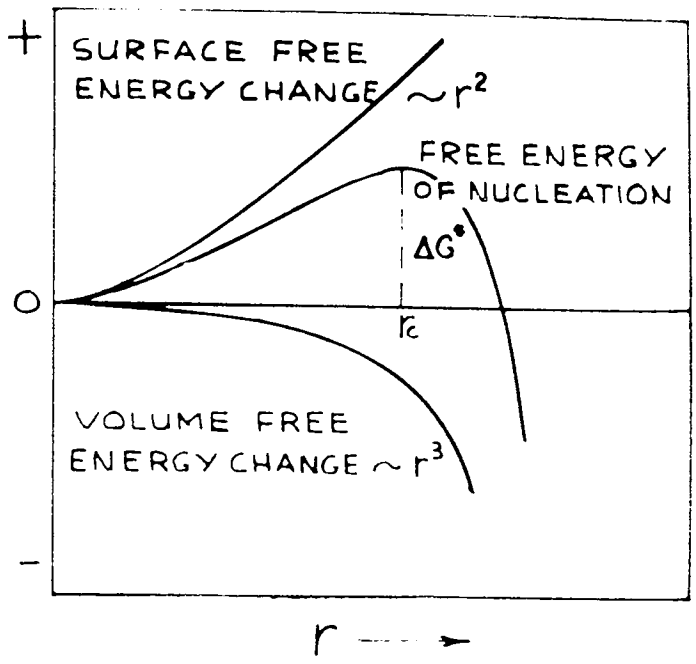

Fig.2.1. Free energy of formation as a function of particle size.

2.1.1.1 Strain Energy Considerations

It is easily shown that some aspects of nucleation such as shape and coherency effects can only be interpreted on the basis of the influence of strain energy. Strain energy in precipitation arises from two sources. Firstly, there are dilatational effects i.e. the precipitate particle may be larger or smaller than the volume of the matrix it replaces, and in either case the particle and

matrix will be in an elastically strained condition. Secondly, the precipitate particle may, especially in the initial stages after its formation, form a coherent interface with the matrix and this will usually give rise to coherency strain energy since the particle and matrix must be strained elastically to maintain a coherency "fit" between the matching planes at the interface. By definition, a fully coherent interface has no surface energy whereas all the energy of a non-coherent interface is surface energy, and therefore, to some extent coherency strain energy and surface energy are interchangeable.

Both the dilatational and coherency strain energies are lower for a disc or plate shaped particle than for a sphere. On the other hand, the surface free energy is lower for a spherical particle, since the latter has the lower surface area per unit volume of precipitate. Nabarro[32] has determined the dilatational strain energy as a function of shape for the special case of highly strained incoherent particles, and the relationship is show diagrammatically in Fig.2.2, in which a is the radius and 2c the thickness of a spheroidal particle.

Nicholson and Kelly[27] have considered the morphology and crystallography of precipitation from many systems and show that where the matrix exhibits anisotropic elastic constants, e.g. in most F.C.C. metals, then the precipitate generally forms as discs on the {100} planes. The maximum

strain energy of the precipitate is then accommodated in the direction of minimum elastic modulus in the matrix. Where the atomic misfit is less than 3%, spherical precipitates are generally formed.

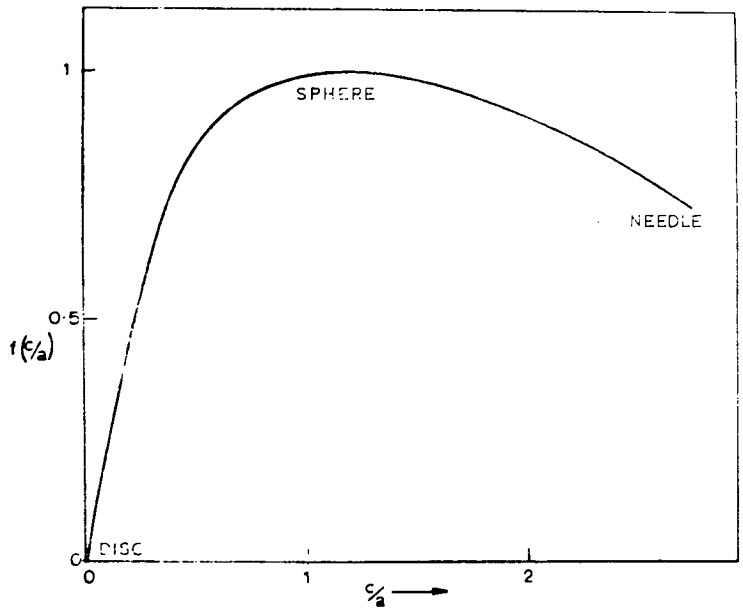

Fig.2.2. Relative strain energy per particle as a function of particle shape, for particles of radius a and thickness 2c.

Friedel[33] suggested that an initially coherent spherical precipitate becomes incoherent when the elastic energy due to the atomic volume difference between matrix and precipitate exceeds the interfacial energy of the precipitate γ. Taking the elastic energy of distortion as equal to $5Gr_0^3\delta^2$ where -

G - shear modulus of matrix

r_0 - precipitate radius at "breakaway"

δ - misfit between matrix and precipitate lattices.

and the surface energy of the non-coherent interface produced at "breakaway" as $4\pi r_o^2 \gamma$, Friedel predicted that precipitates larger in radius than $\frac{4\gamma}{\varepsilon^2 G}$ will be non-coherent. The value of r_o is therefore wholly dependent on the estimated value of interfacial energy between precipitate and matrix.

It follows from these considerations that in the early stages of precipitation when the particles are small and the surface area per unit volume is high, that the surface energy can be reduced or eliminated if the particle is coherent, but as the particle grows and its surface area per unit volume decreases, the coherency strain energy increases faster than the surface energy would increase for a non-coherent particle and a stage is reached when the particle can best minimize its free energy by becoming non-coherent.

In terms of the classical theory of nucleation, the comparison between the nucleation of coherent and non-coherent precipitates can be represented by Fig.2.3.

From Fig.2.3, $\Delta G^{*\prime}$ and r_c' for the coherent particle are lower than ΔG^* and r_c respectively, for the non-coherent particle. Consequently the rate at which coherent nuclei form will be higher than that for non-coherent nuclei. However, at larger particle radii, the free energy curves for the two types of particle cross (C), and beyond this point the non-coherent particle has the lower free energy and is more stable. Thus point C can be

considered as the breakaway point at which coherency ceases to exist and the elastic energy of coherency is replaced by surface energy.

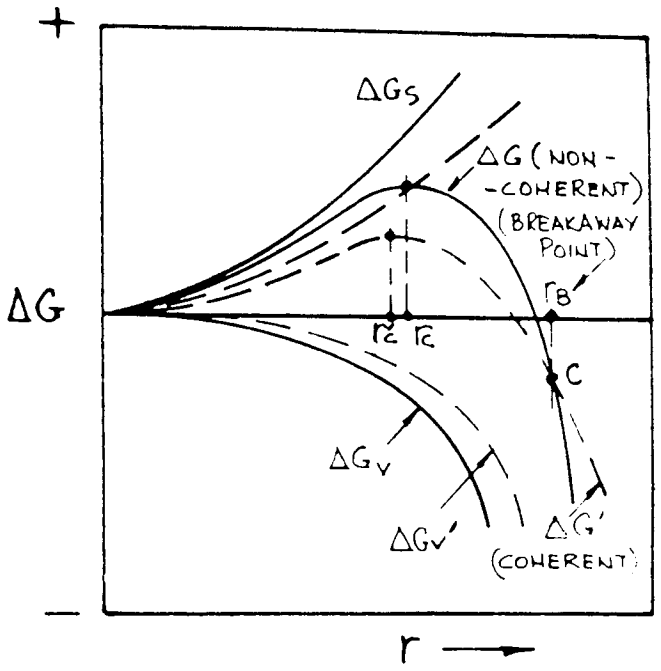

Fig.2.3. Free energy of formation for coherent and non-coherent particles as a function of particle size.

2.1.1.2 Interfacial Energy Considerations

It is clear that the interfacial energy between precipitate and matrix is probably the most important single parameter in controlling the nucleation of precipitates in and consequently the properties and microstructure of, age-hardening materials. Ironically, interfacial energy is one of the more difficult parameters to assess quantitatively in precipitation reactions, and at present three methods are available for its determination, although caution has to be exercised in determining exactly

what one is measuring in each case.

(1) Calorimetric.

(2) Application of the Lifshitz-Wagner theories of Particle Coarsening.

(3) Direct observation of dislocation structures at the interface.

Methods (1) and (2) are applicable to any precipitates, but (3) is obviously limited to semi-coherent precipitates, where such a network can be observed. Only the principle of the method dealing with particle coarsening will be discussed.

(2) Measurement of γ from Lifshitz-Wagner theories

The basic equation describing the coarsening of an aggregate of spherical precipitates is that described by Lifshitz and Slyozov[34] and by Wagner[35]. This predicts that the mean particle size, $\bar{r}_t$ at time t after coarsening has commenced is given by the equation.

$$\bar{r}_t^3 = \bar{r}_o^3 + \frac{8\ D.Co\gamma V_m^2 (t-t_o)}{9RT}$$

where $\bar{r}_o$ is the mean particle size at the start of coarsening i.e. at time t_o

γ is the interfacial free energy of the precipitate
D is the solute diffusivity in the matrix
Co is the equilibrium solute concentration at the temperature T(^oK) and
V_m is the molar concentration of the precipitate phase.

Oriani[36] has shown that providing D is correctly interpreted then this expression describes the coarsening of spherical precipitates in solid matrices. The theory does not take into account the effect of coherency strains on D and C_o, or the creation of dislocation loops at the particle interface. Therefore the best experimental agreement is to be expected from systems with coherent precipitates that have a low misfit at every face with the matrix.

Attempts to measure γ in this way have met with little success due to the fact that the restrictive conditions of Ostwald ripening are not always satisfied during precipitate coarsening. Ardell and Nicholson[37] have obtained the best agreement between theory and experiment for the coarsening of Ni_3Al in a nickel 6.7 wt.% aluminium alloy.

The foregoing thermodynamic treatments assume solute supersaturation to be the dominant factor controlling homogeneous precipitate nucleation. However, recent work by Embury and Nicholson[38] on aluminium alloys has suggested that this is incorrect because the degree of dispersion of precipitates can be sensitive to quenching rate, delay time at room temperature prior to ageing, the rate of heating to the ageing temperature and the presence of trace elements, none of which affects solute supersaturation.

Excess vacancies resulting from quenching the super-saturated solid solution may affect nucleation in many ways. Hardy has proposed that they could form an essential part of the nucleus and this appears likely in systems where the precipitating phase has a specific volume larger than the matrix. Fedorihigi and Thomas[39] have proposed that in systems where the binding energy between vacancy and solute is small, the nucleation processes in general will be accelerated since the excess vacancies can readily return to the matrix after transporting solute to nuclei thereby maintaining the enhanced solute diffusion rates observed in many age-hardening systems. In this case, the vacancies do not change the size of the stable nucleus but increase the probability that embryos will attain this size. Lorimer and Nicholson[40] have studied the effect vacancies have on precipitate nucleation in Aluminium-Zinc-Magnesium alloys and show that precipitate free zones adjacent to grain boundaries in this alloy, formerly attributed to solute denudation are due to vacancy depletion.

2.1.2 Heterogeneous Nucleation

Nucleation in most solid state transformations may be greatly facilitated if hetrogeneous nucleation is possible. This involves the formation of nuclei at particular points throughout the parent phase, where the surface energy, and possibly the strain energy, are

minimized. Such points exist at grain boundaries, dislocations, and at planar defects such as stacking faults.

2.1.2.1 Precipitation at Grain Boundaries

It is a well documented fact that precipitates form more readily at grain boundaries than within grains due to the reduction of the strain energy and interfacial energy terms in the classical nucleation theorems. These effects may lower the activation energy to such an extent that an equilibrium phase is formed in the grain boundary whereas precipitation is either absent or at an earlier stage within the grains e.g. β in Al-Mg.

2.1.2.2 Precipitation at Dislocations

Dislocations may be generated in age-hardening alloys as a result of

(i) quenching stresses

(ii) cold work prior to ageing

(iii) the retention of an excess concentration of vacancies.

The supersaturation of vacancies produced on quenching is a function of the solution treatment temperature. The concentration of vacancies in equilibrium in a crystal at temperature T is given by

$C = A \exp(-E_f/kT)$ where A is a constant

E_f is the energy of formation of a vacancy and

k is Boltzmann's constant.

Simmons and Balluffi[41] report typical values of C for copper quenched from near the melting point as 2×10^{-4}. At room temperature the equilibrium concentration of vacancies is of the order of 10^{-20}, so that prolific nucleation of vacancies must occur either on quenching or subsequent ageing. High supersaturations of vacancies favour the formation of dislocation loops which originate from the collapse of discs of vacancies. Lower supersaturations lead to the formation of dislocation spirals which result from the climb of screw dislocations by the absorption of vacancies.

Preferential nucleation of precipitates at dislocation lines leads to a decrease in the surface energy term in the classical theory since the misfit of the precipitate can be accommodated with a reduction in the line tension of the dislocation. The greater the misfit between solute and solvent atom, the stronger will be the tendency for solute atoms to segregate to dislocations. Hornbogen[42] has demonstrated this tendency using two substitutional iron alloys, iron-gold and iron-copper. The alloys are similar in all respects except that the gold atom is much larger than the iron atom whereas iron and copper atoms are of almost identical size. Precipitation in the iron-copper alloy occurred uniformly throughout the matrix whereas in the iron-gold alloy, precipitates were nucleated only at dislocation lines.

Cahn[43] has treated the kinetics of precipitation at dislocation lines, and concludes that the rate of precipitation on dislocations is greater than the rate of homogeneous precipitation by a factor of approx. 10^{78}. Although experimental findings do not support a factor as high as suggested by Cahn[43], the figure indicates the orders of magnitude involved in precipitation reactions occurring at dislocations.

The nucleation of coherent precipitates does not appear to be assisted by the presence of a dislocation unlike partially coherent precipitates where if the misfit vector is parallel to the Burgers Vector of the dislocation, then the precipitate can be accommodated with a reduction of the total energy of the system.

2.1.2.3 Precipitation at Stacking Faults

A stacking fault is created in F.C.C. lattices by the dissociation of whole dislocations into partial dislocations. Some of the more common dissociations have been conveniently represented by Thompson.[44] Fig.2.4

Stacking faults can influence the nucleation of precipitates in two ways:-

by the (a) Formation of a thin layer of different crystal structure.

or (b) Provision of a partial dislocation.

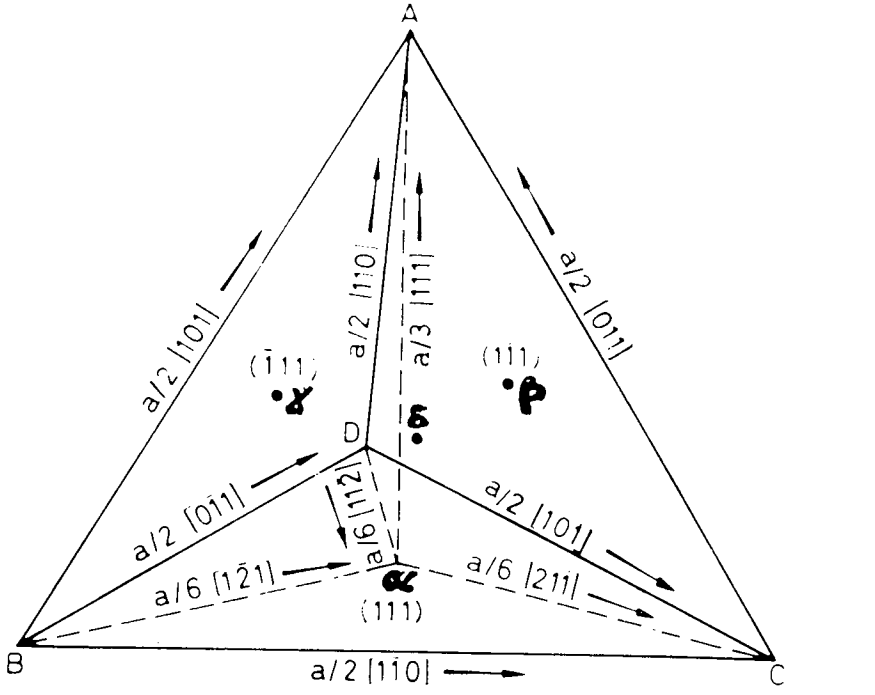

Fig.2.4 Thompson's reference tetrahedron

Suzuki[45] first pointed out that, due to the change in crystal structure within a faulted layer, the equilibrium concentration of solute in the fault may differ from that in the surrounding matrix. Furthermore, segregation of solute atoms to the stacking fault could lead to precipitation if the crystal structure of the fault and precipitate were similar. Cottrell[46] pointed out that the segregation of solute to such faulted regions of the crystal would cause a gradual widening of the partial dislocations bounding the fault because of the localized lowering of the stacking fault energy. The only well established example of the

association of precipitate with stacking faults in this manner is given by Nicholson & Nutting[47] in a study of a precipitation hardenable Aluminium-Silver alloy in which a close packed hexagonal precipitate γ' is formed with a habit relationship:-

$$(111)_{Al} /\!/ (0001)_{\gamma'} \quad \text{or} \quad [1\bar{1}0]_{Al} /\!/ [11\bar{2}0]_{\gamma'}$$

The γ' precipitate has an axial ratio $c/a = 1.59$ which is close to that of the theoretical value of 1.63 for a faulted F.C.C. structure. The fact that this reaction occurs in a matrix possessing an inherently high stacking fault energy lends support to the suggestion made by Cottrell[46].

The energy associated with a dislocation is proportional to the square of its burgers vector and therefore partial dislocations cannot be expected to exert the same influence on precipitate nucleation as do whole dislocations. However, the movement of partial dislocations can be caused by the creation of localized changes in the stacking fault energy of the matrix due to segregation of solute and can therefore be considered as a mobile hetrogeneous nucleating source.

Van Aswegen, Honeycombe and Warrington[48] investigating the tempering behaviour of a niobium stabilized austenitic stainless steel 18Cr/10Ni/1Nb found that stacking faults containing NbC could be grown during

ageing within the temperature range 650°-800°C. They proposed a mechanism involving the nucleation of NbC particles at the partials generated from dislocation interactions i.e. Lomer - Cottrell locks where one partial is rendered sessile while the other moves to form the fault. Propogation of the fault through the matrix occurred by the NbC particles, having grown, shrugging off the partial to a position where it could renew its role as a nucleation site for further precipitation. Silcock and Tunstall[49], carried out a systematic electron microscope investigation of the nature of the stacking faults associated with NbC precipitates in austenitic stainless steel and concluded that the faults were extrinsic, and that they were bound by a Frank sessile and a Shockley partial dislocation. Moreover, they suggested that the factors which appeared to be necessary for the type of stacking fault precipitation observed were:-

1. A low stacking fault energy matrix.
2. A high solute size factor so that segregation to dislocations will occur.
3. Nucleation controlled, to a large extent, by strain energy considerations, so that prolific nucleation occurs at dislocations.
4. An expansion on the formation of the precipitate to facilitate the repulsion of the Frank partial.

5. A precipitate with a fairly simple relationship to the matrix structure.

In further experiments, Silcock was able to show that all of these conditions existed during the precipitation of carbides of niobium, tantalum, vanadium, zirconium and titanium on the partial dislocations bounding stacking faults in tempered austenitic stainless steel. In view of the fact that all five carbides have a simple rock salt structure, the similarity of microstructural features exhibited by these systems is not suprising.

The foregoing discussion of nucleation has included many references to experimental studies of nucleation in the solid state, and illustrates that qualitatively, the theories are in good agreement with experience. However, the few quantitative experiments that have been performed to date indicate that the classical theory of nucleation in its present form is not capable of being applied to solid state transformations. It has been suggested that nucleation is not involved at all in solid state transformations, and that pre-formed nuclei are always present in a phase as groupings of structural imperfections. Dehlinger[50] has shown that it is possible to describe a transition from one lattice to a second in terms of a suitable configuration of dislocations.

the simplest possible example being the stacking fault in F.C.C. structures which is effectively a mono-layer of c.p.h. lattice. If such embryos do exist, then a phase change may be initiated by the growth of these embryos to a size at which they become stable. On this basis, theories of growth can be rationalized in terms of dislocation movement i.e. diffusional growth will occur by dislocation climb due to the migration of solute and vacancies to the embryo, whereas diffusionless growth will occur by the movement of glissile dislocations.

The growth of precipitates from supersaturated solid solutions is an example of diffusional growth and will be discussed briefly.

2.2 Diffusional Growth

The rate of growth of precipitates depends on the rate at which atoms are brought to, or removed from, the interface by diffusion, and the rate at which they cross the interface. During the early stages of growth the area of the interface and the distance over which diffusion is necessary is small, and therefore the rate controlling process is the interface reaction. At larger particle sizes growth becomes limited by the depletion of solute from the solid solution causing a reduction in the concentration gradient and hence the driving force for diffusion. At this stage the flux across the interface is

large due to the increase in area.

Generally the interface and diffusion controlled reactions are of comparable rates and the mathematical models which have been used to analyse the kinetics of diffusional growth are necessarily complex. The main analytical difficulties arise from the complex composition distribution throughout the solid solution when precipitates of varying size are present.

Another means of altering the diffusive flux in a solid solution is provided by the presence of dislocations. Cottrell and Bilby[51] were the first to suggest that misfitting solute atoms would drift to dislocations in order to reduce the total elastic distortion of the lattice. The solute atom will tend to move to that region of the dislocation where the strain is opposite to that associated with the atom, and will therefore form "atmospheres" around the dislocation. In supersaturated solid solutions, precipitate particles nucleate from the atmospheres and further solute drains towards the dislocations, under the action of the stress field, to feed the growing particles. More detailed analyses of the growth of precipitates on dislocations add little to the original analysis of Cottrell and Bilby[51].

The experimental methods available for the kinetic study of diffusional growth processes have been reviewed by Burke[51], and are shown to be on a firmer basis than

those used to study nucleation. The particular techniques used to study the precipitation reactions in the system copper-chromium-zirconium are outlined in the following chapter.

CHAPTER 3.

EXPERIMENTAL PROCEDURE AND TECHNIQUES

EXPERIMENTAL PROCEDURE AND TECHNIQUES

3.1 Materials

The four alloys chosen for examination, and described in section 1.6 were manufactured with the assistance of Johnson Matthey Ltd. at their Wembley research laboratories. 6 kilogram melts were made from the following raw materials:-

	Impurity level
Electrolytic copper	less than 10 p.p.m.
Flake chromium (Murex Ltd.)	less than 100 p.p.m.
50/50 Zirconium-Copper Hardener (I.M.I. Ltd.)	not stated

Melting was performed in the graphite crucible of a vacuum induction furnace and the copper allowed to boil briefly under the prevailing conditions of temperature and pressure ($1250^{\circ}C$ and 10^{-2} mm.Hg), before adding the chromium. The Zirconium-Copper master alloy was introduced at a lower temperature of $1200^{\circ}C$. In order to reduce melting losses, the furnace was pressurized with argon on completion of alloying, and rocked to allow thorough mixing of the alloying constituents. The melts were tapped at 1160-$1180^{\circ}C$ into pre-heated and pre-coated steel moulds of 2" diameter. The billets were radiographed for soundness and then machined to remove any surface scaling defects.

The cast structure was broken down by

homogenization at 800°C under a cracked ammonia atmosphere followed by a rolling and interstage annealing schedule to reduce the billet to rod of 0.75" diameter. The chemical analysis supplied with the material illustrates the degree to which the nominal compositions have been met. (Table IV)

ALLOY	%Cr	%Zr
A. Binary Cu-Cr	0.39	-
B. Binary Cu-Zr	-	0.24
C. Ternary Cu-Cr-Zr	0.33	0.07
D. Ternary Cu-Cr-Zr	0.22	0.20

Table IV

3.2 Test Pieces

The inclusion of chromium and/or zirconium in copper necessitates the use of vacuum equipment for heat treatment operations - especially solution annealing, and consequently imposes limitations on test piece design. A suitable test piece on which to carry out resistivity and mechanical property measurements was found in drawn wire 0.125" diameter and 6" in length, whereas electron microscopy examination was made on heat treated foils 150-250 micron thick obtained by cold rolling transverse slices of the 0.75" diameter starting material.

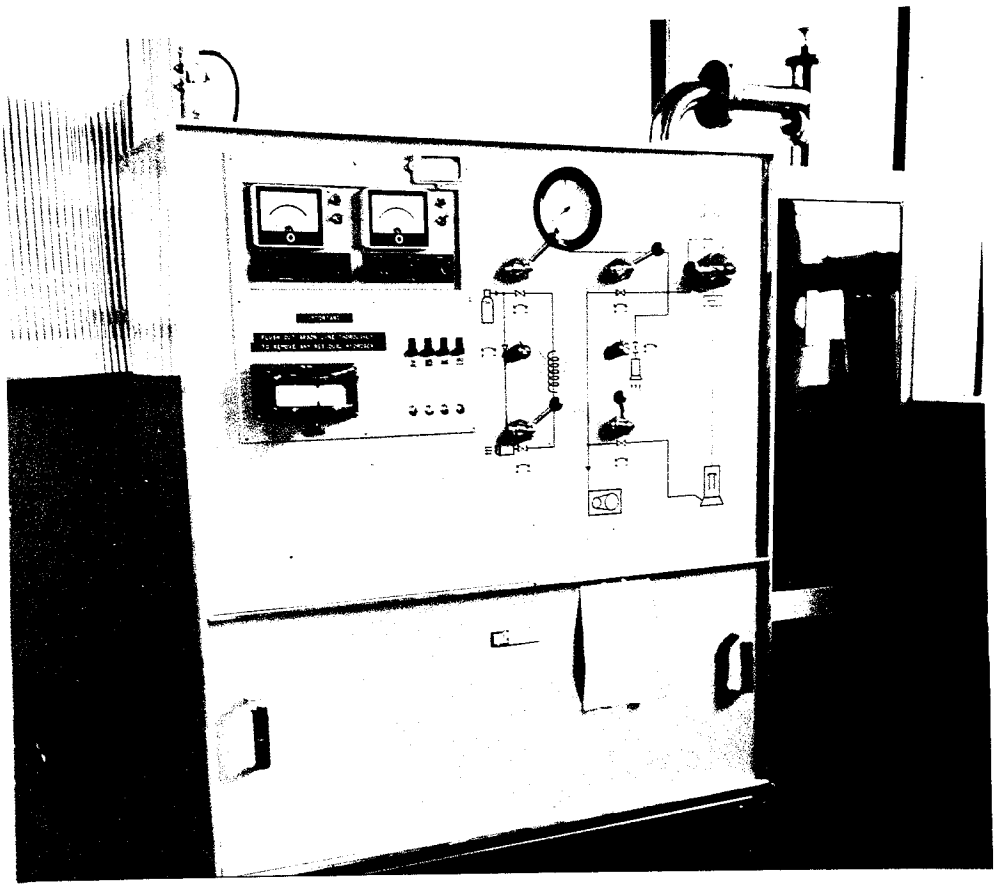

Fig.3.1 Vertically mounted vacuum tube furnace used for the solution heat treatment of materials.

3.3 Heat Treatment

3.3.1 Solution Treatment

In order to reduce the number of controllable variables which exist in any exploration of precipitation hardening systems, the solution treatment of all alloys was carried out at 950°C ±2°C for one hour. The relevent isothermal section Fig.1.7 shows that the alloys under investigation should exist as a single phase solid solution at this temperature. The eutectic occurring in the copper-zirconium system places an upper limit of 970°C on the solution annealing temperature.

A vacuum of better than 2×10^{-5} torr was achieved during solution treatment of all materials at 950°C in the apparatus shown in Fig.3.1. The vacuum seal was broken with super-purity argon (dew point less than 0°C) on conclusion of the solution heat treatment, and the specimen released into the quenching bath situated immediately below the vertically mounted furnace tube.

3.3.2 Ageing

All ageing experiments following room temperature quenching of solution treated material were performed in tube furnaces pressurized with either argon or nitrogen. Heating rates of 300°C/minute were achieved over the 6" furnace hot zone, and temperature control was held to a tolerance of ±1°C. Later experiments showed that the absence of a protective atmosphere at ageing temperatures

below 500°C did not affect subsequent property measurements on heat treated materials.

Experiments involving the quenching of material directly to the ageing temperature had to be performed in fluidized sand baths which could only be controlled to within $\pm 4^{\circ}$C. The abrasive action of the bath introduced difficulties in the subsequent production of electron microscopy specimens from the heat treated foil material. However, these difficutlies were slight in comparison to those introduced when conventional salt baths were tried for such heat treatments -- severe pitting of all specimen surfaces resulted and the method had to be discarded. Heating rates in the order of 1000°C/minute were achieved using fluidized sand baths.

3.4 Electrical Resistivity

3.4.1 Introduction

It was shown in section 1.1.1 that alloying elements exerted least effect on the electrical resistivity of copper when precipitated from solid solution. It follows, therefore, that the measurement of electrical resistivity changes occurring during ageing of solution treated materials can be used to determine the reaction velocity of precipitation reactions within that system. In principle two methods are available, the first involving the measurement of resistivity change on one sample

reacted at the ageing temperature, and the second involving reaction of a series of samples for various times at the ageing temperature. Either method demands that the reaction can be stopped at any required instant, the usual way being to rapidly decrease the temperature. The difficulty with the former method is that continual interuption of the ageing process by quenching and reheating may alter the kinetics of the reaction. The method involving reacting a series of samples for given times obviously places a stringent requirement on the consistency of the samples used, but once this is satisfied then the results obtained from such experiments can be used to derive empirical parameters governing the kinetics of the precipitation process.

3.4.2 Measurement of Resistivity

A potentiometric technique employing a standard double Kelvin bridge circuit was used to measure the resistance of all heat treated specimens. A jig was designed and built such that the potential contact points on the standard 0.125" diameter specimen were 7.95 cms.(l) apart thereby allowing the resistance reading(R)to be directly read from the bridge as the specific resistance or resistivity ρ i.e. since the C.S.A. of the test piece (a) is 0.0795 sq.cms. then $\rho = R \times \frac{a}{l} = R \times 10^{-2}$

The most sensitive range on the bridge for the typical

values measured was obtained using an internal standard resistance of 10^{-4}ohms with a x100 decade arm allowing a range of resistivity values between 0 and 10 $\mu\Omega$ cms^{-3} to be measured to an accuracy of $\pm$0.002 $\mu\Omega$ cms^{-3} at 20°C.

A reference test piece of O.F.H.C. pure copper heat treated to conform with the internationally agreed procedure for annealed copper standards (I.A.C.S.) was available throughout the duration of the work and was used to check the calibration of the bridge and jig periodically. The value corresponded to 101.7% I.A.C.S. or a resistivity of 1.695 $\mu\Omega$ cms^{-3}.

The resistivity of all solution treated specimens was measured prior to ageing, and samples giving values which varied from the mean by greater than 0.1% were rejected. This simple inspection stage satisfied the requirements mentioned above for the method of abstracting kinetic data involving reacting a series of identical samples for various times at each ageing temperature.

Isothermal ageing experiments at temperatures in the range 300-600°C were followed using resistivity measurements for all materials under investigation, and the data treated as follows.

3.4.3. Treatment of Resistivity Data.

Typically, the alloys under consideration transformed in the manner common to most precipitation hardening systems that is, by a nucleation and growth

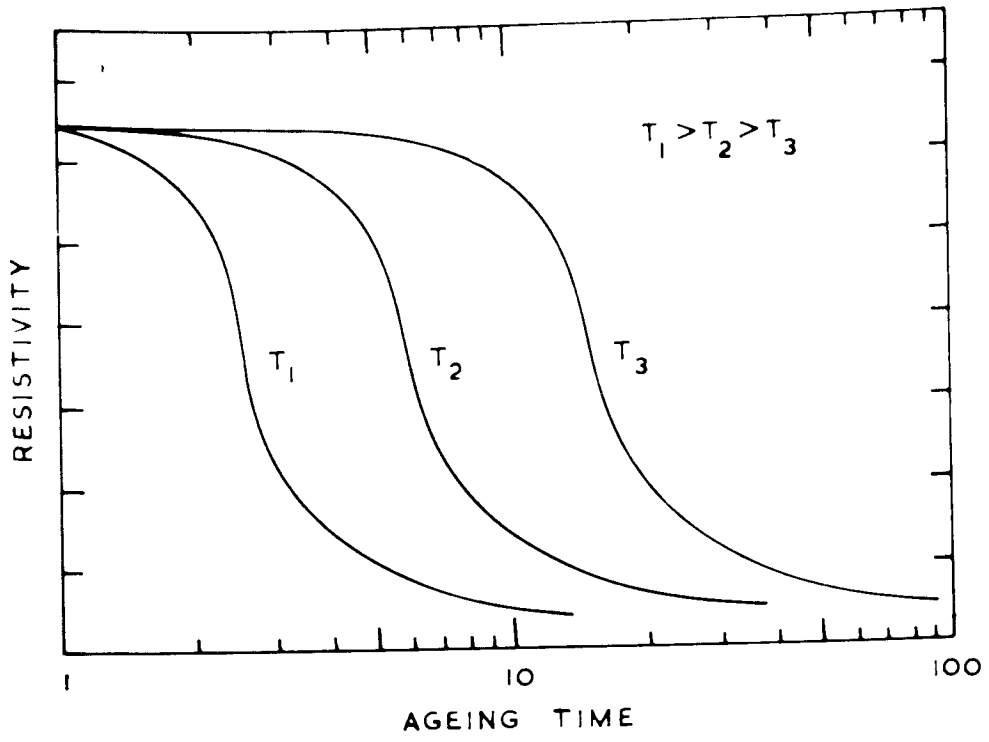

Fig.3.2 Sigmoidal decay curves typical of those obtained during isothermal ageing of the solution treated materials.

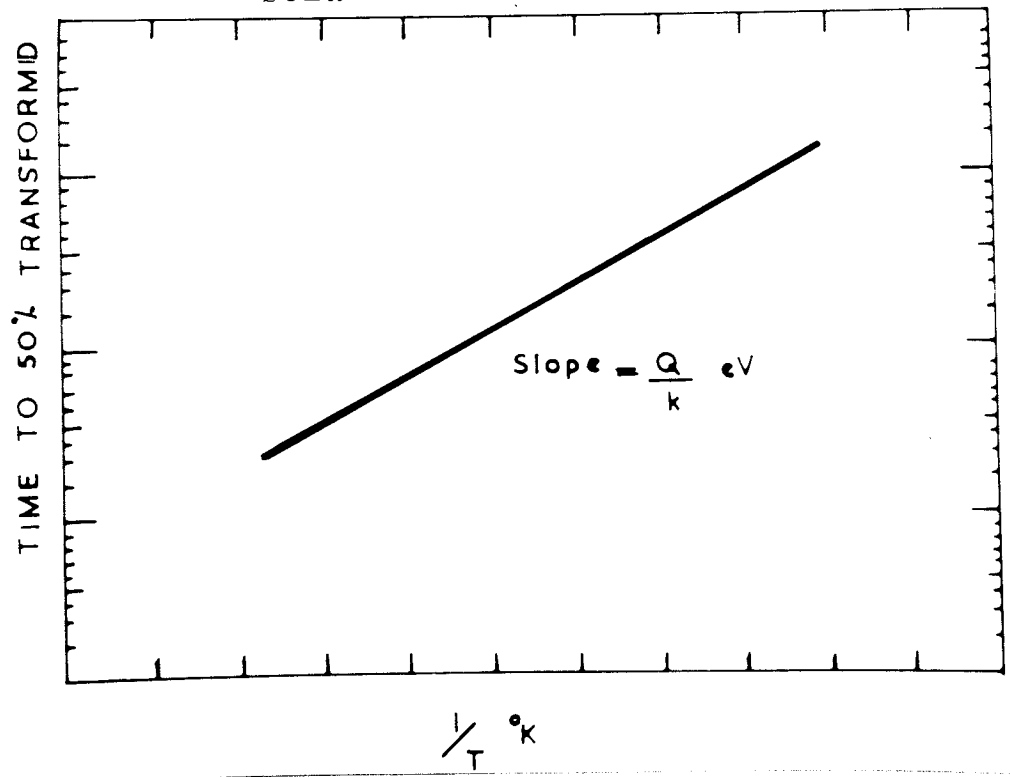

Fig.3.3 Arrhenius graph obtained from the resistivity data shown above.

process. The resistivity data thus yielded families of sigmoidal decay curves when plotted against the logarithm of the time held at the ageing temperature, as shown in Fig.3.2. The time taken to 50% fraction transformed was then plotted against the reciprocal of the absolute ageing temperature to determine whether the empirical activation energy for the precipitation reactions was temperature dependent.

Re-stated, the rate of most reactions on increasing the temperature will increase in accordance with the general Arrhenius rate equation of the type:-

$$\text{Rate of reaction} = A \exp^{-Q/RT}$$

where A is the frequency factor, and Q is the activation energy for the process occurring at $T^{\circ}K$.
Fig.3.3 is a graphical representation of this equation. A marked temperature dependence of the empirical activation energy derived in this way may be taken to signify a change in transformation path, but no fundamental significance can be assigned to the values of such activation energy since they include contributions from the nucleation, and the growth stages of the transformation. The procedure, if repeated for various values of the fraction transformed will reveal any variation of this empirical activation energy with the fraction of material transformed - if none, the reaction is said to be isokinetic that is, the set of

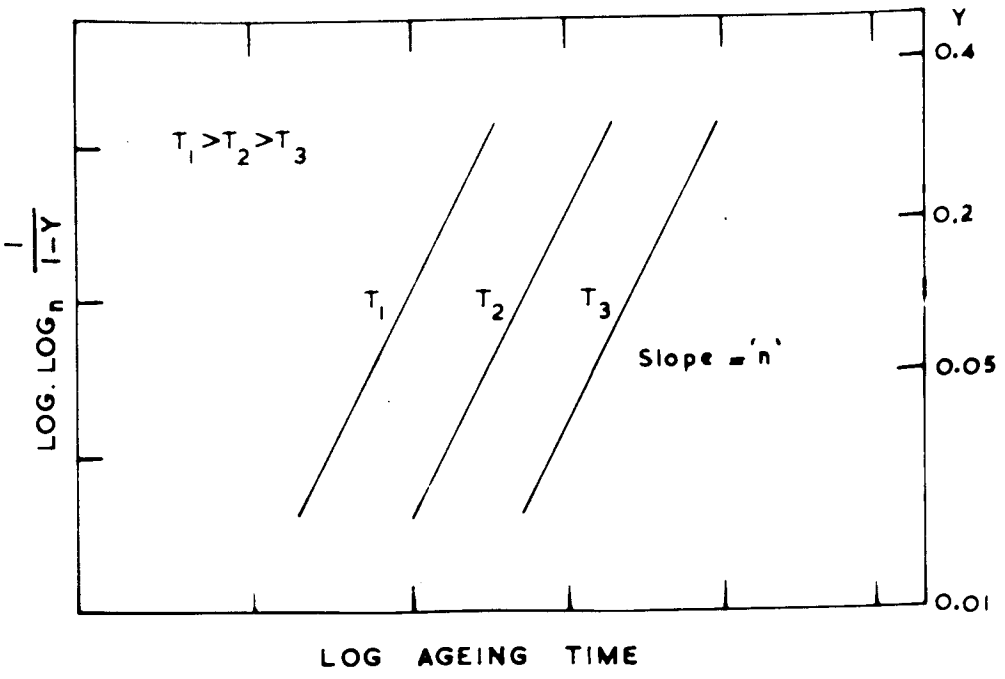

Fig.3.4 Avrami type analysis of resistivity data collected from isothermal ageing experiments.

Model	*n*
Diffusion controlled growth of a fixed number of particles†	3/2
Growth of a fixed number of particles limited by the interface process†	3
Diffusion controlled growth of cylinders in axial direction only†	1
Diffusion controlled growth of discs of constant thickness†	2
Growth on dislocations‡	2/3
Nucleation at a constant rate and diffusion controlled growth	5/2
Growth of a fixed number of eutectoid cells	3
Nucleation at a constant rate and growth of a eutectoid	4

Table V Some values of 'n', the exponent of t in the general rate equation, $y = 1 - e^{-(kt)^n}$. (After Burke[31]).

reaction curves may be brought into identity merely by lateral shift along the log time axis. Further information regarding the kinetics of precipitation in the alloys was obtained by analysing the sigmoidal decay curves in a manner generally accredited to Johnson and Mehl[52]. The general rate equation is given as:-

$$y = 1 - e^{-(kt)^n}$$ where y = fraction transformed
k = rate constant
n = time exponent

An equivalent form is:-

$$\log_n \frac{1}{1-y} = (kt)^n$$

from which, by converting into common logarithms and taking logarithms again

$$\log \log \frac{1}{1-y} = n \log t + n \log k - \log 2.3$$

is obtained. Hence if a reaction conforms to the Johnson Mehl equation, a graph of $\log.\log_n \frac{1}{1-y}$ versus log t is linear as shown in Fig.3.4. The value of the time exponent 'n' is obtained from the slope and has been shown to vary between 0,5 and 6 for diffusional controlled transformations. Burke[31] has listed a typical selection of values of 'n' which have been derived from this type of transformation observed in metallic systems by many workers, notably Avrami[53], and has described the various models of transformation the values are said to represent - see Table V. For such transformations the Johnson-Mehl equation

gives accurate solutions for 'n' up to values of 40% transformation, and therefore the results obtained from the copper alloys have been analysed on this basis.

3.5 Mechanical Properties

3.5.1 Introduction

Unlike single crystal behaviour, the increase in mechanical properties accompanying precipitation reactions in polycrystalline materials cannot be analysed in its component stages. However, a large degree of anisotropy was produced during the production of the standard 0.125" diameter test piece by wire drawing from 0.75" diameter rod without recourse to interstage annealing treatments —— a reduction of 97. R/A. The subsequent mechanical property measurements were therefore expected to be more sensitive to ageing reactions than a test piece machined from a randomly orientated polycrystalline material.

3.5.2 Measurement of Mechanical Properties

Assesment of elastic constants were made on all materials using a Denison (T56 Model) tensile machine and a Houndsfield Extensometer. Where 0.1% proof stress values did not exceed 5 tons/sq.ins. the modulus of elasticity of the materials was taken as that of pure copper i.e. 18×10^6 lbs/sq.ins.

Values for the ultimate tensile strength of the

materials tested are quoted to an experimental accuracy of ±0.5 tons/sq.ins. because of the poorly defined gauge length obtained with wire specimens and the effect of the grips. Similarly, elongation values are expressed on a non-standard gauge length of 3" and are given only as a guide to the properties of the materials. A strain rate corresponding to a cross-head travel of 2 inches per minute was used throughout the tests.

3.6 Electron Microscopy

3.6.1 Foil Preparation

The route by which 200μ thick foil material was produced could be used to exercise some degree of control on the predominant foil orientation observed in the electron microscope. Discs of 0.125" in thickness were cut transversly from the 0.75" diameter starting material and polished on the cut faces to produce a good surface finish after rolling to 200μ — an important pre-requisite to successful electropolishing. By successively limiting the deformation of the disc to 40% reduction in thickness and then annealing at 650°C for ½ hour, predominant orientations of the final foil were {110} planes or {112} planes parallel to the surface. This texture was unaltered after solution treating and ageing the materials.

However, by reducing the discs to foil of 200 microns thick in one stage (a reduction of 94%) a

strong pure metal texture was obtained in all materials which, on solution treating at 950°C, was converted by secondary recrystallization to an equally strong "cube texture" i.e. {100} planes parallel to the surface of the foil. A more detailed account on the crystallography of foil orientations is reported as Appendix I.

The electropolishing of the heat treated foils was satisfactorily performed using the conventional "window technique" as described by Tomlinson[54] in a solution of 66% Methanol : 33% Nitric Acid using a stainless steel cathode and operating at an applied voltage of not less than 10 volts. For preliminary thinning down to approximately 10 microns, the solution could beoperated at temperatures up to 25°C providing the specimen was constantly agitated. Final thinning and perforation was accomplished in the same electrolyte but the current density was limited to 0.02 amps/sq.cms. by lowering the termperature of the bath to approximately -20°C. Specimens for insertion in the electron microscope were cut from the perforated window under cover of ethyl alcohol.

3.6.2 Foil Examination

An Associated Electrical Industries E.M.6G instrument was used for all electron metallographic work, and full use was made of the dark field and high resolution diffraction facilities available on such an instrument. The goniometer stage fitted to the microscope allowed

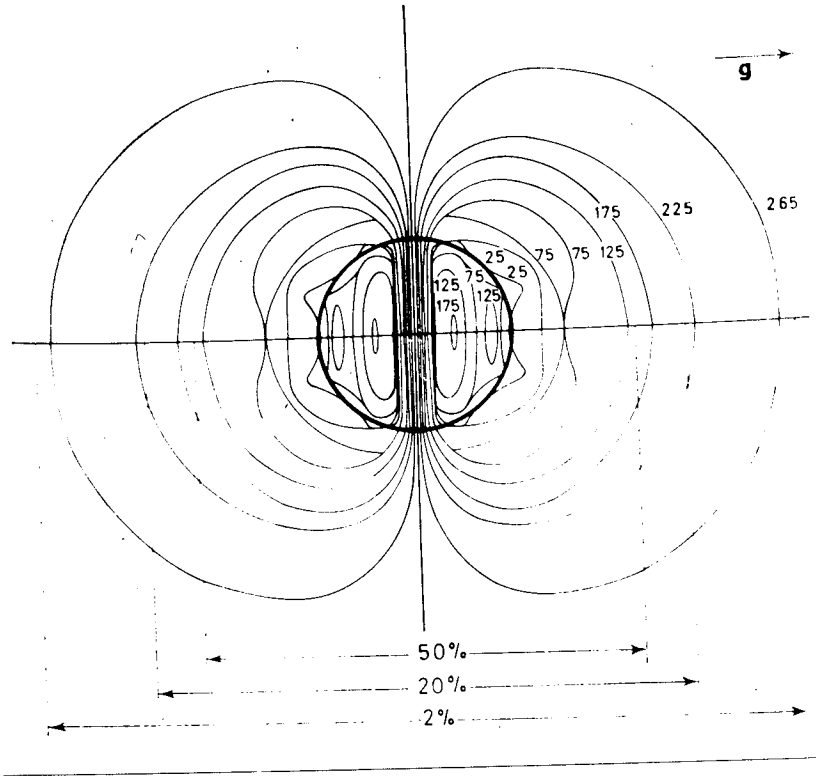

Fig.3.5 Predicted coherency strain field image surrounding an isotropic misfitting sphere in an infinitely isotropic matrix. (Ashby and Brown[55]).

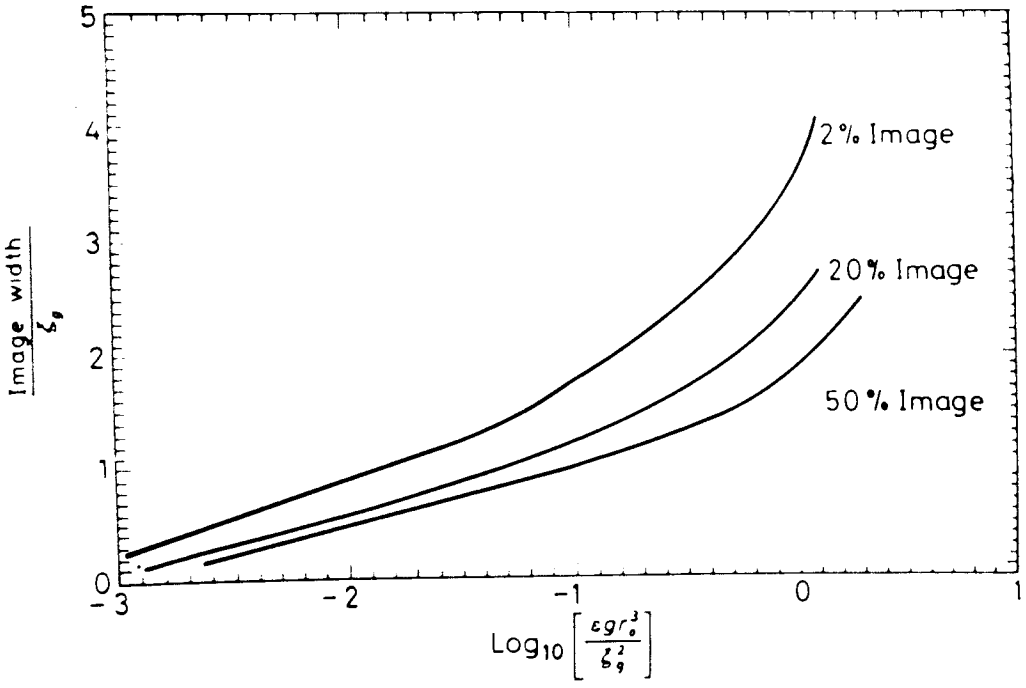

Fig.3.6 Predicted variation of coherency strain field image width for a spherical particle as a function of the diffracting conditions operative, the particle strain and also the particle size. (Ashby and Brown[55]).

$\pm 5^{o}$ of tilt of the specimen cartridge together with 360^{o} rotation. For the majority of observations and experiments performed on the materials this degree of manipulation of the specimen cartridge was found to be adequate but the availability of a high tilt cartridge would have greatly facilitated the determination of the burgers vectors of dislocations.

3.6.3. Quantitative Electron Metallography

3.6.3.1 Introduction

Two of the main metallographic features observed in the alloys investigated were coherency strain fields and stacking faults and therefore a brief survey of quantitative techniques available for the interpretation of such features follows.

3.6.3.2 Coherency Strain Fields

The contrast arising from small coherent particles of a second phase embedded in a matrix has been considered by Ashby and Brown[55]. They have shown that the images of coherency strain fields surrounding an isotropic misfitting sphere take the form shown in Fig.3.5. By observing the coherency strain field images produced around small cobalt particles precipitated in a copper-cobalt alloy, they were able to use the theoretical graph of the variation of image width with particle size, shape and diffraction conditions operative, Fig.3.6, to measure

the "in situ" strain at the precipitate/matrix interface. On calculating the value for "in situ" strain ϵ developed at the interface, no account was taken of the marked elastic anisotropy exhibited by the copper matrix, nevertheless values of strain obtained from the relationship

$$\epsilon = \frac{3K\delta}{3K+2E/_{1-\nu}}$$

where K is the bulk modulus of the precipitate
ν is Poissons Ratio for the precipitate
E is the Elastic Modulus of the matrix
δ is the misfit between the two lattices as given by $\delta = \frac{2(a_1-a_2)}{a_1+a_2}$

are in good agreement with those obtained from measurements of coherency strain field images around 30 of the cobalt particles.

Ashby and Brown[55] also showed that the sense of the strain could be determined from observations of asymmetrical images formed at particles which were within approximately half an extinction distance (ξ)* of either surface of the foil. The method involves observation of the strain fields under "dark field" conditions and noting

* The extinction distance for electrons is given by the expression $\xi = \frac{\pi V \cos\theta}{\lambda F_e(\theta)}$ where V is the volume of the unit cell, λ is the wavelength of the elctrons and $F_e(\theta)$ is related to the atomic scattering factor for electron The extinction distance represents the maximum wavelength of the intensity oscillations which transmitted and diffract beams undergo on passing through a crystal and for low orde planes in metals is of the order of 200-600A°.

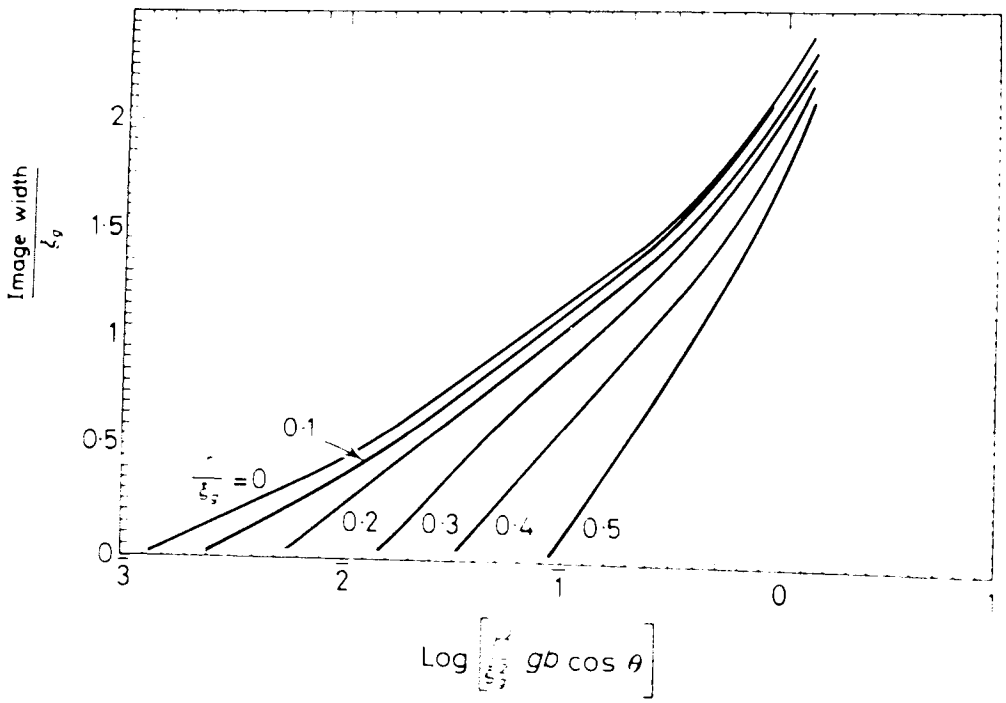

Fig.3.7 Predicted variation of coherency strain field image widths for a disc shaped precipitate.

the asymmetry of the anomalous images with respect to the direction of the operating diffraction vector. These techniques for the determination of the magnitude and sense of strain surrounding spherical isotropic particles have been extended to cover disc shaped particles, but the experimental techniques involved are reported to be considerbaly more difficult. Making the reasonable assumption that the greatest misfit of disc shaped particles occurs normal to the plane of the disc, and that the ratio of the radius of the disc to its thickness is high, Ashby and Brown[55] have again been able to produce a series of relationships between the image width and an expression close to that used for the spherical case. Their results are represented graphically in Fig.3.7. By comparing the observed image widths with those predicted graphically in Fig.3.7, one obtains a value for the expression $\log\left[\frac{r^2}{2}_g gb_p \cos\theta\right]$ in which b_p is related to the misfit δ and hence strain by $b_p = \Delta t.\ \delta$ where Δt is the thickness of the disc.

Any departure from the two special conditions of particle geometry mentioned above introduces extremely cumbersome and difficult mathematical models to take into account the non-isotropic nature of the strain existing at such interfaces. Furthermore, most F.C.C. metals, with the exception of aluminium, have markedly anisotropic elastic constants, which add to the difficulties encountered in deriving values for the "in situ" strain from image width measurements.

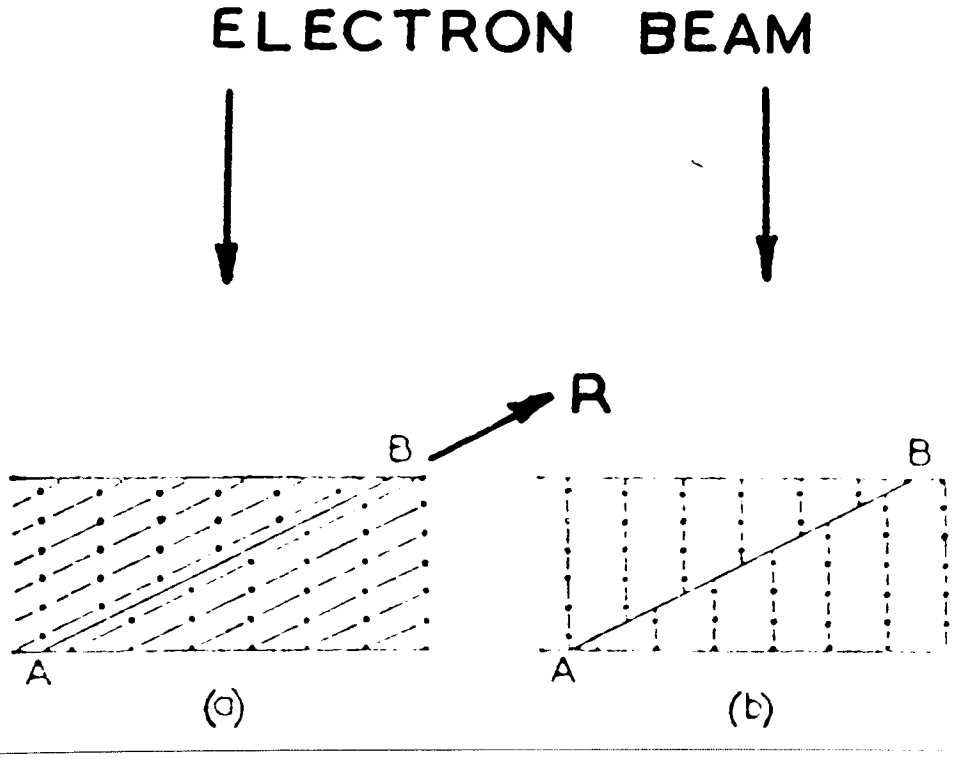

Fig.3.8 Displacements of the reflecting planes at a stacking fault AB. In (a) $g.R = 0$ and no contrast occurs. In (b) $g.R \neq 0$ and interference between waves from above and below the fault gives a fringe pattern.

3.6.3.3 Stacking Fault Contrast

A stacking fault is a planar defect and is observed in the electron microscope due to the displacement of the regular crystal lattice above the fault with respect to that below it and Fig.3.8 is a diagrammatic representation of a fault lying on a plane inclined to the foil surface. Consideration of the ways in which a fault on the (111) plane may be formed in an F.C.C. material shows that the displacement vector, R, may be $\pm\frac{1}{3}a\langle 111\rangle$ if the fault is formed by expansion or collapse of the lattice in a direction perpendicular to the fault; or alternatively, if the fault is formed by shearing parallel to the fault, then the displacement vector can be $\frac{1}{6}a[11\bar{2}]$, $\frac{1}{6}a[\bar{1}2\bar{1}]$, or $\frac{1}{6}a[\bar{2}11]$. If the displacement vector in either case is a lattice translation vector, then stacking fault contrast will not be observed since the two crystals are once again in register. However, even if R is not a lattice translation vector, then the fault will still become invisible when diffracting conditions are such that the product g.R is equal to 0, 1, 2, 3 etc. Clearly, for the stacking faults formed in F.C.C. crystals the invisibility criteria is satisfied when the faults are viewed in g$\langle 220\rangle$ and g$\langle 113\rangle$ reflections.

Whelan and Hirsch[56] have shown that the intensity distribution due to stacking faults on an inclined plane is such that fringes are formed. The spacing between

common fringes is equal to $\frac{t}{\xi_g}$ where t is the foil thickness and ξ_g the extinction distance for the particular diffraction vector operative. Computed image profiles indicate that the intensity of such fringes should be uniform across the fault — the observation that this is not so is due to absorption effects and is the basis of a method for determining the nature of the faults. The method was first used by Hashimoto, Howie and Whelan[57] and involves vie wing the region of the crystal containing the fault in bright field and dark field under two beam conditions i.e. when, s, the parameter describing the deviation from the exact Bragg diffracting condition, approaches zero. The nature of the fringes at the fault intersection with the top and bottom of the foil surface indicates the sense of the phase angle of the fault α . Since $\alpha = 2\pi g.R$ then a knowledge of the operating diffraction conditions allows the sense of the displacement to be determinted. From the dark field image, it is possible to determine the sense of the inclination of the fault plane to the crystal surface since an asymmetrical image is formed due to absorption. Knowing these parameters, the type of fault i.e. intrinsic or extrinsic can be determined unambiguously whether the displacement is taken to be parallel to the fault plane $\frac{1}{6}a\langle 112\rangle$, or perpendicular to the plane $\frac{1}{3}a\langle 111\rangle$. Gevers, Art and Amelinckx[58] have shown that it is only necessary to consider the asymmetrical dark field image with respect to

the diffraction vector operating in order to deduce the nature of the faults, and give the general rule for two classes of reflections. For class A reflections which include $\langle 200 \rangle$, $\langle 222 \rangle$ and $\langle 440 \rangle$, the rule is as follows:- if the origin of the g vector is placed at the centre of the dark field image of the fault, g points towards the light fringe if the fault is intrinsic, and away from it if it is extrinsic regardless of the inclination of the fault to the foil surface. For class B reflections, $\langle 111 \rangle$, $\langle 220 \rangle$, $\langle 400 \rangle$, the opposite rule applies.

The knowledge of fault type and the nature of the partial dislocations bounding the fault enables the mechanism of fault growth to be postulated.

3.6.3.4 Contrast arising from Partial Dislocations

If a dislocation in a F.C.C. crystal dissociates into a pair of partial dislocations on a $\{111\}$ plane, the products of the splitting reaction are either (1) a pair of Shockley partials or (2) a Shockley partial and a Frank partial. The Burgers vector of the Shockley partial is $\frac{1}{6}a\langle 112 \rangle$ and that of the Frank partial $\frac{1}{3}a\langle 111 \rangle$. For both of these partials, the product $g.b$ is no longer an integer, and can take values of 0, $\pm\frac{1}{3}$, $\pm\frac{2}{3}$, ± 1, $\pm\frac{4}{3}$ etc. Dynamical computations show that at the reflecting position i.e. $s = 0$, partial dislocations with $g.b = \frac{1}{3}$ are invisible whilst those with $g.b = \frac{2}{3}$ are visible. However, as with the case for whole dislocations the general invisibility

criteria can only be rigourously applied for dislocations of pure screw orientation. In this connection, it must be remembered that the Frank partial is an edge dislocation and there will be a contribution to the contrast from the displacement normal to the slip plane as well as the main component parallel to the Burgers vector. This effect has been used by Silcock and Tunstall[49] to distinguish between the two partial dislocation bounding stacking faults found in stabilized austenitic stainless steels.

3.7 X-ray Diffraction Techniques

3.7.1 Introduction

The research programme produced two problems requiring the use of X-ray techniques for their solution. Firstly, no decisive data concerning the stoichiometric composition or the crystal structure of the intermediate compound occurring at the copper rich end of the copper zirconium system was available, and since it was this compound which was later thought to be the precipitating phase in the copper zirconium alloy under investigation, a series of experimental alloys bracketing the composition range over which the compound has been reported as occurring were made by electron beam melting techniques, Fig.3.9. The second opportunity to use X-ray diffraction methods, was for the determination of the relative stacking fault energy of all four of the solution treated materials.

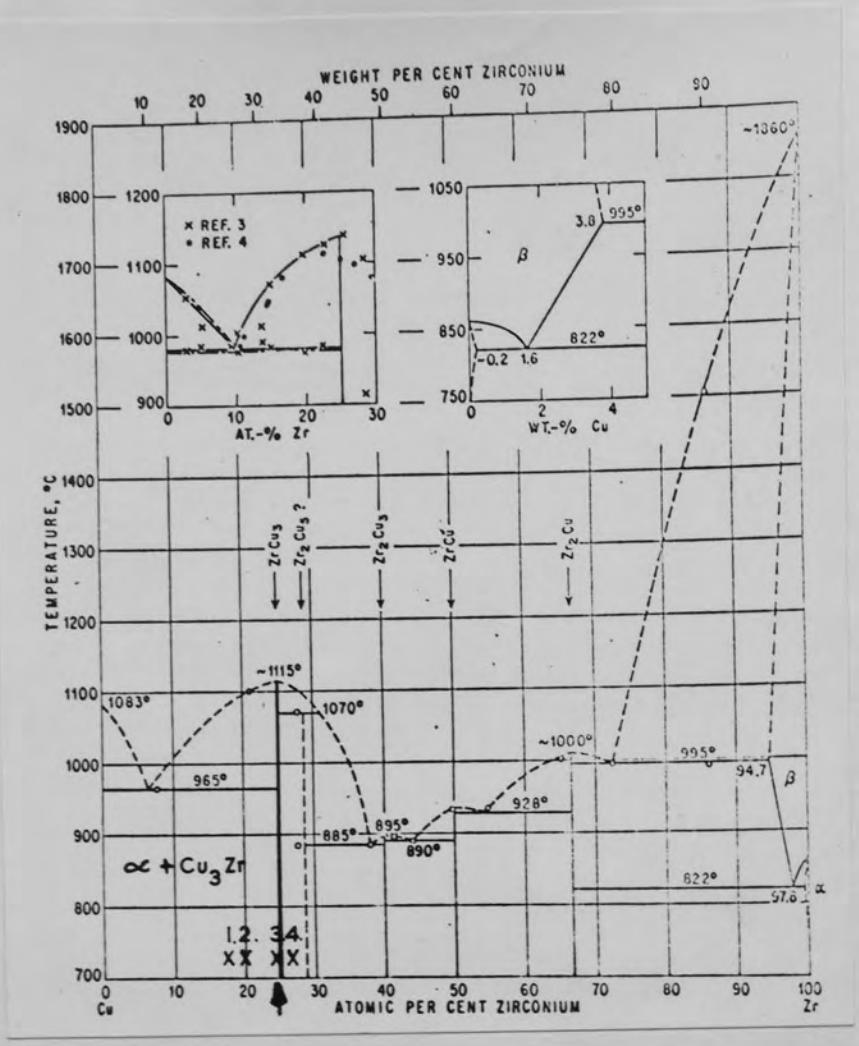

Fig.3.9 Copper zirconium equilibrium diagram showing the nominal compositions of four experimental alloys manufactured for a study of the first copper rich compound in the system.

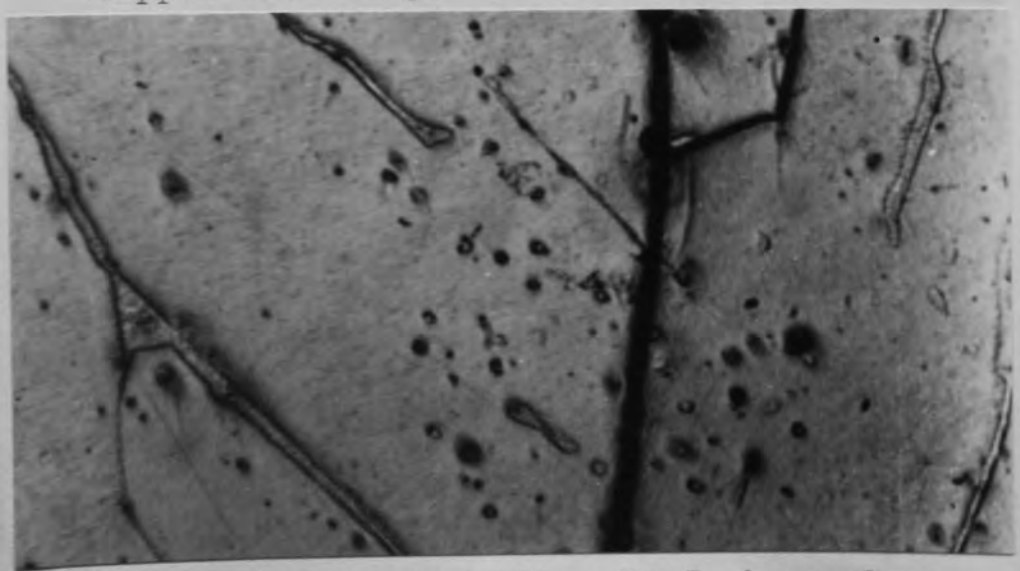

Fig.3.10 Microstructure of alloy No.3 shown above containing 3% Cu_3Zr/Cu eutectic. x 200

3.7.2 Determination of Unknown Compound

The determination of the crystal structure of Cu_3Zr* was attempted by powdering the experimental alloy which exhibited the least amount of Cu_3Zr/Cu eutectic when polished and examined microscopically. The structure of this sample is shown in Fig.3.10.

The powdered sample was irradiated with Cu Kα X-rays in a Debye-Scherrer camera, and the resulting film strip analysed as suggested by Cullity[60].

3.7.3. Determination of Stacking Fault Energy.

A transmission X-ray method, described by Dillamore, Smallman and Roberts[61] using an established dependence of preferred orientation on stacking fault energy was used in an attempt to determine the effect alloying elements chromium and/or zirconium had on the stacking fault energy of the copper solid solution. The principle of the method involved the gradual change in deformation texture obtained when materials of successively lower stacking fault energy are cold rolled in excess of 95%. Copper, when cold rolled by this amount gives rise to a pure metal texture, as shown

---

* Electron microprobe analysis of the samples made for X-ray determinations has recently been carried out by Belk[59] over a range of instrumental operating conditions. He has shown that the heavy absorpiton of zirconium X-rays which normally prevents accurate determinations in zirconium containing alloys can be avoided by analysing the ZrKα radiation emitted at operating potentials in excess of 30Kv. The reported value of 30.4 wt.% zirconium corresponds to Cu_3Zr and since this determination represents the most authorative work on the compound to date, further references to the compound will be by this nomenclature.

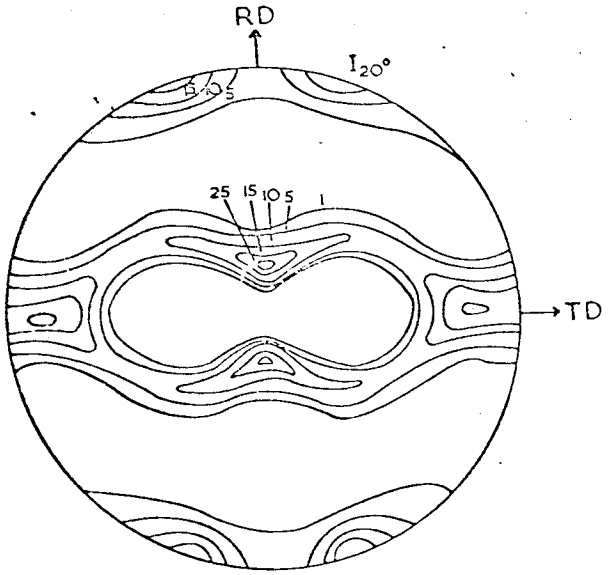

Fig.3.11 (111) pole figure from heavily cold rolled copper. (Pure Metal texture)

$\{110\}\langle 112\rangle + \{112\}\langle 111\rangle$

Fig.3.12 (111) pole figure from heavily cold rolled 70/30 brass (alloy texture).

$\{110\}\langle 112\rangle$

Intensities in arbitary units

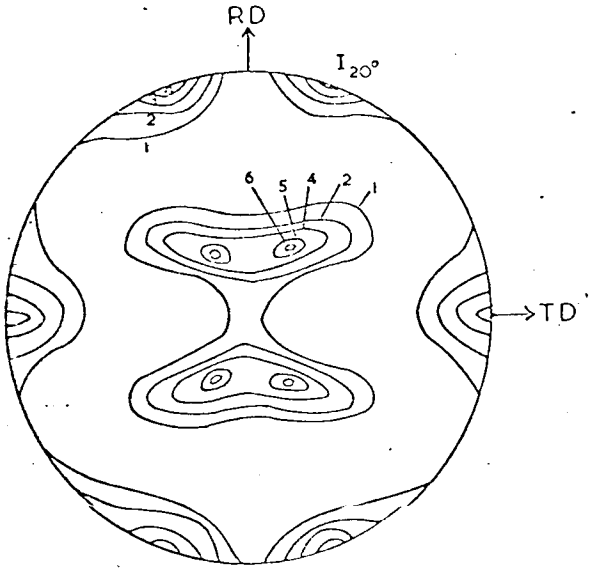

Fig.3.13 Variation of stacking fault energy with observed {111} pole intensity distribution.

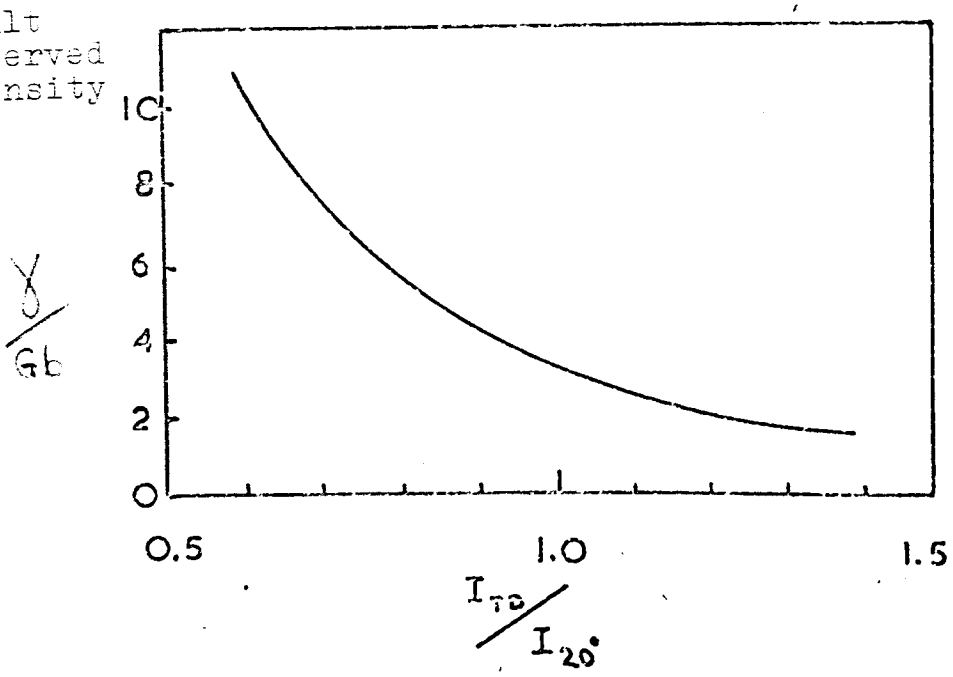

in Fig.3.11. Progressive alloying of copper generally results in a lowering of the stacking fault energy of the system such that a deformation texture transition is accomplished to the so called alloy texture as shown in Fig.3.12. At intermediate stages, the process of lowering of stacking fault energy can be followed by noting the change in ratio of the $\{111\}$ pole intensities at the transverse direction, to that occurring at $20^{\circ}C$ to the rolling direction. Diagrammatically the variation of stacking fault energy γ with this ratio is shown in Fig.3.13. A pure copper sample and a copper 2% aluminium alloy were processessed in the same manner as the four alloys containing chromium and/or zirconium to provide reference values of stacking fault energy.

CHAPTER 4.

THE ALLOY COPPER-0.4% CHROMIUM

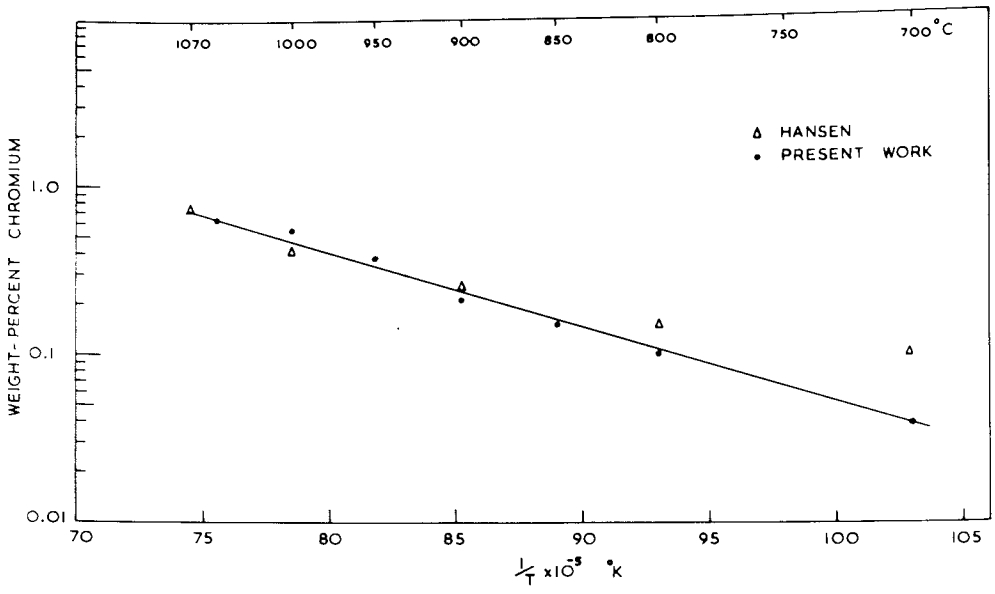

Fig 4.1 Comparison of the solubility of chromium in copper with published results.

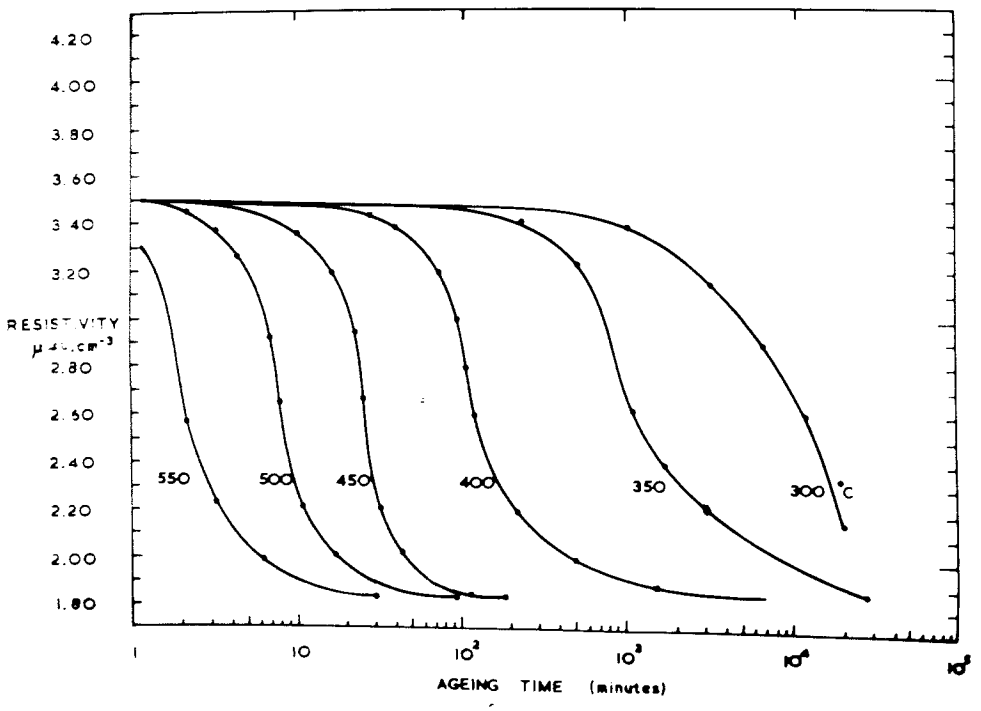

Fig. 4.2 Sigmoidal decay curves obtained from isothermal ageing experiments. Alloy solution treated at 950°C.

COPPER - 0.4% CHROMIUM

4.1 Electrical Resistivity

4.1.1 Solubility

The solubility of chromium in copper over the range 700°C - 950°C was compared with published results by taking the increase in resistivity due to chromium in solid solution to be that of 0.00481 $\mu\Omega cms^{-3}$/10 p.p.m. solute as suggested by Pawlek and Reichel[2] (see section 1.1.1 Table I), and to assume linearity up to the limit of solid solubility for each temperature. The results are plotted in Fig.4.1 and when extrapolated to the eutectic temperature of 1070°C show fair agreement with solubilities quoted by other workers.

The minimum resistivity attained at 20°C, after fully ageing the solution treated alloy in the range 350°C - 550°C was constant at 1.83 $\mu\Omega cms^{-3}$. This corresponds to a solubility of 0.03% chromium which is identical to the value obtained by Raub and Engel quoted in the paper by Gregory et.al.[1], and is equivalent to a conductivity of 94.5% I.A.C.S.

4.1.2 Isothermal Ageing Data

The precipitation of chromium from the solid solution in the range of ageing temperatures 300°C - 550°C yielded the sigmoidal decay curves illustrated in Fig.4.2. The empirical activation energy, Q_e , for the process was

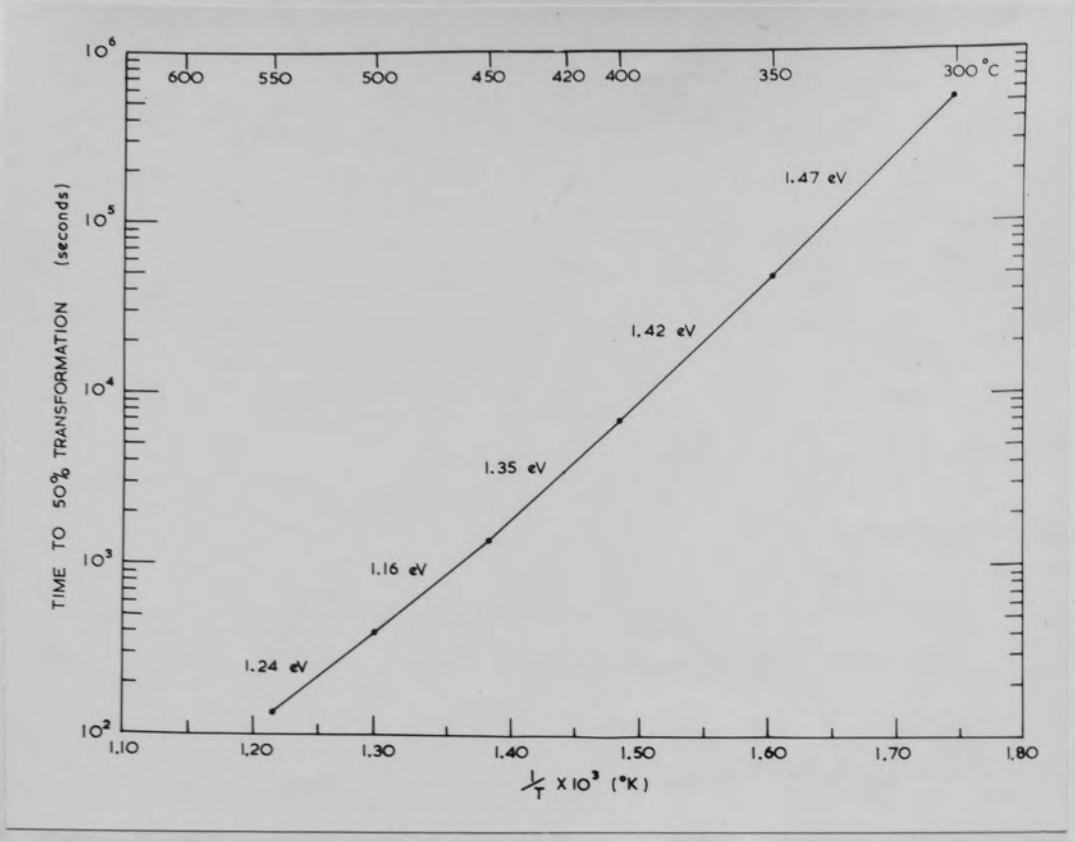

Fig. 4.3 Arrhenius plot of resistivity data.

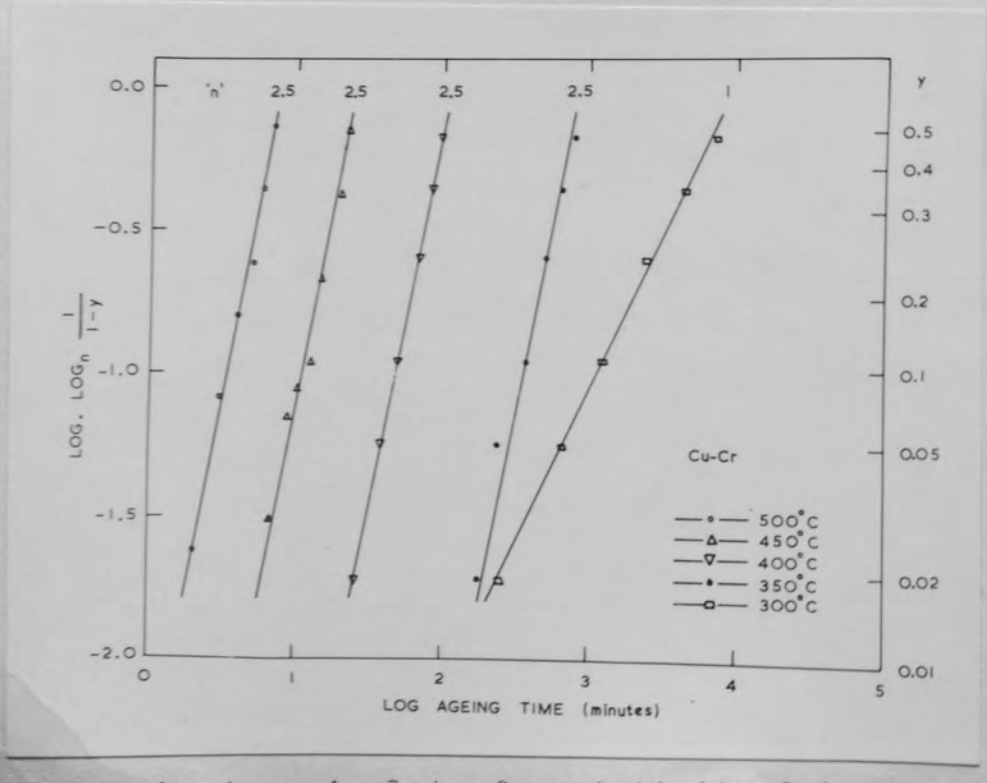

Fig. 4.4 Avrami plot of resistivity data.

derived by plotting the time taken to 50% transformation against the reciprocal of the absolute ageing temperature. Fig.4.3 describes the results obtained and illustrates that the temperature dependence of Q_c is minimal. Values of Q_e taken at various fractions of the transformation give similar results and indicated that the reaction was isokinetic over the range 350°C - 500°C. An Avrami[53] plot of the data confirmed that this interpretation was correct since a constant value for the time exponent 'n' of $\frac{5}{2}$ was obtained over the same range of ageing temperatures. Fig.4.4. The extremely rapid rate of rejection of chromium which occurred on ageing at 550°C did not allow sufficiently accurate resistivity data to be collected for an analysis of this type to be carried out. At 300°C, the rejection of chromium proceeded with a time exponent of unity, which, according to Ham[62], is consistent with a process involving the diffustion controlled growth of cylinders in their axial direction only. The value of $n = \frac{5}{2}$ obtained at higher ageing temperatures is shown by Burke[31] to relate to the condition where nucleation occurs at a constant rate, and that the growth of such nuclei is again diffusion controlled (see Table V).

The resistivity data for the ageing process indicates that the ageing process is essentially a simple one, and that it appears to proceed by a similar mechanism over the range of ageing temperatures investigated.

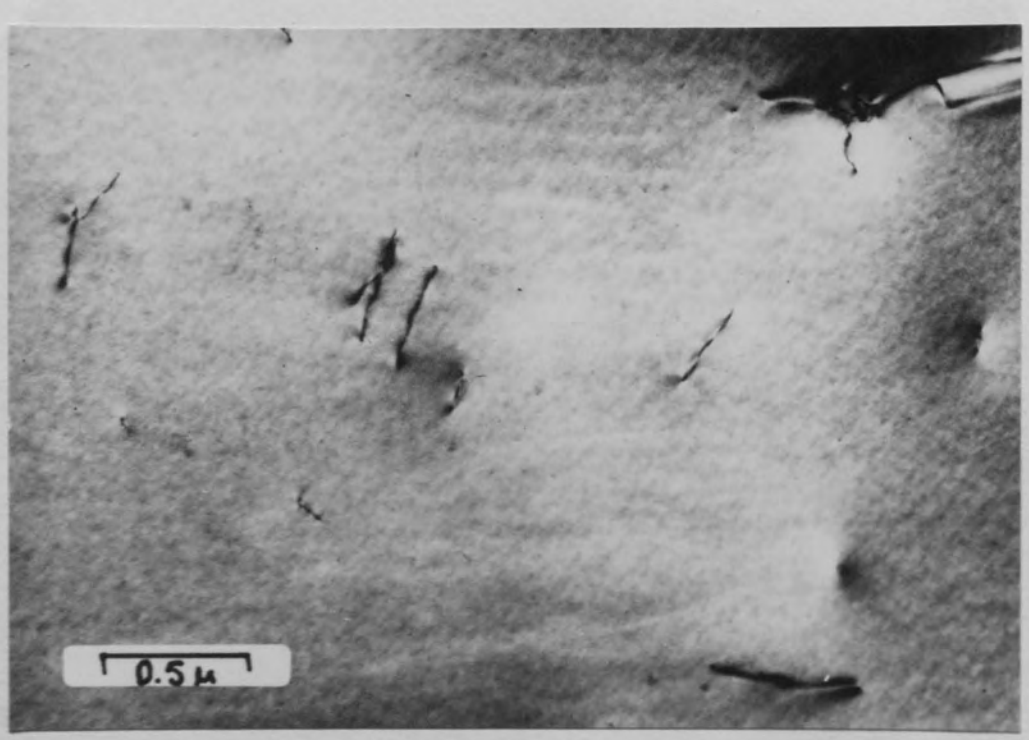

Fig.4.5 Solution Treated at 950°C and water quenched.

4.2 Metallography

4.2.1 Optical Metallography

The grain size of the material after solution treating at 950°C for ½ - 1 hour was 0.1 mm. as estimated from standard A.S.T.M. grain size charts for non-ferrous materials. After prolonged ageing at temperatures up to 550°C, no measurable increase in grain size was observed. The microstructure was typical of a wrought and annealed copper alloy, showing a high density of annealing twins.

4.2.2 Electron Metallography

4.2.2.1 Solution Treated Material

After water quenching to 20°C from the solution treatment temperature of 950°C, the alloy was found to contain no defect structures resulting from the elimination of the excess vacancy concentration. Fig.4.5 is typical of the structure obtained, and shows a featureless matrix threaded by a few dislocation lines. The measurement of dislocation densities in thin foils is extremely unreliable, and little credence can be given to figures looseley quoted in published papers except where detailed descriptions of the techniques used are given. Generally, most figures quoted are underestimates of the dislocation density of the bulk material, due to the loss which inevitably occurs on thinning and also to the fact that in most observations the diffracting conditions operating ensure that a proportion of the total dislocations present will be invisible.

4.2.2.2 Aged Materials

4.2.2.2.1 General

From the resistivity data, heat treatment cycles could be chosen such that the precipitation reactions were observed at any given point in the overall transformation. However, this was found unnecessary since within the heat treatment range 350°C - 600°C, ageing proceeded by the rejection of particles of chromium in the copper matrix and generated structures differing only in terms of precipitate size and dispersion.

The main features and dispersion of the precipitate may be obtained from a study of Figs.4.6, 4.7, 4.8, and 4.9 which are micrographs of a series of samples aged at 400, 450, 500 and 600°C respectively for 2 hours*. At 400°C the presence of the precipitate is inferred from the characteristic structure factor contrast produced in regions of the foil which are stongly diffracting i.e. at Bragg contours. In Fig.4.7, aged at 450°C, the precipitates are visible as discrete black dots 60A° in diameter. Increasing the ageing temperature to 500°C illustrates that the particles maintain a coherent interface with the copper matrix, and that the coherency strain fields surrounding

---

* A 2 hour heat treatment allows maximum conductivity to be attained in samples aged at and above 450°C and thus signifies that these materials are fully transformed. The sample aged at 400°C corresponds to a 50% transformed structure.

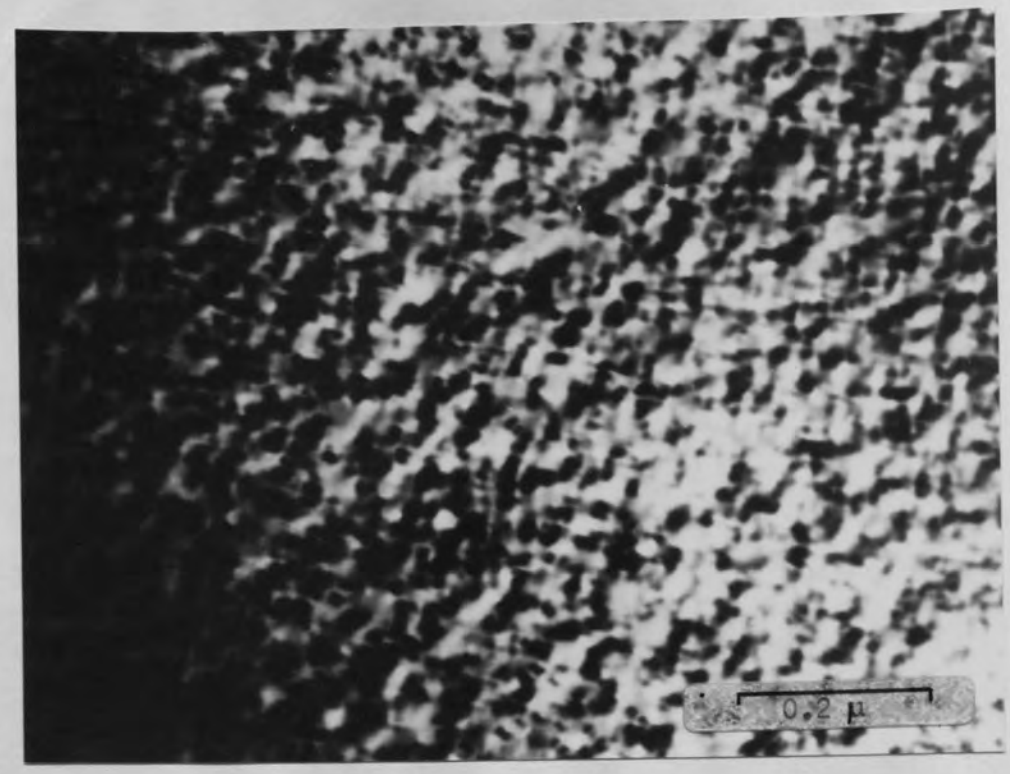

Fig.4.6 Aged at 400°C for 2 hours. The presence of precipitate is inferred from the characteristic "structure factor" contrast obtained near Bragg contours.

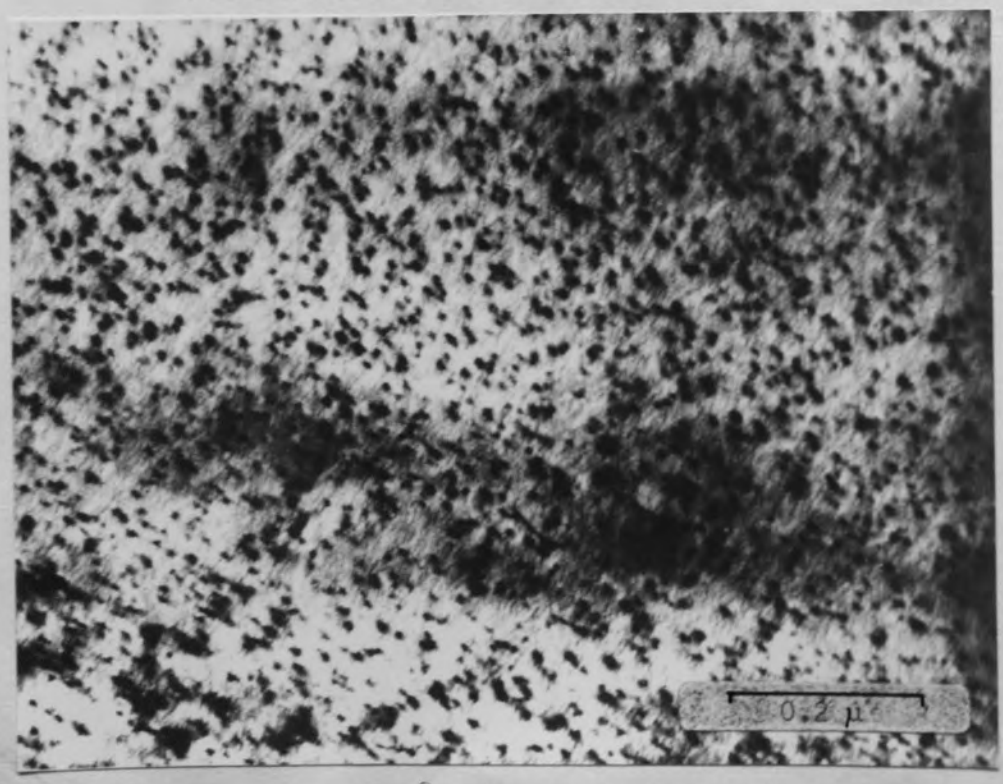

Fig.4.7 Aged at 450°C for 2 hours. Chromium particles are imaged by virtue of the coherency strain fields produced at the particle-matrix interface.

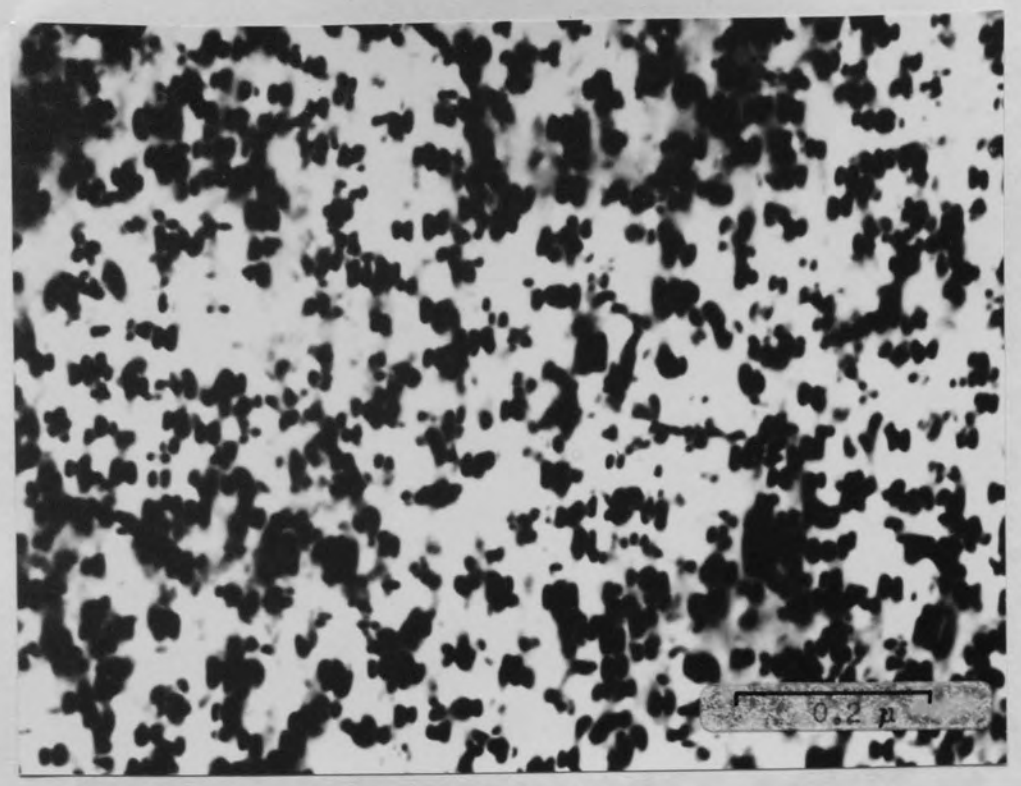

Fig.4.8 Aged at 500°C for 2 hours.

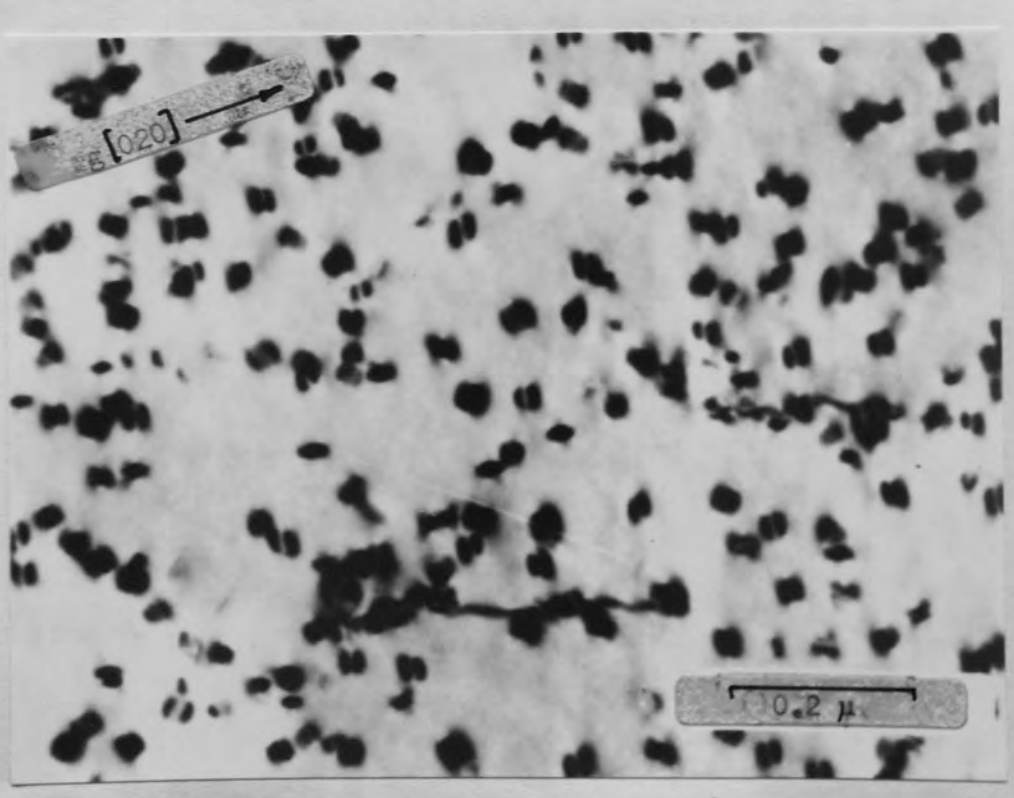

Fig.4.9 Aged at 600°C for 2 hours.

the particles are split by a line of no contrast which is perpendicular to the operating reciprocal lattice vector g, Fig.4.8. This is more clearly shown in Fig.4.9 for the sample aged at 600°C.

Observations of the very fine structure of the alloy aged below 450°C were necessarily made in regions of the foil where high order bend contours crossed, these being areas of maximum visibility for small particles e.g. Fig.4.10. The precipitates present in material aged above 450°C could be detected as discrete particles exhibiting coherency strain fields when viewed under 2-beam conditions, and since previous workers[55] have explained the formation of such images using the 2-beam dynamical theories of electron diffraction, then the most useful structures for analysis are those formed when the alloy is aged above 450°C.

4.3. Crystallography

4.3.1 Coherency Strain Field Observations

A line of 'no contrast' is always observed perpendicular to the operating diffraction vector for particles giving rise to symmetrical coherency strains in a matrix. If the image of the strain fields is symmetrical about this line of no contrast for many diffracting conditions then it may be assumed that for an isotropic matrix, the particle generating the strain is spherical. Observations

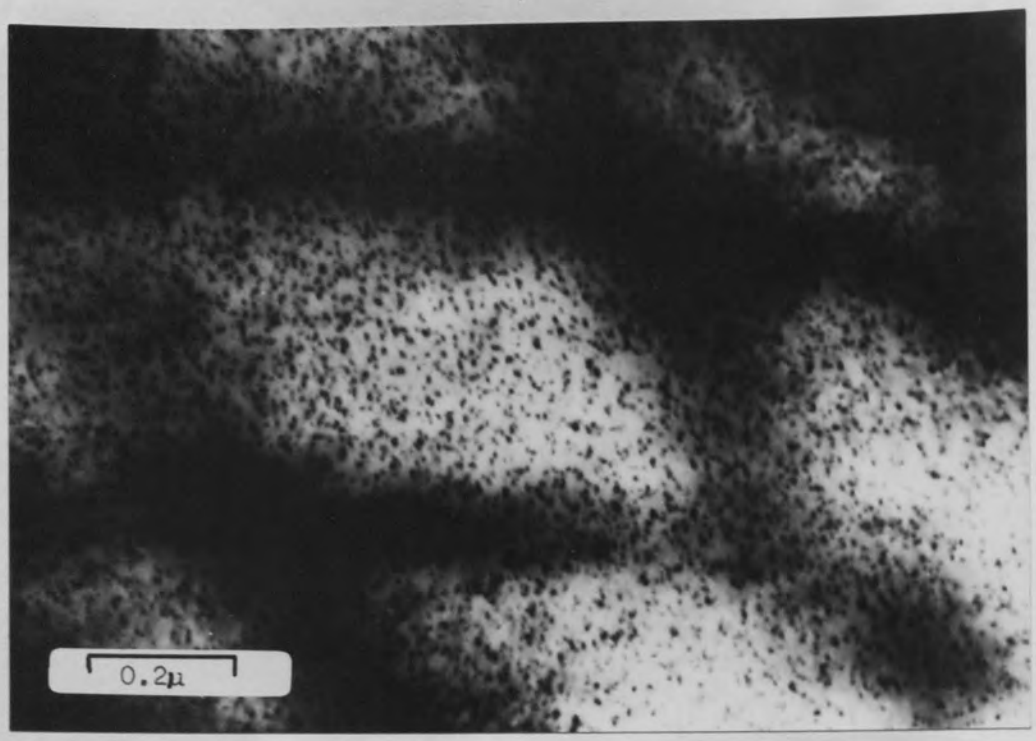

Fig.4.10 Aged at 400°C for 1 day. Areas of maximum visibility of small chromium particles, obtained where high order bend contours intersect.

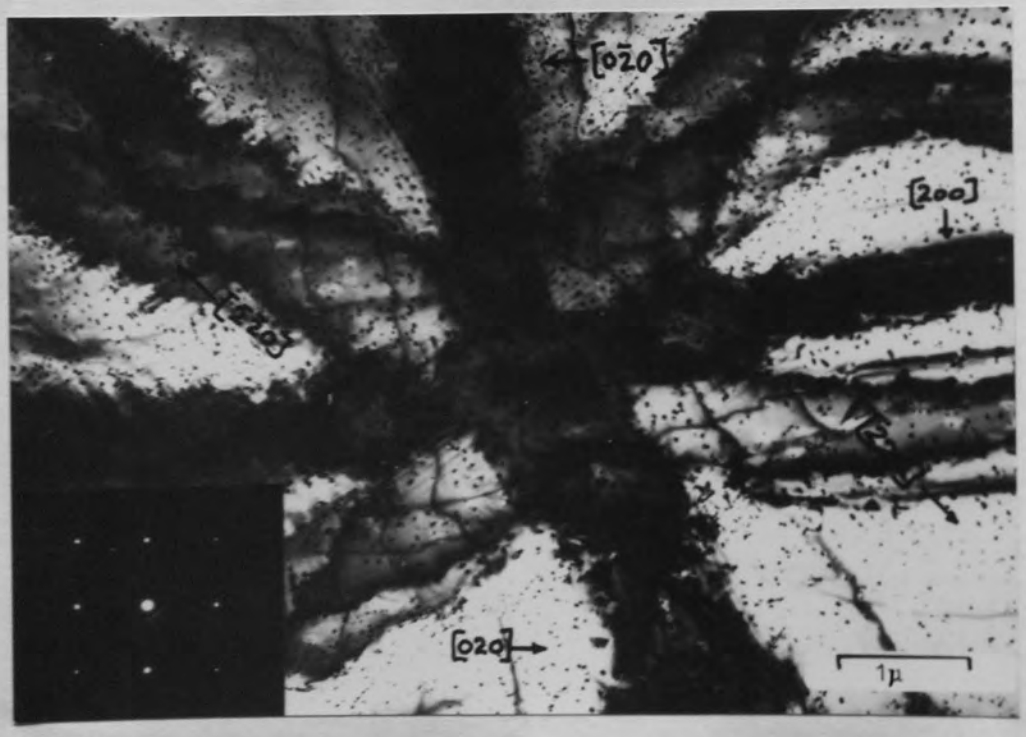

Fig.4.11 Hemispherically buckled foil near (001) orientation, aged at 600°C. The variation of strain field contrast with many operating diffraction vectors can be determined from such regions.

of the strain fields around the precipitated particles in copper chromium under various diffracting conditions suggest that the preciptate is not spherical, and may be illustrated by reference to Fig.4.11. The so called "spider" of bend contours has been produced in a hemispherically buckled foil and contains a region at the hub which is orientated with [001] direction exactly parallel to the electron beam. The associated electron diffraction pattern is from that region, and is orientated with respect to the micrograph allowing the bend contours to be indexed in the manner shown. The micrograph is criss-crossed very faintly with slip traces arising from the disruption of a surface oxide film due to dislocation movement across the foil in $\langle 110 \rangle$ directions — a further guide to the crystallographic directions in the foil.

The effect of many beam conditions on the line of no contrast and image width is shown more clearly in Fig.4.12, and is obtained from material aged at 600°C. The corresponding diffraction pattern is indexed by the convention that the foil normal is assigned all positive indices, in this case [001], and shows that diffraction is occurring with equal magnitude from the $(\bar{2}\bar{2}0)$ and (020) planes, thereby producing images which have their line of no contrast perpendicular to either of the two principal diffraction vectors. The asymmetry of these images, for example at A,B,C, and D on the micrograph, suggests that the particles

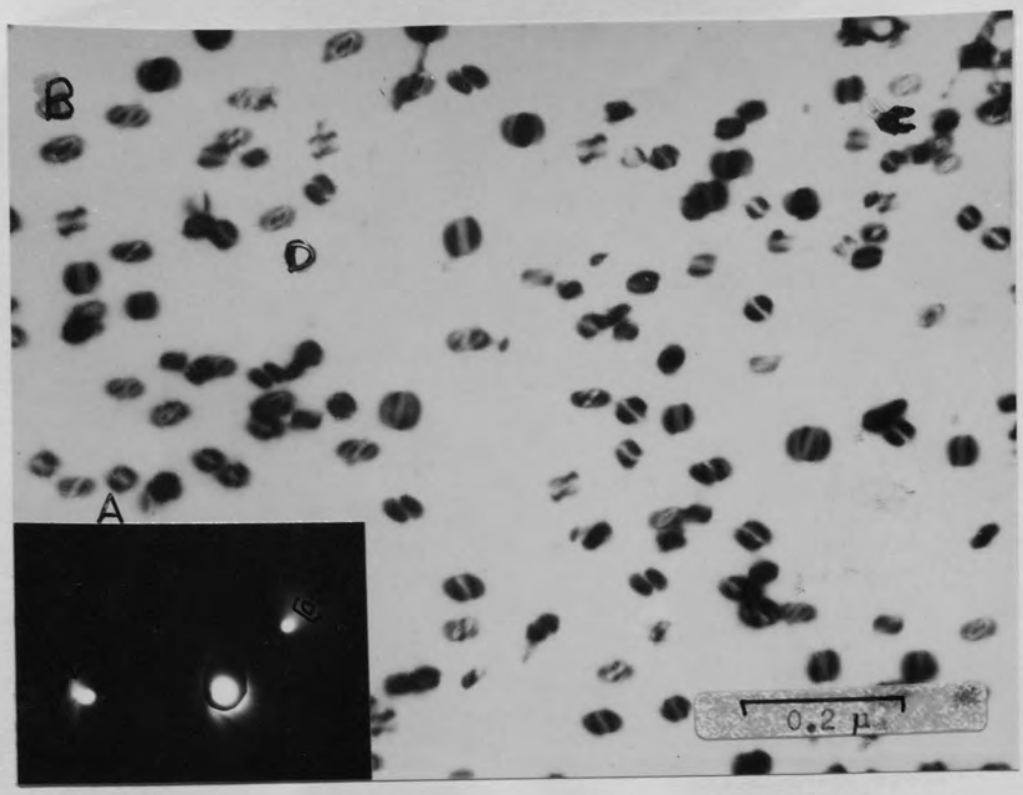

Fig.4.12 Effect of many beam conditions on the image profile of coherency strain fields around chromium particles.

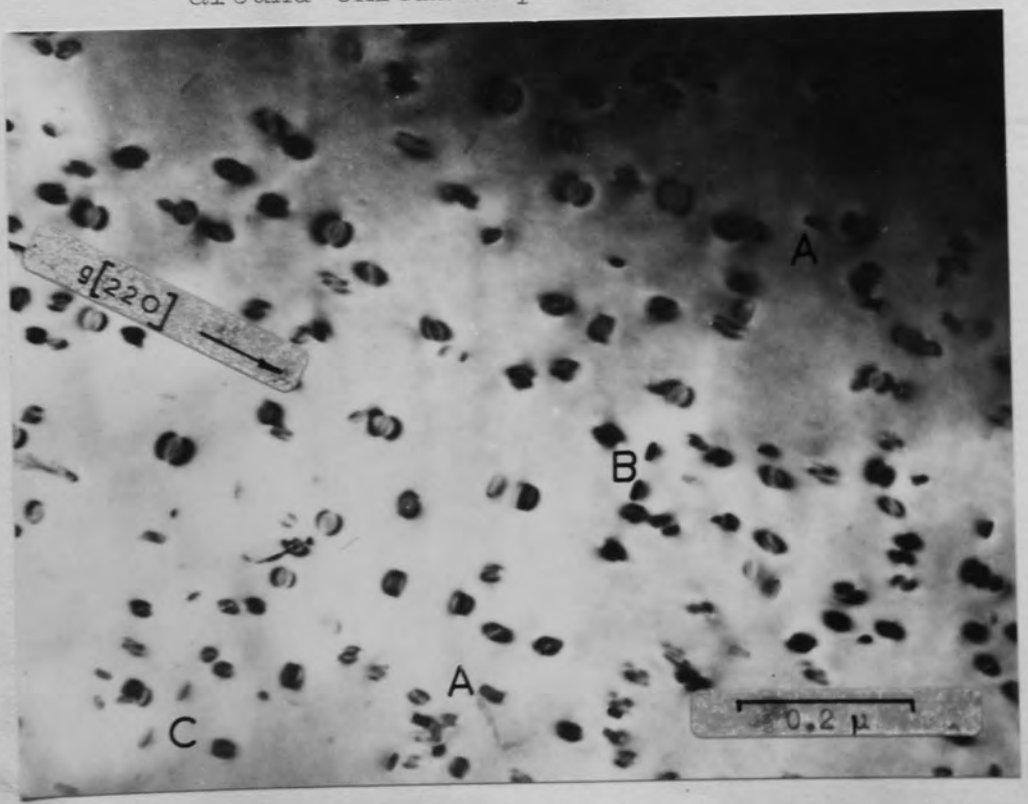

Fig.4.13 Coherency strain field imaged viewed in regions of the foil where s, the deviation from the Bragg diffracting position, approaches zero. The morphology of the chromium precipitate is evident from this micrograph.

are non-spherical. Confirmation of this is obtained when the precipitates are viewed under two beam conditions as in Fig.4.13 taken with the (220) plane strongly diffracting. Under such conditions, only the coherency strain occurring in the direction $[220]$ is imaged, and it is along this direction that some of the precipitates are observed to have grown, not as spheres, but as rod shaped particles (A). Furthermore, some of the particles (B) lie along the orthoganal direction $[\bar{2}20]$ and are visible due to the relaxation of their coherency strain fields, which has presumably occurred at the foil surfaces. It follows that observations of the precipitated particles, free from coherency strain field effects, are best carried out in very thin regions of the foil, and Fig.4.14 shows such an observation made near the edge of a "cube-texture" orientated foil. The foil orientation, near (001), is evident from the pattern etched on the foil surface during preparation*, and by reference to this crystallographic "compass", the axial direction of the rod shaped particles is clearly along the $\langle 110 \rangle$ directions in the copper matrix.

4.3.2 Electron Diffraction Observations

The precipitated particles contributed to the electron diffraction pattern of the alloy most strongly

* It is not uncommon for etch pits to appear near the edge of electrochemically prepared foil samples from such heavily textured material as Fig.4.15 shows.

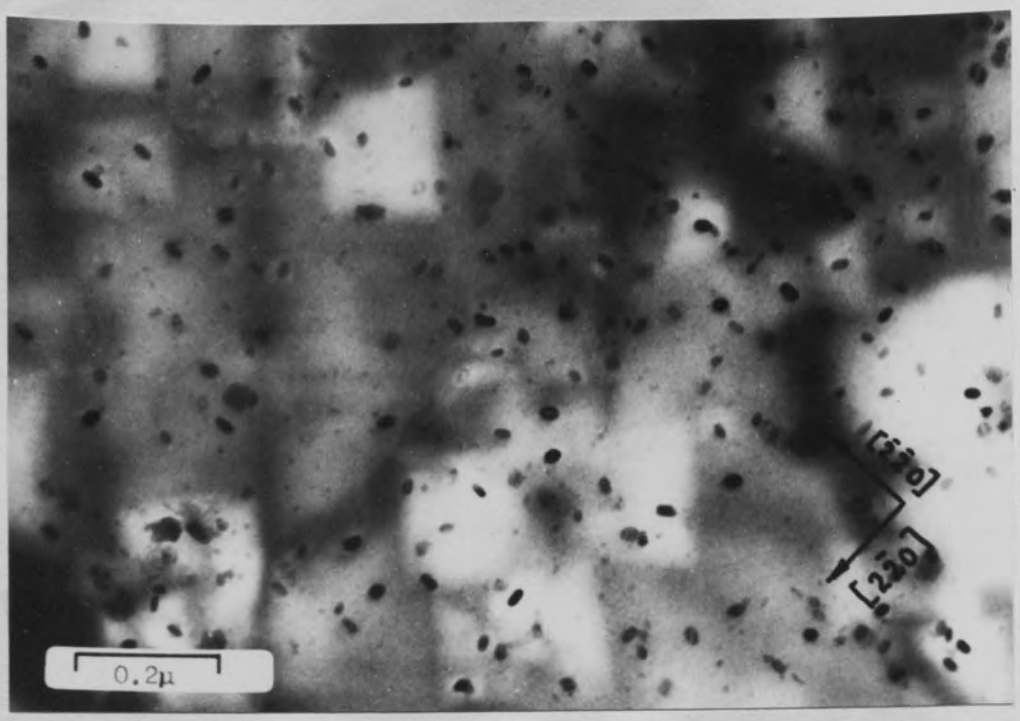

Fig.4.14 Illustrating the relaxation of strain fields between precipitate and matrix which occurs in regions near the edge of thin foils.

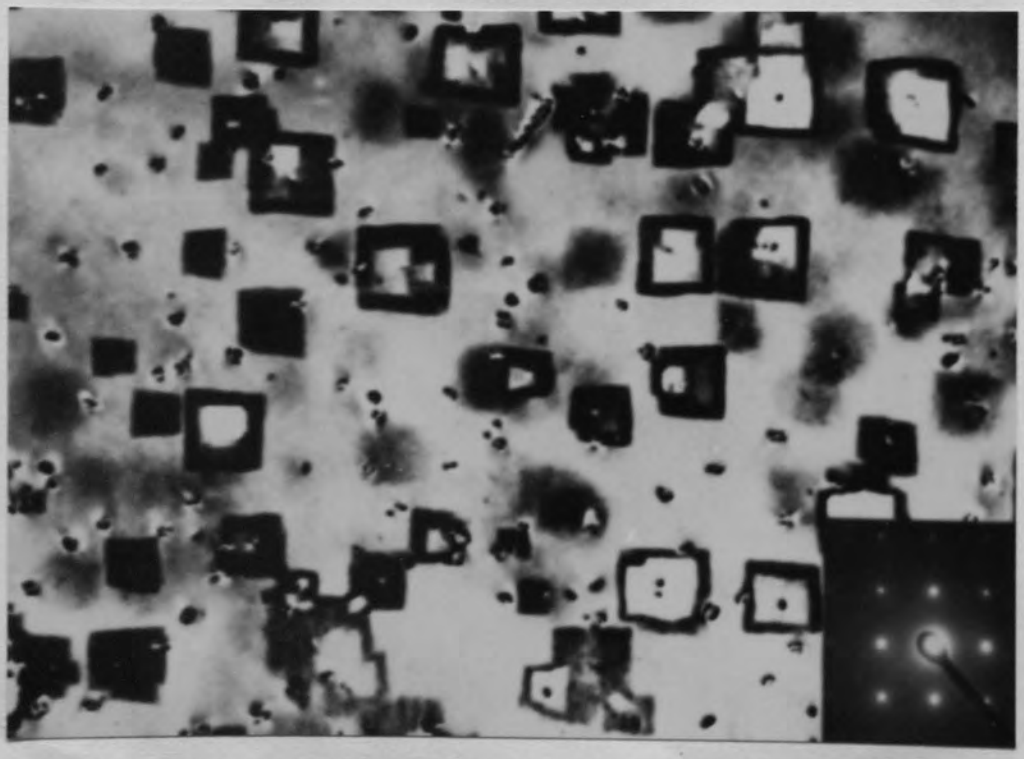

Fig.4.15 Etch Pits formed in electropolished foils processed to obtain a marked "cube-texture" on heat treatment. Foil orientation (001).

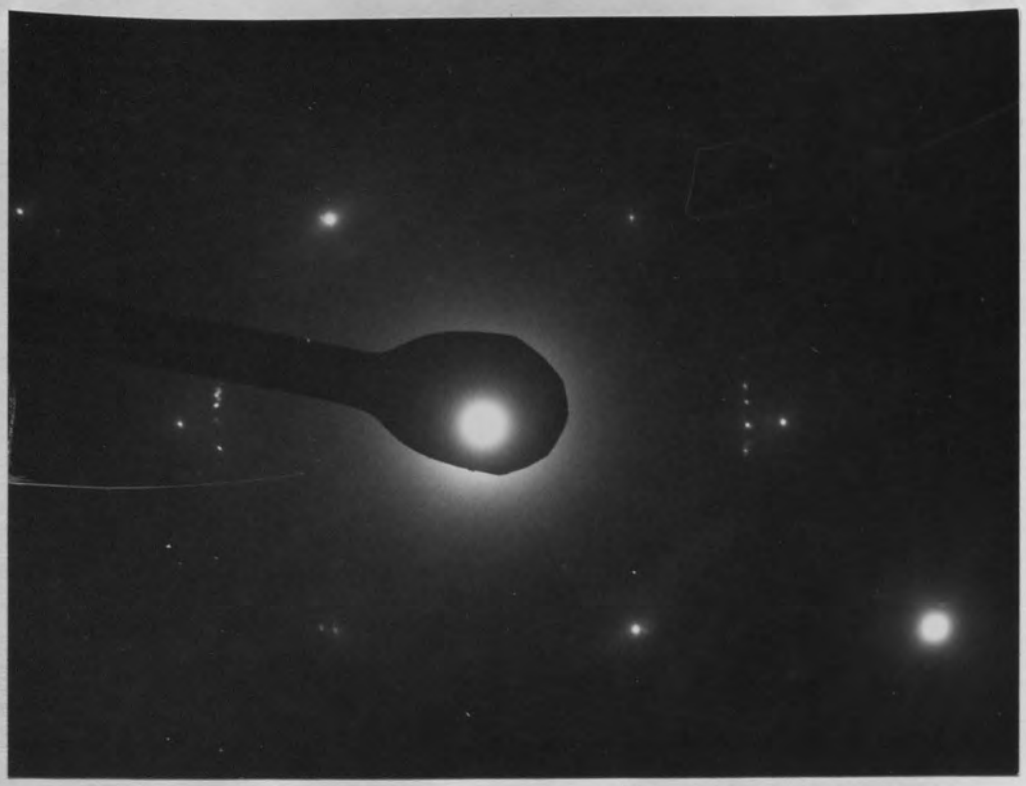

Fig.4.16 Typical selected area diffraction pattern from alloy aged at 600°C showing chromium precipitate spots superposed on the copper matrix diffraction pattern. Foil orientation near (110).

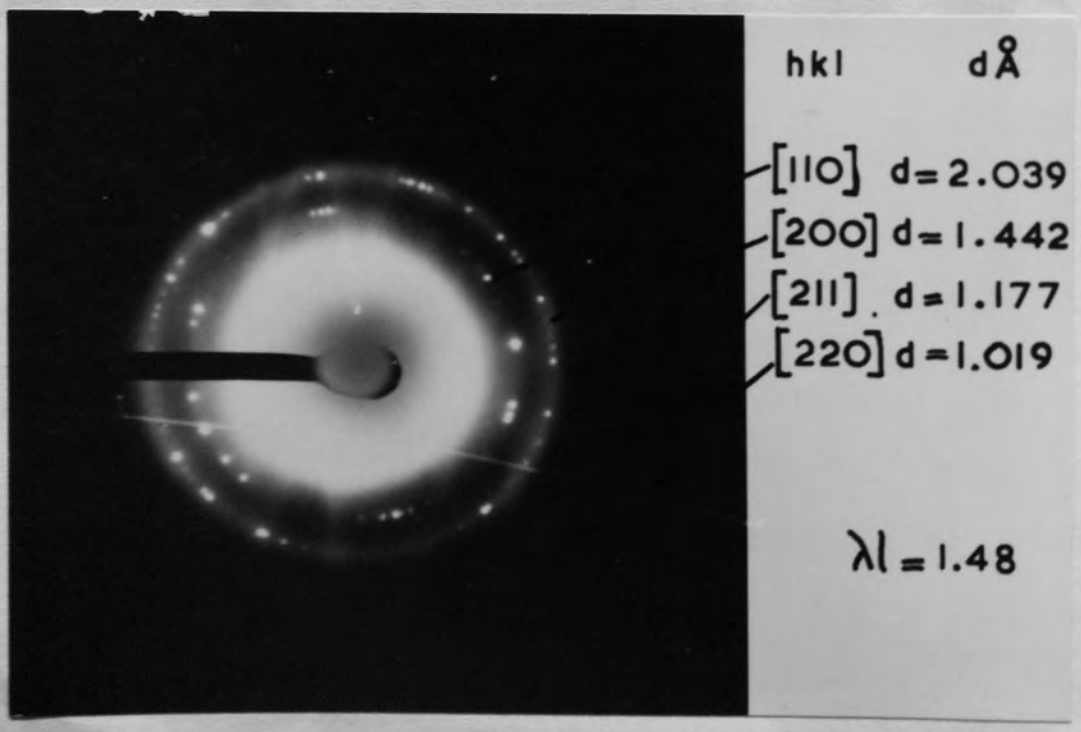

Fig.4.17 Diffraction pattern obtained from chromium particles extracted from alloy aged at 600°C.

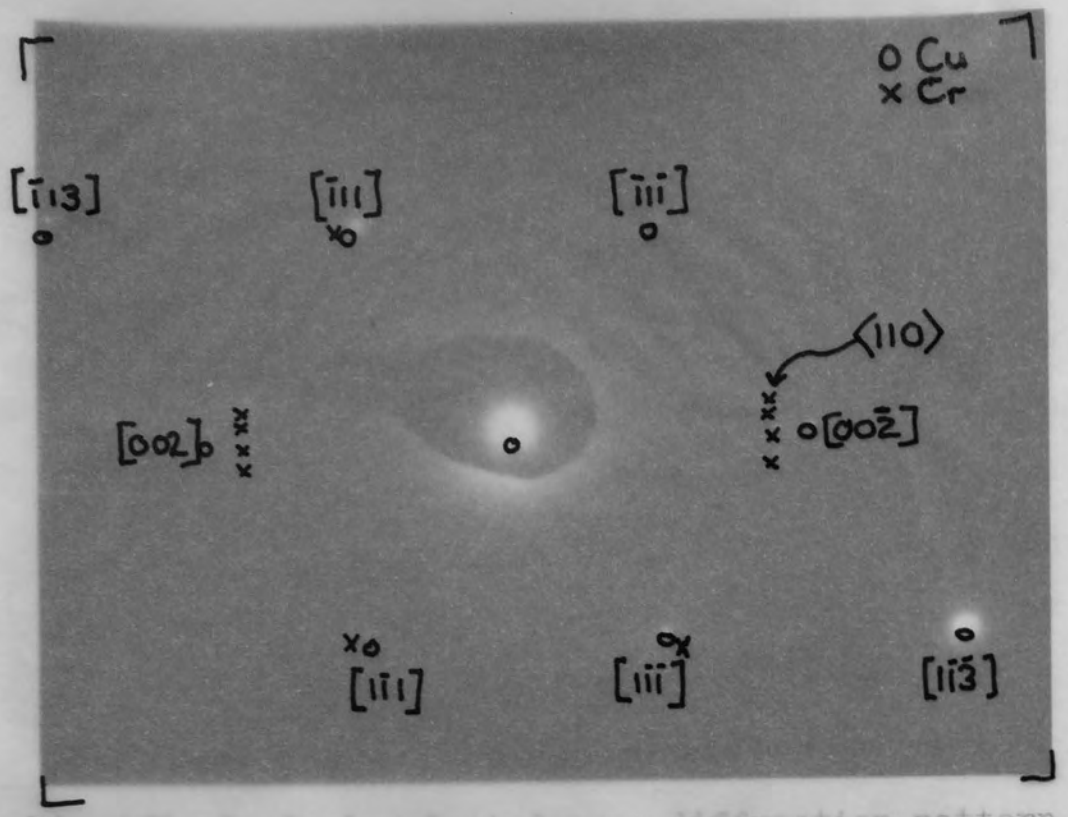

Fig.4.16 Typical selected area diffraction pattern from alloy aged at 600°C showing chromium precipitate spots superposed on the copper matrix diffraction pattern. Foil orientation near (110).

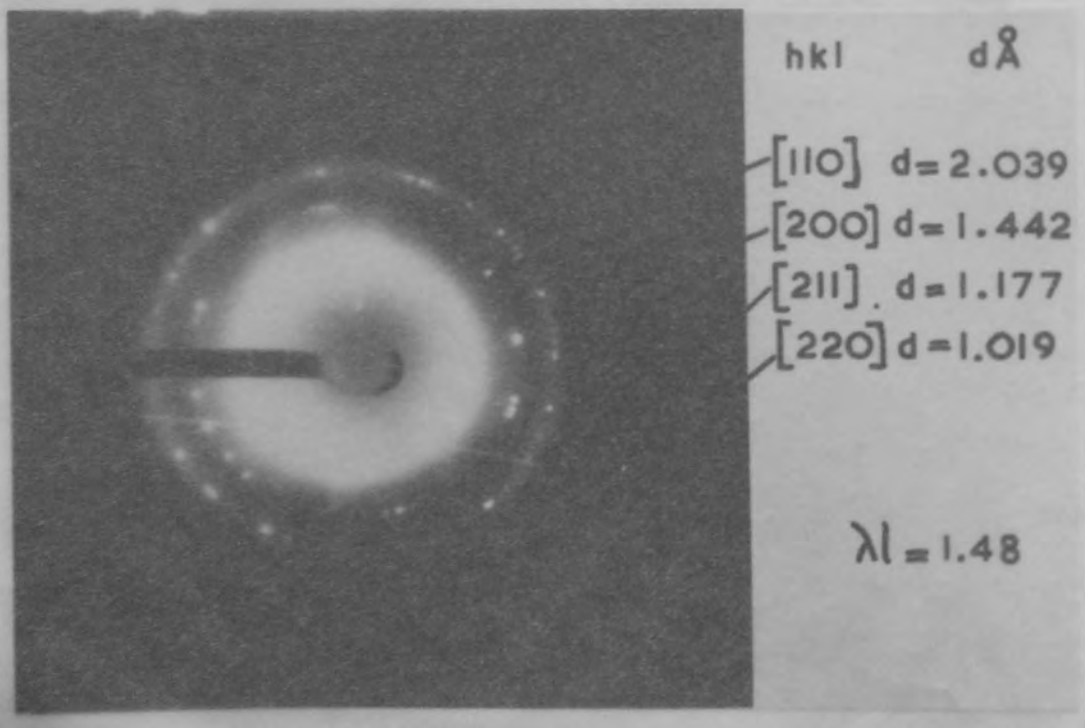

Fig.4.17 Diffraction pattern obtained from chromium particles extracted from alloy aged at 600°C.

when the alloy was overaged, that is, when the bulk fraction of precipitate was at a maximum in the foil. A re-examination of Fig.4.13 shows that certain precipitates are orientated such that they are diffracting strongly (A) and (B) whereas others are not (C). Diffraction patterns obtained from areas containing strongly diffracting particles showed that the particles exhibited an orientation relationship with the copper matrix, a typical pattern being that illustrated in Fig.4.16 taken from a foil overaged at 550°C having an orientation near to [110] direction parallel to the electron beam. The precipitate diffraction spots appear in two groups inside the [002] reciprocal lattice points of the copper matrix, and singly in close association with the four ⟨111⟩ reflections of the matrix, and are all equidistant from the origin. Knowing that the matrix diffraction pattern of an overaged alloy is virtually pure copper, the precipitate reflections were capable of being analysed accurately in terms of the interplanar spacing 'd' they represented, and were found to equal that of the 'd' spacing for the {110} planes in pure chromium. The presence of the 110 reflection indicates that the chromium is precipitated in its normal form i.e. body centred cubic. These conclusions were verified using a carbon extraction replica technique, the precipitate diffraction pattern of which is shown in Fig.4.17.

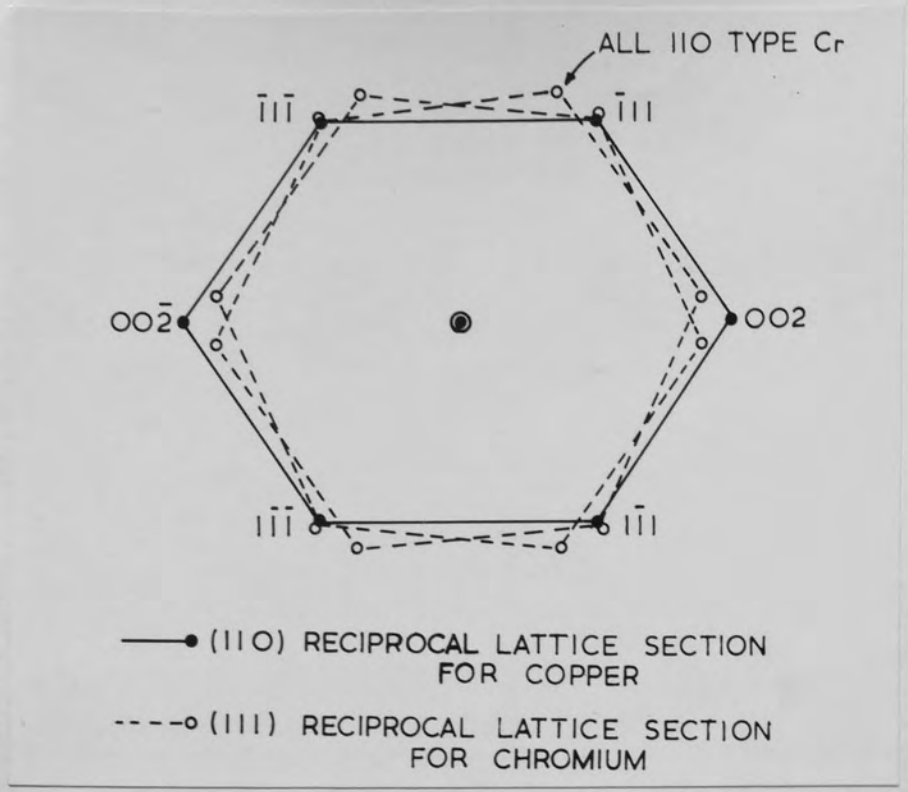

Fig.4.18 Predicted reciprocal lattice points expected from chromium embedded in a copper (110) foil, when arranged in a Kurdjemov-Sachs orientation relationship.

Fig.4.19 Alloy overaged at 550°C for 2 days.
(a) dark field image taken with g[022]
(b) Bright field image.
(c) dark field image using chromium precipitate diffraction spot.

4.3.3 Interpretation

A study of the reciprocal lattice sections arising from B.C.C. materials shows that a crystal with its $\langle 111 \rangle$ parallel to the electron beam generates a section containing six 110 reflections based on a perfect hexagon and it is possible to derive the diffraction pattern shown in Fig.4.16 by superimposing this reciprocal lattice section on that of a $\langle 110 \rangle$ section for copper as shown in Fig. 4.18.

Thus by assuming an orientation relationship of $\{110\}_{Cu} // \{111\}_{Cr}$ we have arrived at the well known Kurdjemov-Sachs crystallographic relationship first shown to exist for the allotropic transformation of iron from a F.C.C. to a B.C.C. structure. The series of micrographs illustrated in Fig.4.19 of the alloy aged at 550°C for 2 days includes a dark field image taken with a matrix diffraction spot Fig.4.19(a) and also one taken with a chromium precipitate spot Fig.4.19(c), and shows that the rods grow in $\langle 110 \rangle$ directions in the copper matrix.

Having assumed the crystallographic relationship between the matrix and precipitate to be of the type suggested by Kurdjemov and Sachs, it is possible to compare the "fit" of the copper and chromium lattices when orientated in this way and to test the observation that the particles grow as rods in the matrix $\langle 110 \rangle$ directions. Firstly, the Kurdjemov and Sachs relationship may be written for the

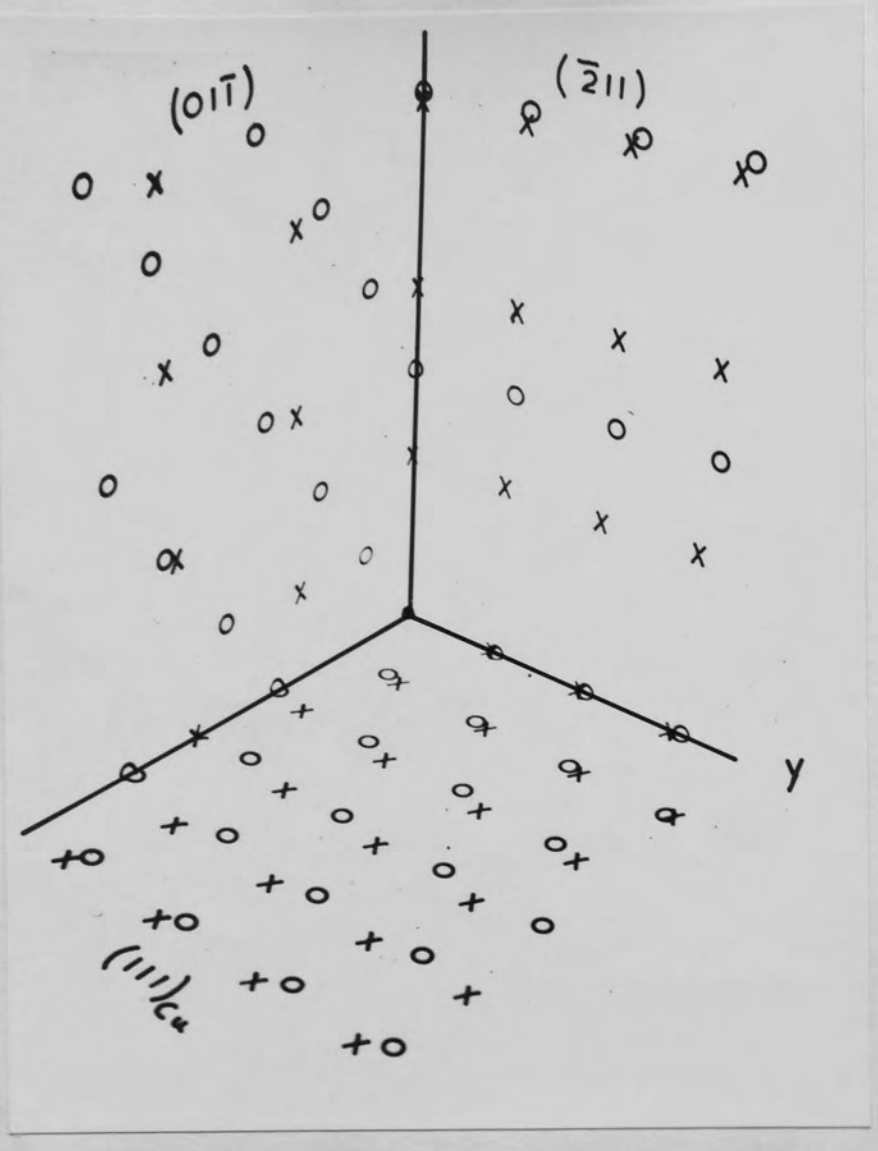

Fig.4.20 Lattice positions of chromium atoms with respect to copper atoms when arranged in the orientation relationship:-

$(11\bar{1})$Cr // $(01\bar{1})$ Cu

$[\bar{1}10]$Cr // $[111]$ Cu

system copper chromium as:-

$$(11\bar{1})_{Cr} \;//\; (01\bar{1})_{Cu}$$

$$(\bar{1}10)_{Cr} \;//\; (111)_{Cu}$$

which in turn implies that:-

$$(112)_{Cr} \;//\; (\bar{2}11)_{Cu}$$

The lattice sites of these three mutually perpendicular planes have been drawn out on a three dimensional model and photographed as in Fig.4.20, the open circles representing the position of the copper matrix lattice sites, and the crosses the corresponding chromium precipitate lattice sites when arranged in a Kurdjemov-Sachs orientation relationship. The small misfit along the copper $[01\bar{1}]$ direction is immediately apparent from this model. By viewing the $(01\bar{1})$ plane of the copper along the line representing the y axis in Fig.4.20 and considering the atomic positions of chromium on this plane, we can describe an area, starting from the origin, in which the chromium positions are some arbitrary fraction of the interatomic spacing 'd' of the copper atom positions and call this an area of "good fit". The dotted line in Fig.4.21 represents such an area for atoms within $d/3$ and gives an indication of the cross section of a precipitate growing in the $[01\bar{1}]$ direction. By a similar analysis in the $[111]$ direction, the shape of the region of "good fit" is shown in the

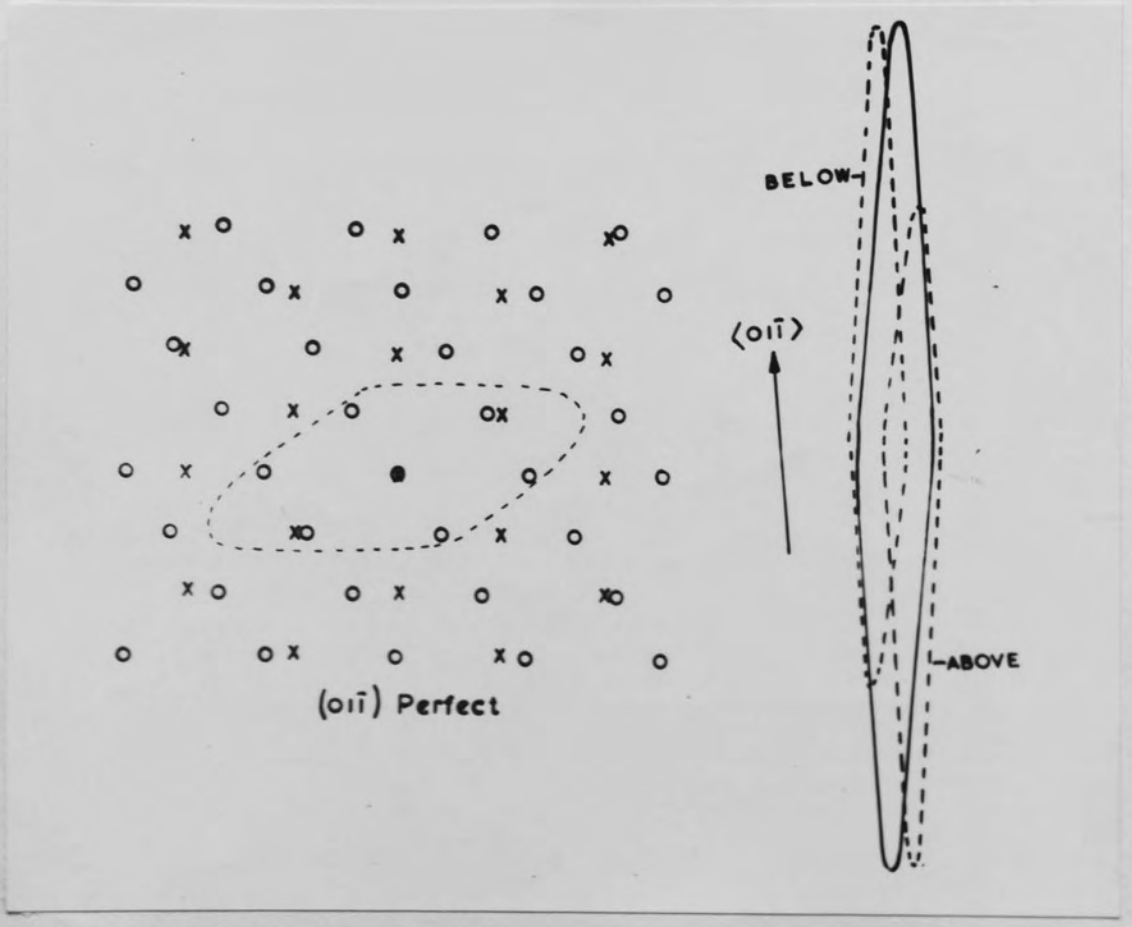

Fig.4.21 Area of "good-fit" between chromium and copper atoms described on the (011̄) plane, and on three (111) planes of the matrix.

same diagram for the (111) plane passing through the origin, and for one above and below it, indicating that the chromium would take up the position of least misfit and hence least strain energy as a rod shaped particle growing in the $[0\bar{1}1]$ direction in the copper matrix. The number of atoms within this region have been calculated as 338 by taking the fraction of chromium atoms to be within $d/3$ of the copper atom sites. Added weight is given to this analysis by considering the variation of elastic constants with crystallographic direction for pure copper. The values of shear modulus, G, are:-

$$\text{Minimum } G_{\langle 111 \rangle} = 3.05 \times 10^{11} \text{ dynes.cms}^{-2}$$

$$\text{Maximum } G_{\langle 100 \rangle} = 7.56 \times 10^{11} \text{ dynes.cms}^{-2}$$

The calculated value for $G_{\langle 110 \rangle}$ is 3.61×10^{11} dynes.cms^{-2}, and therefore the growth of the chromium particles occurs in a direction which exhibits a value of shear modulus close to the minimum value for copper.

A further, and not unrelated consideration which can be used to support the proposed orientation relationship for chromium particles precipitated in copper entails a comparison of the lattice constants for chromium and copper with those of iron, the material in which the transformation was first noted. The only value for the lattice parameter of austenite (F.C.C.) available in the A.S.T.M. Powder Index file is that determined by Goldshmidt who quotes an

approximate value of 3.60 A°.

F.C.C.	a A°	B.C.C.	a A°
Copper	3.6150	Chromium	2.8839
Austenite	3.60	Alpha Iron	2.8664

Taking the misfit δ between the lattices when in a Kurdjemov-Sachs orientation relationship as:-

$$\delta = \frac{2\,(d_{111(F.C.C.)} - d_{110(B.C.C.)})}{d_{111(F.C.C.)} + d_{110(B.C.C.)}}$$

then for iron δ = 0.0256, which is very close to that for chromium particles precipitated in copper at δ = 0.0238.

4.4 Quantitative Analysis of Strain Fields

4.4.1 Introduction

The quantitate treatments applied by Ashby and Brown[55] to the analysis of strain field images around spherical or disc shaped precipitates embedded in an isotropic matrix are, in their present form, inadequate to deal with the results described above for chromium particles in copper. However, the general features of the strain fields observed around the rod shaped chromium particles are qualitatively in agreement with the observations made in the simpler systems.

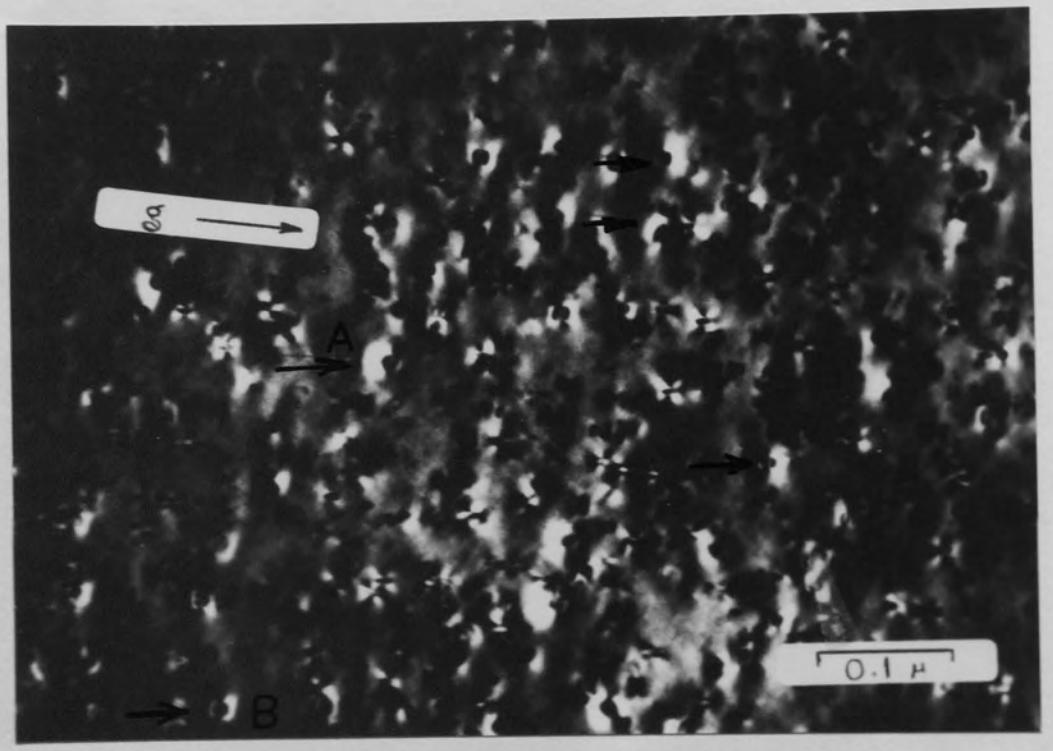

Fig.4.22 Anomalous strain field images (arrowed) from chromium particles near the foil surface.

4.4.2 Anomalous Images

When the coherent chromium particles are within approximately half an extinction distance of the foil surface, asymmetrical images are produced, due to the surface relaxation of the strain field. These images can be used to deduce the sense of the strain around the precipitated chromium particles using the method suggested by Ashby and Brown[55] and outlined in section 3.6.3.2. Fig.4.22 shows a typical dark field image of the structure of material aged at 600°C and anomalous images are arrowed. In the dark field micrograph, the asymmetry of the image depends only on g, the reciprocal lattice vector, and examination of images at A and B in Fig.4.22 illustrates that the sense of the strain is not constant around the rod shaped precipitates. Images at A show a bright 'lobe' on the negative side of g indicating that the strain is positive. The images at B show the reverse and consequently correspond to a negative strain. A consideration of the misfit surface of a rod shaped chromium particle growing along the [110] direction in the markedly anisotropic copper matrix confirms that the circumferential strain is expected to exhibit positive and negative values as shown in Fig.4.23. The relative lattice positions of chromium atoms are shown on a copper (111) plane, when the two lattices are in a Kurdjumov-Sachs orientation relationship.

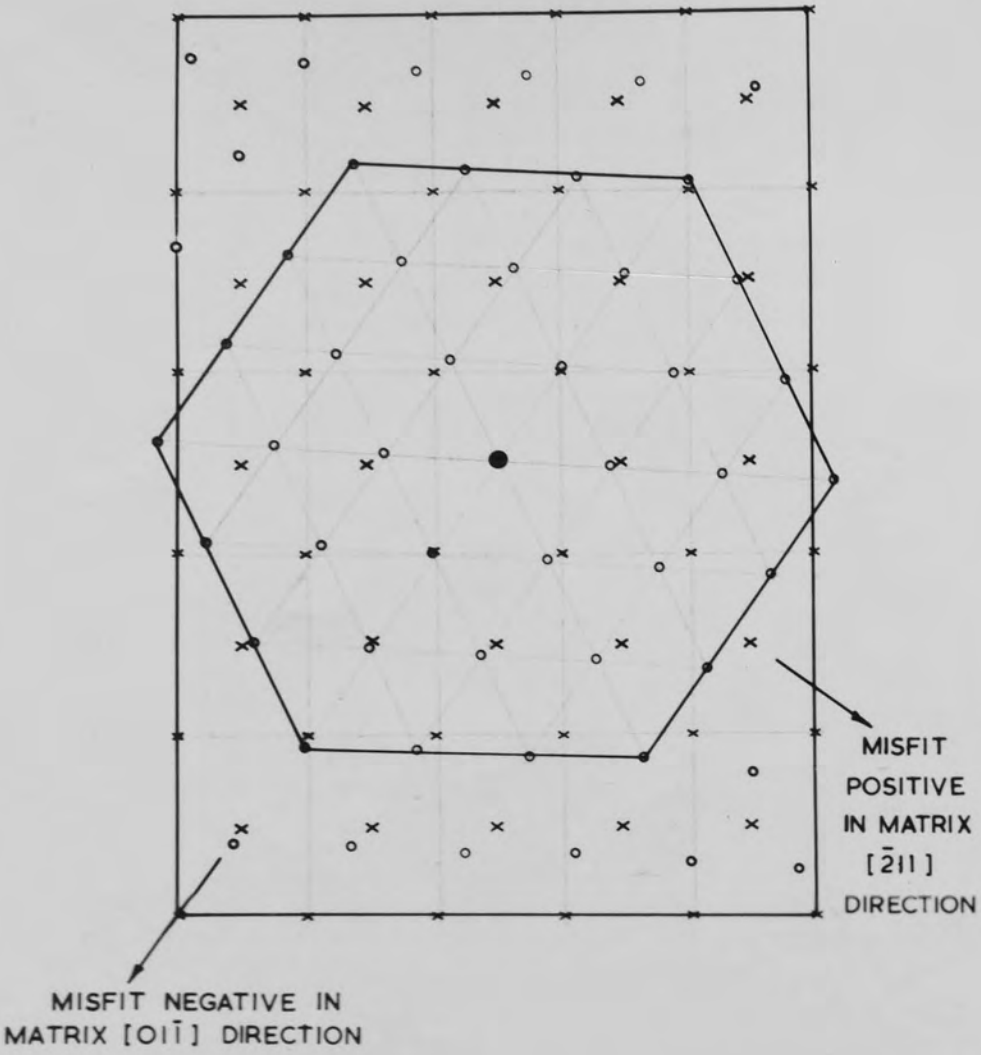

o COPPER ATOM LATTICE POSITIONS ON THE (111) PLANE.

x CORRESPONDING CHROMIUM SITES OBTAINED WHEN THE TWO LATTICES ARE IN A KURDJUMOV–SACHS CRYSTALLOGRAPHIC ORIENTATION RELATIONSHIP.

$$[111]_{Cu} \parallel [\bar{1}10]_{Cr} \; ; \; [01\bar{1}]_{Cu} \parallel [11\bar{1}]_{Cr} \; ; \; [\bar{2}11]_{Cu} \parallel [112]_{Cr}$$

Fig.4.23 Predicted variation of strain between chromium and copper lattices in a Kurdjumov-Sachs orientation relationship.

From Fig.423, the misfit δ in the matrix $[0\bar{1}1]$ direction is negative and has value of -3.3% as calculated from the formula $\delta = \frac{2(a_1-a_2)}{a_1+a_2}$. However, in the matrix $[\bar{2}11]$ direction the misfit is 7.1% and is positive. Since the modulus of rigidity of chromium is greater than that of copper, the matrix is under a compressive stress in this direction whilst the chromium particles maintain a coherent interface with the copper matrix.

A similar analysis in the matrix [111] direction gives a negative value of strain equal to -3.3%. The experimentally observed variation of the sense of the strain field surrounding chromium particles is thus qualified.

4.4.3 Image Widths

The variation of image width with reciprocal lattice vector has already been shown to qualitatively obey the rules suggested by Ashby and Brown[55]. This is considered as the limit to which their analysis can fairly be applied to this system, since the necessary conditions of isotropy in particle and matrix elastic constants, and in strain have been shown not to exist during the growth of chromium particles in copper.

4.5 Particle Coarsening Experiment

4.5.1 Introduction

It has been shown in section 2.2.1.2 that the accurate measurement of interfacial energy between precipitate and matrix is difficult due to the restrictive conditions which apply during true Ostwald ripening. An experiment was performed in order to see if these conditions were being met during coarsening, and also to attempt to obtain an indication of the magnitude of the interfacial energy since metallographic observations indicate that this should be low to explain the retention of coherency at high ageing temperatures, and also the low misfit existing between particle and matrix when arranged in a Kurdjomov-Sachs orientation relationship.

4.5.2. Experimental Conditions

The measurements of particle size after ageing at 600°C for 1, 2, 4, 8 and 16 hours were carried out in regions of the foil where the coherency strain fields had been removed due to surface relaxation. Fig.4.14 shows a typical region used for measurement of particle size, and since the particles grow as rods, then all measurements recorded are for the axial length of the particle. Even after 16 hours ageing treatment, the aspect ratio of the rods did not exceed 2, and therefore the mathematical treatment of the coarsening behaviour of spheroids can be used to give an approximate solution for the interfacial

energy of chromium particles within the copper matrix.

4.5.3. Measurement of Interfacial Energy γ

The growth of the average particle as a function of time is given by:-

$$\bar{r}^m - \bar{r}_o^m = k(t - t_o) \quad .. \quad ..(1)$$

where $\bar{r}$ is the average particle radius at time t. $\bar{r}_o$ is the average particle radius at the onset of coarsening t_o, and k is a rate constant given by:-

$$k = \frac{8\gamma D.c_o V_m^2}{9RT} \quad .. \quad ..(2)$$

Ageing at 600°C causes the chromium to be rejected from solid solution very rapidly, and maximum conductivity is attained after 3 minutes. At times greater than 3 minutes the particles can be considered to coarsen by an Ostwald ripening mechanism. Since the particle size is less than 50 A^o after this heat treatment, then the value for m in equation(1)can be obtained from the slope of a log - log plot of particle size versus ageing time, since r_o and t_o are small. The rate constant can be obtained graphically from the slope of log $\bar{r}^m$ v log t, and compared with the calculated value in order to btain an estimate for γ, the energy of the precipitate-matrix interface.

The histogram in Fig.4.24 shows that the conditions of Ostwald ripening are being obeyed, that is, the

$\frac{L_{max}}{\bar{L}}$ = 1.73 1.42 1.43 1.35 1.48

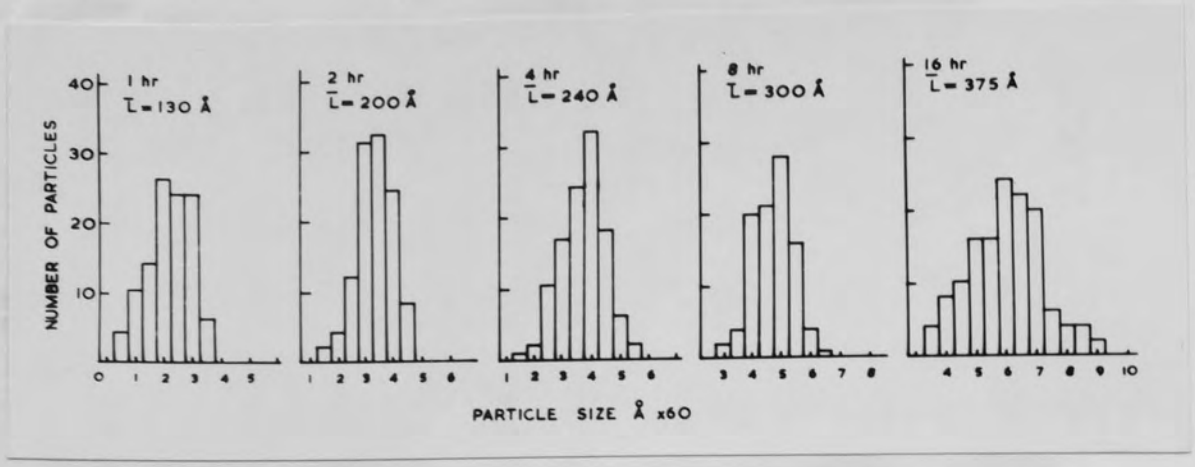

Fig.4.24 Particle size distribution on coarsening at 600°C.

Fig.4.25 Mean Particle length v ageing time.

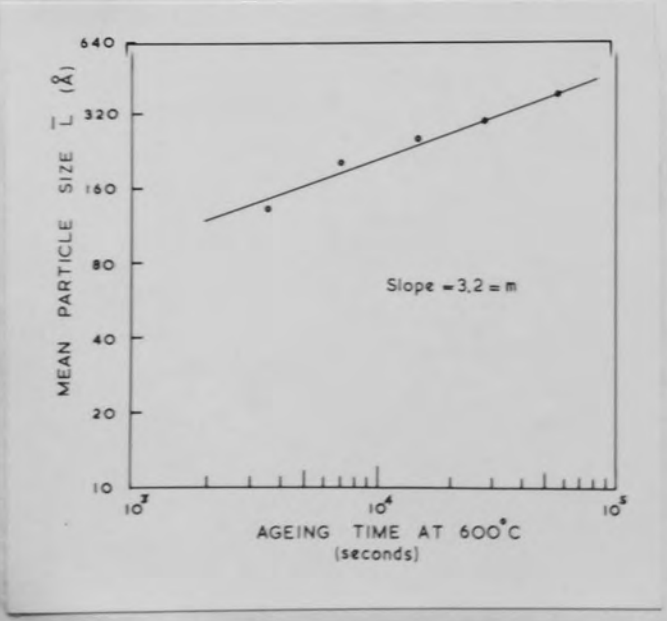

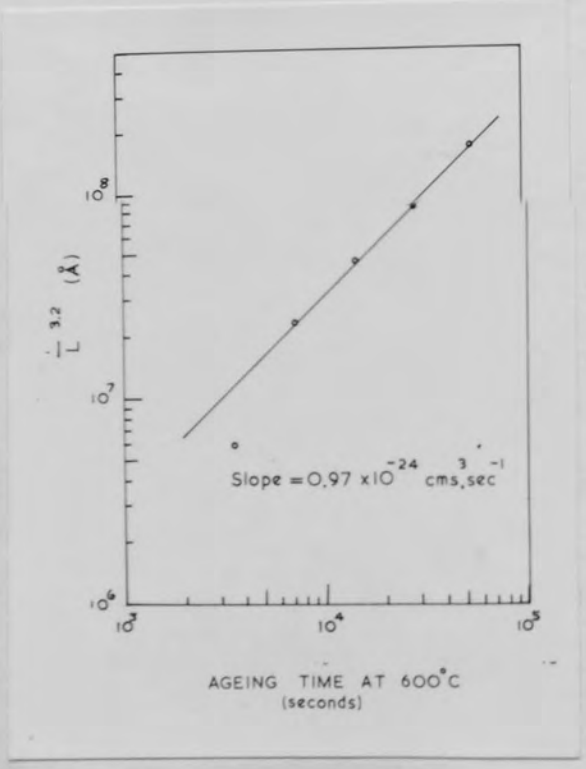

Fig.4.26 Plot of $\bar{L}^{3.2}$ v ageing time to give, k, the rate constant.

distribution of particle sizes remains nearly constant while the mean particle length increases with ageing time. Fig.4.25 yields a value of m = 3.2 which substantiates the fact that the particles are nearly spherical over the range of experimental conditions, since m = 3 for spherical particles. Graphically, the rate constant is 0.97×10^{-24} $cms.^3 sec.^{-1}$ as shown in Fig.4.26. The absence of diffusion data for chromium in copper is a serious source of error in the calculation of the rate constant, and the assumed value at 600°C of approximately 10^{-15} is obtained from the reported diffusion coefficient of nickel in copper since chromium and nickel exhibit similar atomic radii with respect to copper.

At 600°C, for chromium in copper:-

$D = 10^{-15} cms.^2 sec.^{-1}$

$c_o = 6.23 \times 10^{-3} gms.cms.^{-3}$

$Vm = 8.13$

$R = 8.314 \times 10^7 ergs.deg.K^{-1} mole^{-1}$

$T = 873\ ^oK$

Therefore $$k = \frac{8 \times 10^{-15} \times 6.23 \times 10^{-3} \times (8.13)^2 \times \gamma}{9 \times 8.314 \times 10^7 \times 873}$$

$$= 0.49\gamma \times 10^{-26} cms.^3 sec.^{-1}$$

Comparing the calculated value of k with that obtained experimentally yields a value for the interfacial energy of the precipitated particles thus $\gamma = \frac{0.97 \times 10^{-24}}{0.49 \times 10^{-26}} = 197 ergs/cm^2$.

Although the order of magnitude of this value is solely dependent on the correct interpretation of the diffusivity of chromium in the matrix at 600°C, it nevertheless provides a value which is in good agreement with that derived for the simpler case of cobalt particles in copper where a value of γ = 150 ergs.cms.$^{-2}$ is quoted,[63] for particles having a misfit of approximately 2% with the copper matrix. Furthermore, the small misfit of δ = 0.0256 between the chromium particles and the copper matrix, and the retention of coherency after long ageing times support a value of interfacial energy of this magnitude.

4.6 Direct Quenching Experiments

4.6.1 Introduction

The nucleation of precipitates from a metastable solid solution has been shown to be dependent on both the solute and vacancy super-saturation produced on quenching. A high supersaturation generally favours copious homogeneous nucleation whereas at low supersaturations a precipitate will tend to nucleate hetrogeneously and grow rapidly by drawing solute from regions adjacent to it before homogeneous precipitation begins, and therefore its presence will be obvious on a micrograph. The effect of solute supersaturation on the nucleation stage in most precipitation systems is difficult to seperate from vacancy super-

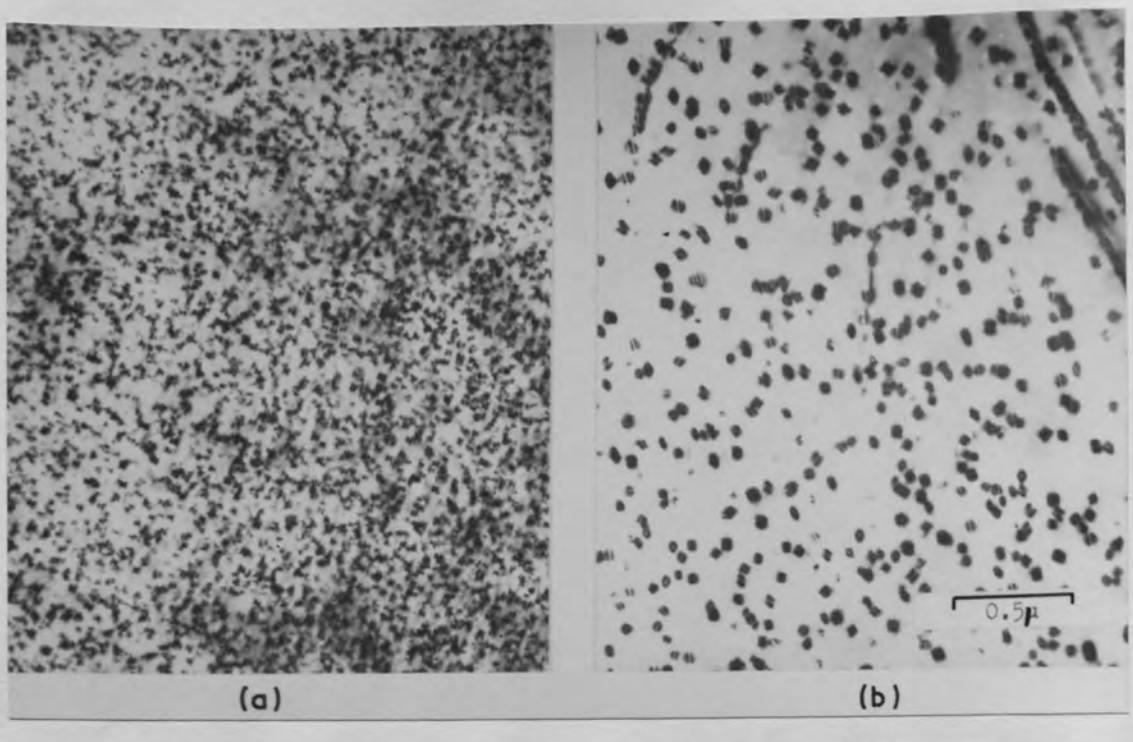

Fig.4.27 Comparison of precipitate dispersion after
(a) room temperature quenching and ageing at 500°C for 2 hours and
(b) direct quenched to the ageing temperature.

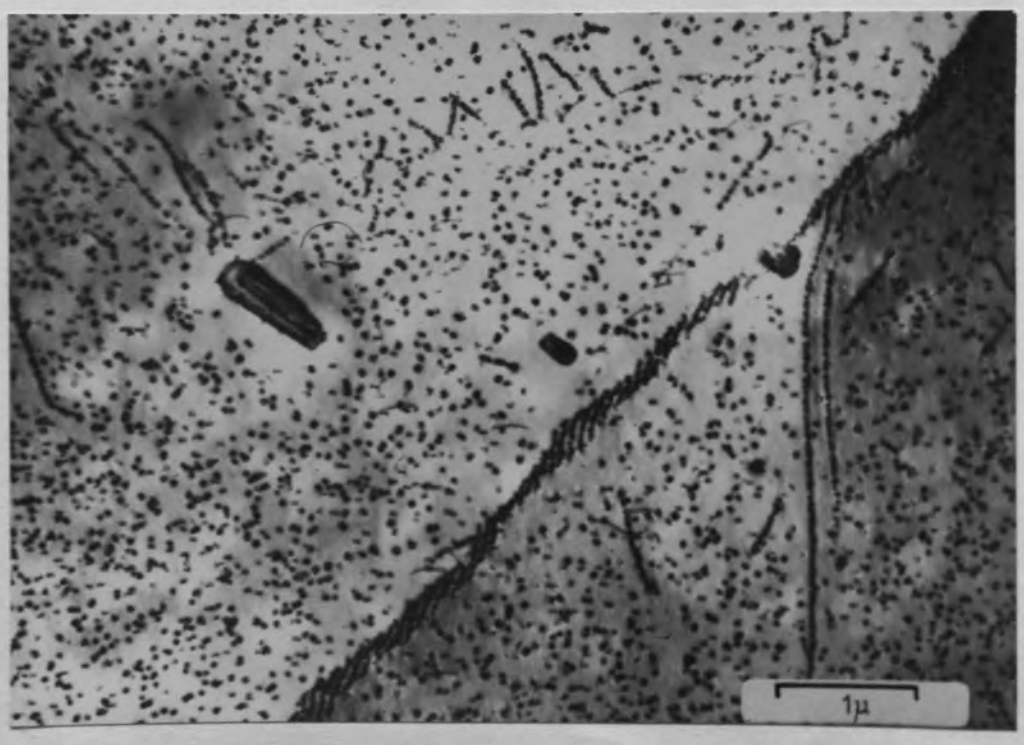

Fig.4.28 Hetrogeneous nucleation of chromium particles at dislocation arrays in material direct quenched to 500°C.

saturation effects when the solid solution is formed by quenching to room temperature. However, by quenching directly to the ageing temperature, the excess vacancy concentration can be eliminated rapidly at such vacancy sinks as dislocations and grain boundaries, and the corresponding effect on precipitate nucleation measured. A series of experiments performed on Al-Mg-Zn alloys by Lorimer[64] ably demonstrates the profound effect of vacancy supersaturation on precipitate nucleation.

4.6.2 Results

A comparison of the structure of copper chromium direct quenched to 500°C with that obtained after water quenching and then aging at 500°C illustrates the effect of supersaturation on precipitate nucleation, Fig.4.27. In the room temperature quenched material, the number of active nuclei for homogeneous precipitation, which is taken as the number of particles present per unit volume of matrix, is twice that of the number present in the direct quenched material, which is a direct consequence of decreasing the supersaturation. A more striking difference between the two structures is that the direct quenched material contains a high density of dislocations with respect to the room temperature quenched material. The dislocations are generally in the form of low angle sub-boundaries as shown in Fig.4.28 and are heavily decorated with the chromium precipitate. The regions of solute

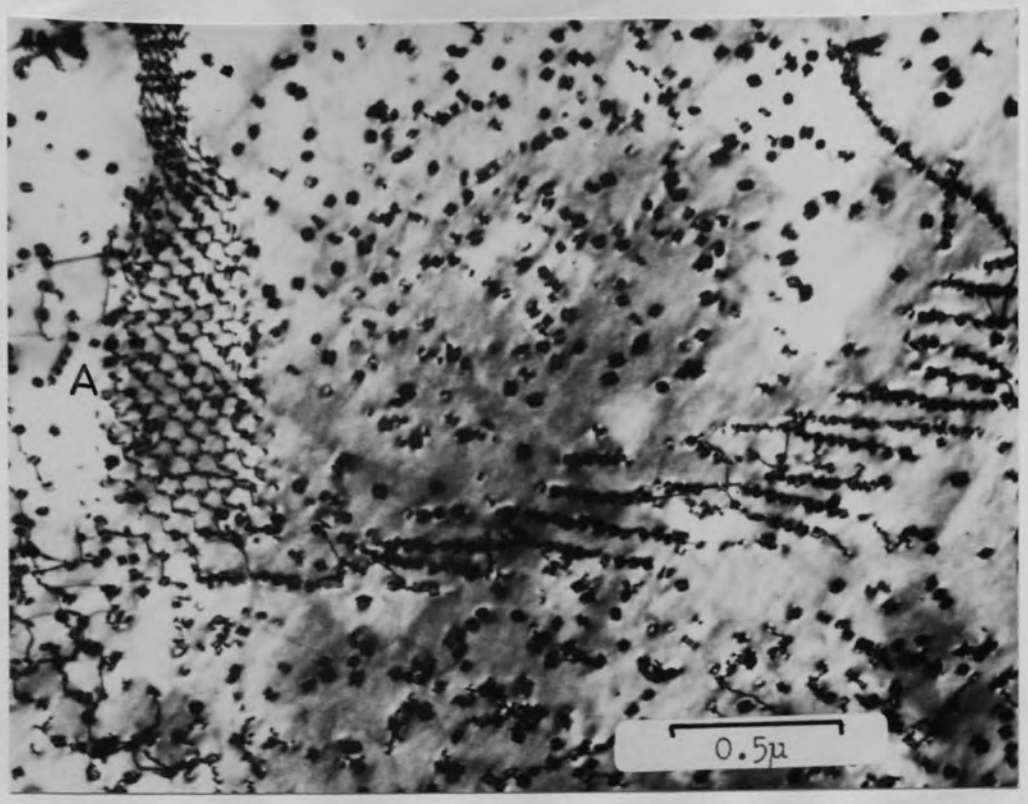

Fig.4.29 Low angle boundaries in direct quenched material showing dislocation networks containing chromium particles.

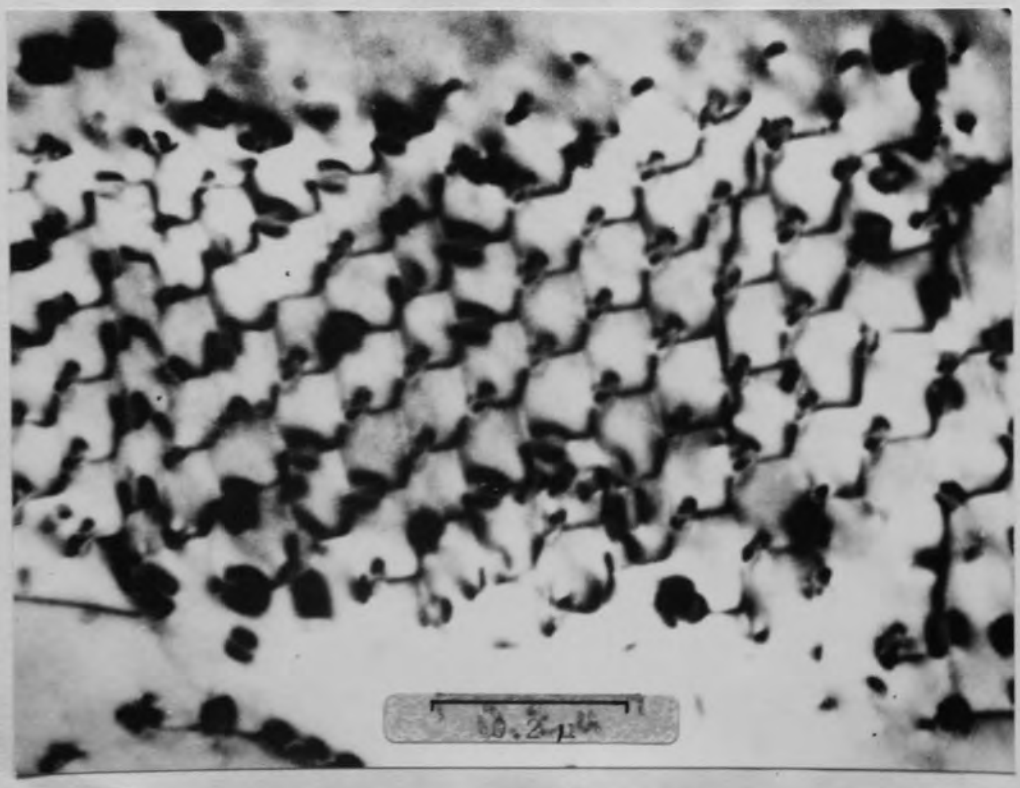

Fig.4.31 Area (A) in Fig.4.29 showing that precipitation has occurred only at alternate nodes.

denudation around the sub-boundaries are small, and the size of precipitate found on such dislocation networks does not differ from that precipitated homogeneously within the matrix.

A further example of hetrogeneous nucleation of chromium in the direct quenched material is illustrated in Fig.4.29. The dislocation network shown in this micrograph contains a region (A) where the individual dislocations are arranged in a manner typical of that formed by intersecting extended dislocations. The Lomer--Cottrell nodes formed by such intersections have been discussed by Whelan[65], and can be represented diagrammatically as in Fig.4.30. The partial dislocations in a node are considered to be in equilibrium under a force due to their line tension and a force due to the stacking fault energy, and detailed observation of such nodes in an array of intersecting dislocations shows that the nodes are alternately extended and contracted. Fig.4.31 is a magnified image of the region (A) in Fig.4.29 and shows that the chromium has precipitated only on alternate nodes.

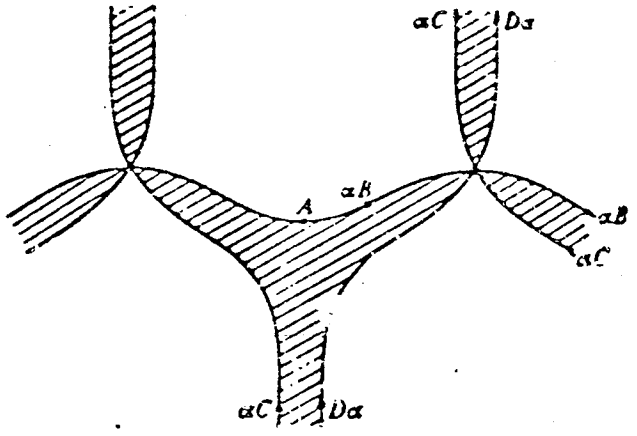

Fig.4.30. Extended node of a network of dislocations.(after Whelan)

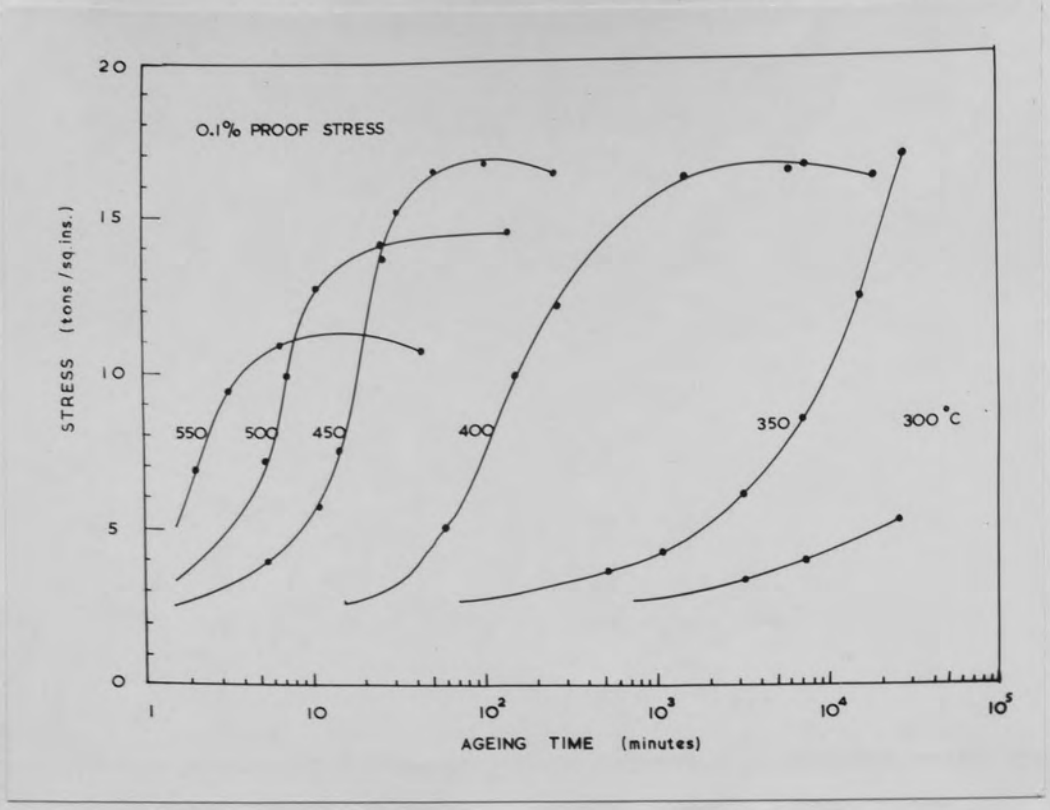

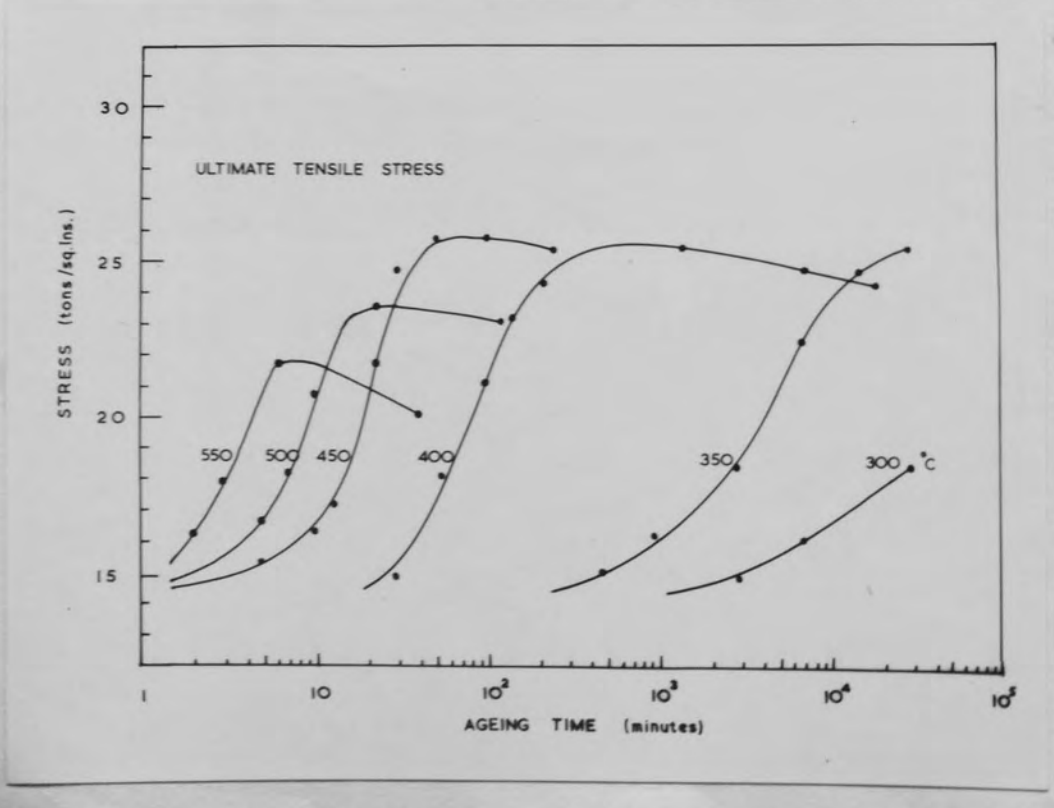

Fig.4.32 Mechancial Test results from isothermally aged material.

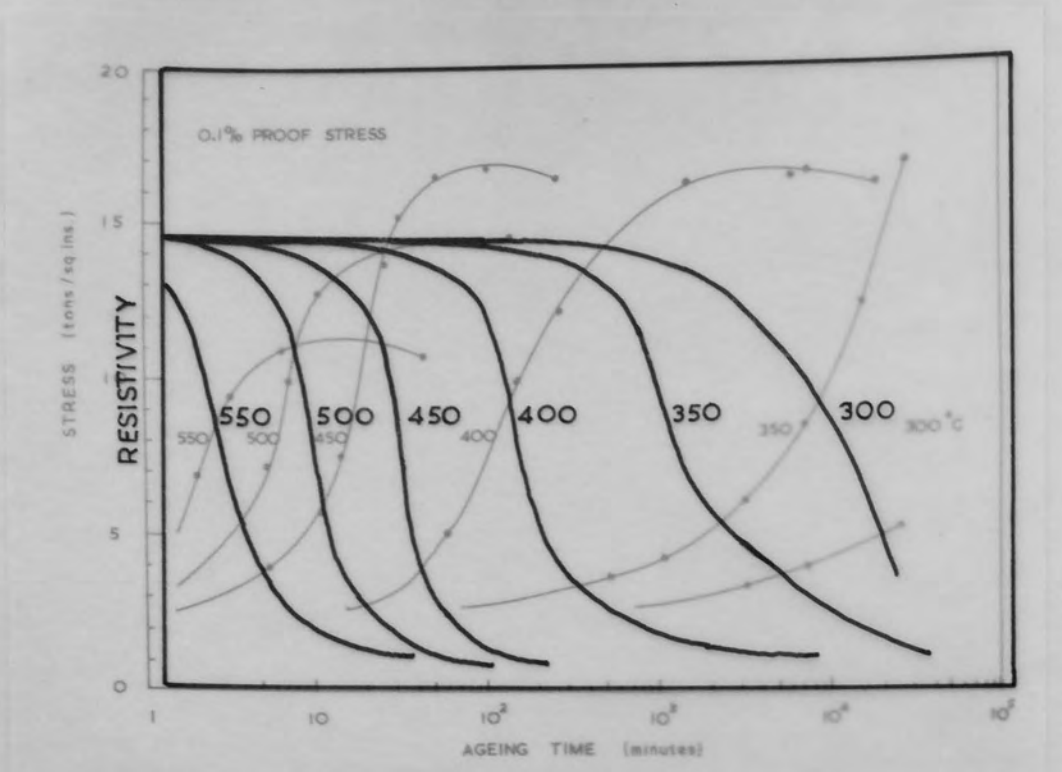

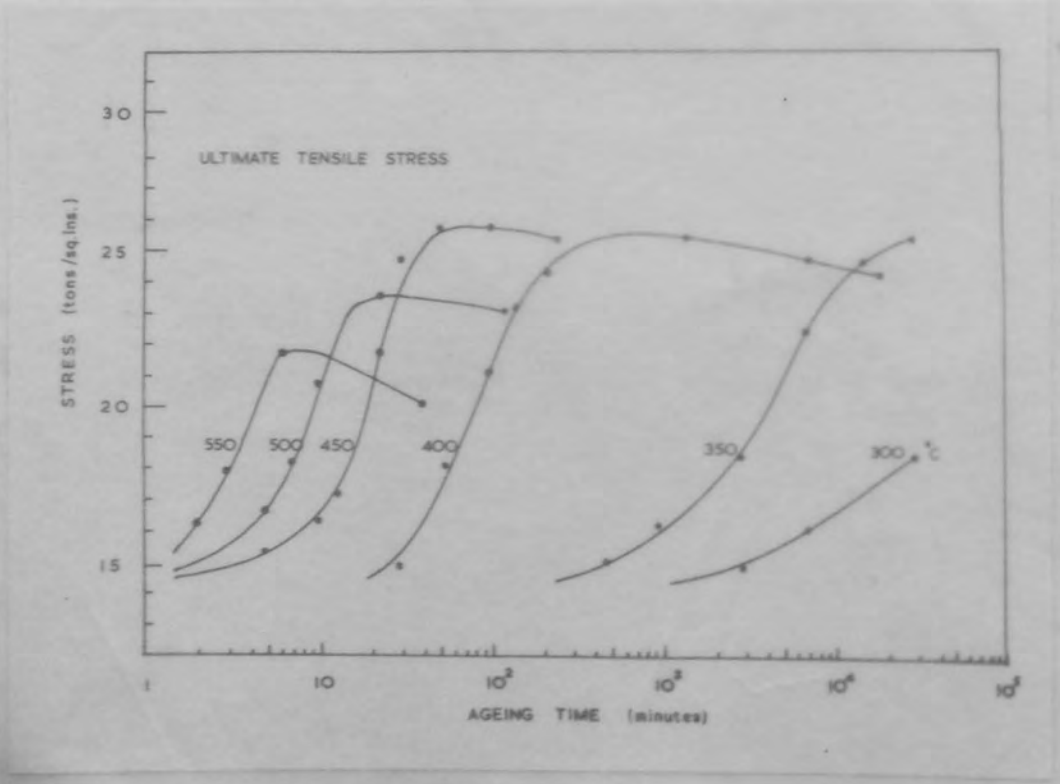

Fig.4.32 Mechancial Test results from isothermally aged material.

Further evidence will be shown in a later section that the region of stacking fault present in an extended node presents a favourable nucleation site for chromium.

4.7 Mechanical Properties of Aged Cu-Cr

The mechanical test results are displayed in Fig.4.32 and the resitivity data is reproduced in order to illustrate that the attainment of peak strength and maximum conductivity are coincident over the range of ageing temperatures investigated. The response to age-hardening is recorded with equal merit by the ultimate tensile strength and 0.1% proof stress measurements and a maximum value for both is obtained in material aged at 350 - 450°C. The maximum value obtained for the flow stress of the aged material correspond to $6 \times 10^{-3}G$ where G is the shear modulus of pure copper. The results suggest that the same mechanism of strengthening is provided on ageing the material over the whole range of temperatures studied.

4.8 Concluding Summary

The kinetic data collected from resistivity measurements on isothermally aged specimens has proved to be a useful means of following the transformations attending the breakdown of the solid solution formed in copper chromium. and reflects accurately the main features of the metallographic observations. The Avrami data predicts the

presence of rod shaped particles and suggests that the growth of chromium in copper is diffusion limited over the range of ageing temperatures studied. The electron microscope has been used quantitatively to show that the rod shaped particles precipitate copiously and maintain a coherent interface and a Kurdjomov--Sachs type crystallographic orientation relationship with the copper matrix during ageing. This precipitation behaviour is consistent with the low value of 200 ergs/cm^2 obtained for the interfacial energy between chromium particle and matrix.

Direct quenching the solution treated alloy to the ageing temperature has shown that the precipitate dispersion is reduced by a half due to the rapid lowering of solute supersaturation and diffusivity accompanying such heat treatment cycles. Hetrogeneous nucleation on dislocations is more prominent in direct quenched materials, and observations have been made which suggest that stacking faults may provide similar hetrogeneous nucleation sites for the chromium particles.

CHAPTER 5.

THE ALLOY COPPER-0.24% ZIRCONIUM

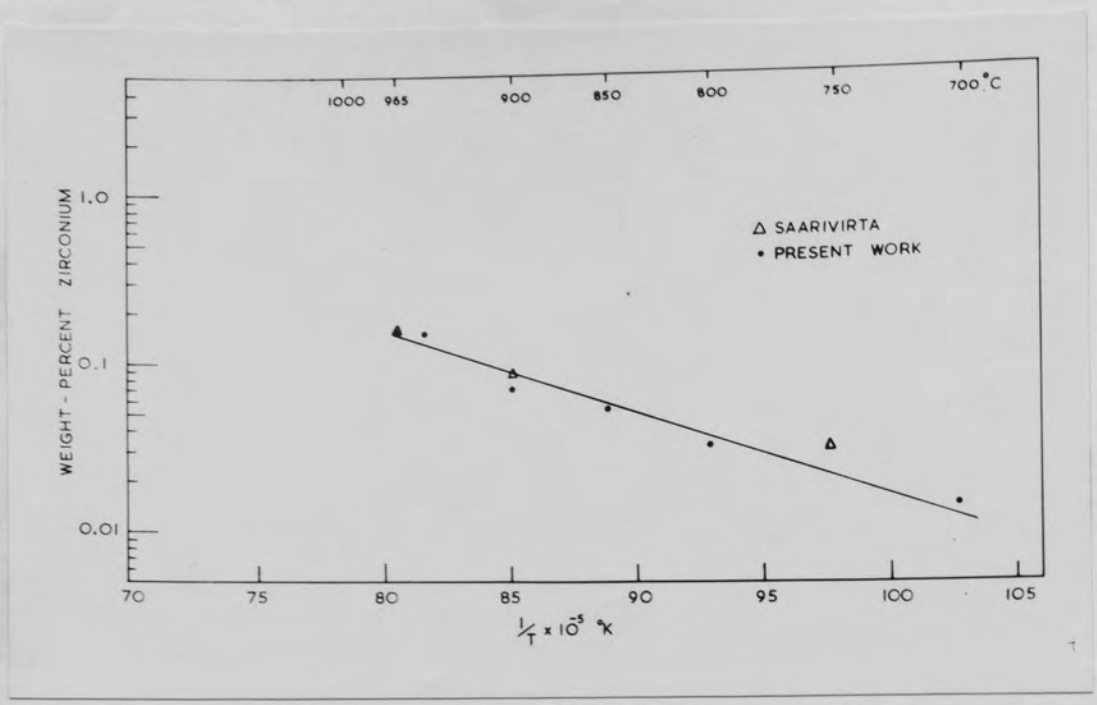

Fig 5.1 Comparison of the solubility of zirconium in copper with published results.

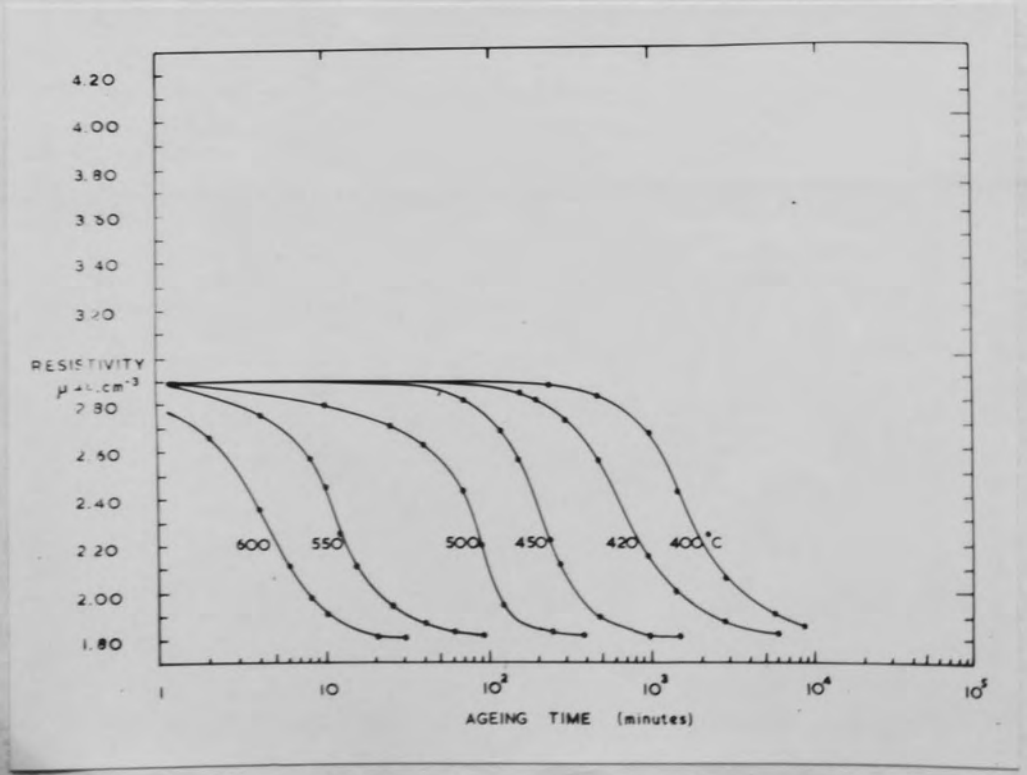

Fig.5.2 Sigmoidal decay curves obtained from isothermal ageing experiments. Alloy solution treated at 950°C.

COPPER - 0.24% ZIRCONIUM

5.1. Electrical Resistivity

5.1.1 Solubility

If it is assumed that the maximum solubility of zirconium in copper is that reported by Saarivirta[10] i.e. 0.15% at 965°C, and that the resistivity changes in the solid solution obey a linear relationship with the zirconium content of the solid solution then the resistivity observed at 965°C in the 0.24% zirconium alloy can be used to obtain an incremental value for the increase in resistivity due to zirconium. The value obtained is 0.0086 $\mu\Omega cms^{-3}$/10 p.p.m. solute (a figure twice that of chromium) thereby allowing the solubility over the range 700°- 965°C to be plotted from a series of isochronal annealing experiments as shown in Fig.5.1. The minimum resistivity attained at 20°C after fully ageing the solution treated alloy in the range 400-600°C was constant at 1.81 $\mu\Omega cms^{-3}$ which is equivalent to a conductivity of 95.5% I.A.C.S., and a minimum solubility of 0.014 wt.%.Zr.

5.1.2 Isothermal Ageing Data

The precipitation of zirconium from copper over the range of ageing temperatures 400°- 600°C yielded the sigmoidal decay curves shown in Fig.5.2. The empirical activation energy, Qe, for the process was derived by plotting the time taken to 50% transformation against the

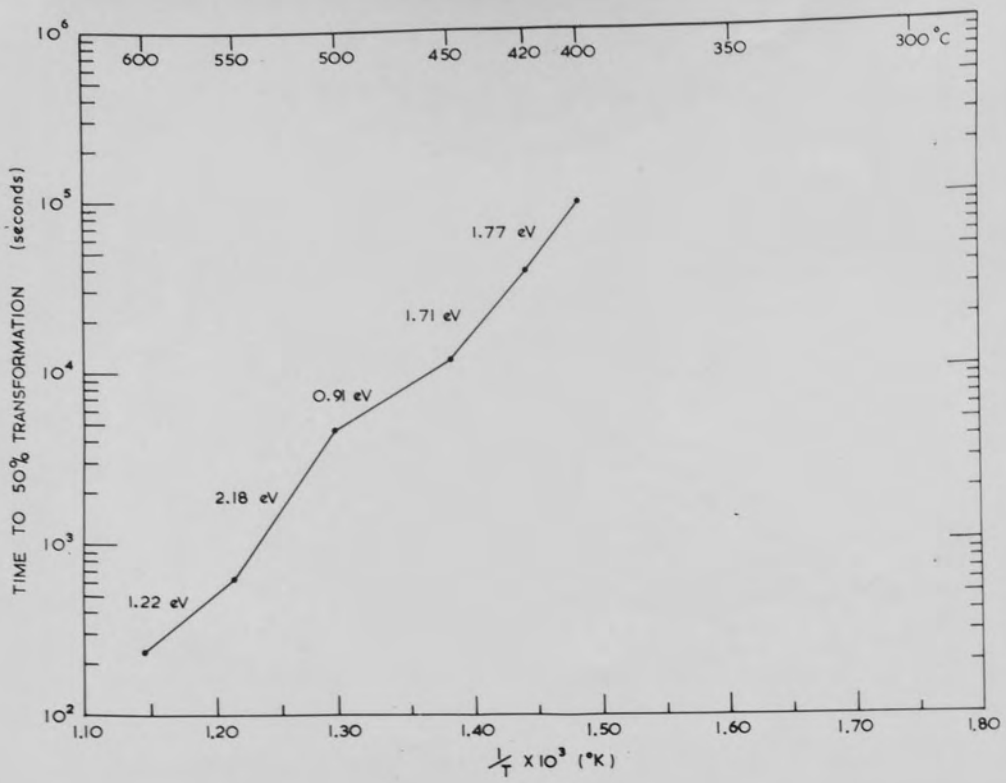

Fig. 5.3 Arrhenius plot of resistivity data.

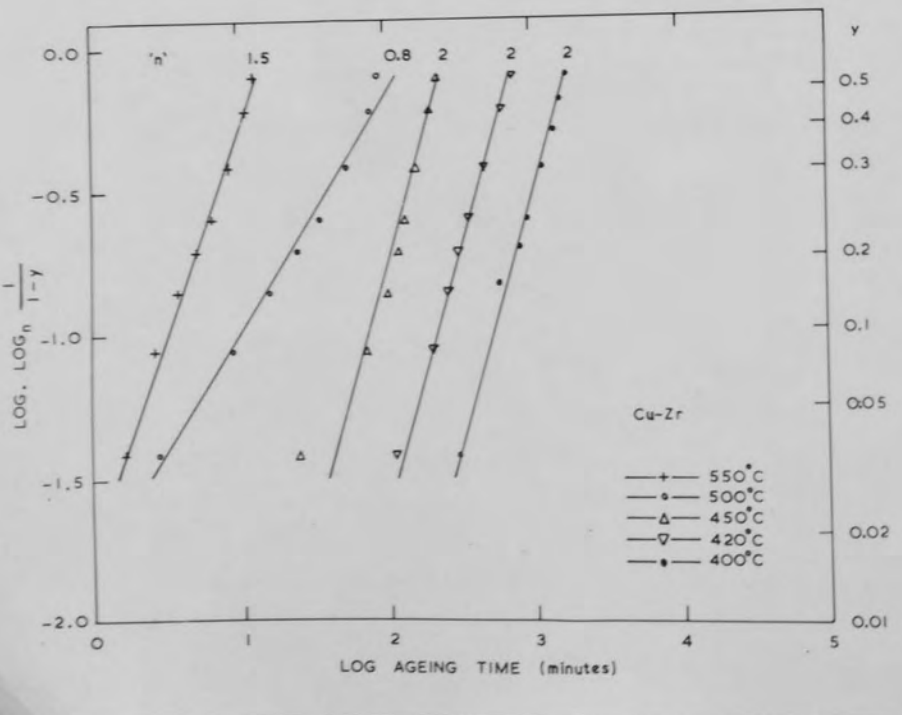

Fig. 5.4 Avrami plot of resistivity data.

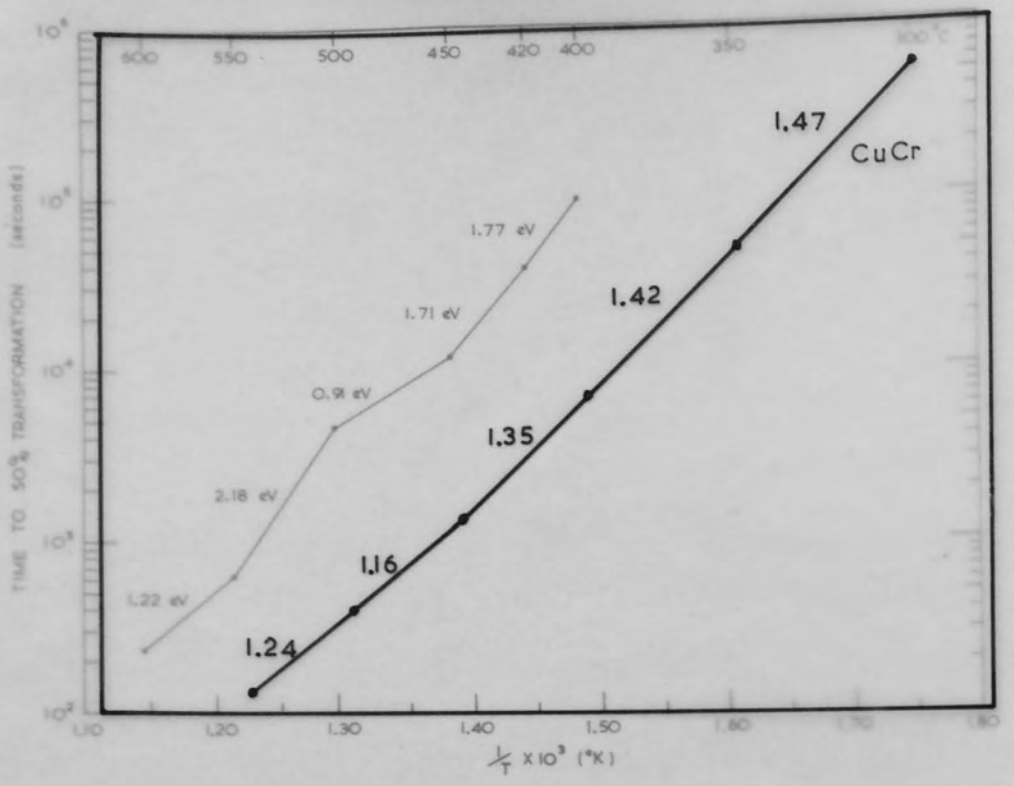

Fig. 5.3 Arrhenius plot of resistivity data.

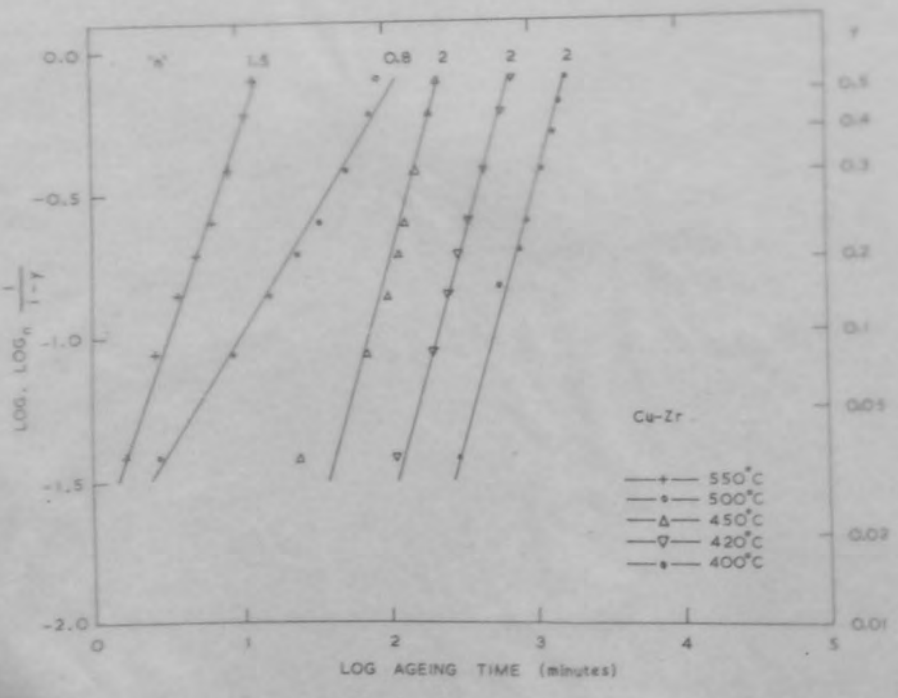

Fig. 5.4 Avrami plot of resistivity data.

reciprocal of the absolute ageing temperature. Fig.5.3 describes the results obtained, and a tracing of the results from the copper chromium alloy is interleaved for comparison. The increased incubation period observed in the Cu-Zr alloy for similar ageing temperatures to those used for Cu-Cr is immediately apparent by the vertical shift of the data on the time scale. Fig.5.3 also shows that the empirical activation energy for the precipitation processes in Cu-Zr is a temperature sensitive function, and that above 450°C, to proceed, the reaction requires only one half of the activation energy observed at the lower temperatures. This behaviour is reflected in the Avrami plot of the resistivity data, Fig.5.4, which shows that above 450°C, the value of the time exponent 'n' changes and hence the reaction proceeds via a different path. The material when aged below 450°C gives rise to a time exponent of n = 2. The same exponent has been used by Ham[62] to describe the diffusion controlled growth of discs of constant thickness. Above 450°C, the time exponent for the process is no longer constant, and no model for the type of transformation occurring at the higher temperatures can be suggested. However, the large reduction of empirical activation energy observed between 450°- 500°C suggests that the nucleation stage of the transformation is modified over this temperature range.

It was suggested in section 3.4.3 that the precise

Fig.5.5 Solution treated at 950°C and water quenched.

x 75

values of the empirical activation energy were difficult to interpret in terms of atomic behaviour during transformation. However, the term is expected to convey approximate information on the relative diffusion rates of solute atoms during transformation, when the transformation process is known to be that of homogeneous nucleation of the precipitating phase. If the data for Cu-Cr is compared with that of Cu-Zr over the range 350°- 450°C, the respective values of 1.4 eV and 1.75 eV, are obtained and suggest that the diffusion rate of zirconium through the copper lattice is slower than that of chromium. Although no diffusion data is available for either of these cases, a comparison of the atomic radii of the chromium and zirconium atoms with that of copper shows that the misfit of the chromium atom in a copper lattice is 2.3%, whereas that of zirconium is 25%. This may be manifested as a difference in the diffusion coefficient for the two systems and consequently reflected in the values of the empirical activation energy for the precipitation reactions.

5.2 Metallography

5.2.1 Optical Metallography

The microstructure of the solution treated material was similar to that described for copper chromium except that the measured grain size was 0.2 mm. Fig.5.5 shows the structure at a magnification of X 75 after

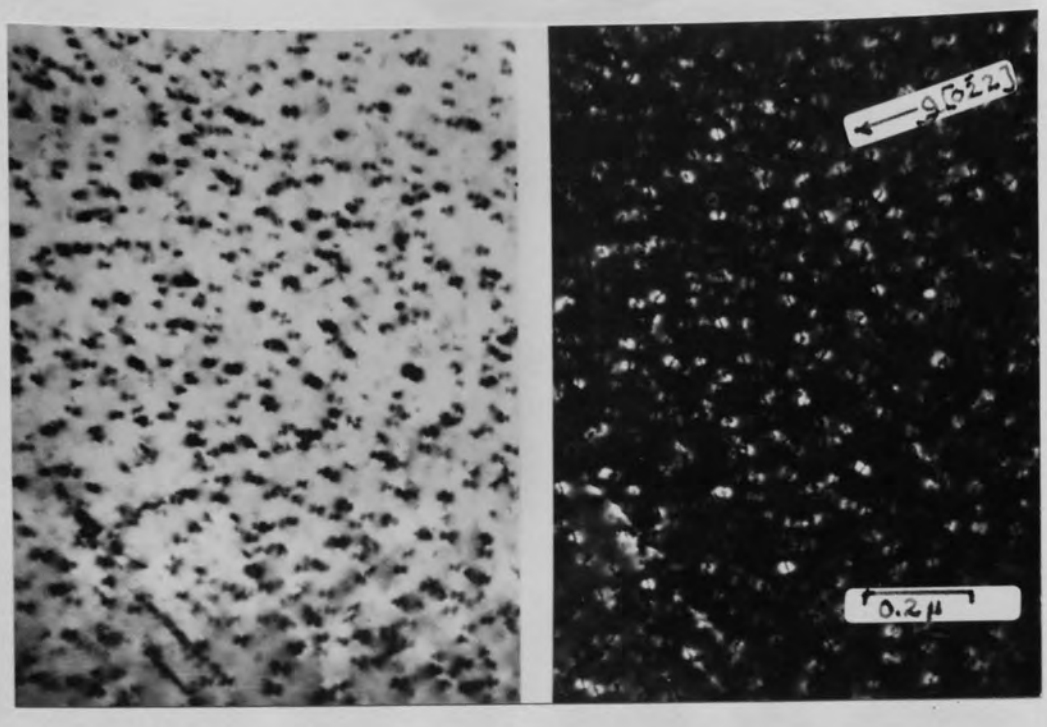

Fig.5.6 Aged at 400°C for 30 hours.

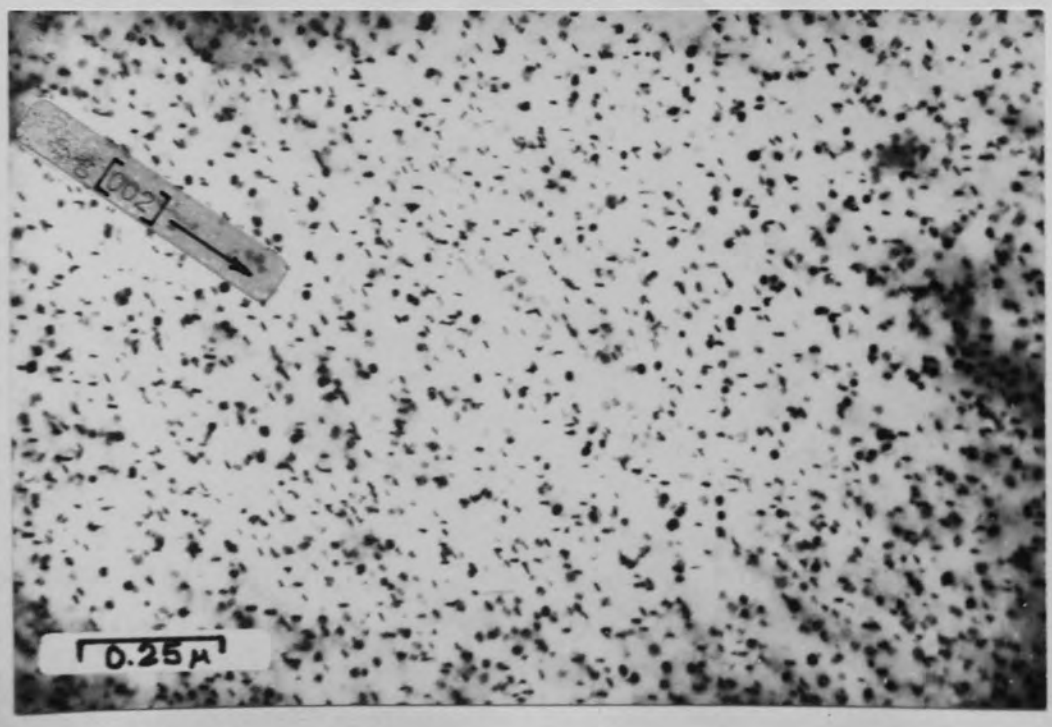

Fig.5.7 Aged at 420°C for 24 hours.

solution annealing at 950°C for 1 hour. Furthermore, the electron microstructure of the solution treated material exhibited the same featureless structure described for copper chromium.

5.2.2 Electron Metallography of Aged Material

5.2.2.1 General

The kinetic data indicates that the precipitation processes occur with similar values of activation energy below 450°C, and that above this temperature, there is a possible change in transformation path. The observed microstructures can conveniently be sub-divided into two stages, those observed below 450°C and those at and above 450°C.

5.2.2.2 Stage 1 - Alloy aged below 450°C

The initial stages of decomposition of the super-saturated solid solution were examined at 400°C, and produced microstructures typical of that shown in Fig.5.6. The bright field image illustrates that the precipitate has grown to approximately 100Å in length on completion of the transformation at this temperature, and that it maintains a coherent interface with the copper matrix. The dark field micrograph shows that the coherency strain is accommodated in the copper matrix, and suggests that the precipitate is disc or rod shaped. Ageing at 420°C for 24 hours confirms that precipitation occurs by the homogeneous nucleation of disc shaped precipitates and is shown in Fig.5.7. From this

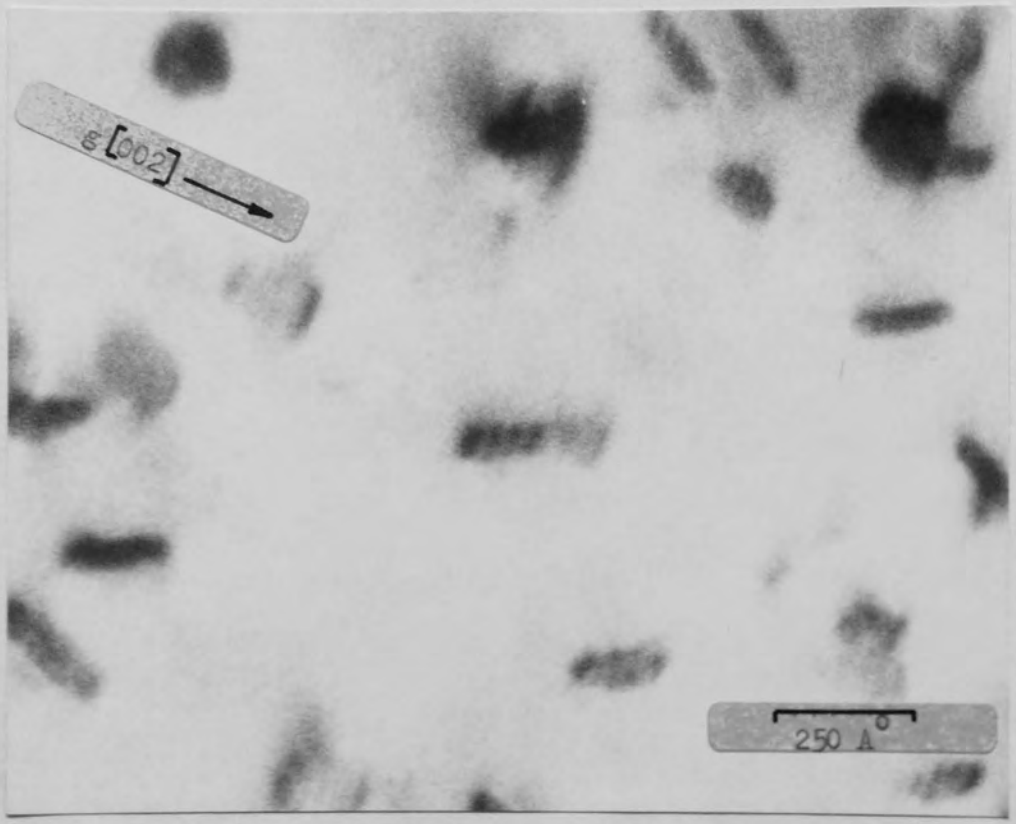

Fig.5.8 Moire fringes observed parallel to $\{002\}_{Cu}$ in disc shaped precipitates.

micrograph, it is evident that the disc shaped precipitates lie on the {111} planes of the copper matrix, and form a Widmanstätten pattern. Those precipitates inclined at $35^{o}16'$ to the (110) foil surface i.e. on the planes (111) or (11$\bar{1}$), exhibit coherency strain fields with their line of no contrast perpendicular to <002>. On closer examination of the disc shaped precipitates lying on those {111} planes which are "edge on" in the (110) foil i.e. on (1$\bar{1}\bar{1}$) or (1$\bar{1}$1), moire fringes were observed in the precipitate running parallel to the cube planes of the matrix as shown in Fig.5.8. The presence of moire fringes indicates that the lattice mismatch is small in the plane of the disc between the (002) plane in the matrix and some unknown plane (hkl) in the precipitate, and accounts for the earlier observation of coherency strain fields around the precipitate. The interplanar spacing, d, of the precipitate plane (hkl) which generates a moire pattern at the particle/matrix interface due to the small difference in 'd' between $(002)_{Cu}$ and $(hkl)_{Ppte.}$, may be calculated as follows:-

For parallel fringes:-

$$d_{effective} = \frac{d_1 . d_2}{d_1 - d_2}$$

From Fig.5.8 the effective 'd' spacing is the spacing of the moire pattern fringes, which is $35A^{o}$. The two values

which arise for the precipitate planes (hkl) are:-

(a) 1.720A° or (b) 1.910A°

Consequently, the misfit, δ, in the matrix <002> directions is:-

$$\delta = \frac{2(d_1-d_2)}{d_1+d_2} = 0.0544 \text{ or approx. } 5\%$$

This value for the misfit between the precipitate (hkl) plane and (002) plane in the matrix can be used to predict the size at which the precipitate is likely to become inchoherent. Brooks[67] has treated the case for the fitting together of two crystals of slightly different lattice parameter and shown that the introduction of an array of dislocations of burgers vector, b, at distances along the planar interface of D will relieve the misfit strain δ thereby forming a non-coherent interface.

For the case observed above, then the precipitate can be considered as having a planar interface coherent with the matrix (hence the reason for growing as a disc) and so when the precipitate achieves a diameter D then the strain can be relieved by the introduction of a dislocation i.e. when $D = \frac{b}{\delta} = \frac{3.6 \times 10^{-8}}{5.4 \times 10^{-2}} = 70A^{\circ}$

This can be considered as a lower limit since it may prove difficult to nucleate the necessary interfacial dislocations, but discs of precipitate approximately 200A° in diameter are observed at higher ageing temperatures which give

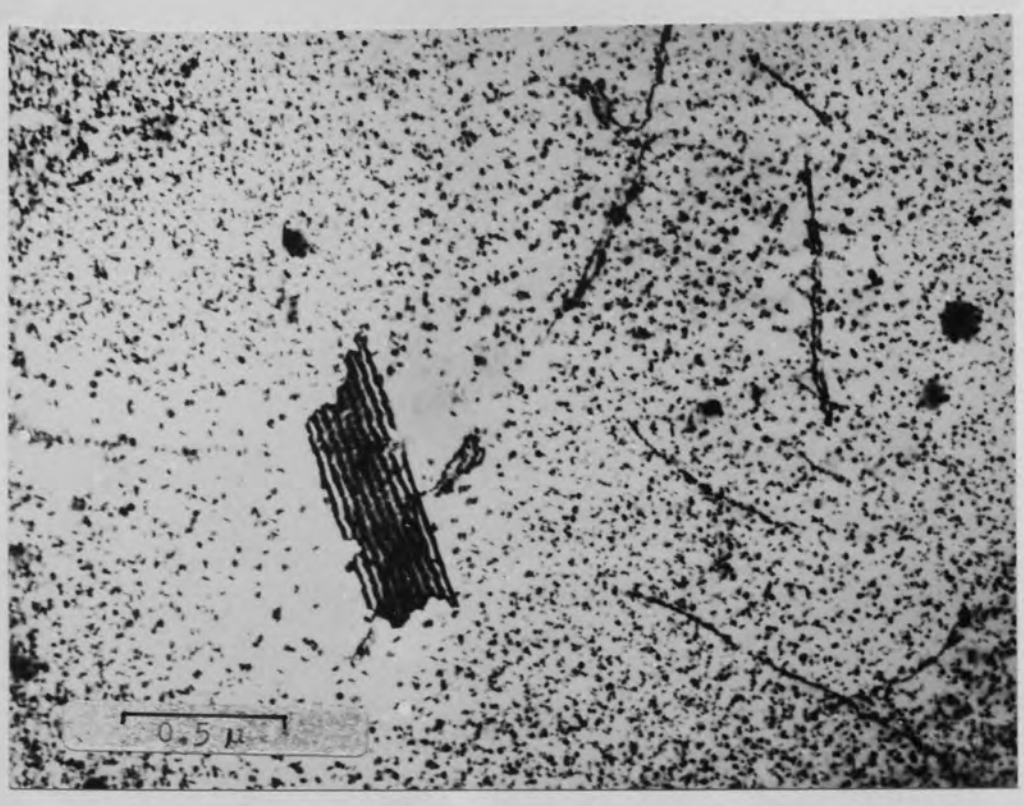

Fig.5.9 Hetrogeneous nucleation sources in the alloy aged at 420°C

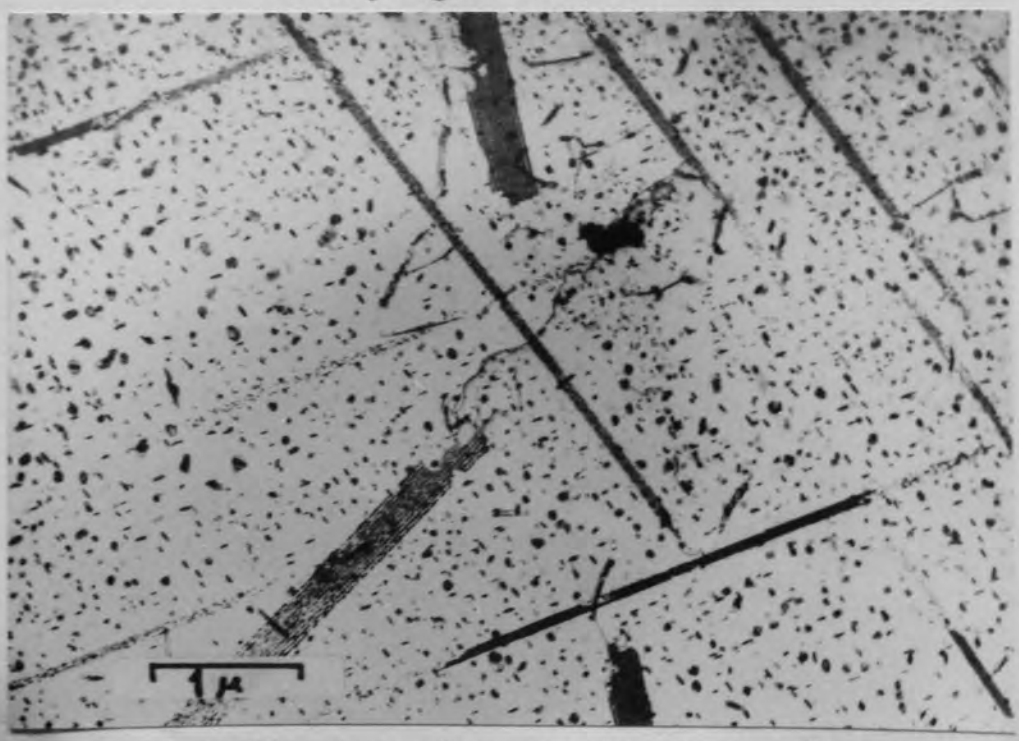

Fig.5.10 Fully transformed structure after ageing at 450°C.

contrast effects indicating a total loss of coherency.

The precipitation of the copper zirconium compound from the solid solution also occurs to a limited extent on any hetrogeneous nucleation sites, particularly dislocation lines. Fig.5.9 shows localized regions of precipitate denudation around dislocation lines in a material aged at 420°C, and also shows a stacking fault which has grown during ageing and provided a further hetrogeneous nucleation source. The importance of stacking faults as nucleation sources for the precipitate becomes more apparent as the ageing temperature is increased to 450°C.

5.2.2.3 Stage 2 - Alloy aged at 450°C and above

It has been shown from the resistivity data, that the empirical activation energy for the precipitation process changes abruptly on ageing at temperatures of 450°C and above. The precipitation reactions described above, are modified when the alloy is aged at 450°C by the growth of stacking faults during ageing to produce structures typified by Fig. 5.10. The homogeneously nucleated precipitate no longer maintains a coherent interface with the matrix, but it retains the same crystallographic habit relationship reported above.

A comparison of the precipitate size and dispersion in material aged to completion at 420°C and 450°C is shown in Fig.5.11 and demonstrates the different growth rates which

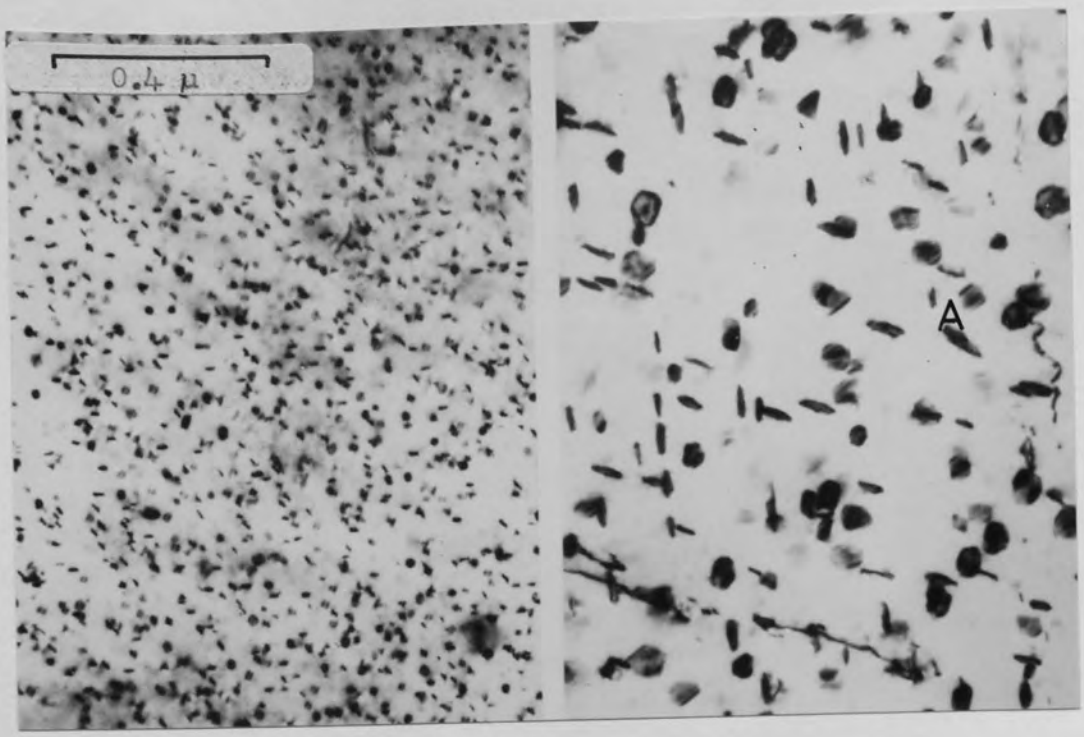

Fig.5.11 Comparison of precipitate size after ageing at (a) 420°C - 24 hours
(b) 450°C - 21 hours

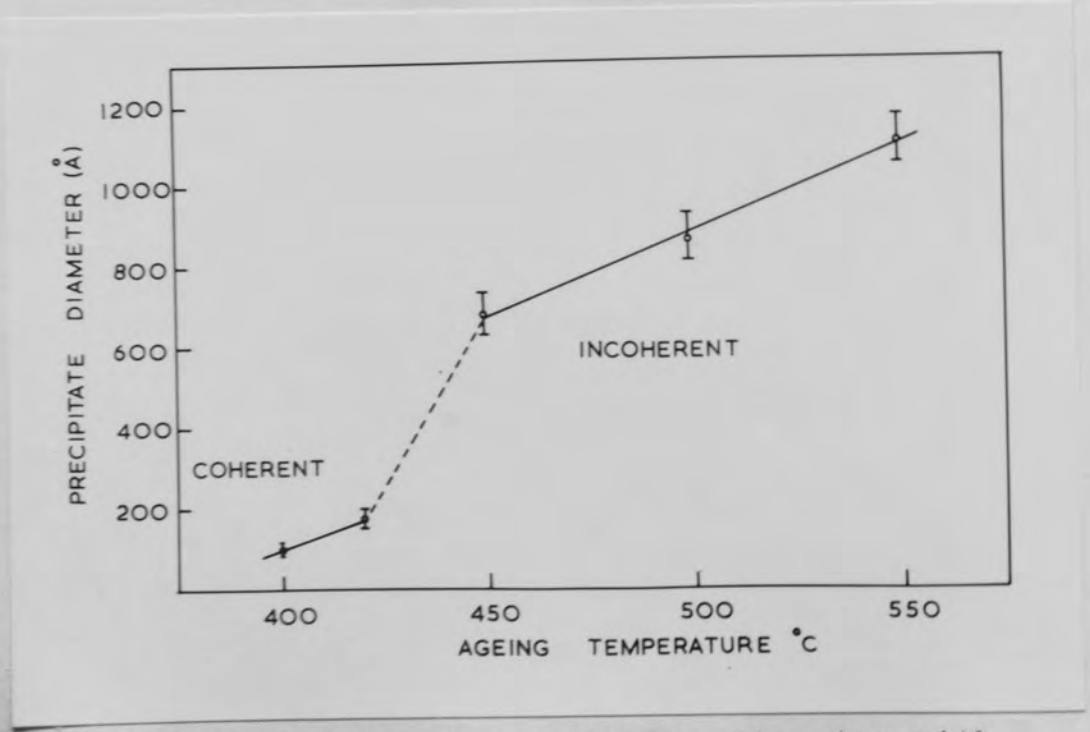

Fig.5.12 Variation of precipitate diameter with ageing temperature.

Fig.5.13 Aged at 500°C for 1 hour.

Fig.5.14 Aged at 550°C for 1 hour.

apply to coherent and non-coherent particles due to the strong influence of interfacial energy on the coarsening behaviour of precipitates.

The disc shaped precipitates lying on the inclined {111} planes in the material aged at 450°C, are large enough to produce displacement fringes in the precipitate as at (A), for the particular set of diffraction conditions operating. The sudden increase in precipitate size on ageing at 450°C and above is depicted graphically in Fig.5.12 and includes particle size measurements on the material aged at 450°, 500°and 550°C. At the higher ageing temperatures, the fraction of homogeneously nucleated precipitation decreases until at 550°C, only isolated patches of precipitation in this form are observed. Consequently, the fraction of hetrogeneously nucleated precipitation increases as ageing is continued above 450°C, and at 500°C, the competition for solute by stacking faults and undissociated dislocations accounts for the bulk of the precipitation. This change is illustrated by comparing the microstructures of the alloy aged to completion at 450°, 500° and 550°C as shown in Figs.5.10, 5.13, 5.14, respectively. In the alloy aged at 550°C, Fig.5.14, stacking fault contrast is quickly destroyed by the rapid growth of the precipitate as shown at (A), and the majority of precipitation occurs on undissociated dislocation ribbons as at (B).

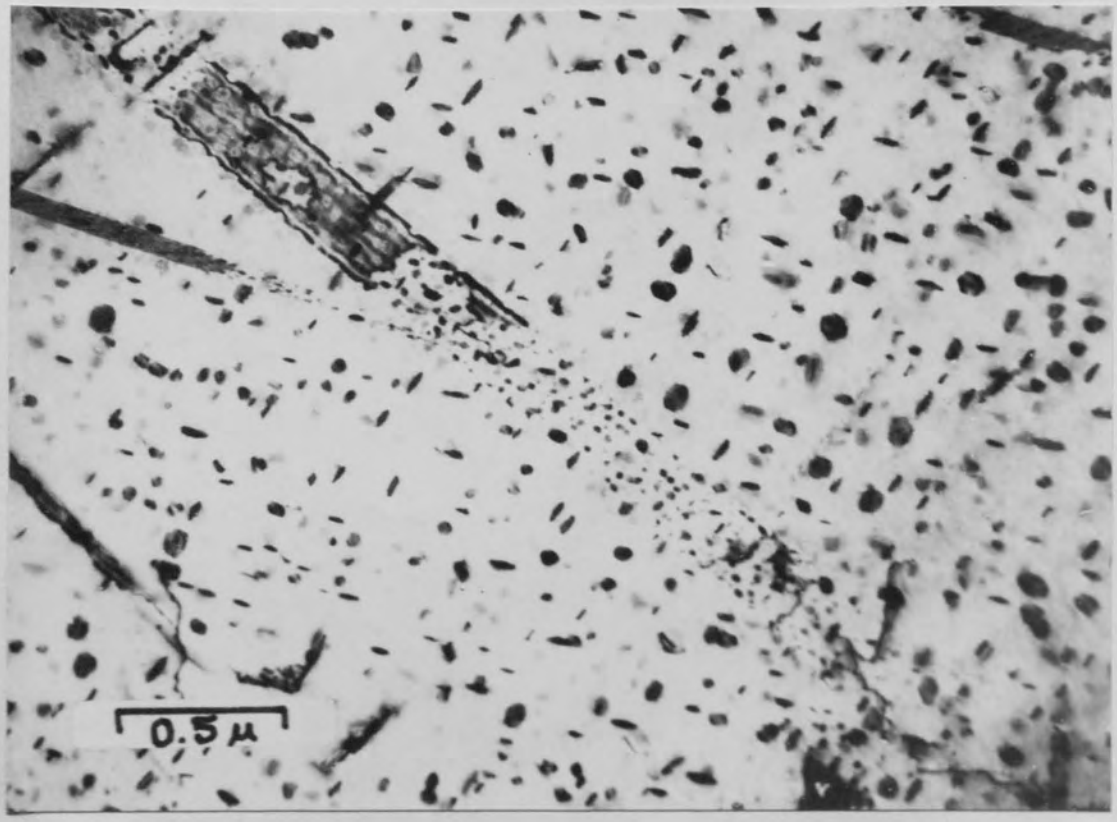

Fig.5.15 Illustrating the creation of islands of perfect crystal within stacking faults when the alloy is overaged.

The continued ageing of the material beyond the recovery of maximum conductivity also results in the removal of the stacking fault fringe contrast, and reveals the presence of the precipitate within the fault - a detailed analysis of which follows.

5.2.3 Stacking Faults formed in the alloy aged at 450°C

5.2.3.1 General Contrast of the Faults

In agreement with the detailed theory of stacking fault contrast[66], under all diffraction conditions, other than when ⟨220⟩ or ⟨113⟩ reflections are operating strongly, the faults are visible as a series of straight fringes which run parallel to the intersection of the fault plane with the foil surface.

The presence of precipitates within the fault causes rippling of the fault fringes as shown in Fig.5.10. Furthermore, the growth of favourably orientated precipitates within the fault create islands of perfect crystal as shown in Fig.5.15 thereby removing the fringe contrast. Fringe contrast is also removed at the intersections of the fault plane with the foil surface, and with other faults as in Fig.5.13. The possible mechanism for the creation and re-association of the partial dislocations necessary to remove the stacking fault is discussed in a later section.

5.2.3.2 Precipitation within the Faults

The removal of fringe contrast in the overaged material allows the identification of the precipitate

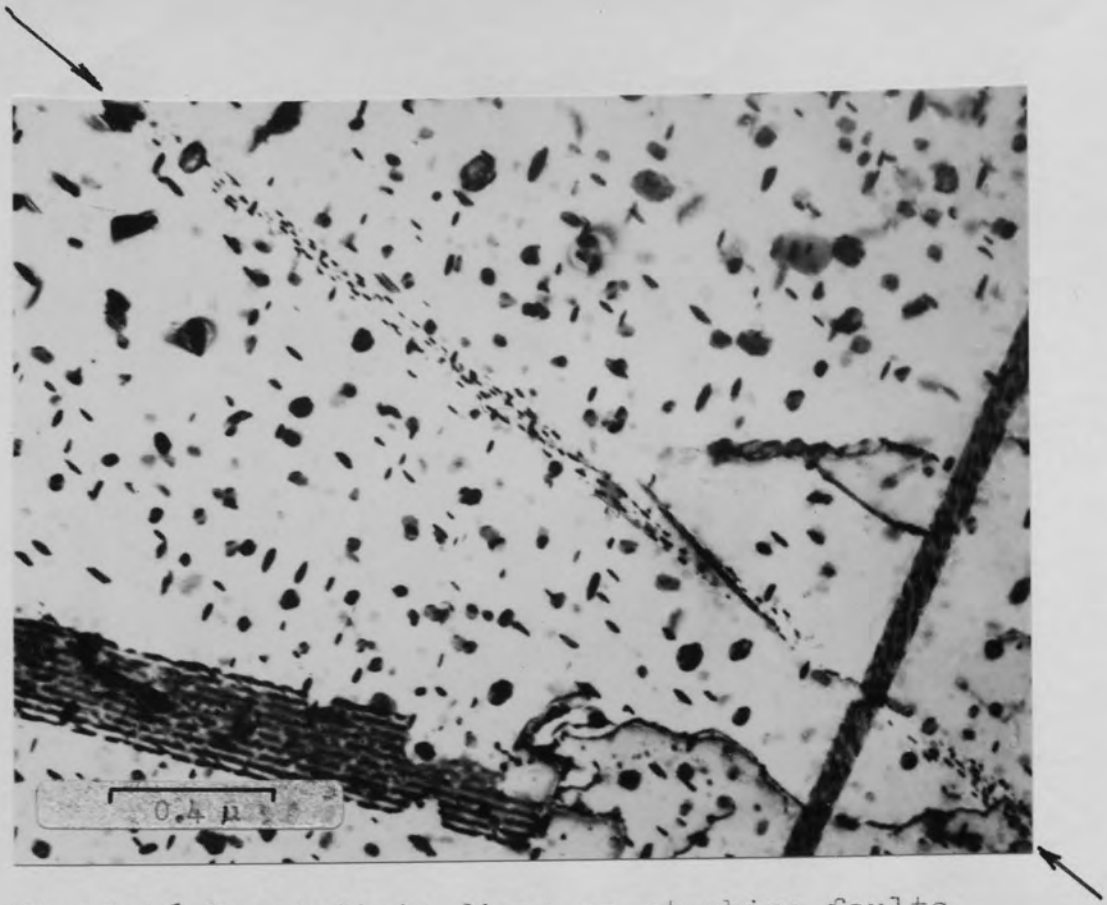

Fig.5.16 Precipitate discs on stacking faults formed on those {111} planes perpendicular to the foil surface. Aged at 450°C.

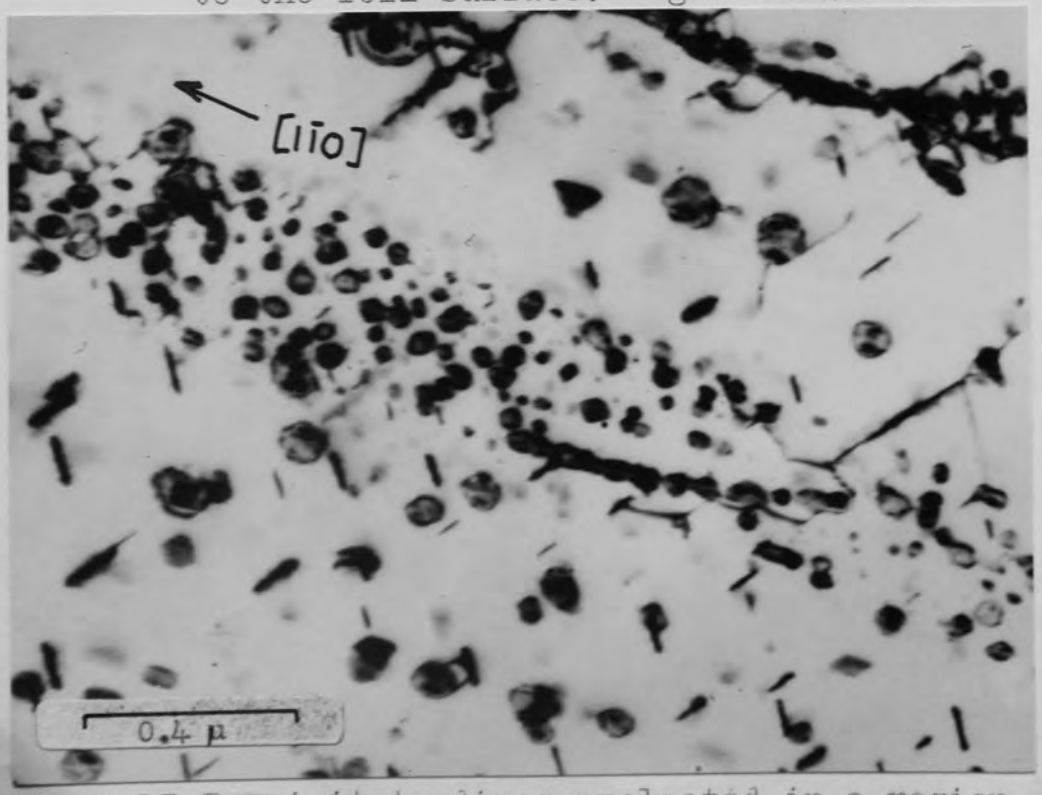

Fig.5.17 Precipitate discs nucleated in a region traversed by an expanding stacking fault aged at 550°C.

within the fault. Fig.5.16 is an enlargement of an area from Fig.5.10 and when viewed in conjunction with Fig.5.17 obtained from the alloy aged at 550°C, illustrates that the precipitate within the fault is identical to that precipitated homogeneously in the matrix, except in size.

5.2.3.3.Nature of the Faults

Using the method of Gevers[58] et.al. outlined in Section 3.6.3.3 it was possible to identify both extrinsic and intrinsic stacking faults in the aged alloys. From approximately 100 observations of fault type made at various stages of transformation in the range 450°- 500°C, the ratio of extrinsic to intrinsic faults was found to be 10 : 1. In general, the intrinsic faults were shorter than the extrinsic type for equivalent heat treatments, although observations of intrinsic faults of equal length to extrinsic faults have been made. The sample size of one hundred is not considered large enough to base any firm conclusion concerning the respective length of each type of fault observed. Figs.5.18, 5.19 and 5.20 represent a selection of faulted structures produced at the stated ageing temperatures and illustrates the analysis procedure adopted. Both types of fault were found to contain the Cu_3Zr precipitate discs.

5.2.3.4 Nature of the Partial Dislocations bounding the Faults

The identification of the partial dislocations bounding stacking faults found in the aged copper zirconium

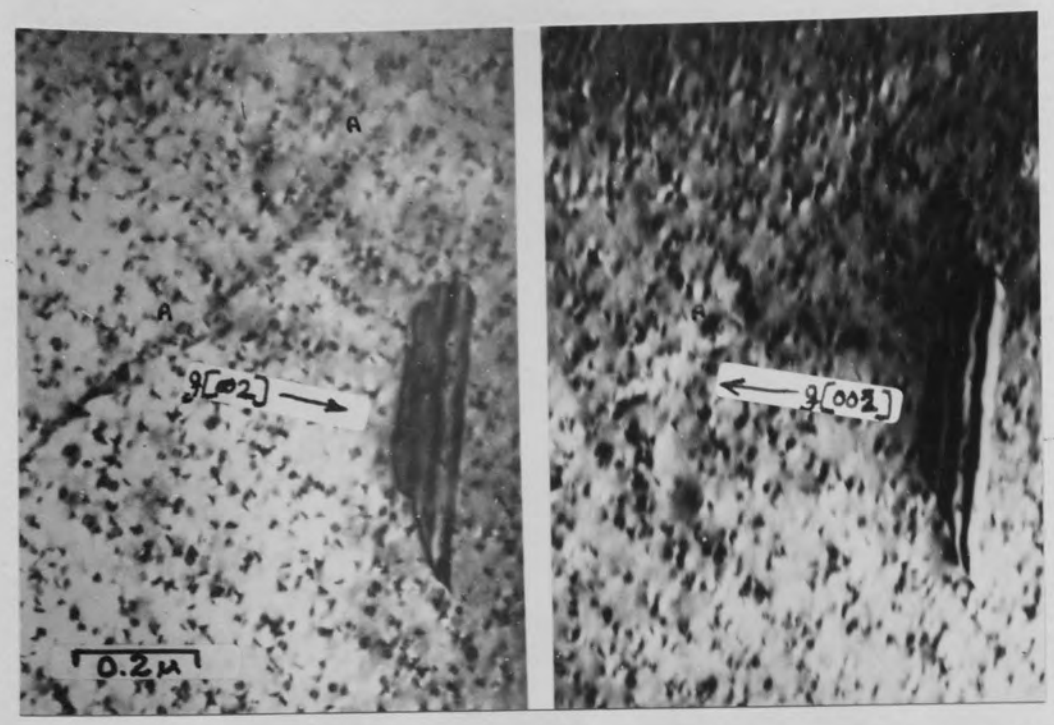

Fig.5.18 Extrinsic faults formed in the alloy aged at 420°C.

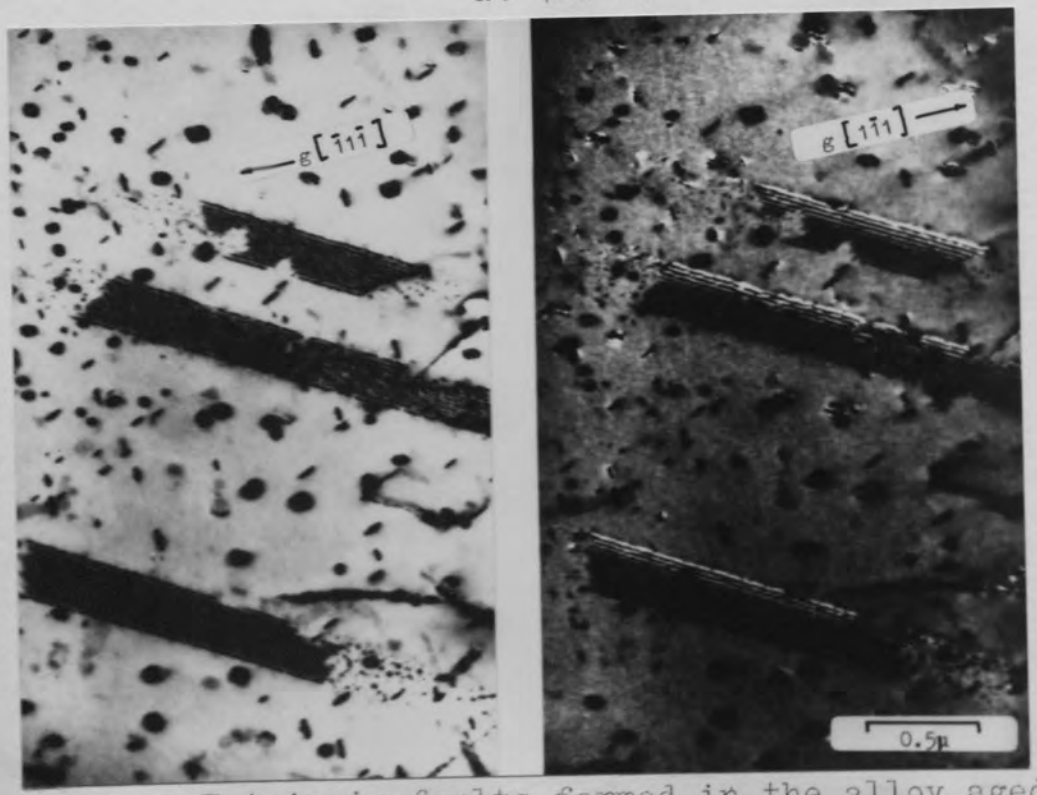

Fig.5.19 Extrinsic faults formed in the alloy aged at 500°C.

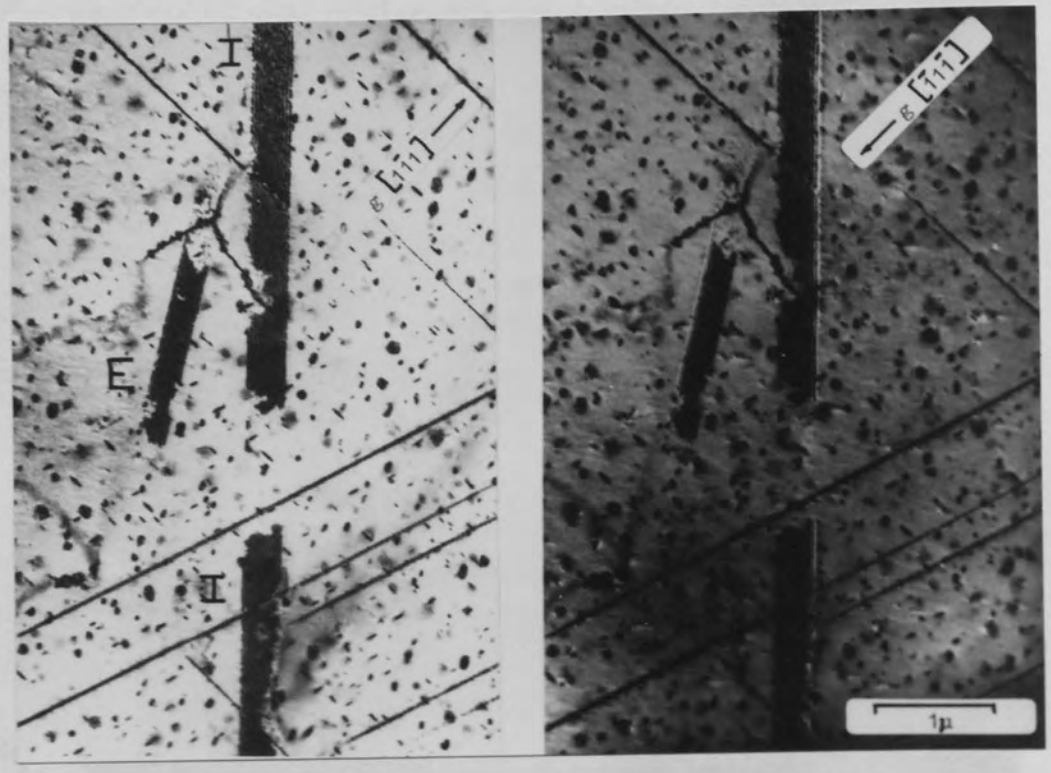

Fig.5.20 Faults formed in the alloy direct quenced to the ageing temperatures of 470°C.

E - Extrinsic Fault

I - Intrinsic Fault

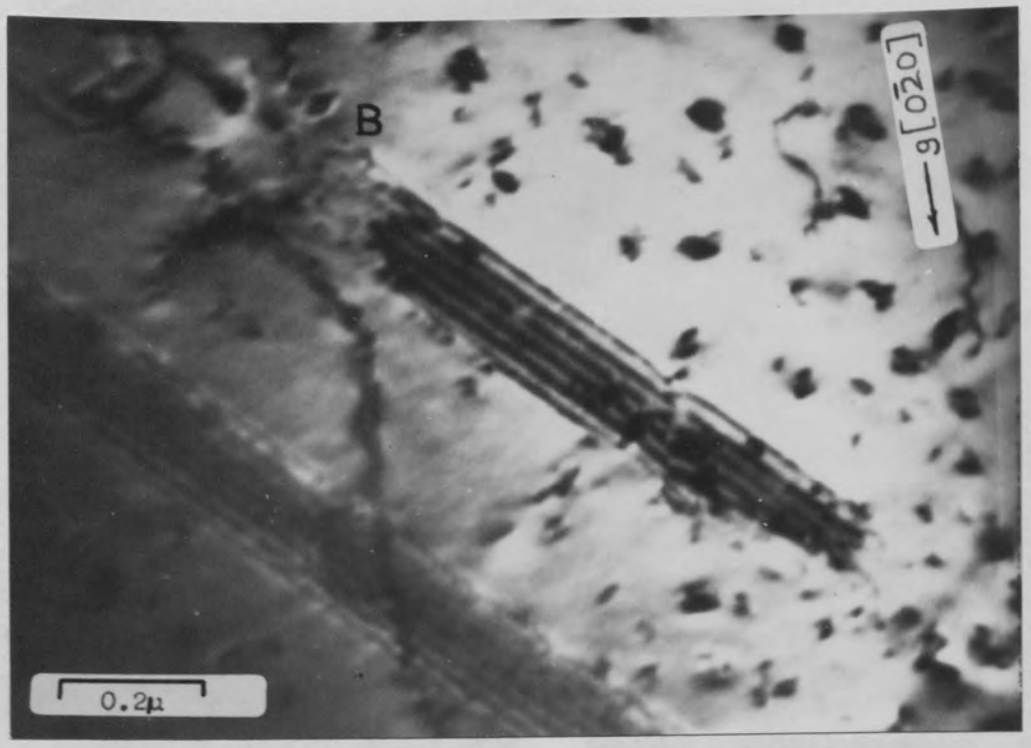

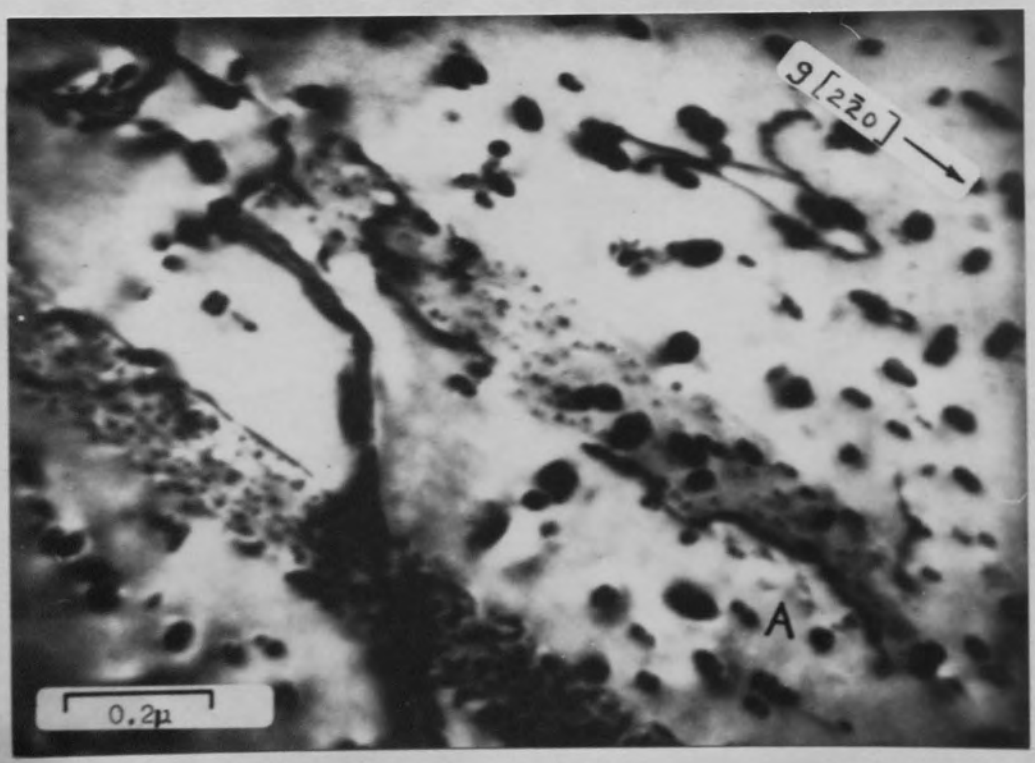

Fig.5.21 Faults formed in the alloy aged at 420°C.
Foil orientation near (001).

alloy involved extensive manipulation of the single tilt goniometer stage fitted to the microscope, in order to obtain the maximum number of different diffracting conditions necessary for the unique determination of the burgers vectors of the partials.

The modifications to Hirsh, Howie and Whelans[68] general invisibility criterion by Silcock and Tunstall[49] were recognized, and care taken to ensure that faults were analysed strictly under two-beam conditions, and, in the case of the $\langle 220 \rangle$ type reflection, in areas as close to the exact Bragg diffracting position in the foil as possible. The results obtained are unquestionably representative of the contrast produced by two Shockley partial dislocations bounding each end of the fault, and Fig.5.21 is a typical fault viewed with $g[2\bar{2}0]$ and then $g[0\bar{2}0]$ reflections operating strongly. The analysis of Fig.5.21 is as follows:-

The foil orientation is (001), and the top fault lies on either the (111) or ($\bar{1}\bar{1}$1) plane inclined to the foil surface at approximately 55°.

The partial discloations lying in the (111) plane are tabulated overleaf and the magnitudes of $g.b$ and $\frac{1}{8}\, g.b \wedge u$ listed for the reflections $g[0\bar{2}0]$ and $g[2\bar{2}0]$. The term $\frac{1}{8}\, g.b \wedge u$ assumes significance for dislocations having large edge components.

Reflection	b	g.b	$\frac{1}{8}$ g.b$\wedge$u
$[0\bar{2}0]$	$\frac{1}{3}$ $[111]$	$-\frac{2}{3}$	$0 \rightarrow \pm 0.118$
	$\frac{1}{6}$ $[\bar{2}11]$	$-\frac{1}{3}$	$0 \rightarrow \pm 0.059$
	$\frac{1}{6}$ $[1\bar{2}1]$	$\frac{2}{3}$	$0 \rightarrow \pm 0.059$
	$\frac{1}{6}$ $[11\bar{2}]$	$-\frac{1}{3}$	$0 \rightarrow \pm 0.059$
$[2\bar{2}0]$	$\frac{1}{3}$ $[111]$	0	$0 \rightarrow 0.2042$
	$\frac{1}{6}$ $[\bar{2}11]$	-1	0
	$\frac{1}{6}$ $[1\bar{2}1]$	1	0
	$\frac{1}{6}$ $[11\bar{2}]$	0	0

For the top fault in either reflection, the left hand partial is visible and the right hand partial invisible and therefore the left hand partial is $\frac{1}{6}[1\bar{2}1]$, and the right hand partial is $\frac{1}{6}[11\bar{2}]$.

The partial dislocation removing the fault contrast from the fault intersection with the foil surface at A is also a Shockley of Burgers vector $\frac{1}{6}[1\bar{2}1]$.

The fault frings disappear in $g[2\bar{2}0]$ as predicted by theory since g.R = 0, and reveal the precipitate within the fault. The dislocation at B in the $g[0\bar{2}0]$ micrograph was originally the leading partial of the expanding fault, but has been converted to a unit dislocation of Burgers vector $\frac{1}{2}a[101]$ by the recombination of two partial dislocations. The dissocation producing the fault on the (111) plane may therefore be written:-

$$\frac{1}{2}a[0\bar{1}1] \longrightarrow \frac{1}{6}a[1\bar{2}1] + \frac{1}{6}a[\bar{1}\bar{1}2]$$

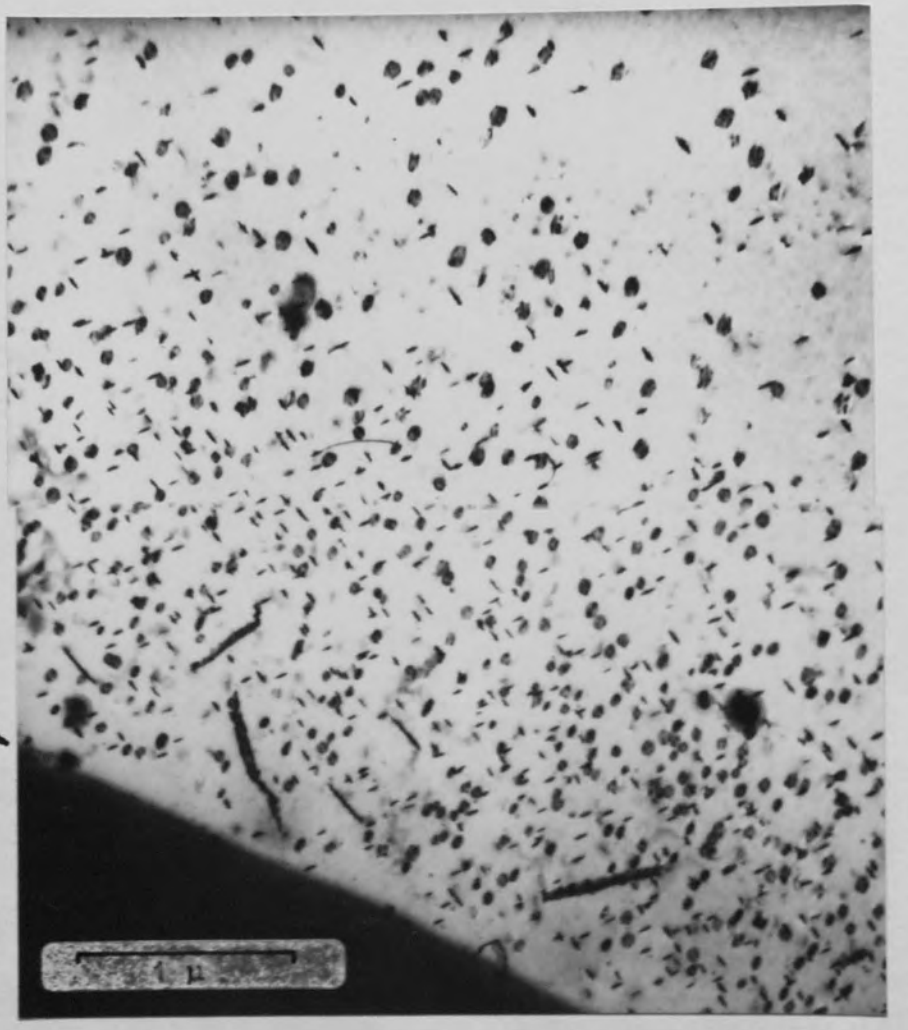

Fig.5.22 Precipitate enhanced region adjacent to grain boundaries in the alloy aged to 40% transformation at 500°C.

and represents the dissociation of a glissile dislocation into two Shockley partial dislocations in the (111) plane of the copper matrix.

5.2.3.5 Stacking Fault Density

The maximum number of stacking faults occurred in the structure when aged between 450°and 475°C. From micrographs similar to that shown in Fig.5.10, the number of faults has been estimated to be approximately $2 \times 10^{12}/cms^3$. The maximum diameter to which the faults grow is 3 to 5μ when aged at 500°C.

5.2.4 Precipitation near Grain Boundaries

Another microstructural feature of the alloy which becomes evident when aged above 450°C, is the presence of an enhanced region of precipitation adjacent to grain boundaries. The band of precipitate varies from 3 to 5μ in width and is illustrated in Fig.5.22 for the alloy aged to 40% transformation at 500°C. The precipitate band is evident during the very early stages of transformation indicating that the nuclei are stabilized during the quenching operation. If the number of active nucleation sites for precipitaton is taken as the number of precipitates present per unit volume, then the ratio of sites in the band adjacent to the grain boundary to those in the centre of the grain is 5:1. The precipitate size is correspondingly smaller in these regions, and for the alloy aged at 500°C,

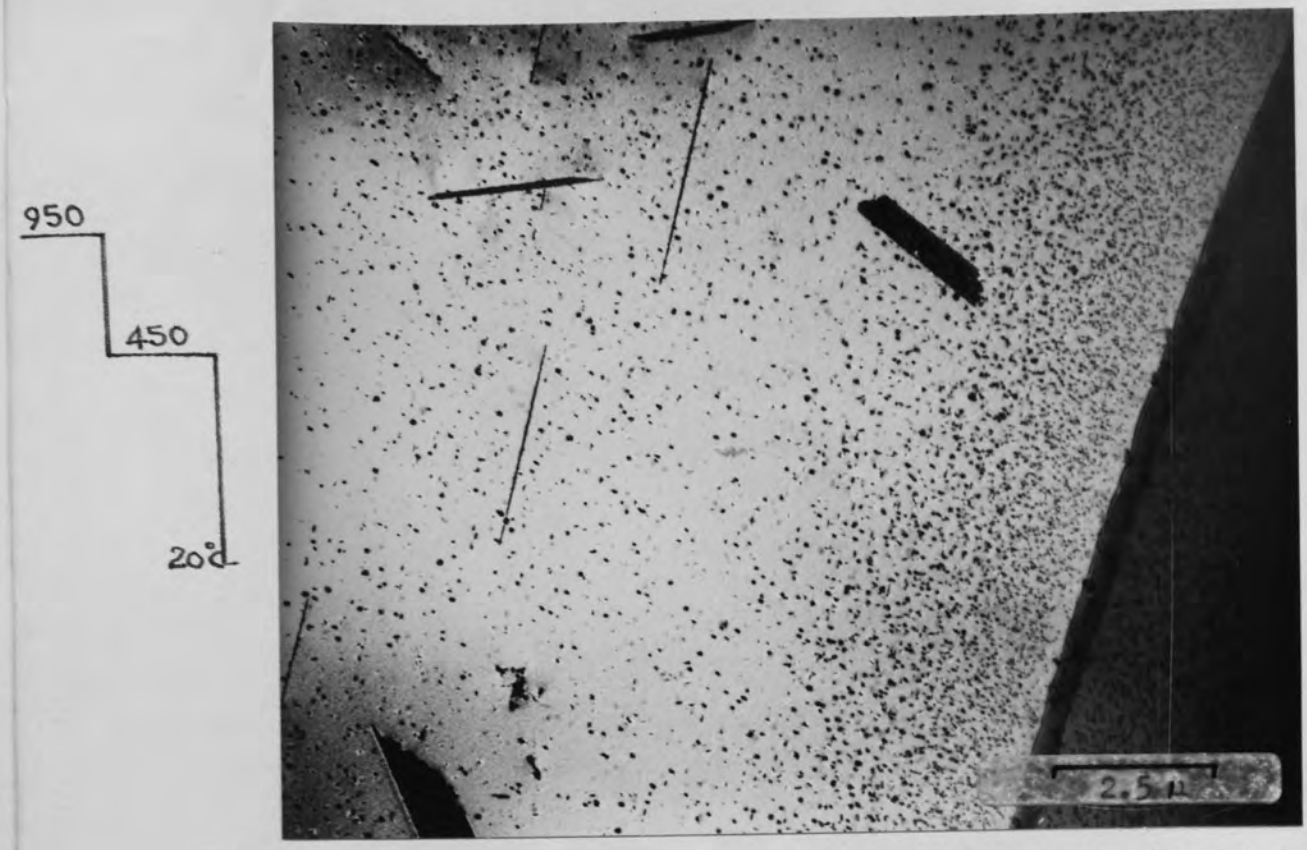

Fig.5.23 Stacking fault behaviour near grain boundary regions of precipitate enhancement.

Fig.5.24 Early stages of formation of precipitate enhanced zone.

the precipitate within the bands is 450 - 500Å diameter whilst that in the centre of the grain is 900 - 1000Å diameter. It is noticable that stacking faults stop abruptly on reaching these regions of enchanced precipitation Fig.5.23, but that undissociated dislocations, where present, form nucleating centres for the precipitate within the bands, Fig.5.24.

This behaviour is difficult to reconcile with current theories of precipitation near grain boundaries since it has been shown that the vacancy concentration profile existing near grain boundaries on quenching solution treated materials takes the form given in Fig.5.25 for several aluminium alloys.[38] The interpretation of the profile suggests that precipitate free zones should be observed near grain boundaries if precipitate nucleation requires the presence of a critical vacancy concentration in order to proceed. If it is assumed that the zirconium content is evenly distributed throughout the alloy, then the accepted model for the vacancy profile at grain

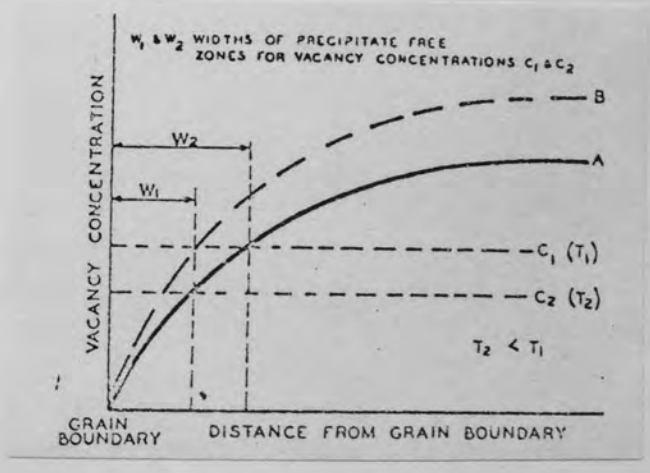

Fig.5.25 Schematic representation of vancany concentration profiles adjacent to a grain boundary. (after Embury & Nicholson)

Fig.5.26 Dark field image taken with weak precipitate diffraction spot of material aged at 450°C.

boundaries formed on quenching cannot be used in order to explain the precipitate enhancement observed in copper zirconium. However, the presence of this precipitate enhanced zone in the alloy direct quenched to the ageing temperature Fig.5.23 suggests that the grain boundary cannot be acting as a vacancy source, and therefore a satisfactory explanation of this phenomenon must invoke a consideration of not only vacancy profiles, but also the possible solute profiles likely to arise during the heat treatment of this material.

5.3 Identification of Precipitate

5.3.1 Selected Area Electron Diffraction

The bulk fraction of the precipitate present in the aged alloy was too small to give rise to very strong diffraction spots, and consequently the crystallographic data concerning the precipitate is limited to a few interplanar spacings of dubious value. Wherever possible, the weak diffraction spots arising from the precipitate were used to form dark field images and Fig.5.26 obtained using such reflections, shows that the matrix precipitate is the same as that found in the stacking faults in a material aged at 450°C.

Extraction replicas of the aged material did not produce any further information regarding the precipitate crystal structure, and therefore it was decided to manufacture

a series of high zirconium containing alloys to investigate the first intermetallic compound Cu_3Zr occurring in the system Cu-Zr, by X-ray methods.

5.3.2 X-ray analysis of Cu_3Zr

The Debye-Schirrer film strip obtained from a powdered sample of the alloy shown in Fig.3.10 could not be analysed uniquely in the time available. The complex pattern could not be fitted to the two simple structures, cubic and hexagonal using the methods suggested by Cullity[60]. Examination of the list of 'd' spacings obtained from the film using Hull-Davey charts for tetragonal lattices also failed to identify the crystal structure of the compound.

Subsequent work on this compound by Edwards[69] in this laboratory has suggested that the data may be fitted to an orthorhombic structure and the main conclusions of his work are summarized together with the film strip obtained from the sample shown in Fig.3.10, in Appendix II.

5.4 Mechanical Property Measurements

Unlike copper chromium, the U.T.S. of the aged material does not suggest any response to ageing Fig.5.27. However, the 0.1% proof stress measurements indicate that there is a substantial increase in strength on ageing the solution treated material, and that peak values of 8.5tons/sq.ins. are reached at temperatures below 450°C, corresponding

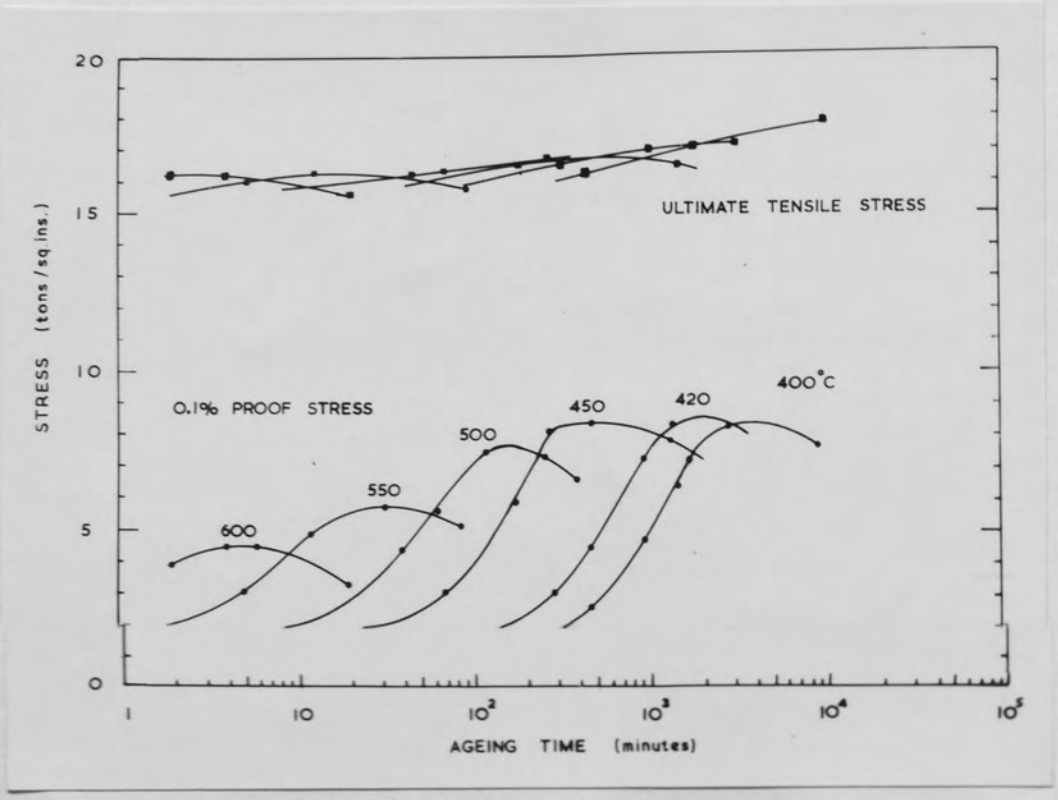

Fig.5.27 Mechanical test results from isothermally aged materials.

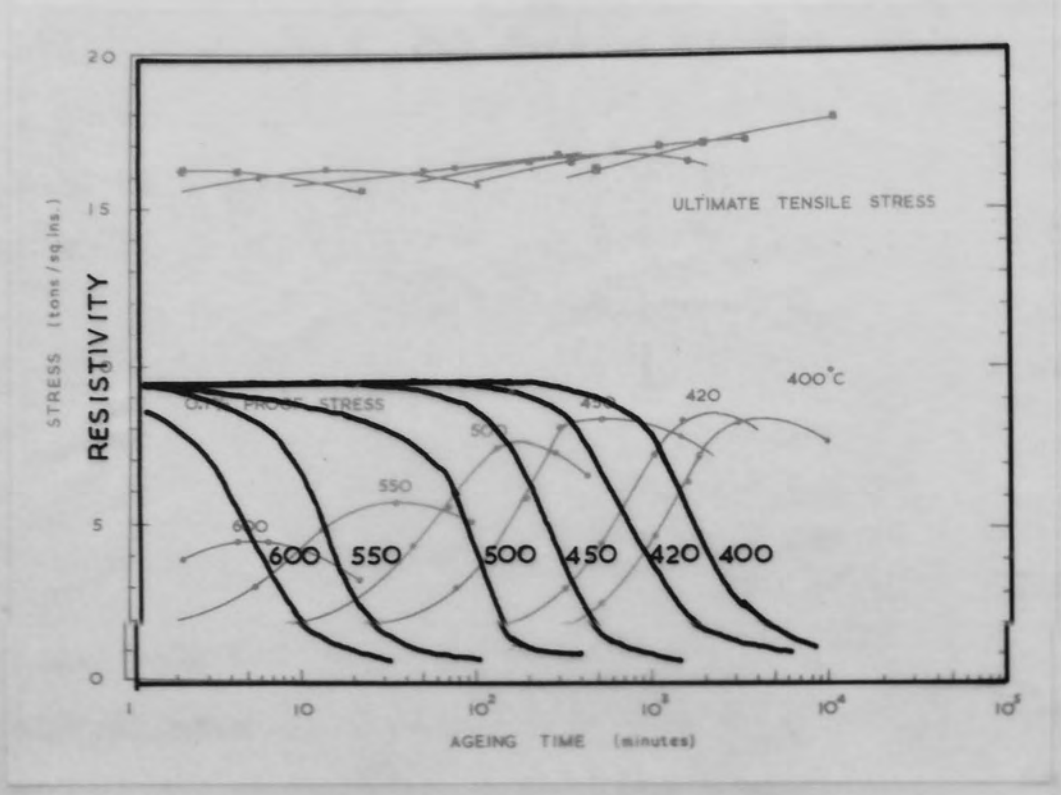

Fig.5.27 Mechanical test results from isothermally aged materials.

to approximately 3 x 10^{-3}G. The poorer mechanical strength of this alloy with respect to copper chromium is related to the precipitate morphology since it has been shown by Nabarro[32] that disc shaped precipitates produce the least strain in a metallic system. The near constant values of U.T.S. for this material indicate that precipitate discs on the {111} planes of the copper matrix do not give rise to a high work hardening rate during tensile deformation. The resistivity data shown in Fig.5.2 is re-produced to illustrate that the attainment of peak strength is coincident with that of maximum conductivity in the aged alloy.

5.5 Concluding Summary

The kinetic analysis of the aged material has been used to detect the growth of stacking faults in the alloy on ageing at temperatures in excess of 450°C. The Avrami analysis is in keeping with metallographic observations below 450°C, in that disc shaped precipitates are nucleated homogeneouslywithin the matrix, but when stacking faults grow and begin to provide an important nucleating source in the aged alloy, the analysis can not be interpreted on the basis of established models of transformation.

The onset of stacking fault growth in the alloy corresponds closely to the temperature at which the precipitate, thought to be Cu_3Zr, becomes incoherent, and

consequently, the interfacial energy term in the classical theories of homogeneous nucleation rises steeply with the result that the nucleation of Cu_3Zr requires either the formation of larger clusters of zirconium atoms in the copper matrix or alternatively, hetrogeneous nucleation sources in order to proceed at a rate consistent with the kinetic data. A mobile hetrogeneous nucleation source is provided in the form of expanding partial dislocations of the type $\frac{1}{6}a\langle 112\rangle$, thereby generating long stacking fault ribbons during ageing of which the extrinsic is preferred to the intrinsic type. The failure of the faults to grow into regions adjacent to grain boundaries is explained by the presence of a refined band of homogeneously nucleated precipitate parallel to the boundaries.

The poor mechanical properties obtained from the aged alloy are due to the morphology and to the rapid coarsening of the precipitate which occurs on ageing above $450^{o}C$.

CHAPTER 6.

THE ALLOY COPPER-0.3% CHROMIUM-0.07% ZIRCONIUM

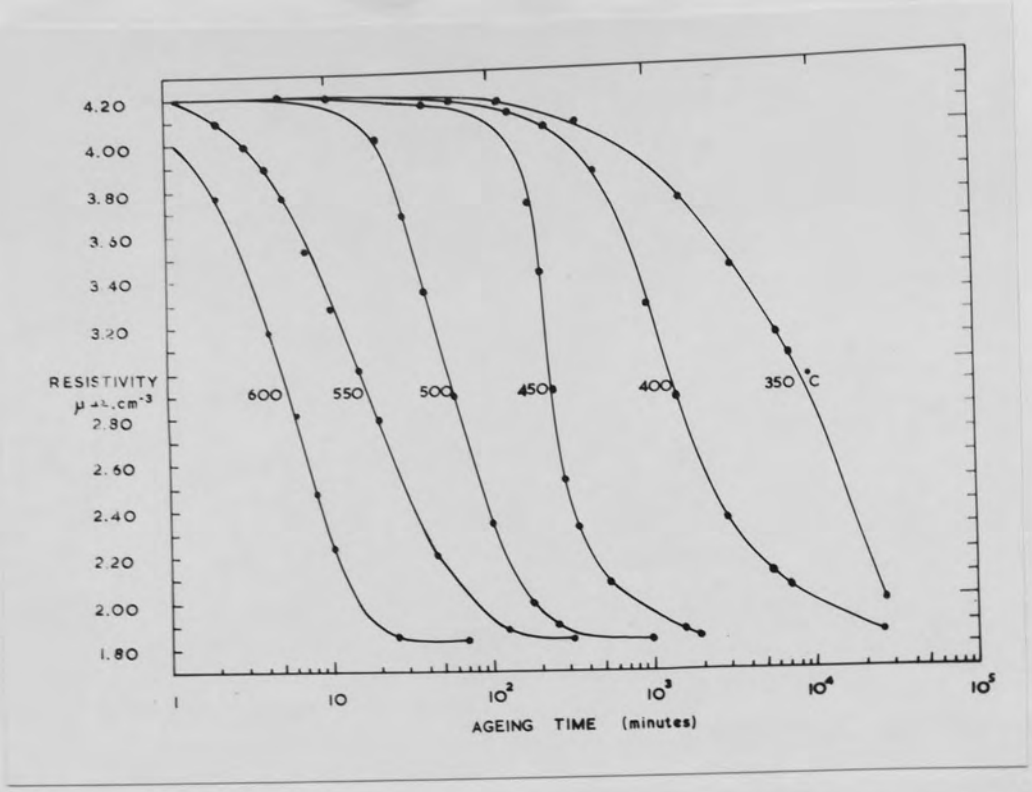

Fig.6.1 Sigmoidal decay curves obtained from isothermal ageing experiments. Alloy solution treated at 950°C.

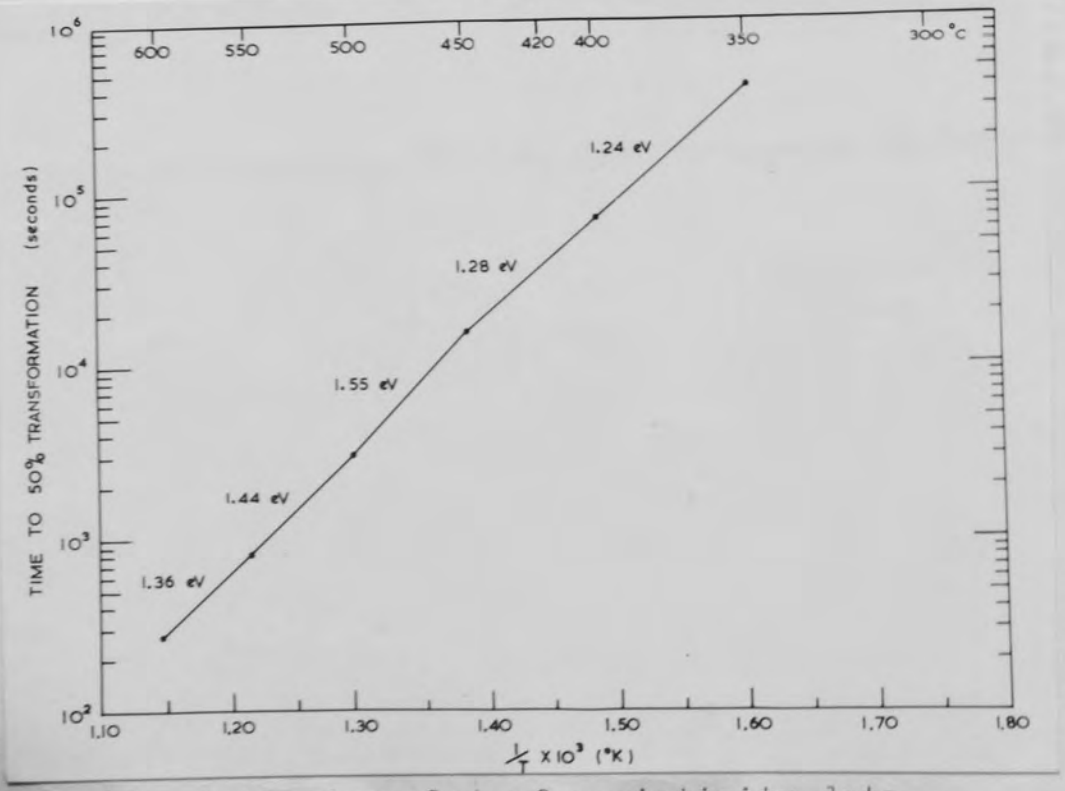

Fig.6.2 Arrhenius plot of resistivity data.

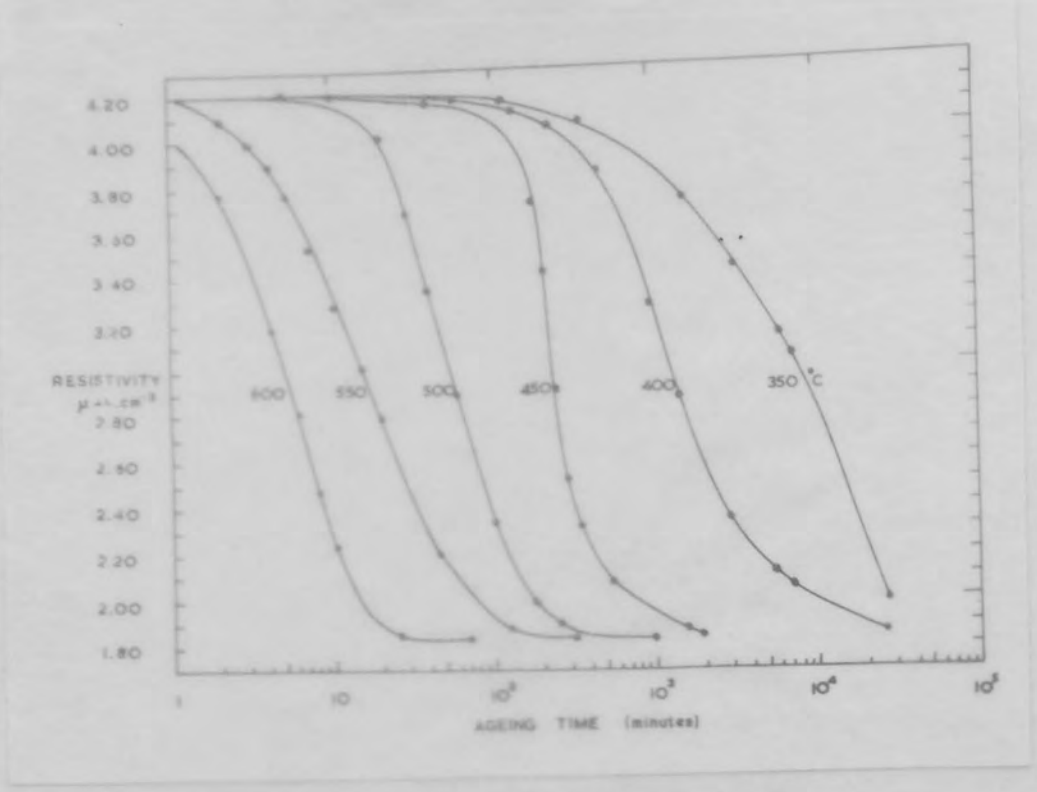

Fig.6.1 Sigmoidal decay curves obtained from isothermal ageing experiments. Alloy solution treated at 950°C.

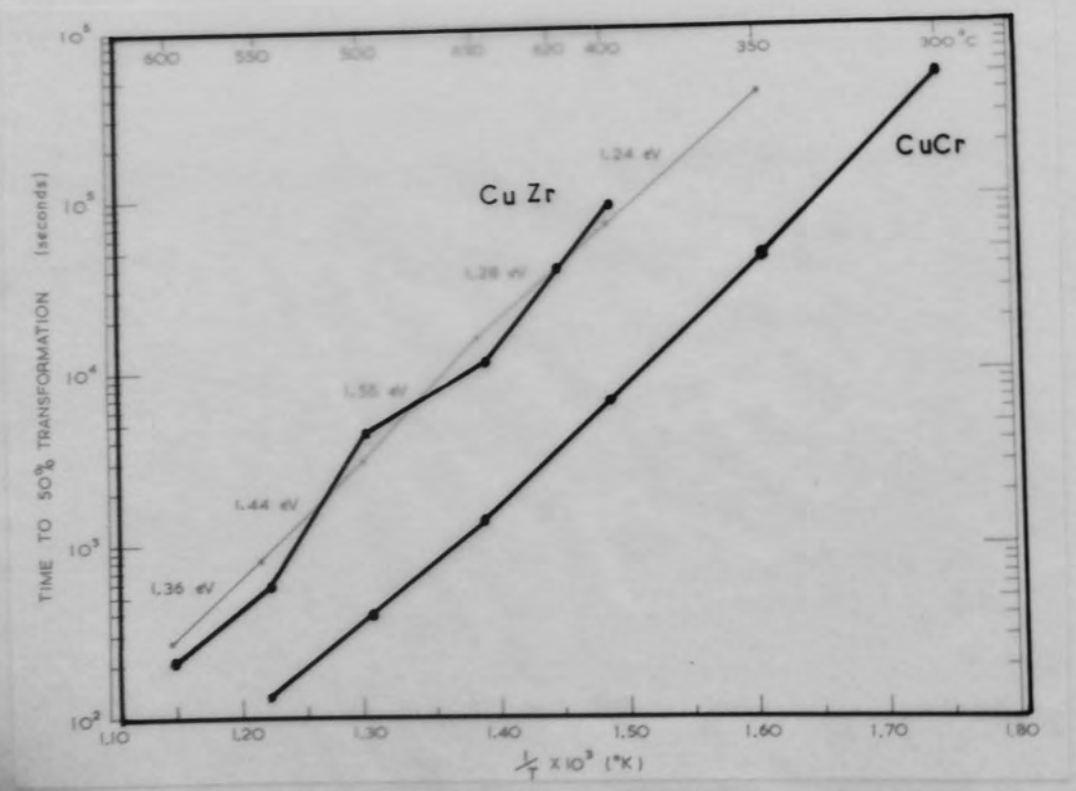

Fig.6.2 Arrhenius plot of resistivity data.

6.1 Electrical Resistivity

6.1.1 Solubility

The resistivity of the material solution treated at 950°C was 4.20 $\mu\Omega cms^{-3}$ and the minimum value attained after ageing 1.83 $\mu\Omega cms^{-3}$ (equivalent to 94.5% I.A.C.S.). These figures cannot be interpreted in terms of the solubility of each alloying element since the effects may not be additive.

6.1.2 Isothermal Ageing Data

The precipitation reactions in this alloy, over the range 350°-600°C, yielded the sigmoidal decay curves plotted in Fig.6.1. From these results, the empirical activation energy obtained for the transformation is shown in Fig.6.2, in conjunction with the results of the two binary alloys discussed earlier.

The trace addition of zirconium to copper chromium retards the rate of transformation by a factor of ten for the same ageing temperatures, but once under way, the transformation proceeds with an almost identical value of activation energy Q_e. The value of Q_e shows no temperature sensitivity over the range 350°- 600°C, but does exhibit a sensitivity to the volume fraction transformed which is best illustrated in the Avrami plot Fig.6.3. From the Avrami type analysis, the reaction cannot be described as

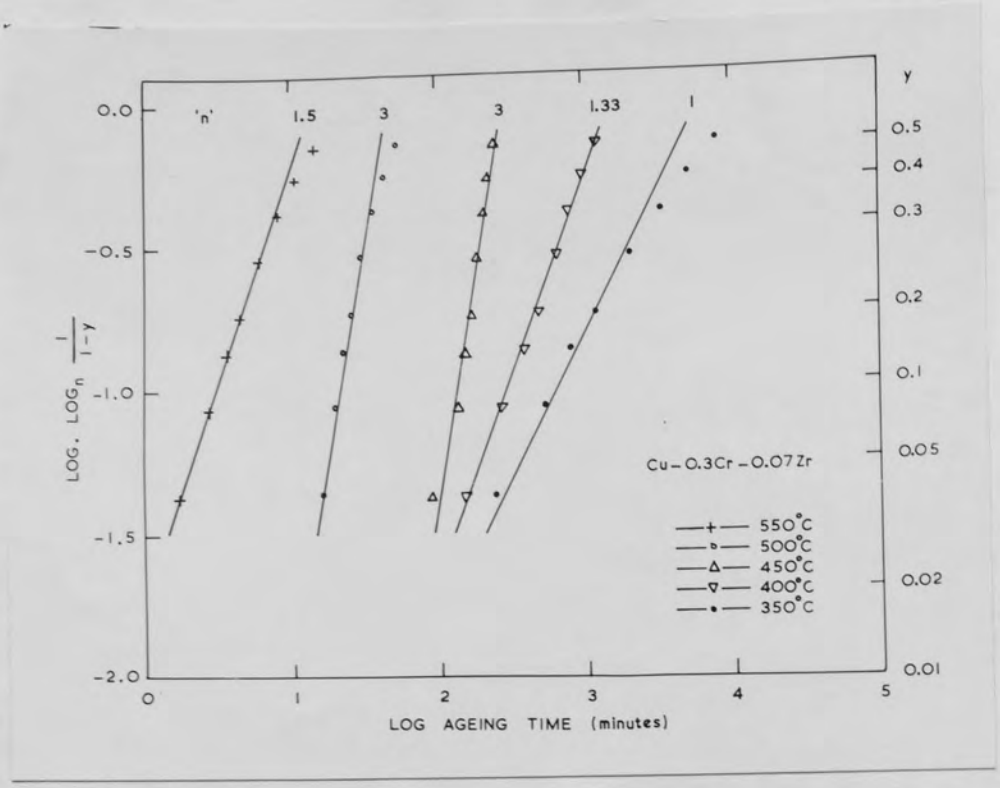

Fig.6.3 Avrami plot of resistivity data.

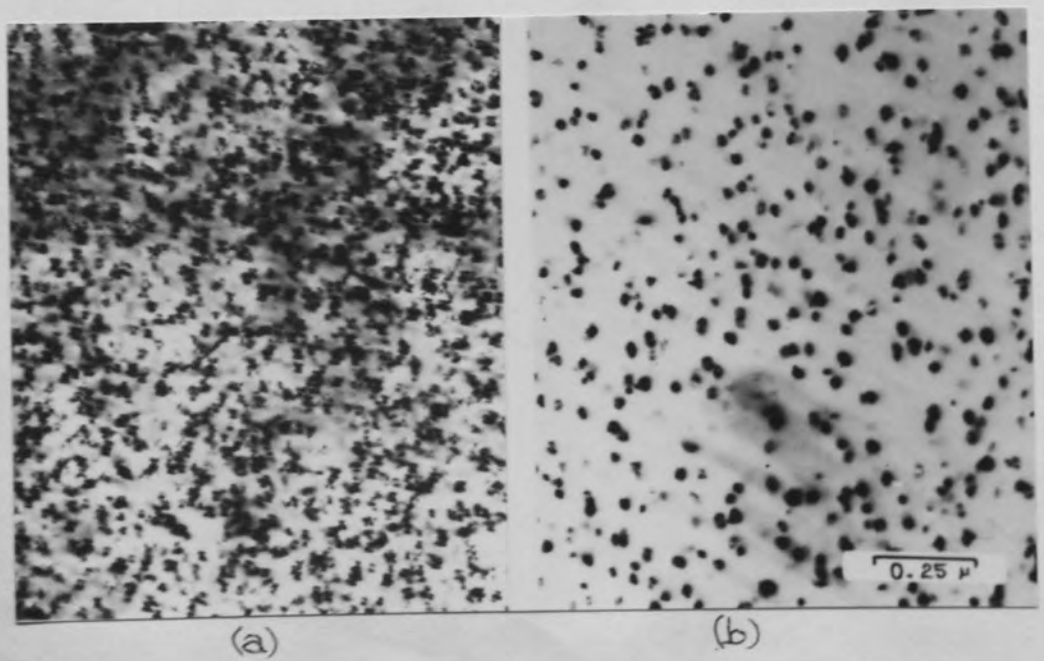

Fig.6.4 (a) Cu-Cr aged at 500°C
(b) Cu-0.3%Cr-0.07%Zr aged at 500°C.

isokinetic, nor can a simple transformation model be applied to explain the variety of values obtained for the time exponent 'n'. The value of unity at 350°C is equivalent to that found for the low temperature transformation in copper chromium. The larger values of 'n' found at the intermediate ageing temperatures 450°- 500°C suggest that growth of the precipitate is limited by some form of interface control. However, the main interpretation placed on the values of 'n' must be to show that no single process is dominating the transformation, unlike the binary copper chromium.

6.2 Metallography

Both the optical and electron microstructure of the solution treated alloy were identical to the structures illustrated in section 4.2.2.1 for copper chromium, and thus the only features to be described in detail are those of the aged material.

6.2.1 Electron Metallography of the Aged Material

Using the kinetic data collected from isothermal ageing experiments, the alloy was aged to completion at temperatures of 400°, 500°, 550°and 600°C and the resultant microstructure compared with those obtained at similar ageing temperatures for copper chromium. The structures were found to be indistinguishable except in terms of the degree of dispersion of the precipitate, and the composite micrograph shown in Fig.6.4 affords a comparison of the

structure of the ternary alloy aged at 500°C to completion with that of copper chromium aged at the same temperature. The precipitate gave rise to its own diffraction pattern when the alloy was overaged, and was identified as body centred cubic chromium. The analysis of diffraction patterns obtained from this alloy gave identical results to those already described for copper chromium.

In an effort to elucidate the mechanism by which this trace addition of 0.07% zirconium to Copper chromium, slowed down the precipitation kinetics at a given ageing temperature, without noticably affecting the precipitate type and morphology a series of direct quenching experiments were performed.

6.2.2 Direct Quenching Experiments

The purpose of direct quenching to the ageing temperature in allowing an assessment of the role of excess vacancies on precipitation reactions has already been outlined in section 4.6.1.

Direct quenching copper chromium to the ageing temperature has been shown to reduce the number of effective nucleii formed on subsequent ageing, see Fig.4.27, and the effect is attributed to the rapid loss of vacancies to sinks during the quenching treatment. Consequently, the microstructures of the ternary alloy were compared with those of copper chromium for similar direct quenching cycles and typical results are given in Fig.6.5. The two

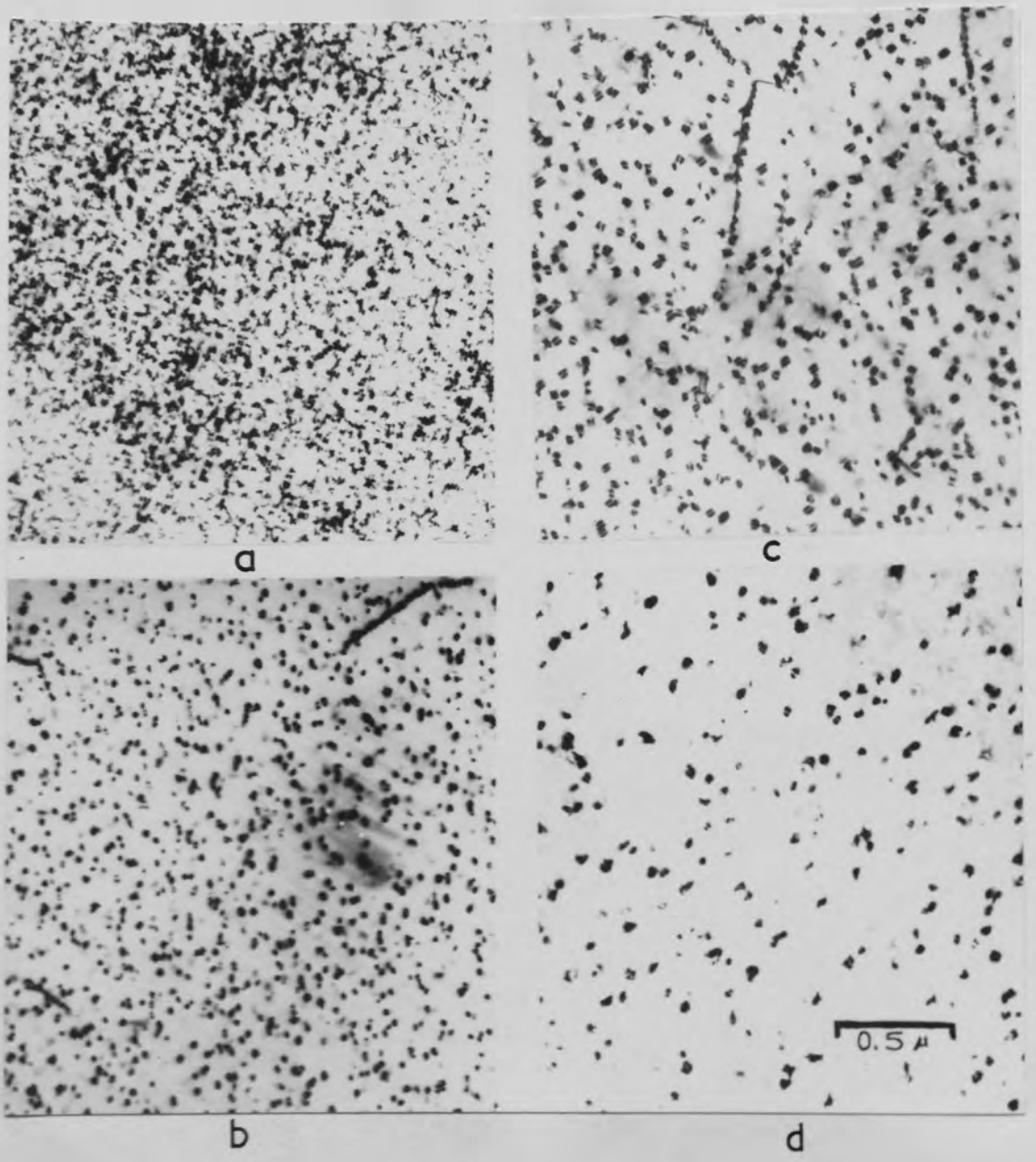

Fig.6.5 (a) Cu-Cr aged at 500°C.
(b) Cu-0.3Cr-0.07Zr aged at 500°C.
(c) Cu-Cr direct quenched to 500°C.
(d) Cu-0.3Cr-0.07Zr direct quenched to 500°C.

materials direct quenched to 500°C are compared with the same materials which have been water quenched to 20°C and then aged at 500°C. The numbers of active nucleii have been estimated from such micrographs by counting the number of particles present (inferred from the strain field images) per unit volume and are tabulated below for materials solution treated at 950°C.

MATERIAL	HEAT TREATMENT CYCLE	NUMBER OF NUCLEII
Cu - 0.4% Cr	Quenched to 20°C from 950°C and aged at 500°C for 2 hours	$2 \times 10^{11}.cms^{-3}$
	Direct quenched to 500°C from 950°C and held 2 hours	$8 \times 10^{10}.cms^{-3}$
Cu - 0.3% Cr 0.07% Zr	Quenched to 20°C from 950°C and aged at 500°C for 2 hours	$9 \times 10^{10}.cms^{-3}$
	Direct quenched to 500°C from 950°C and held for 2 hours	$4 \times 10^{10}.cms^{-3}$

TABLE VI

From Table VI it will be noted that the dispersion of chromium precipitates in direct quenched Cu-Cr is very close to that obtained for the conventionally aged ternary alloy.

The possible interpretation of these results

without accurately known diffusion data of zirconium and chromium in copper is necessarily specultative, but the evidence does suggest two mechanisms by which the trace addition of 0.07% zirconium may modify the precipitation of chromium from copper, these being:-

(a) By interacting with the excess vacancies formed during the quench, thereby reducing the diffusivity of the copper matrix, and hence the rate at which embryos attain the critical size for nucleation.

or (b) By modifying the interfacial energy between the chromium precipitate and the matrix.

The resistivity data when plotted to give values for the empirical activation energy for the ageing processes in the alloy, Fig.6.2, supports (a) since the ageing reaction proceeds with a similar value of Q_e to that observed in copper chromium, whilst the Avrami analysis, Fig.6.3, shows by virtue of the variety of values for the time exponent 'n' of the process that diffusion and interface processes are controlling the rate of growth of the precipitate, and is evidence in support of (b). The microstructure of the ternary alloy aged at 500°C and shown in Fig.6.5 is expected to correspond to the condition when the interface control is most marked since a time expondent of n = 3 is obtained during ageing at 500°C.

A lack of data concerning the binding energies between zirconium atoms and vacancies does not allow a quantitative analysis to be applied to the mechanism postulated in (a), where the zirconium atom is thought to capture the excess vacancies created during the quench. However, the large atomic radii of zirconium with respect to copper and chromium (25% misfit) is thought to be a significant guide to the value of binding energy between vacancy and zirconium atom. The concentration of vacancies expected in the solution treated alloy at 950°C is given by:-

$$C_{950^\circ C} = A \exp\left(-\frac{E_f}{kT}\right)$$

where A is an entropy term, not accurately known, but usually given a value between one and ten. E_f is the energy required for the formation of a vacancy in the matrix, and k is Boltzmanns constant.

For copper, E_f approx. 1eV

$k = 8.6 \times 10^{-5}$ eV.deg.$^{-1}$

Therefore,

$$C_{950^\circ C} = A \exp\left(-\frac{1}{8.6 \times 10^{-5} \times 1223}\right)$$

$$= A \exp(-9.5)$$

Assuming A = 1, then:-

$C_{950^\circ C} = 8 \times 10^{-5}$ or if A = 10, the vacancy concentration = 8×10^{-4}. Therefore, the zirconium in the ternary alloy, at 0.07wt.% ≡ 0.065 atomic % or 6.5×10^{-4} is present in sufficient quantity to trap the excess vacancies produced on quenching to room temperature on a one to one atom : vacancy.ratio.

$$\frac{L_{max}}{\bar{L}} = 2.10 \qquad 1.65 \qquad 1.88 \qquad 1.66 \qquad 1.54$$

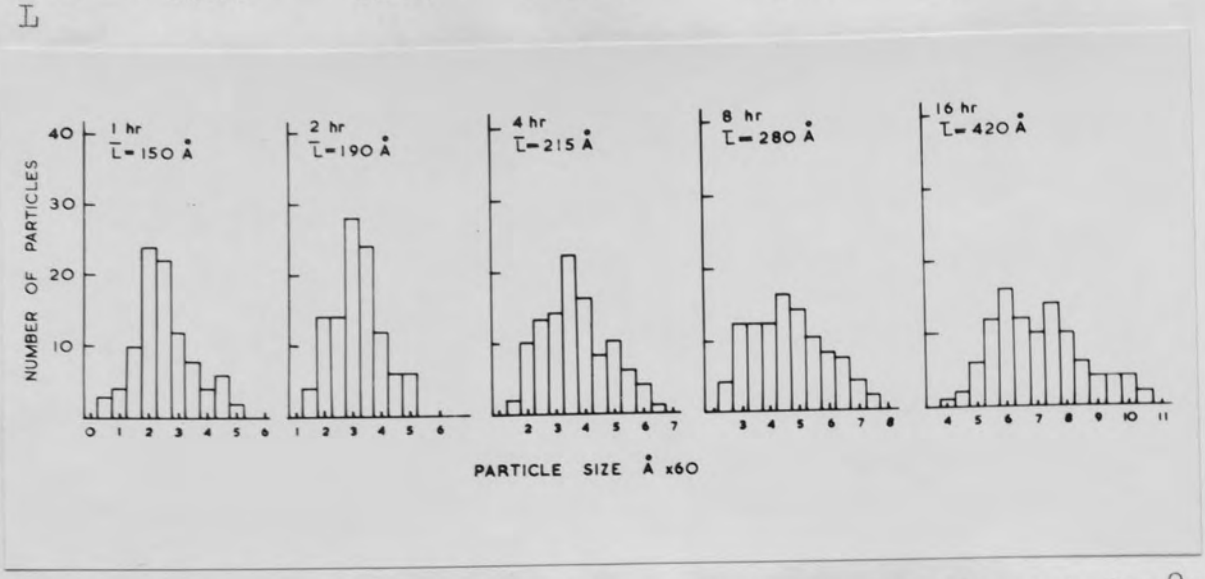

Fig.6.6 Particle size distribution on coarsening at 600°C.

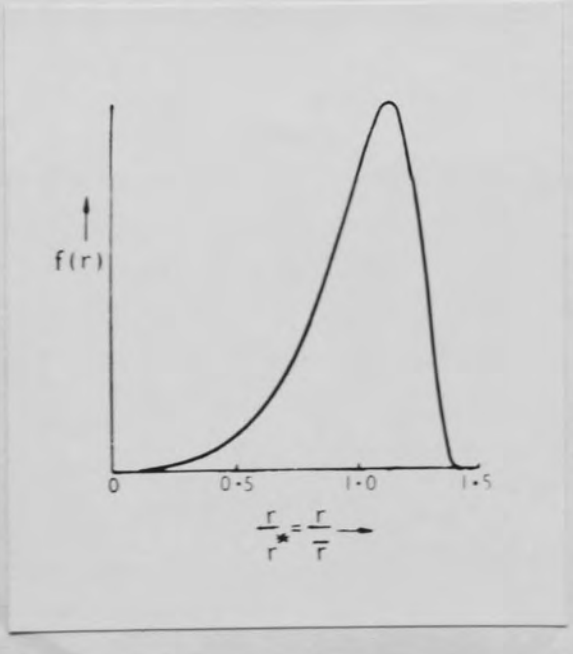

Fig.6.7 The form of particle-size distribution f(r) predicted after long periods of time under conditions of diffusion-controlled growth.

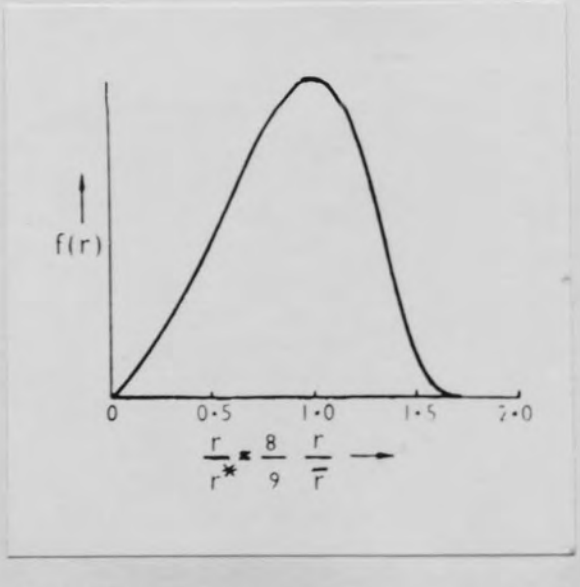

Fig.6.8 The form of particle-size distribution f(r) predicted after a long period of interface-controlled growth.

It is much more difficult to present a quantitative argument for the mechanism involving a modifaction to the interfacial energy between the chromium precipitate and copper matrix by the zirconium atoms present. The difficulties attending the derivation of the interfacial energy of 200 ergs.cms^{-2} for the precipitate in the binary Cu-Cr have already been described, and it can be appreciated that the presence of a third element, and hence another unknown diffusion coefficient produces unsurmountable analytical problems. This is reflected in an attempt to repeat the particle coarsening experiment previously described for copper chromium. The histogram shown in Fig.6.6 of particle size measurements made on the ternary alloy overaged at 600°C illustrates that the distribution of ostensibly chromium particles is more diffuse than for the binary Cu-Cr alloy.

The form of particle size distibution predicted after long periods of ageing is plotted in Figs.6.7 and 6.8 from the equations of Wagner,[35] Liftshitz and Slyzov[34] for the conditions of diffusion controlled growth and interface controlled growth respectively. Both conditions give rise to a sharp cut-off in the distribution such that no particles exist that have a radius of greater than 1.5 times the mean radius of the distribution for diffusion controlled growth, and greater than twice the mean radius for interface controlled growth. Examination of the histogram shown

in Fig.4.24 for Cu-Cr shows that except for the shortest coarsening time of one hour, values of the ratio $\frac{L\ max}{\bar{L}}$ where L max is the maxiumum length of chromium rod observed, and $\bar{L}$ is the mean length of the particle size distribution, range from 1.35 - 1.48, whereas the histograms in Fig.6.6 for the ternary alloy give ratios of $\frac{L\ max}{\bar{L}}$ ranging from 1.54 - 2.10 for identical heat treatment conditions. The higher value obtained for the ternary alloy implies that the growth of the chromium precipitate in the presence of a trace addition of zirconium is not solely diffusion limited, and consequently, the coarsening of the precipitates during ageing does not take place by an Ostwald ripening mechanism. The high initial values of $\frac{L\ max}{\bar{L}}$ obtained after one hour coarsening in both systems suggests that selected growth of particles nucleated during the early stages of decomposition of the solid solution has occurred, producing a particle size distribution which is not wholly attributable to a ripening mechanism.

In keeping with the resistivity data, the coarsening experiment provides further evidence to suggest that the zirconium atoms modify the interface between chromium particles and copper matrix during ageing, and it may be expected that, due to the large misfit of zirconium atoms with respect to copper and chromium, its incorporation into the interface would lead to an overall reduction in the strain energy of the system.

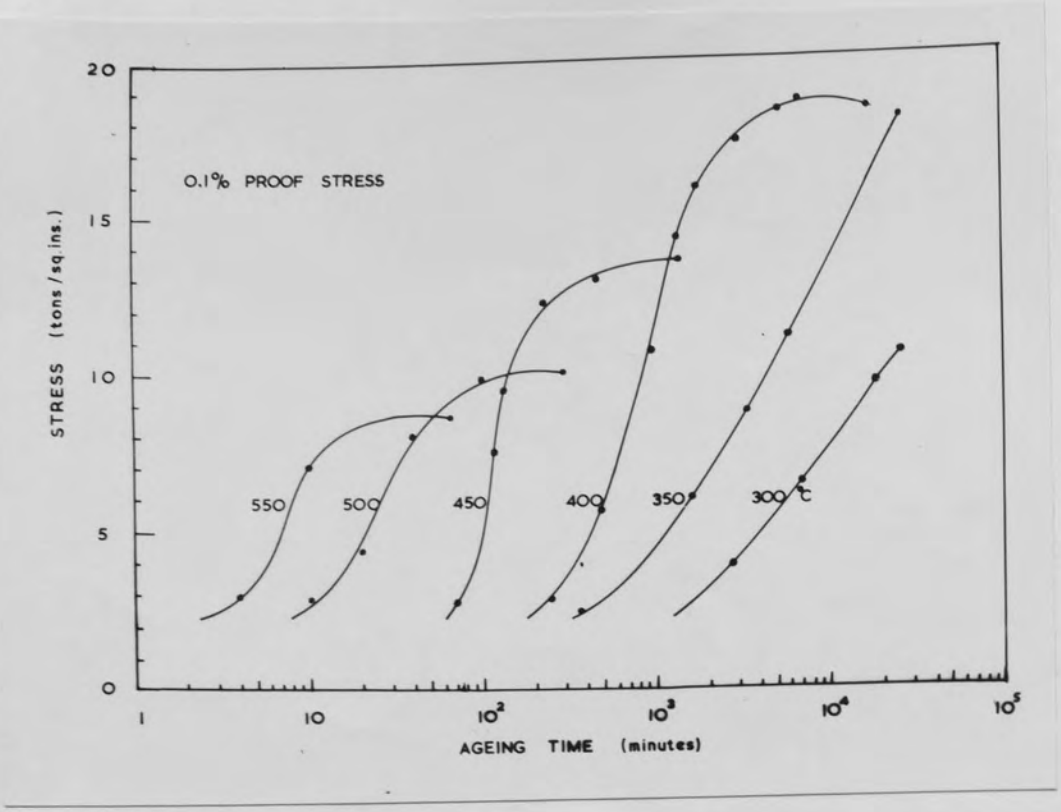

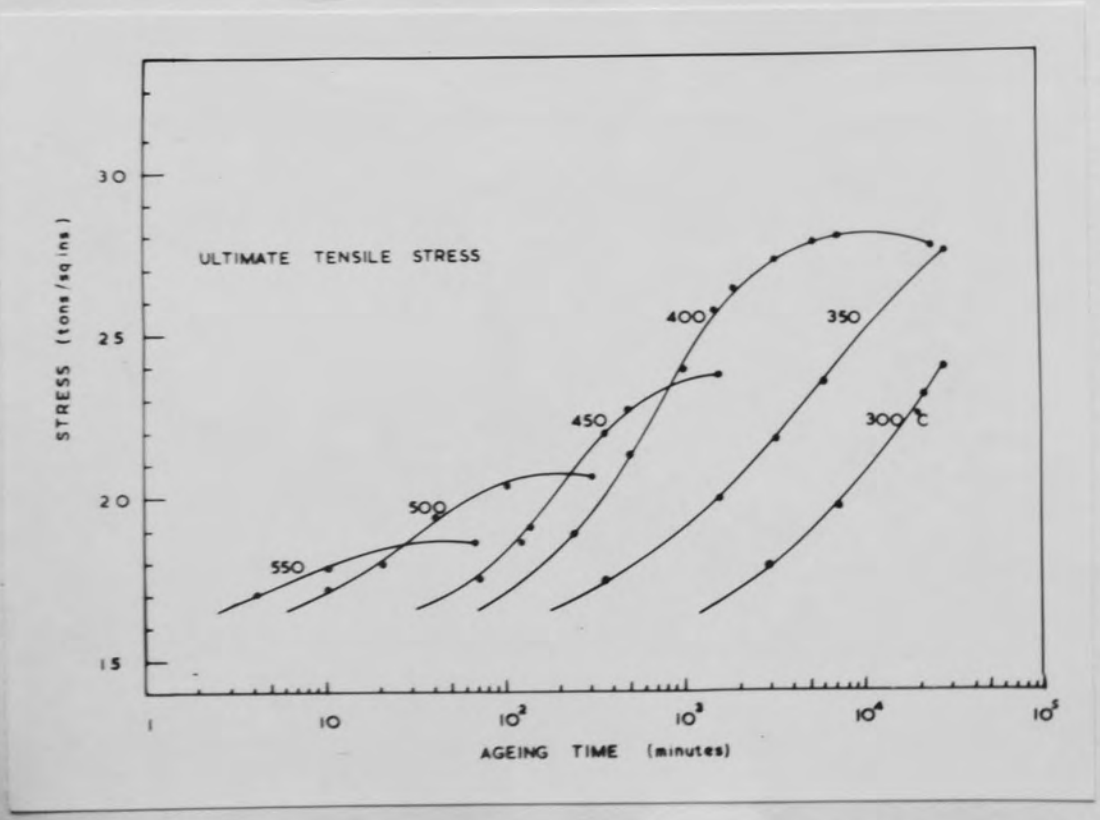

Fig.6.9 Mechanical test results from isothermally aged materials.

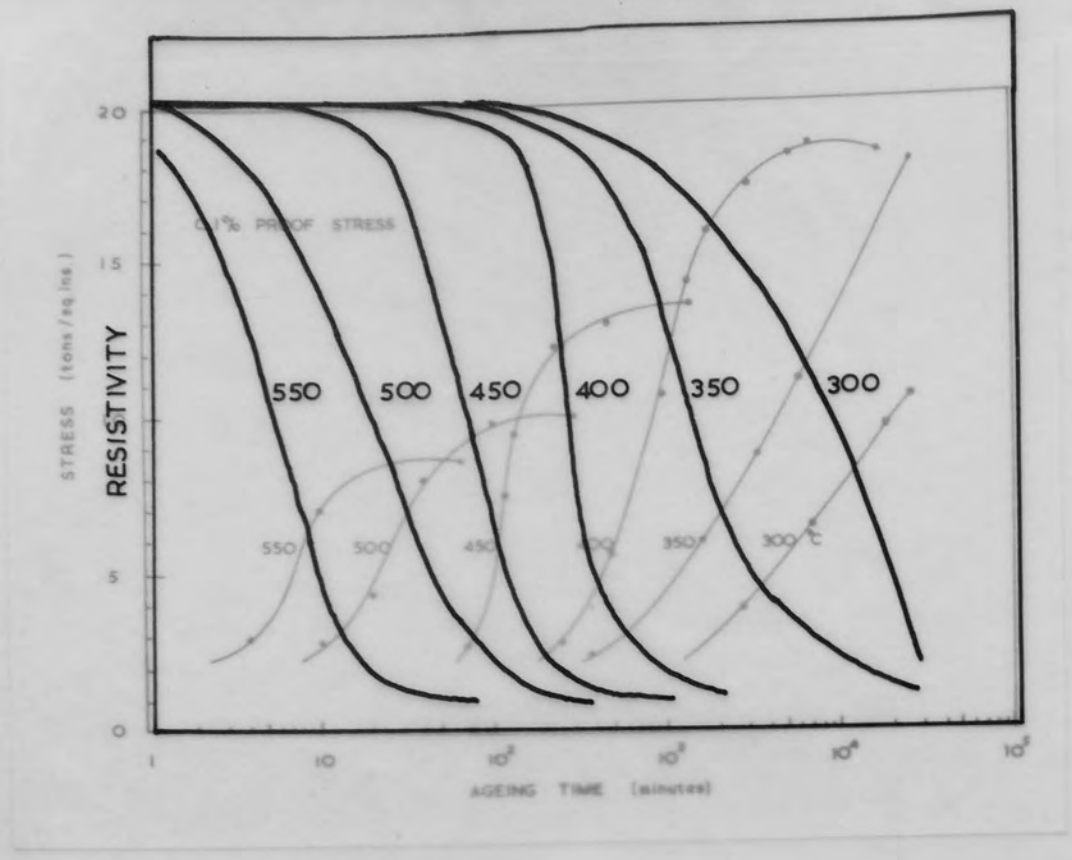

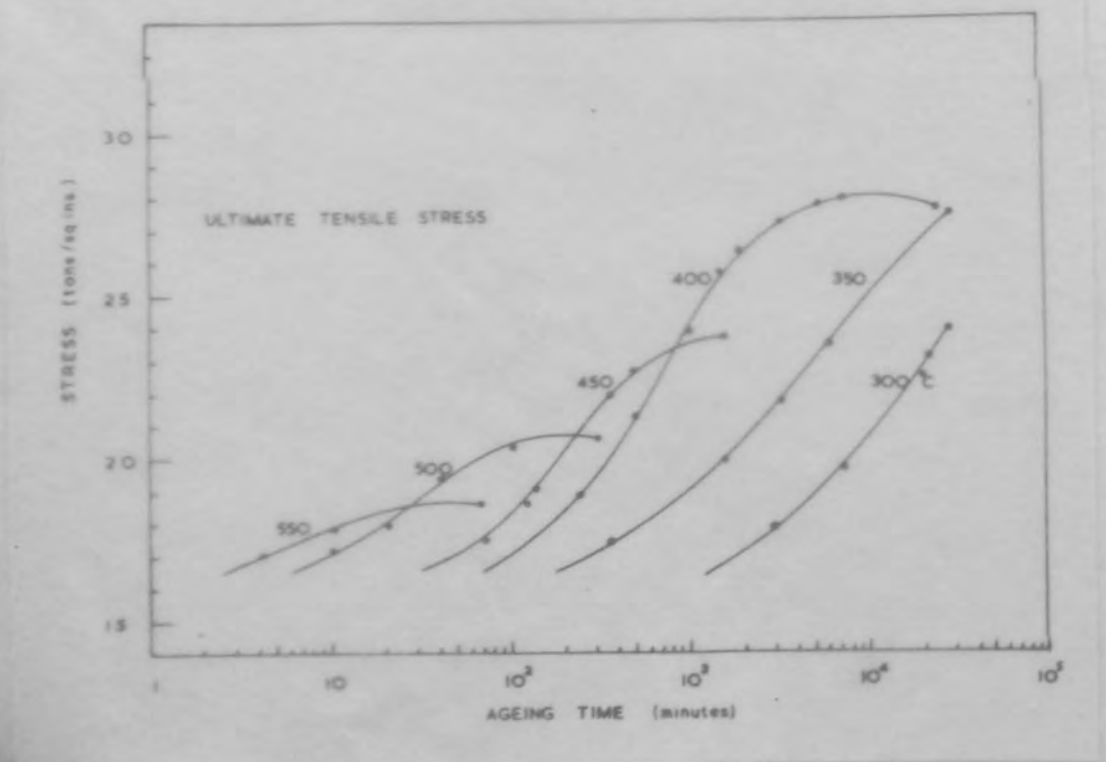

Fig.6.9 Mechanical test results from isothermally aged materials.

6.3 Mechanical Properties

Values of 0.1% proof stress and U.T.S. are presented in Fig.6.9, obtained from isothermal ageing experiments over the range 350°- 550°C. The alloy showed a pronounced variation of mechanical properties with ageing temperature, and when aged above 400°C, suffered a rapid drop in strength. Peak strength was developed in the alloy after either one week at 400°C or three weeks at 350°C, and corresponded to a proof stress of 18.5 tons/sq.ins. which is equivalent to 6.4×10^{-3}G. In this condition, the modulus of elasticity of the alloy increased from that of pure copper(18×10^6lbs/sq.ins.) to a value of 22×10^6lbs/sq.ins.

6.4 Concluding Summary

The addition of 0.07% by weight of zirconium to copper chromium retards the rate of rejection of B.C.C. chromium particles from solid solution by a factor of ten for equivalent ageing cycles, and modifies the growth of the precipitate as reflected in the resistivity results. The metallographic features of the alloy, which differ little from copper chromium, are explained in terms of the interaction of zirconium atoms with vacancies and can also be reconciled with the proposed modification to the precipitate - matrix interfacial energy obtained from particle coarsening experiments and resistivity data.

The mechanical properties of the aged alloy decrease faster than copper chromium at the higher ageing temperatures because of the coarser dispersion of chromium particles obtained when zirconium is present.

CHAPTER 7.

THE ALLOY COPPER-0.2% CHROMIUM-0.2% ZIRCONIUM

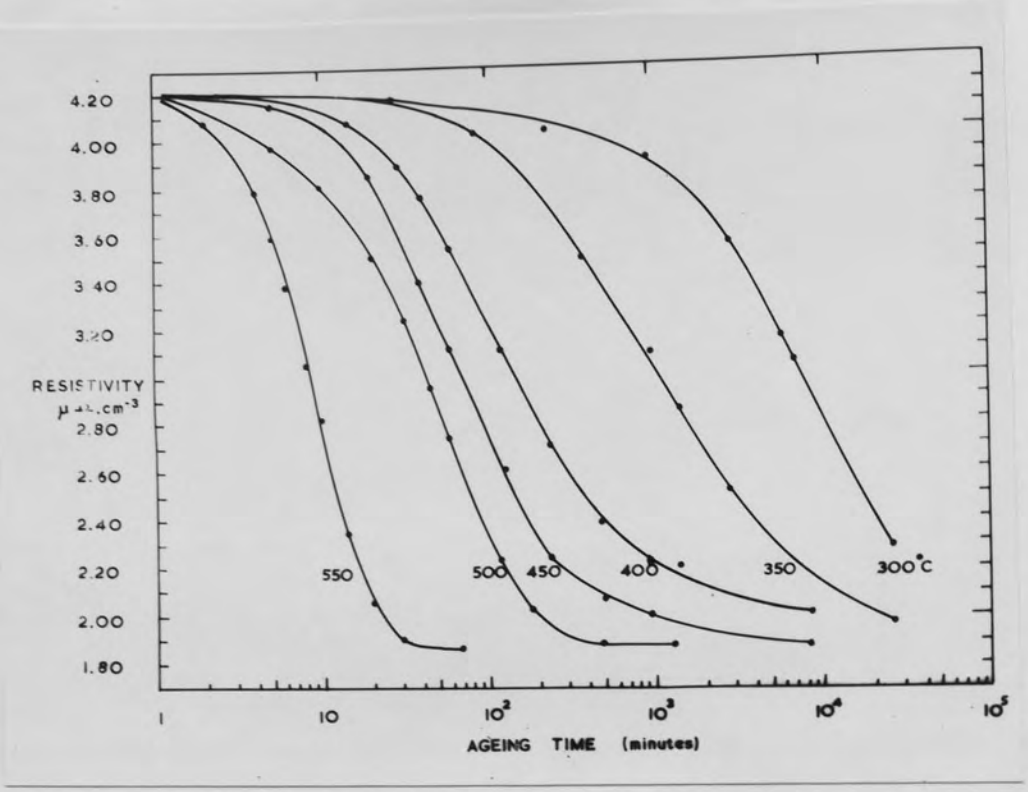

Fig. 7.1 Sigmoidal decay curves obtained from isothermal ageing experiments. Alloy solution treated at 950°C.

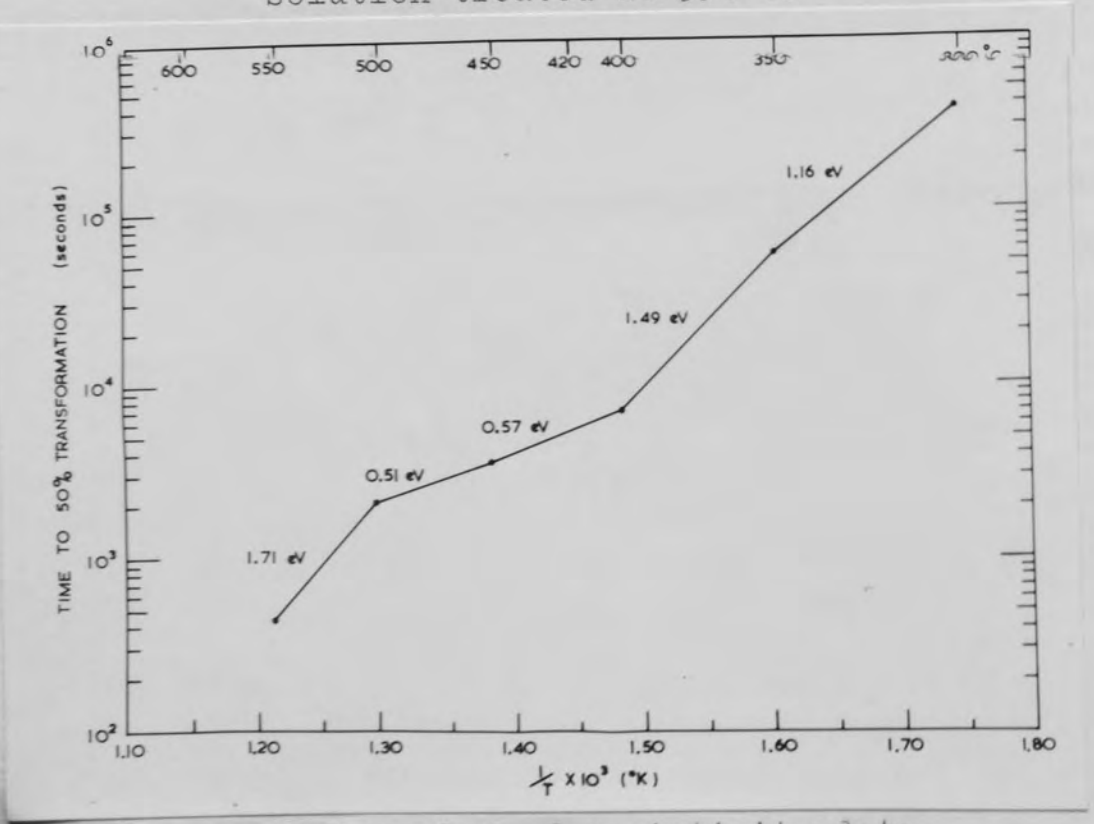

Fig. 7.2 Arrhenius plot of resistivity data.

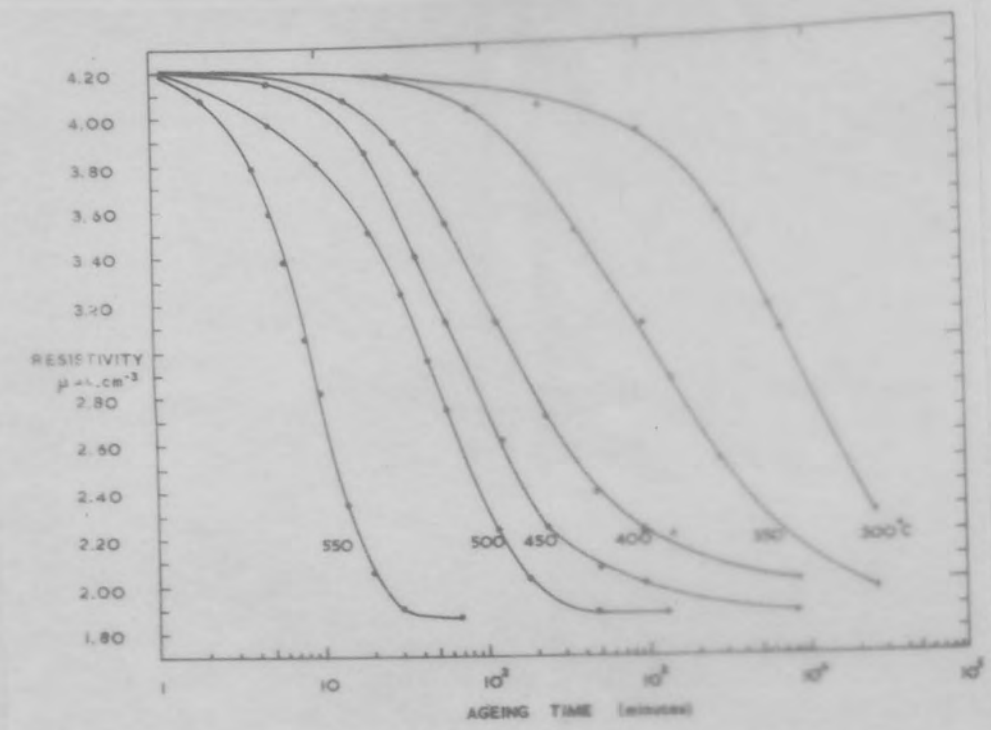

Fig. 7.1 Sigmoidal decay curves obtained from isothermal ageing experiments. Alloy solution treated at 950°C.

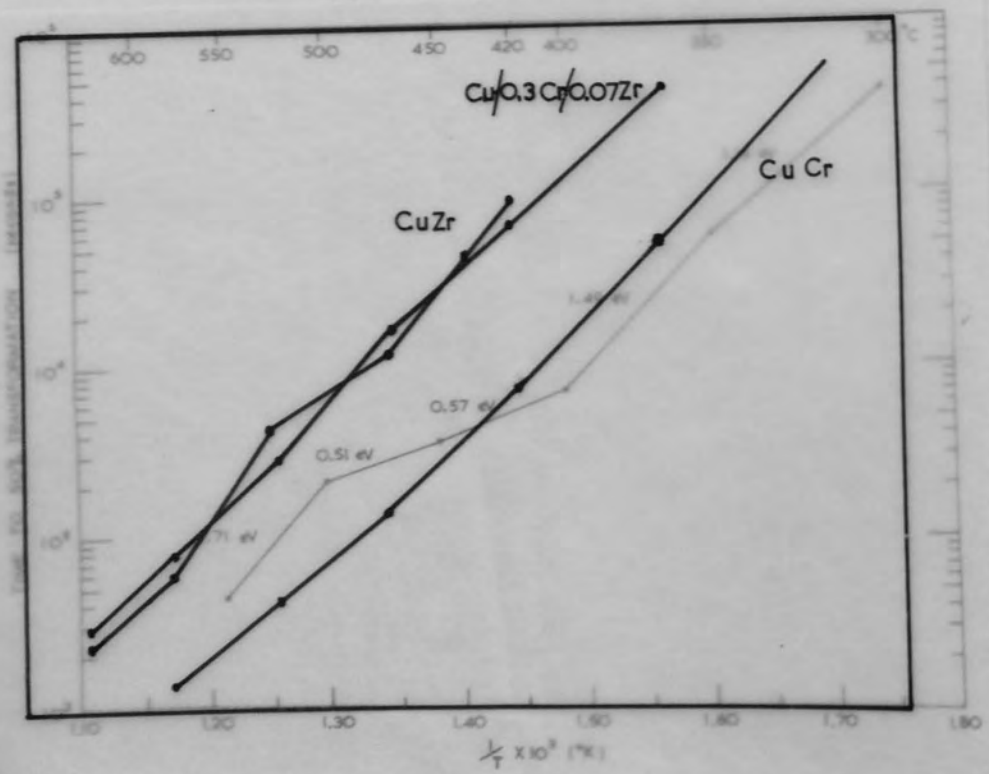

Fig. 7.2 Arrhenius plot of resistivity data.

7.1 Electrical Resistivity

7.1.1 Solubility

The resistivity of the alloy solution treated at 950°C was 4.18 $\mu\Omega cms^{-3}$, and the minimum value attained after ageing 1.88 $\mu\Omega cms^{-3}$ (equivalent to 92% I.A.C.S.) The latter value indicates an increased solubility of one or both alloying elements in the copper matrix at the ageing temperatures used in comparison with the previously discussed ternary alloy.

7.1.2 Isothermal Ageing Data

The precipitation reactions in this alloy, over the range 300°- 550°C yielded the sigmoidal decay curves displayed in Fig7.1. The empirical activation energies derived from these results are given in Fig.7.2 in conjunction with the combined results of the other three alloys studied. Over the ageing temperature range 300°- 400° the value of Q_e follows closely that obtained for Cu-Cr, at approximately 1.4 eV, but above 400°C, the value of Q_e falls dramatically to a value between 0.5 and 0.6 eV, only to rise again to 1.7 eV on ageing the alloy at temperatures above 500°C. The precipitation sequence is therefore expected to be very similar to that found in copper zirconium except that the critical ageing temperature at which the transformation path is predicted to alter in

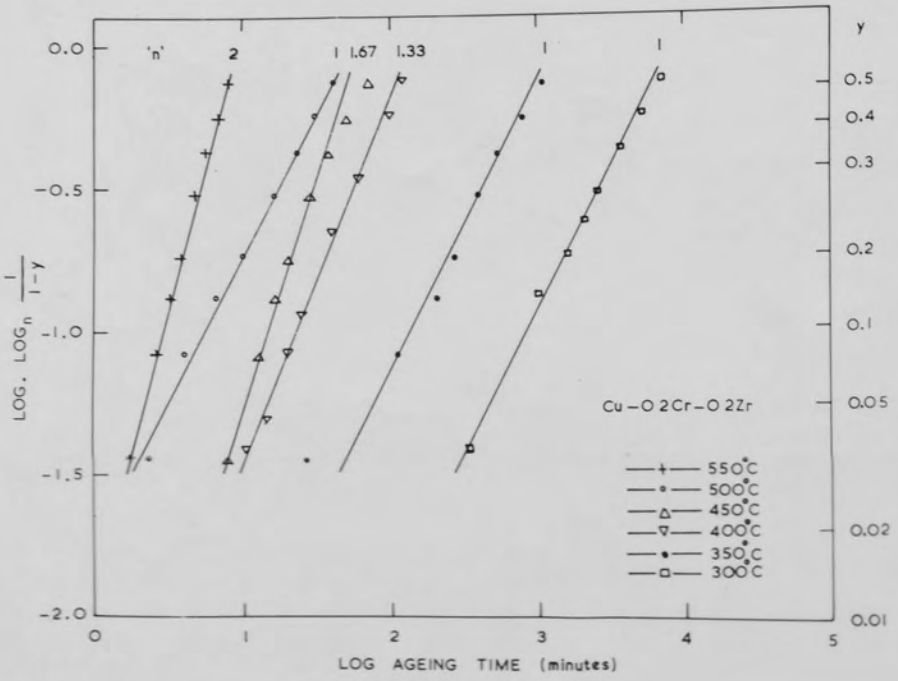

Fig.7.3 Avrami plot of resistivity data.

this alloy is 400°C.

The Avrami plot of the data for this alloy, Fig.7.3, also gives an indication of the proposed change in transformation path at 400°C and is to be compared with the plot for copper zirconium (see Fig.5.4) where the value of 'n' changes from a constant value of 2 to a lower exponent when aged above 450°C, the temperature at which stacking fault precipitation becomes predominant. Above 400°C in the ternary alloy, the values of 'n' range from 1 to 2 and it is difficult to interpret these values for a system in which it is possible for the solid solution to break down via the precipitation of Cr_2Zr, or Cu_3Zr plus Cr.

7.2 Electron Metallography

The solution treated material exhibited an identical structure to that found in all other solution treated alloys studied, and it is only necessary to describe the features observed in the aged alloy by electron metallography. Once again, it is convenient to subdivide the microstructures observed on the basis of the empirical activation energy plot shown in Fig.7.2.

7.2.1. Stage 1 - Alloy aged at 400°C and below

The precipitate formed at ageing temperatures up to 400°C was inferred from the micrographs by the "structure factor" type of contrast it generated near strongly

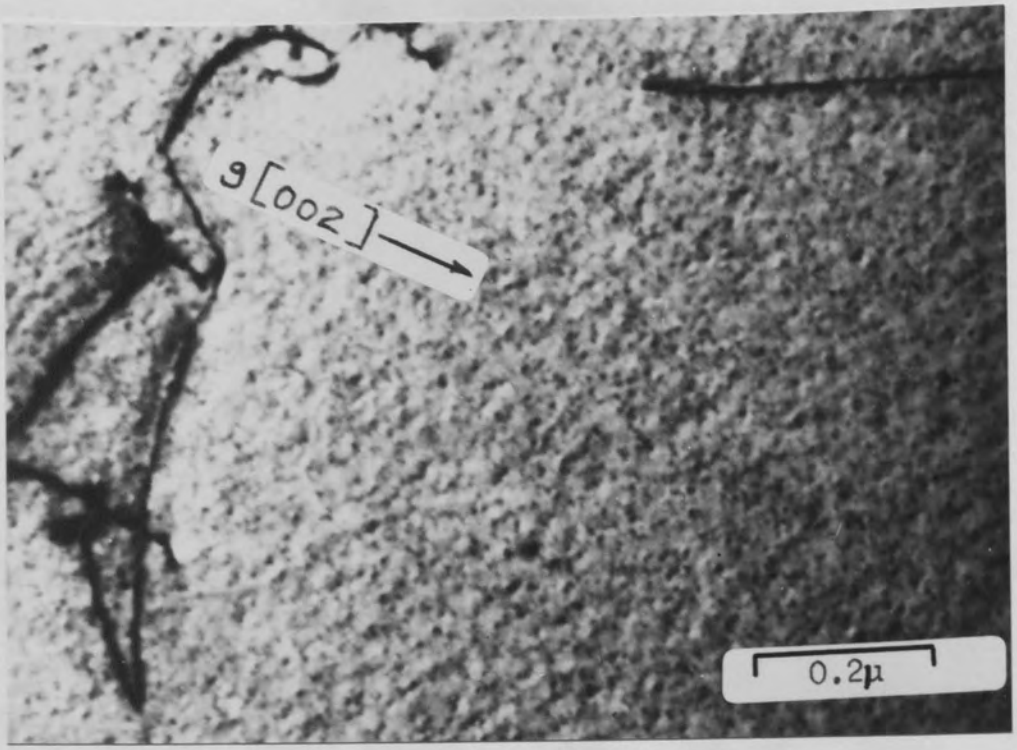

Fig.7.4 Aged at 400°C for 1 day.

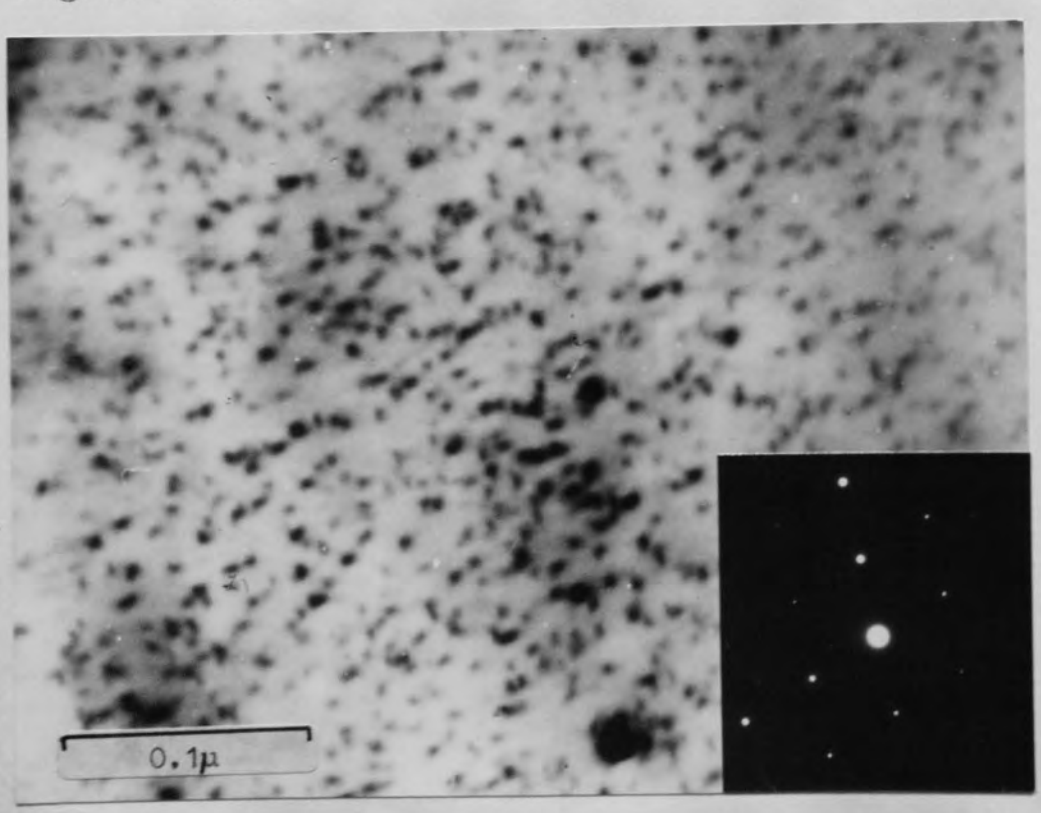

Fig.7.5 Aged at 400°C for 2 days.

diffracting regions of the foil, Fig.7.4. Prolonged ageing at 400°C caused the precipitate to grow large enough to be resolved in the electron microscope and Fig.7.5 shows a typical structure aged for two days at 400°C. The diameter of the precipitates is approximately 30A° after this heat treatment, and clear images can only be obtained in those regions of the foil in which the diffracting conditions are such that the electron beam is very close to a simple zone axis. The diffraction pattern taken from the area shown in Fig.7.5 is superposed on the micrograph to illustrate that "many-beam" conditions are operative. The pattern represents a foil orientation exactly aligned with its {110} planes normal to the electron beam. Similar structures have been observed in Al-Ag alloys by Nicholson and Nutting[47], and were described as spherical Guinier-Preston zones rich in silver. At present, insufficient data is available to establish the chemical composition of the zones found in this copper based ternary alloy when aged at temperatures below 400°C. However, the resistivity data suggests that the majority of the chromium and zirconium are out of solution in materials heat treated to correspond to a microstructure shown in Fig.7.5 and therefore it might be inferred that the zones contain both these elements. The fact that the zones are made visible by differences in the structure factor between matrix and zone suggests that they contain

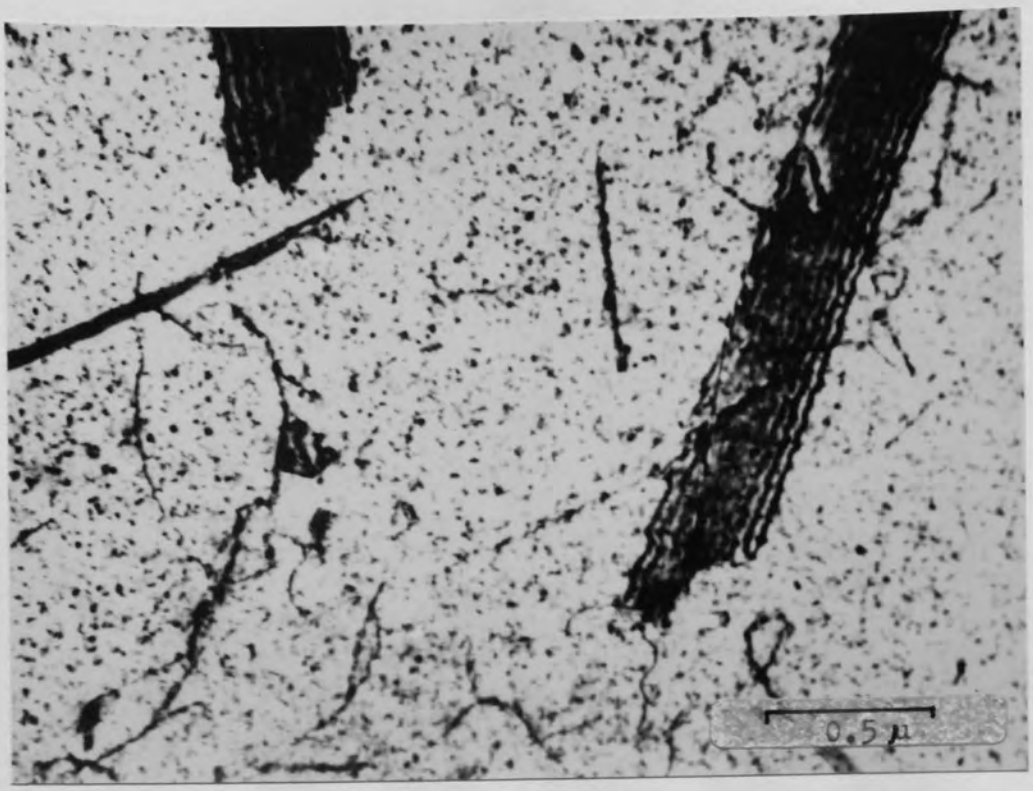

Fig.7.6 Aged at 450°C to a condition of maximum conductivity.

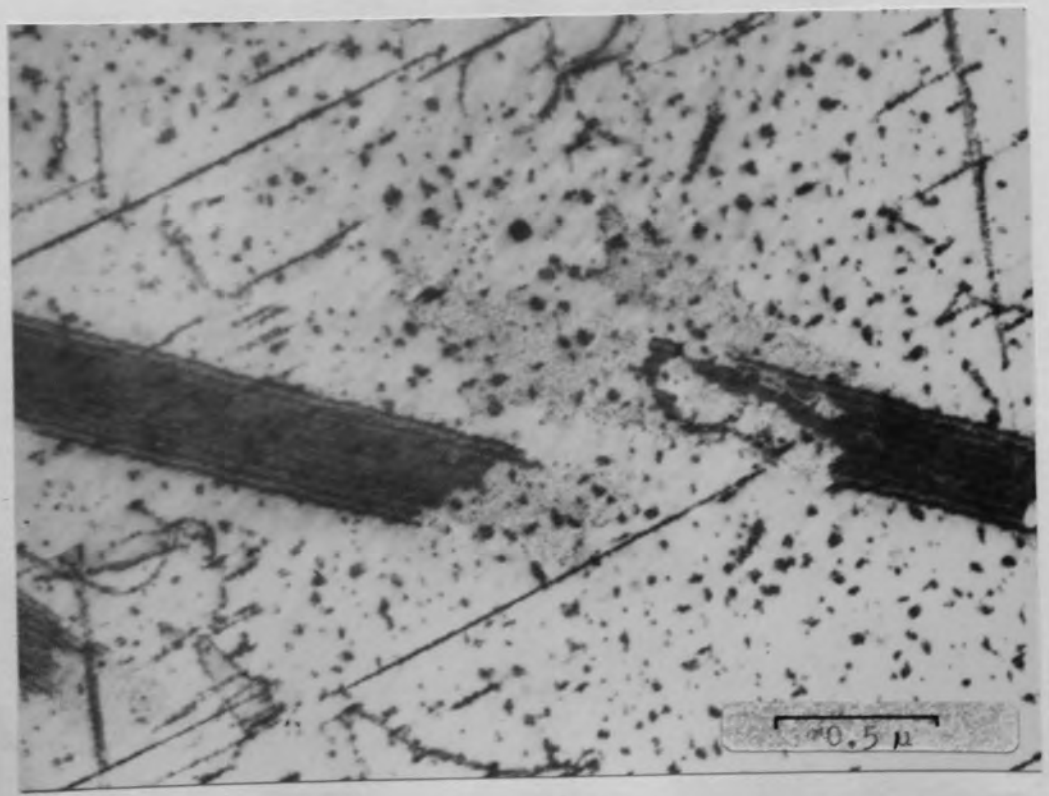

Fig.7.7 Aged at 500°C to a condition of maximum conductivity.

the higher atomic number element, zirconium.

7.2.2 Stage 2 Alloy aged above 400°C.

7.2.2.1 General

When aged within the temperature range over which the lower activation energy applies, stacking faults were observed to grow commensurate with general homogeneous precipitation in the alloy matrix. Typical structures obtained when the solution treated alloy was aged to completion i.e. the recovery of maximum conductivity, at 450°C, and 500°C are shown in Figs.7.6 and 7.7 respectively. The alloy aged at 500°C contained the highest density of stacking faults, and was estimated from micrographs such as that shown in Fig.7.8, as $3 \times 10^{12} \cdot cms^{-3}$, which is very close to that found in the copper zirconium alloy at $2 \times 10^{12} \cdot cms^{-3}$.

Ageing above 500°C increased the ratio of precipitation on undissociated dislocations to that found in the matrix and on stacking faults, and at 600°C the majority of precipitate was found on undissociated dislocations as shown in Fig.7.9

Close examination of Fig.7.7 shows that the precipitate contained in the fault, which is most clearly seen where the fringe contrast has been removed, is much finer than in the corresponding structure described earlier for copper zirconium alloys (see Fig.5.10). The nature of this precipitate, and of the faults, was determined in the

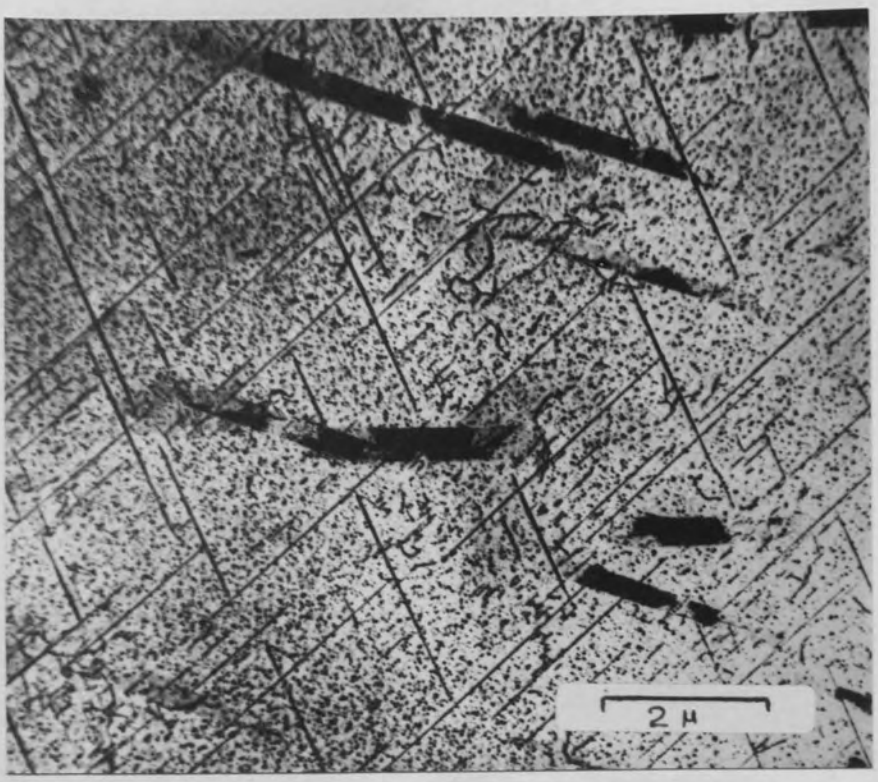

Fig.7.8 Aged at 500°C. Typical micrograph used to estimate the density of stacking faults.

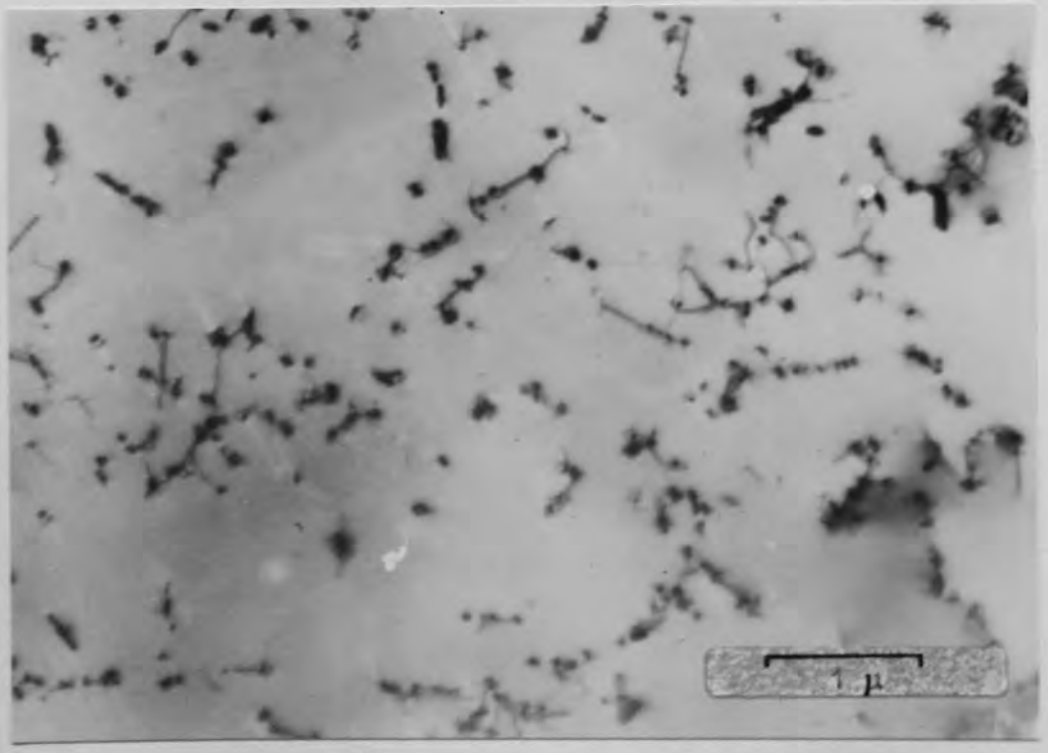

Fig.7.9 Aged at 600°C. Precipitation predominantly on undissociated dislocations.

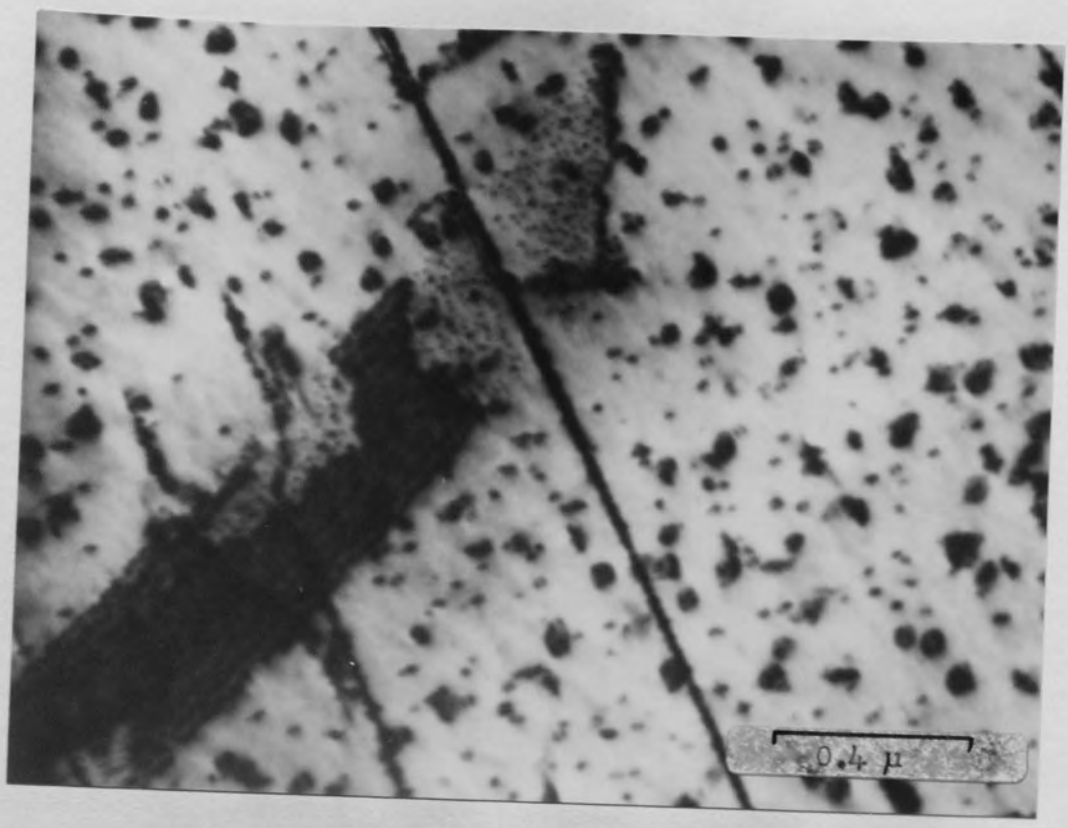

Fig.7.10 Aged beyond the recovery of maximum conductivity at 500°C. Fine chromium precipitates are revealed in those regions traversed by stacking faults.

Fig.7.11 Typical selected area diffraction pattern from regions shown in Fig.7.10. (110) Foil

following manner.

7.2.2.2 Precipitate within the faults

The fine precipitates revealed in regions of the fault which have been converted to perfect crystal by dislocation movement are shown in Fig.7.10. On overaging the alloy at 500°C, it was possible to identify the precipitate as B.C.C. chromium by selected area diffraction techniques. The diffraction patterns obtained from regions containing stacking faults in the alloy were similar to those described for the overaged copper chromium alloy, with the strong <110> type chromium diffraction spots found inside the matrix <002> reflections, as shown in Fig.7.11. Dark field images of the faults obtained with the chromium precipitate reflections confirm the presence of chromium within the fault, and Fig.7.12 illustrates a fault inclined at 35° to a (110) foil surface.

7.2.2.3 Nature of the faults

As with copper zirconium, it was possible to identify both extrinsic and intrinsic stacking faults in the alloy aged above 400°C. The ratio of extrinsic to intrinsic faulting measured in samples aged between 415°C and 500°C, and determined from observations of approximately 100 faults, was 7 : 1. Both types of fault were found to contain the chromium precipitate and Fig.7.13 illustrates the extrinsic nature of such faults in material aged at 415°C, whilst Fig.7.14 illustrates the

Fig.7.12 Dark field image of stacking fault taken with chromium precipitate reflection.

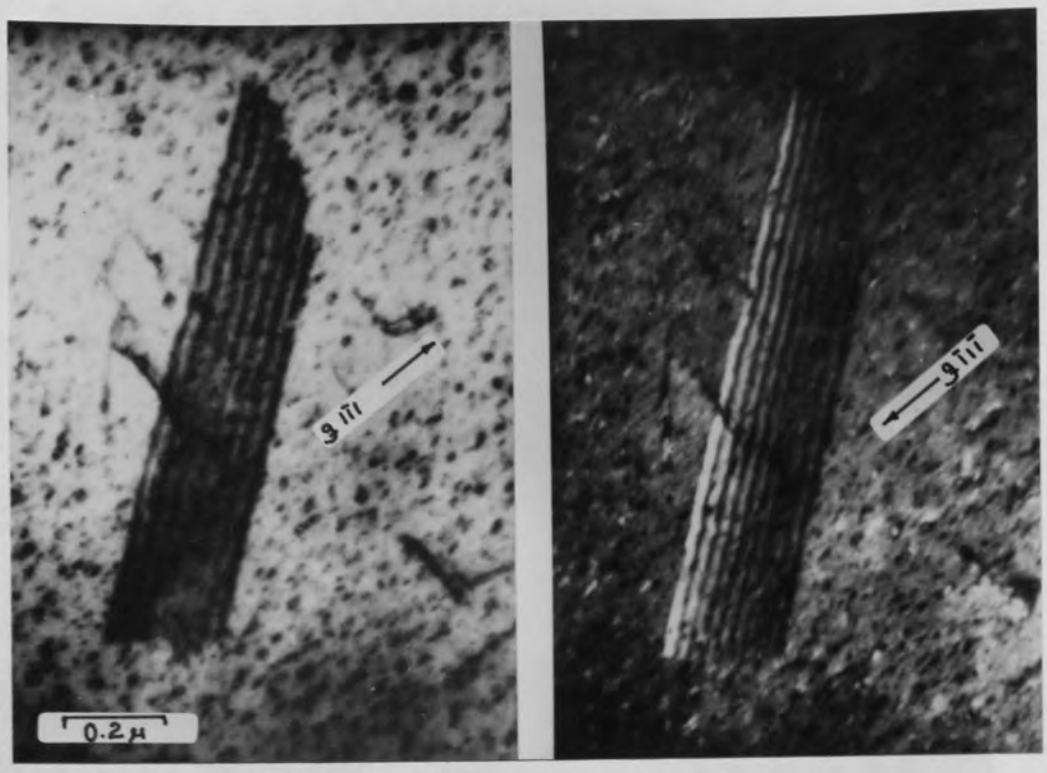

Fig.7.13 Extrinsic faults in material aged at 415°C.

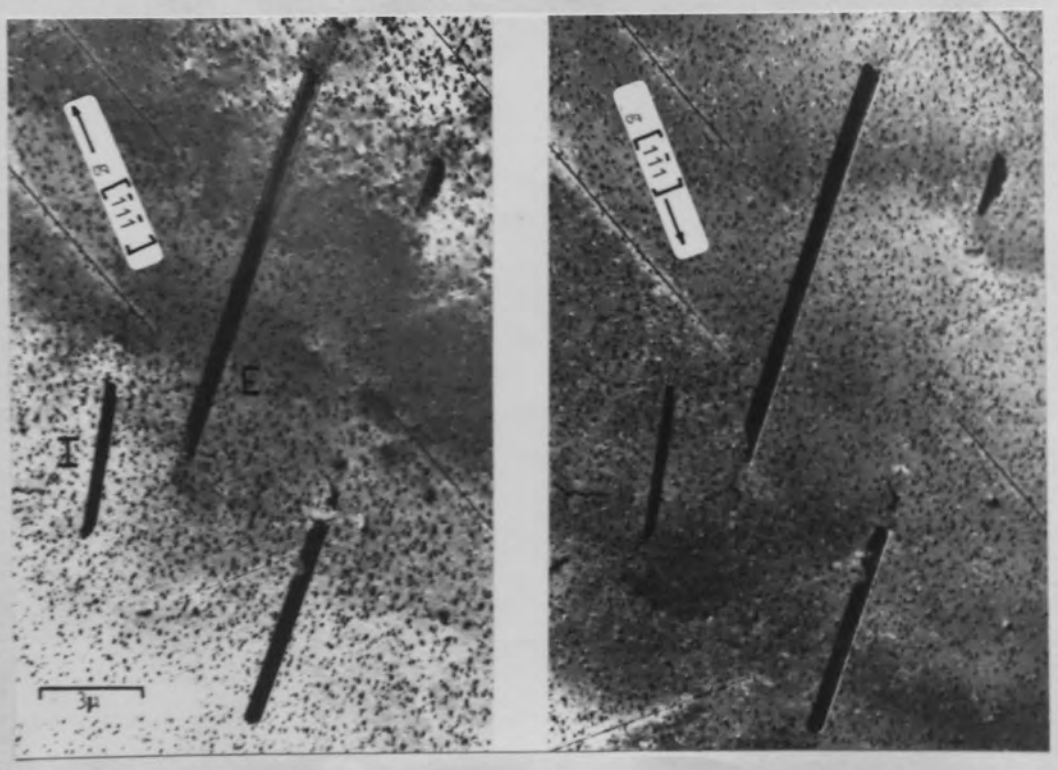

Fig.7.14 Extrinsic and Intrinsic faults in material direct quenched to 470°C.

presence of both type of faults in the alloy direct quenched to ageing temperatures of 470°- 500°C.

7.2.2.4 Nature of the partial dislocations bounding the faults

The experimental conditions previously described for copper zirconium in section 5.2.3.4 were adhered to, and results obtained suggest that the dislocations bounding the faults examined are Shockley partials of the type $\frac{1}{6}a\langle 112\rangle$.

Fig.7.15 is a typical result taken from an alloy aged to 90% transformation at 415°C, and shows the fault viewed in $g[1\bar{1}1]$ and $g[\bar{2}20]$. The analysis of Fig.7.15 is as follows:- the foil orientation is near (110) and therefore the fault lies on either the (111) or the $(11\bar{1})$ plane, inclined to the foil surface at approx. 35°. The partial dislocations lying in the (111) plane are tabulated below and the scalar quantities g.b and $\frac{1}{8}$ g.b$\wedge$u listed for the reflections $g[\bar{1}\bar{1}\bar{1}]$ and $g[\bar{2}20]$.

Reflection	b	g.b	$\frac{1}{8}$ g.b$\wedge$u
$[\bar{1}\bar{1}\bar{1}]$	$\frac{1}{3}[111]$	$-\frac{1}{3}$	$0 \rightarrow \pm 0.118$
	$\frac{1}{6}[\bar{2}11]$	$-\frac{2}{3}$	$0 \rightarrow \pm 0.029$
	$\frac{1}{6}[1\bar{2}1]$	$+\frac{1}{3}$	$0 \rightarrow \pm 0.029$
	$\frac{1}{6}[11\bar{2}]$	$+\frac{1}{3}$	$0 \rightarrow \pm 0.029$
$[\bar{2}20]$	$\frac{1}{3}[111]$	0	$0 \rightarrow 0.2042$
	$\frac{1}{6}[\bar{2}11]$	+1	0
	$\frac{1}{6}[1\bar{2}1]$	-1	0
	$\frac{1}{6}[11\bar{2}]$	0	0

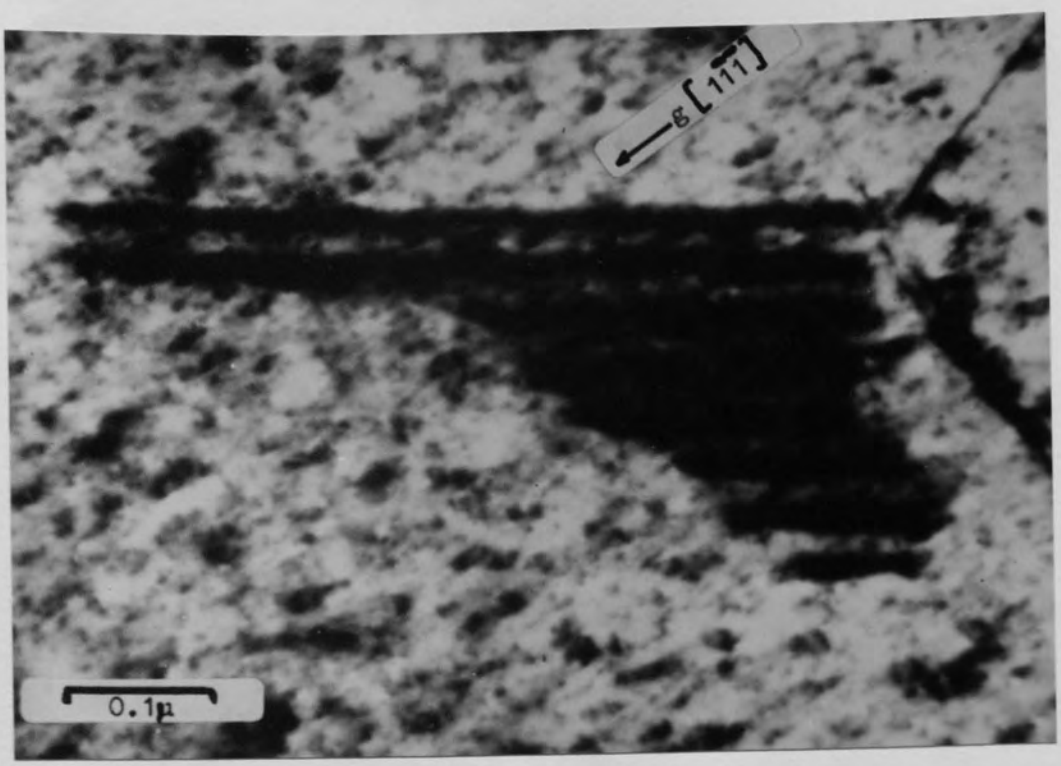

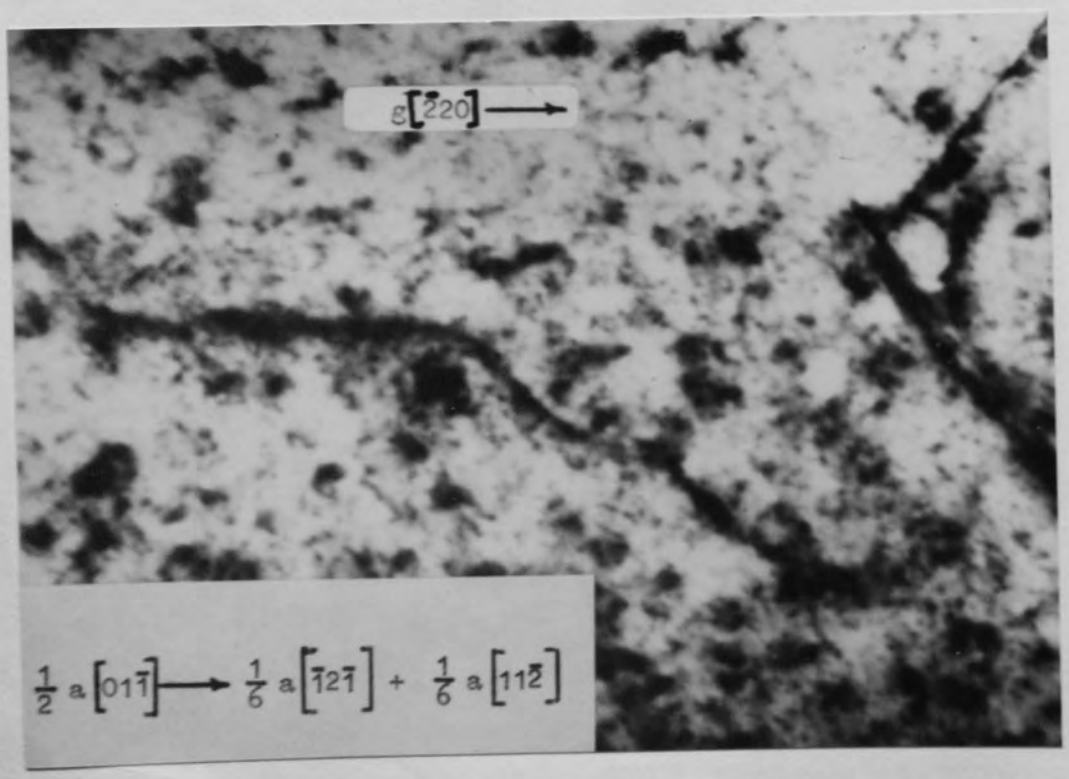

Fig.7.15 Faults formed in the alloy aged at 415°C.

In Fig.7.15, for the $[\bar{1}\bar{1}\bar{1}]$ reflection both the left hand partial and the right hand partial are invisible, whereas in the $[\bar{2}20]$ reflection only the right hand partial is invisible, therefore, the left hand partial is $\frac{1}{6}[\bar{1}2\bar{1}]$, and since no dotted contrast, characteristic of a Frank partial dislocation is evident at the right hand boundary of the fault, then the Burgers vector of the right hand partial dislocation is $\frac{1}{6}[11\bar{2}]$ The dislocation reaction producing the fault may therefore be written:-

$$\tfrac{1}{2}a[01\bar{1}] \longrightarrow \tfrac{1}{6}a[\bar{1}2\bar{1}] + \tfrac{1}{6}a[11\bar{2}]$$

Two possible intersecting faults lying on the $(\bar{1}11)$ and $(\bar{1}1\bar{1})$ planes respectively are also visible at the right hand edge of Fig.7.15 and their proximity to the fault previously analysed may be significant since faults can be nucleated readily from the stair rod dislocation formed at such intersections as shown by Goodhew et.al.[70]

7.2.2.5 Nucleation of Stacking Faults

Foils were examined after ageing times corresponding to 15%, 35% and 70% transformation at 415°C as determined by resistivity measurements in an attempt to follow the early stages of stacking fault formation in the alloy. Stacking faults were first observed after 35% transformation as shown at A in Fig.7.16, together with regions containing a marked increase in dislocation density

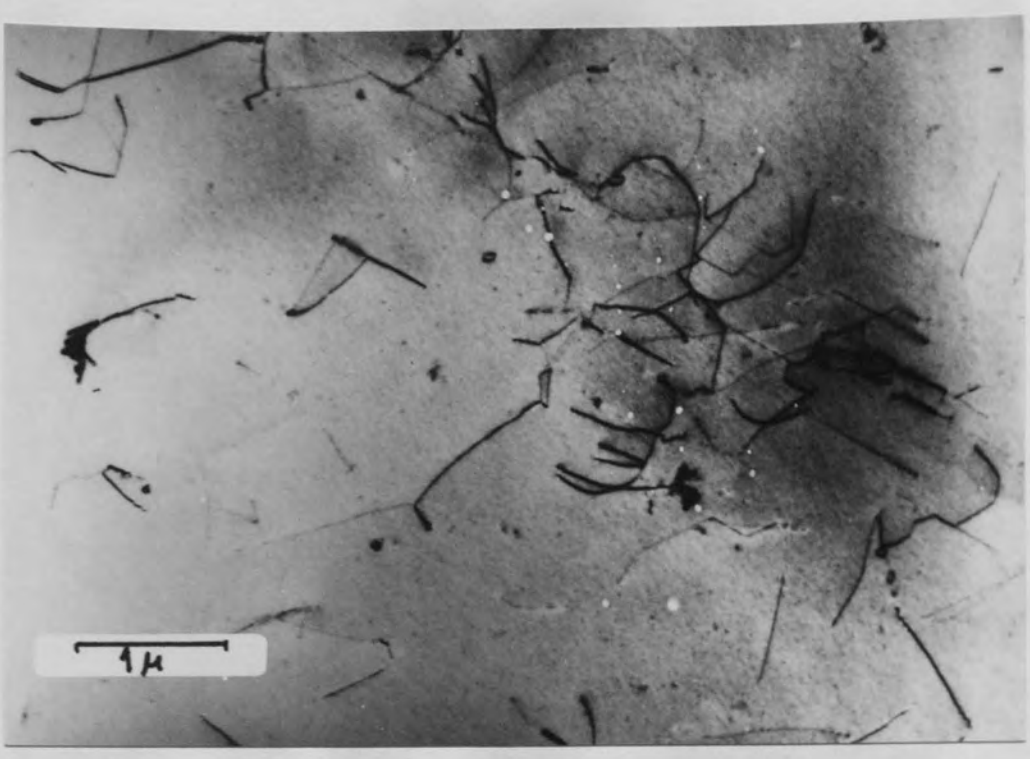

Fig.7.16 Aged to 35% transformation at 415°C.

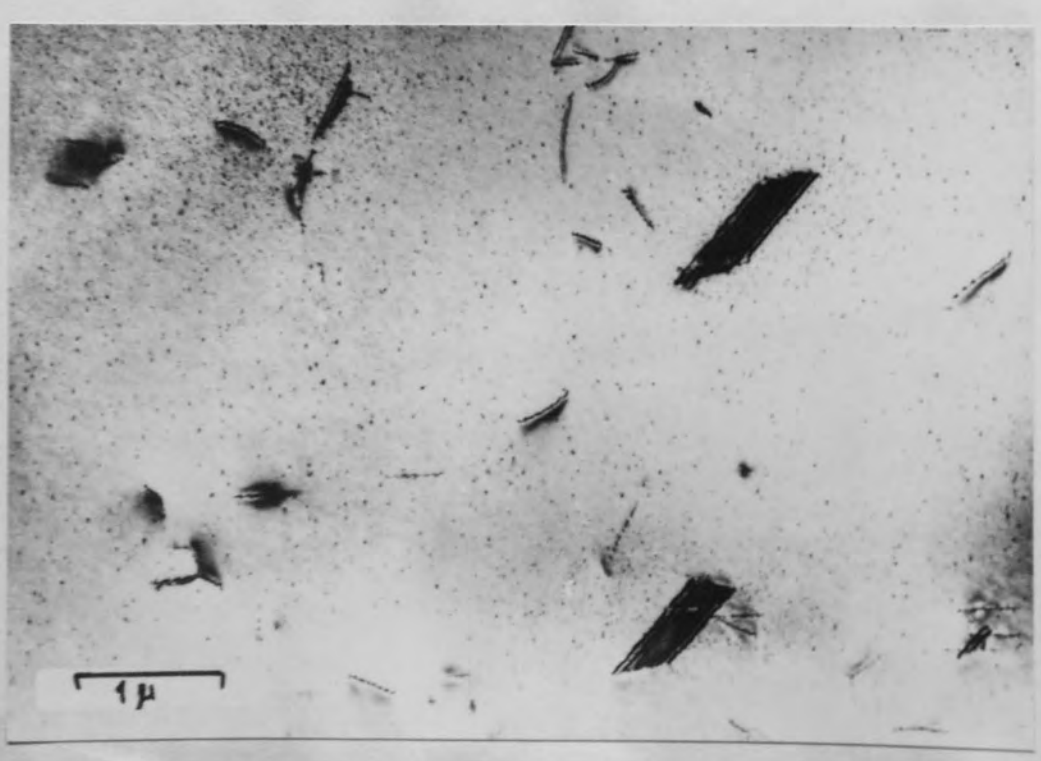

Fig.7.17 Aged to 70% transformation at 415°C.

from that of the solution treated material. The small faults observed after 35% transformation were always in association with part of a whole dislocation, and further ageing to 70% transformation clearly indicated that the faults grow from dislocation lines lying along slip planes which intersect the plane on which the fault subsequently grows as shown in Fig.7.17. This micrograph also illustrates that only a small number of the total dislocation lines present in the aged material are associated with stacking faults, and furthermore, that general homogeneous precipitation is occurring concurrently with stacking fault growth.

7.2.2.6 Matrix Precipitates

Both the incoherent disc shaped Cu_3Zr precipitate and coherent chromium particles could be recognized in the matrix of material aged at 450°C and above.

The chromium particles were the size expected from a knowledge of the behaviour of the binary Cu-Cr, but the Cu_3Zr precipitates present were smaller by a factor of two for corresponding ageing temperatures. The morphology of the matrix precipitates in the ternary alloy suggested that a certain degree of hetrogeneous nucleation of one precipitate by the other had occurred during ageing. Fig.7.18 shows bright field and dark field images of the material aged at 500°C taken with a chromium precipitate reflection and illustrates the presence of chromium within the matrix and stacking faults.

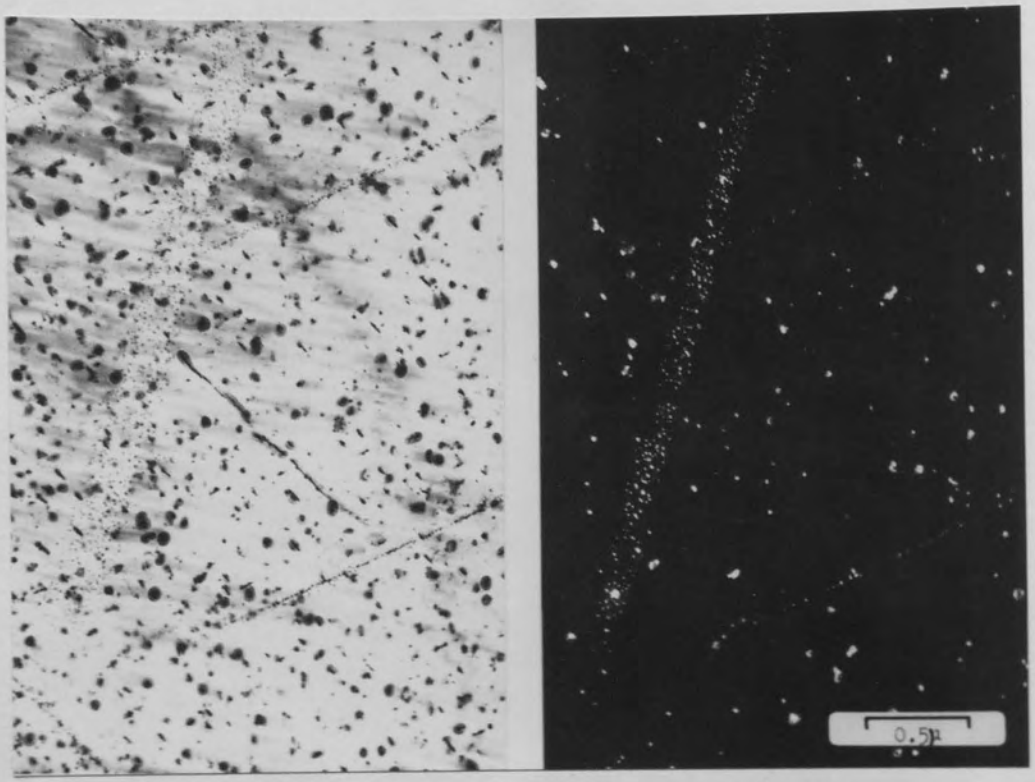

(a) (b)

g.7.18 Alloy aged at 500°C. (a) Bright field
(b) Dark field taken with chromium precipitate reflection.

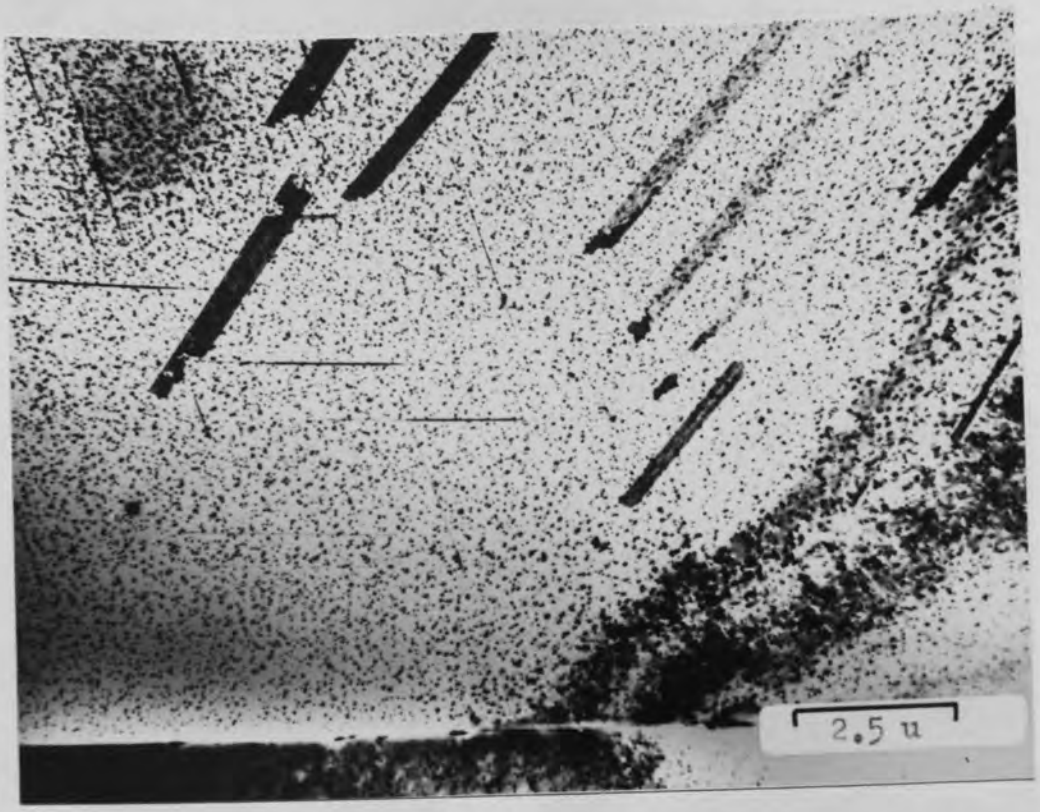

Fig.7.19 Direct quenched to 425°C and held for 4 hours.

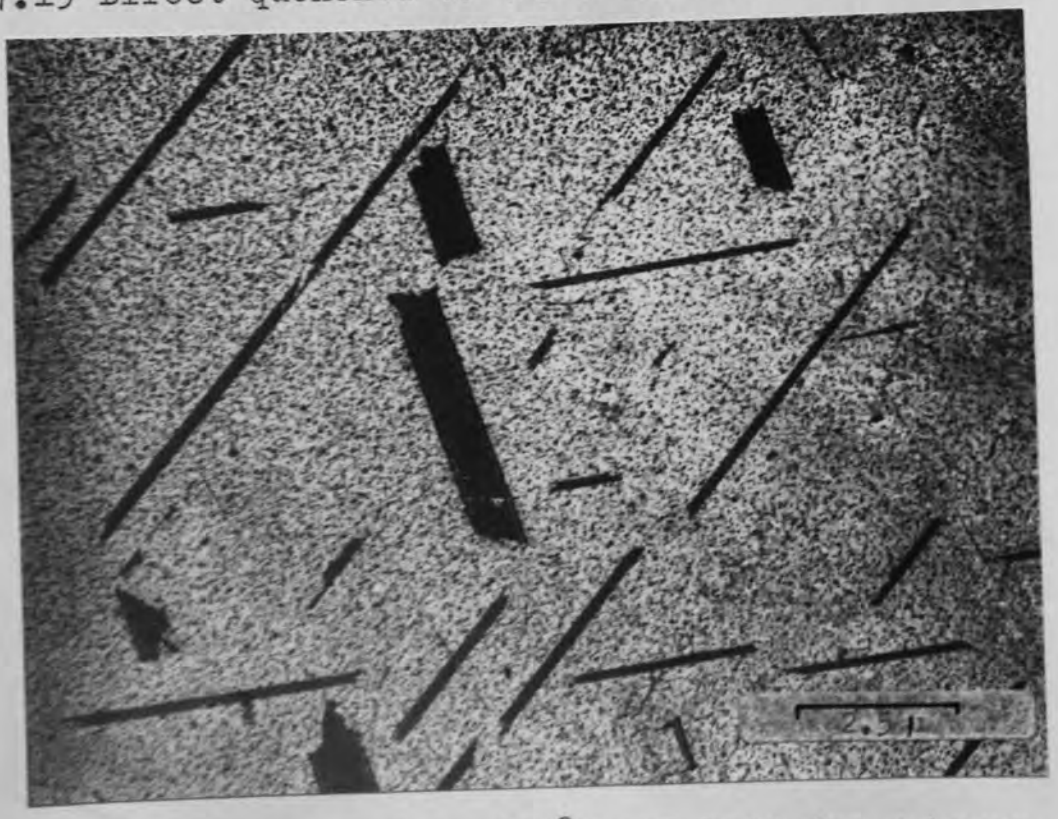

Fig.7.20 Direct quenched to 450°C and held for 4 hours.

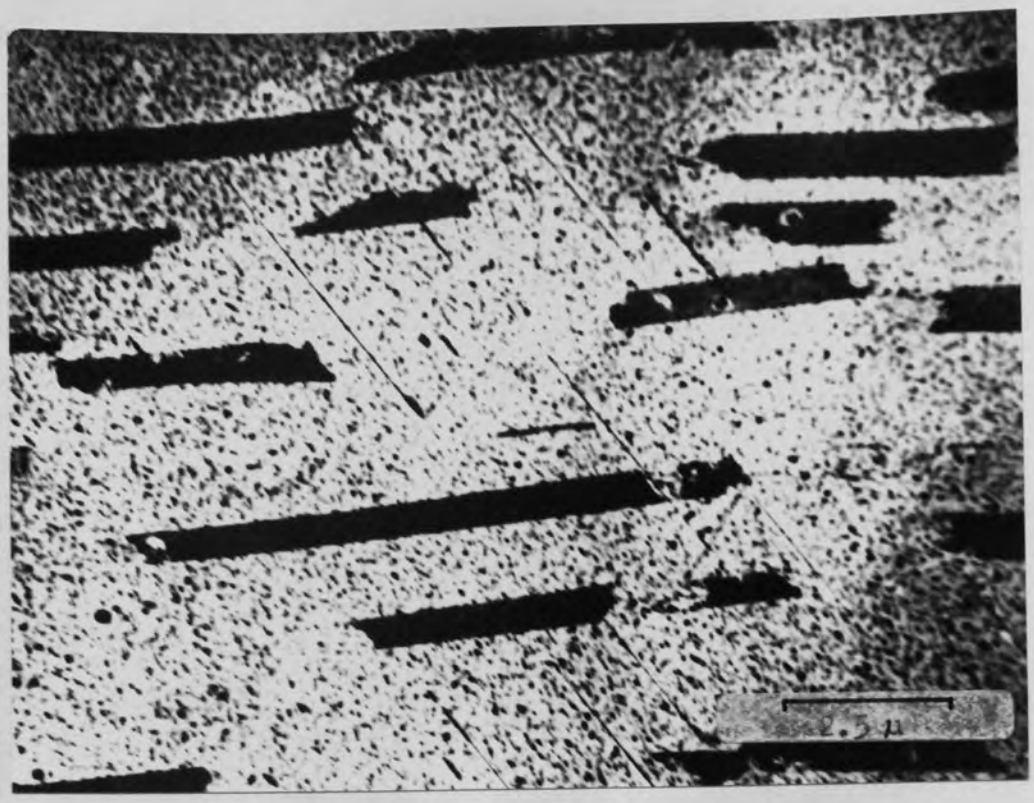

Fig.7.21 Direct quenched to 470°C and held for 4 hours.

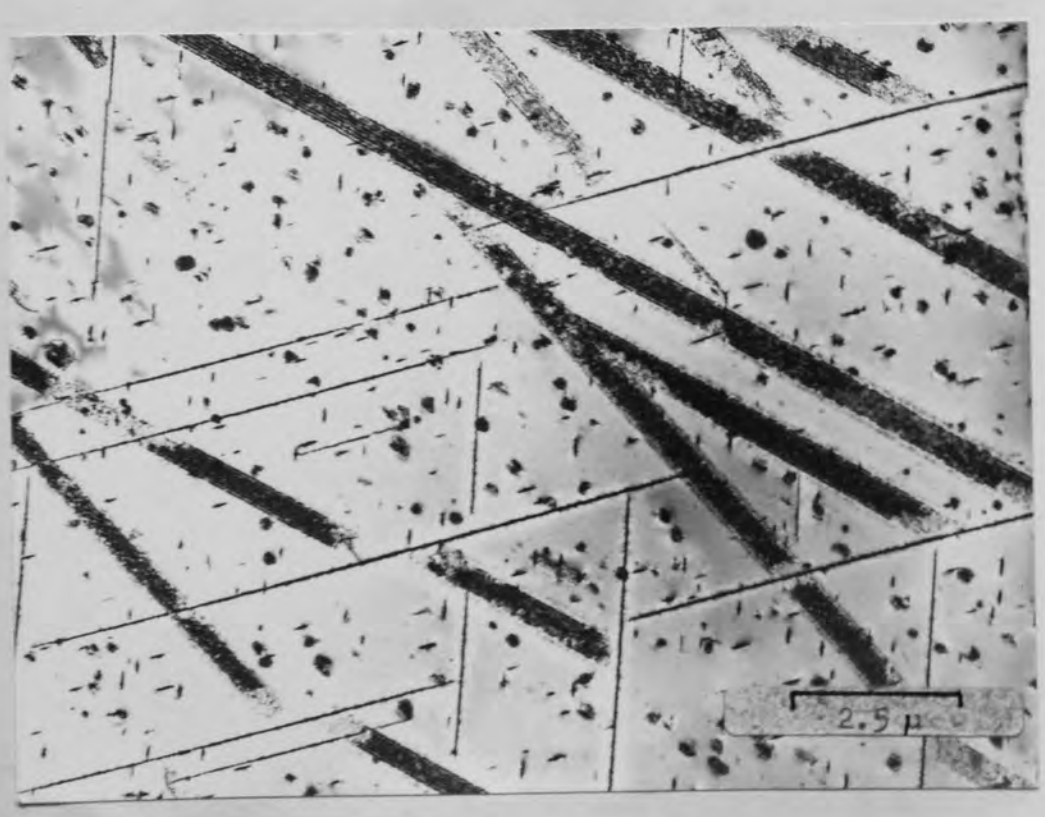

Fig.7.22 Direct quenched to 500°C and held for 4 hours.

With the knowledge that the nucleation conditions necessary for each of the matrix precipitates present in the ternary alloy are different, a series of direct quenching experiments were performed to determine the relative sensitivity of the observed precipitation reactions to vacancy and solute supersaturation.

7.3 Direct Quenching Experiments

7.3.1 Grain Interior

The four micrographs shown in Figs.7.19,7.20, 7.21 and 7.22 represent the structures developed in the alloy on direct quecning to 425°, 450°, 470°and 500°C respectively and holding at these temperatures for four hours. The major structural change occurs in the alloy quenched to 500°C whereupon the matrix/precipitate undergoes rapid coarsening. The stacking faults present in the alloy increase in length with progressively increasing quenching temperature until after four hours at 500°C, faults of 15 microns diameter are observed. The fault density remains constant over this range of ageing temperatures at approximately 1×10^{11}.cms^{-3} i.e. a factor of 10 less than the stacking fault density observed in the room temperature quenched alloy (c.f. Fig.7.8).

The matrix precipitate present after these four heat treatment cycles is found to be the Cu_3Zr precipitate, and Fig.7.23 shows more clearly that the precipitate

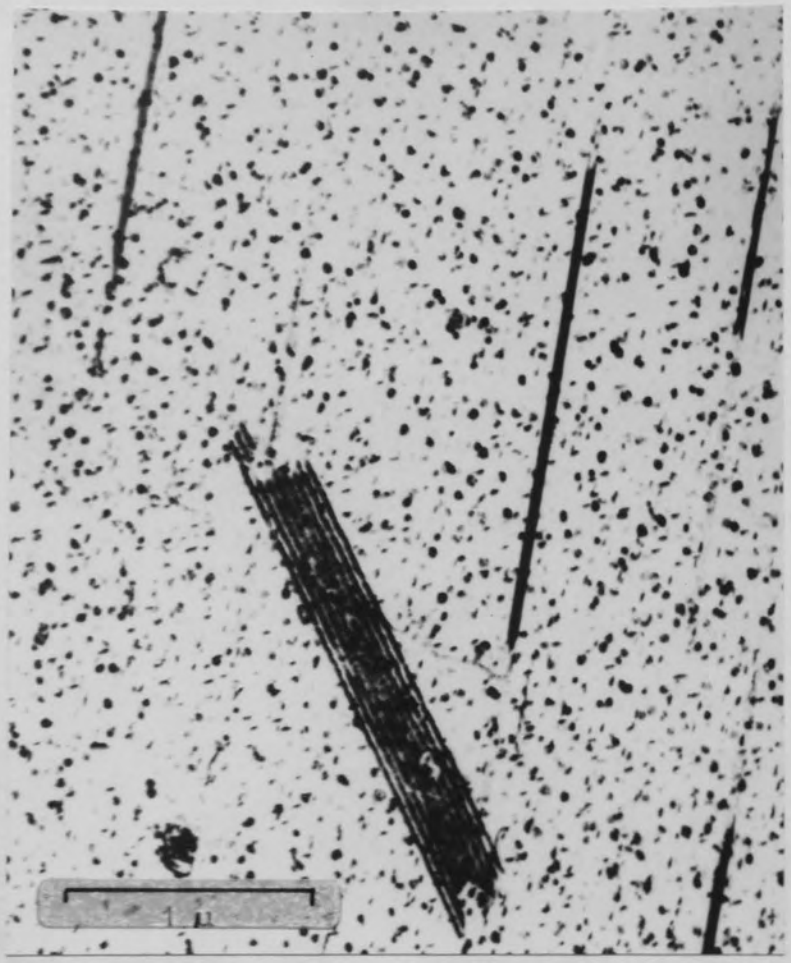

Fig.7.23 Direct quenched to 425°C illustrating the presence of the disc shaped Cu_3Zr precipitate in the matrix.

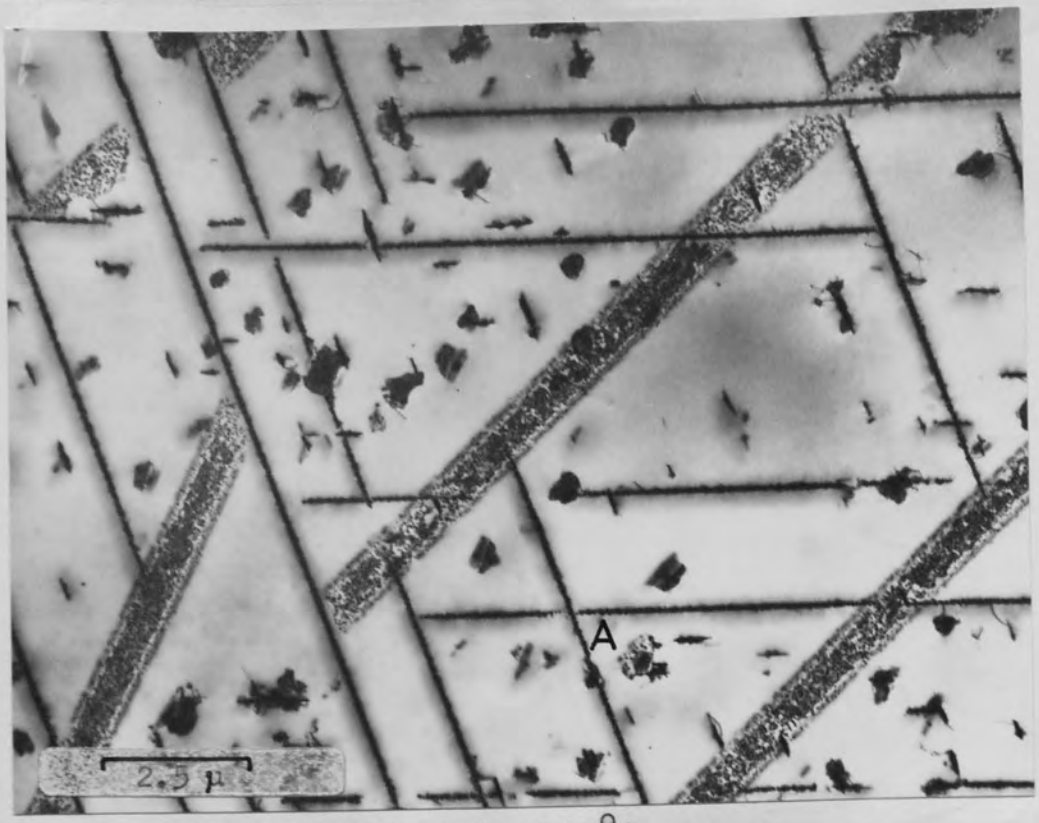

Fig.7.24 Direct quenched to 500°C.

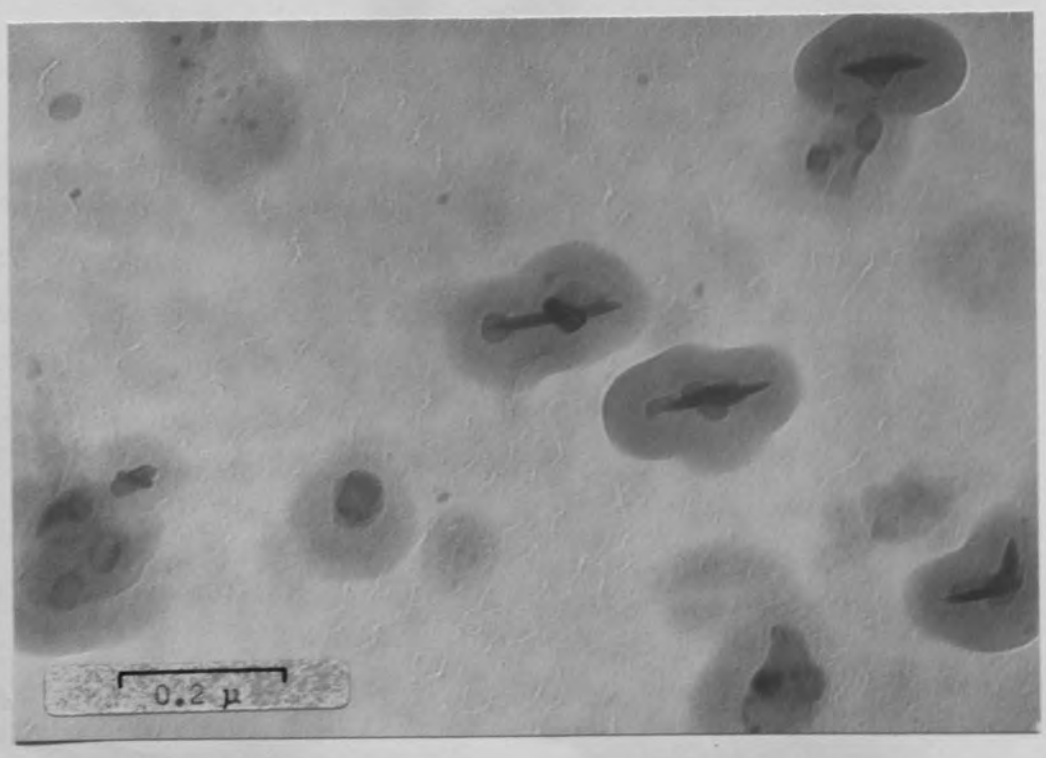

Fig.7.25 Extraction replica of material direct quenched to 500°C.

is incoherent, disc shaped, and is growing on the {111} planes in the copper matrix. The chromium particles are absent from the matrix, and are only found within those regions of the crystal traversed by the stacking fault. By tilting the foil such that the fringe contrast disappears from the stacking fault bands, the chromium within the faults can be clearly observed as in Fig.7.24 direct quenched to 500°C. Occasionally, some chromium particles are found in association with the Cu_3Zr precipitate, and are either nucleated by dislocation loops shrugged off by the growing disc shaped precipitate as at A in Fig.7.24, or at the edges of the matrix precipitate as shown in Fig.7.25 which is an extraction replica taken from a specimen direct quenched to 500°C. However, it is pertinent to note from these direct quenching experiments, that the chromium does not nucleate homogeneously within the matrix.

7.3.2 Grain Boundary Regions

The structures developed near grain boundary regions in this alloy closely follow those generated in copper zirconium and described in section 5.2.4. A precipitate enhanced region develops parallel to grain boundaries in the early stages of ageing before stacking faults begin to grow. Precipitation within these regions leads to a rapid impoverishment of the zirconium solute atoms and subsequently restricts the growth of stacking

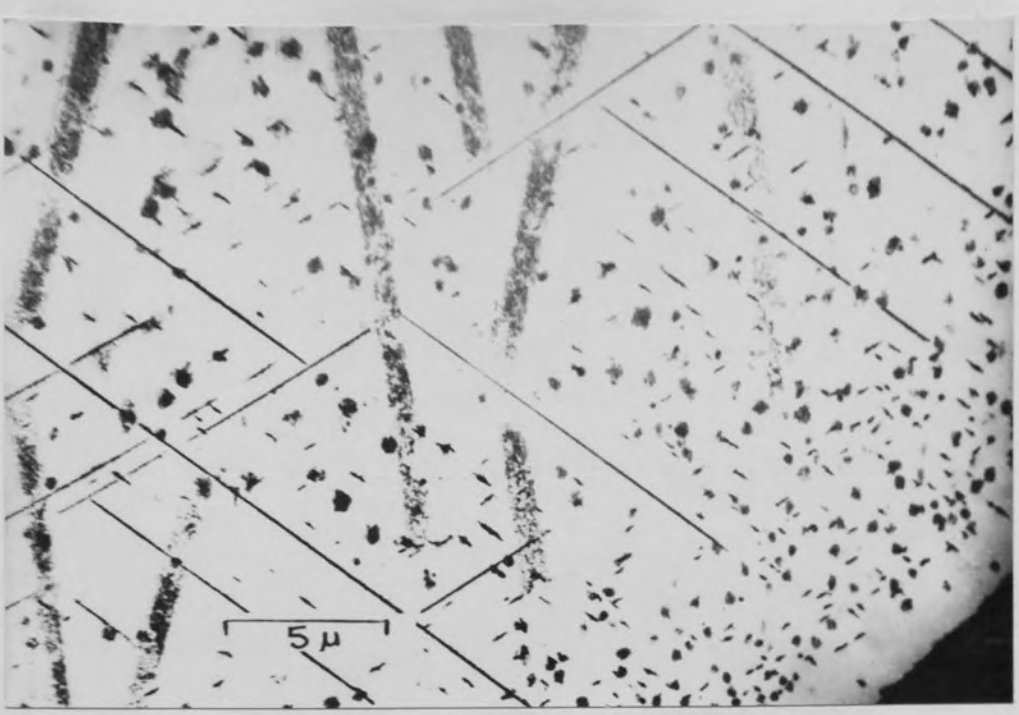

Fig.7.26 Grain boundary regions in material direct quenched to 500°C.

Fig.7.27 As Fig.7.26.

faults into such regions as shown in Fig.7.26 direct quenched to 500°C. The number of nucleation sites within the centre of the grain may be compared with those in the precipitate enhanced band for the Cu_3Zr precipitate from such micrographs, by counting the number of precipitates per unit volume in each region. A ratio of 5 : 1 is obtained in favour of the precipitate band near the grain boundaries. Consequently, in alloys direct quenched to the lower temperatures of 425°- 470°C, or room temperature quenched and aged, the band is not immediately apparent since the precipitation of Cu_3Zr is very much finer in these cases than when the alloy is quenched to 500°C e.g. Fig.7.19.

As well as a region of precipitate enhancement the alloy some 3 - 5u wide, also exhibits a precipitate free zone (P.F.Z.) on either side of the grain boundaries as shown in Fig.7.27. The P.F.Z. extends for 1 micron on either side of the grain boundary, and cannot be wholly attributed to vacancy depletion because the large amount of zirconium bearing precipitate within the grain boundaries is expected to produce a solute depleted region adjacent to the boundary.

The presence of the precipitate enhanced region in the direct quenched material indicates that the grain boundaries are not acting as vacancy sources, since no excess vacancies are present to pump back into the grain interior under the action of a concentration gradient after

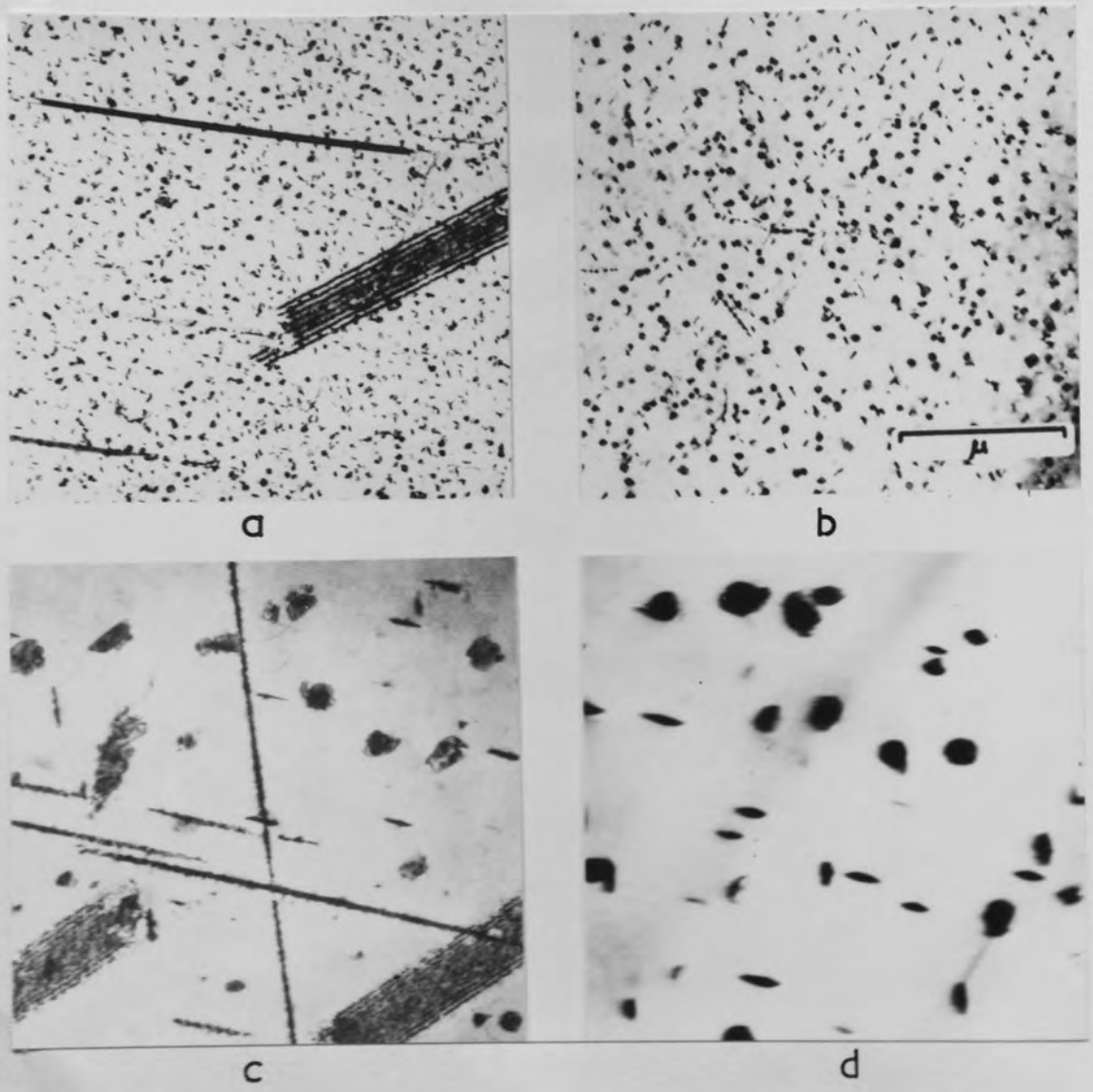

Fig.7.28 (a) Cu-0.2Cr-0.2Zr direct quenched to 425°C.
(b) Cu-0.24Zr direct quenched to 425°C.
(c) Cu-0.2Cr-0.2Zr direct quenched to 500°C.
(d) Cu-0.24Zr direct quenched to 500°C.

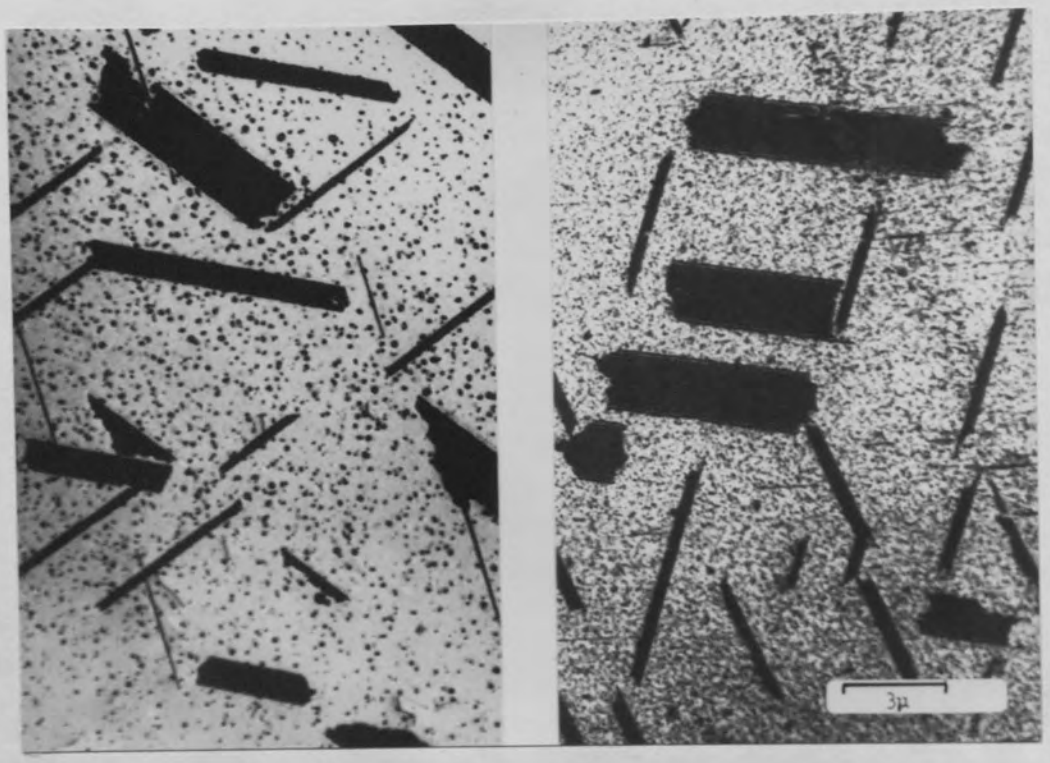

(a) (b)

Fig.7.29 (a) Cu-0.24Zr) direct quenched to 450°C
(b) Cu-0.2Cr-0.2Zr)

such heat treatment cycles.

It is instructive to consider at this point the similarities which exist between the structures of the direct quenched alloy and those developed in copper zirconium given similar treatments.

7.3.3 Cu-Zr v Cu - 0.2Cr - 0.2Zr

The composite micrograph shown in Fig.7.28 illustrates that, given the same heat treatment cycle, the matrix precipitate of Cu_3Zr is substanially the same in terms of precipitate size and dispersion for both materials. The temperature at which the Cu_3Zr begins to coarsen rapidly in the copper zirconium alloy is lower than that in the ternary, and this difference for the alloys direct quenched to 450°C is illustrated by Fig.7.29. Both materials, when direct quenched to this ageing temperature generate similar stacking fault densities and mean lengths in the microstructure, and the presence of chromium in the ternary seemingly has no affect on the rate of fault growth nor on the maximum fault length achieved. It can be concluded, therefore, that the presence of stacking faults in the ternary alloy is a function of the presence of zirconium in the material. On this basis, the behaviour of faults in regions close to grain boundaries in both alloys can be rationalized in terms of the rapid rejection of zirconium from solid solution as Cu_3Zr which occurs in these regions.

In an attempt to correlate the presence of zirconium in the solution treated alloys with the subsequent growth of stacking faults on ageing, the materials were solution treated, cold rolled 95% and then examined using the X-ray transmission method suggested by Dillamore et.al.[61] and discussed in section 3.7.3.

7.4 X-ray analysis of solution treated alloys

The textures expected on heavily cold rolling the solution treated copper based alloys have been described in section 3.7.3 and attempts were made to investigate the relationship of the intensity of $\{111\}$ poles at the direction transverse to the rolling direction with that at 20° to the rolling direction. The results obtained gave ratios of $I_{td}/I_{20^{\circ}}$ which were almost identical from alloy to alloy but which could not be used to give a sensible value of stacking fault energy using the established dependence of this ratio on fault energy described in Fig.3.13. Roberts[71] has suggested that this method of estimating stacking fault energy from deformation textures is particularly sensitive to instrumental conditions, and that the figures given in their paper may only apply to their particular instrumental settings. Furthermore, intensity measurements obtained from transmission methods of X-ray analysis are often unreliable due to the stringent requirements placed upon the variation of specimen thickness.

An experiment involving a similar principle was performed in the hope of deriving at least a qualitative indication of the variations of stacking fault energy thought to exist in the four alloys studied. This involved subjecting the solution treated alloys to deformations of 95% by cold rolling and then re-solution treating the materials. It has already been demonstrated in Chapter 4 that such treatments promote the formation of a strong cube texture in copper chromium, and therefore each of the alloys was examined by a standard reflection technique to assess the resistance to cube texture formation since this is formed from a pure metal deformation texture by a rotation of 30° about the $\{111\}$ poles.

The results, together with those for a pure copper sample are presented in Figs.7.30 - 7.34 inclusive and show that Cu-Cr, Cu-Zr and pure copper develop equally strong "cube-textures" after such mechanical and thermal treatments, whilst the two ternary alloys show less tendency to develop this texture. A Cu-2%Al sample was also included in the experiment, but showed no sign of "cube-texture"; this is to be expected since the stacking fault energy of this material[72] has been reported as 18 ergs.cms^{-2} and therefore the "alloy-texture" will be formed on cold rolling.

From these results, the difference in <u>macro</u> stacking fault energy between the binary materials Cu-Cr

Figs.7.30 - 7.34

(111) Pole intensity examined in the range $45^{o} \rightarrow 65^{o}$ to the rolling plane.

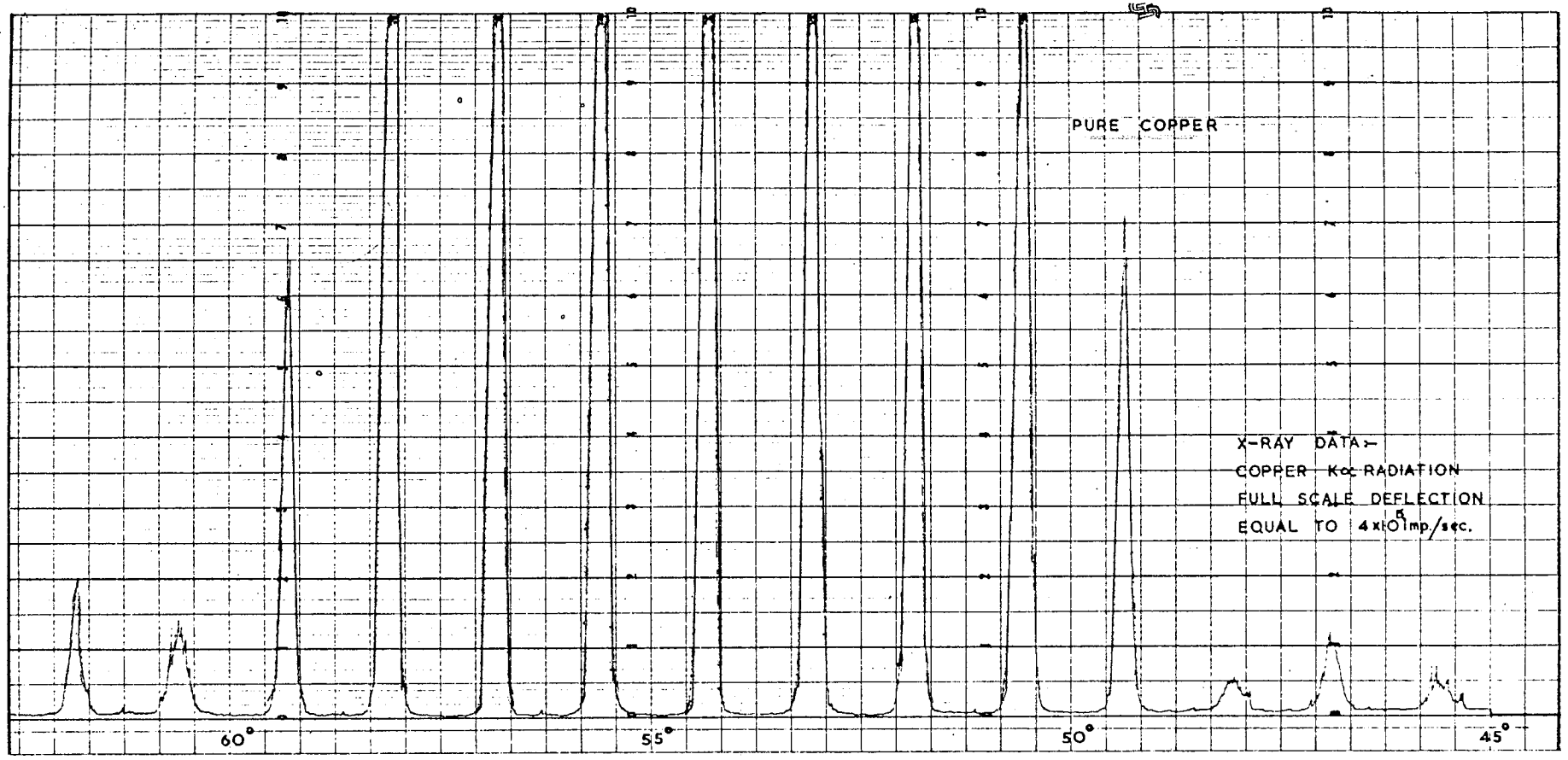
PURE COPPER
X-RAY DATA:-
COPPER Kα RADIATION
FULL SCALE DEFLECTION
EQUAL TO 4x10⁵ imp/sec.
60°
55°
50°
45°

Fig. 7.30

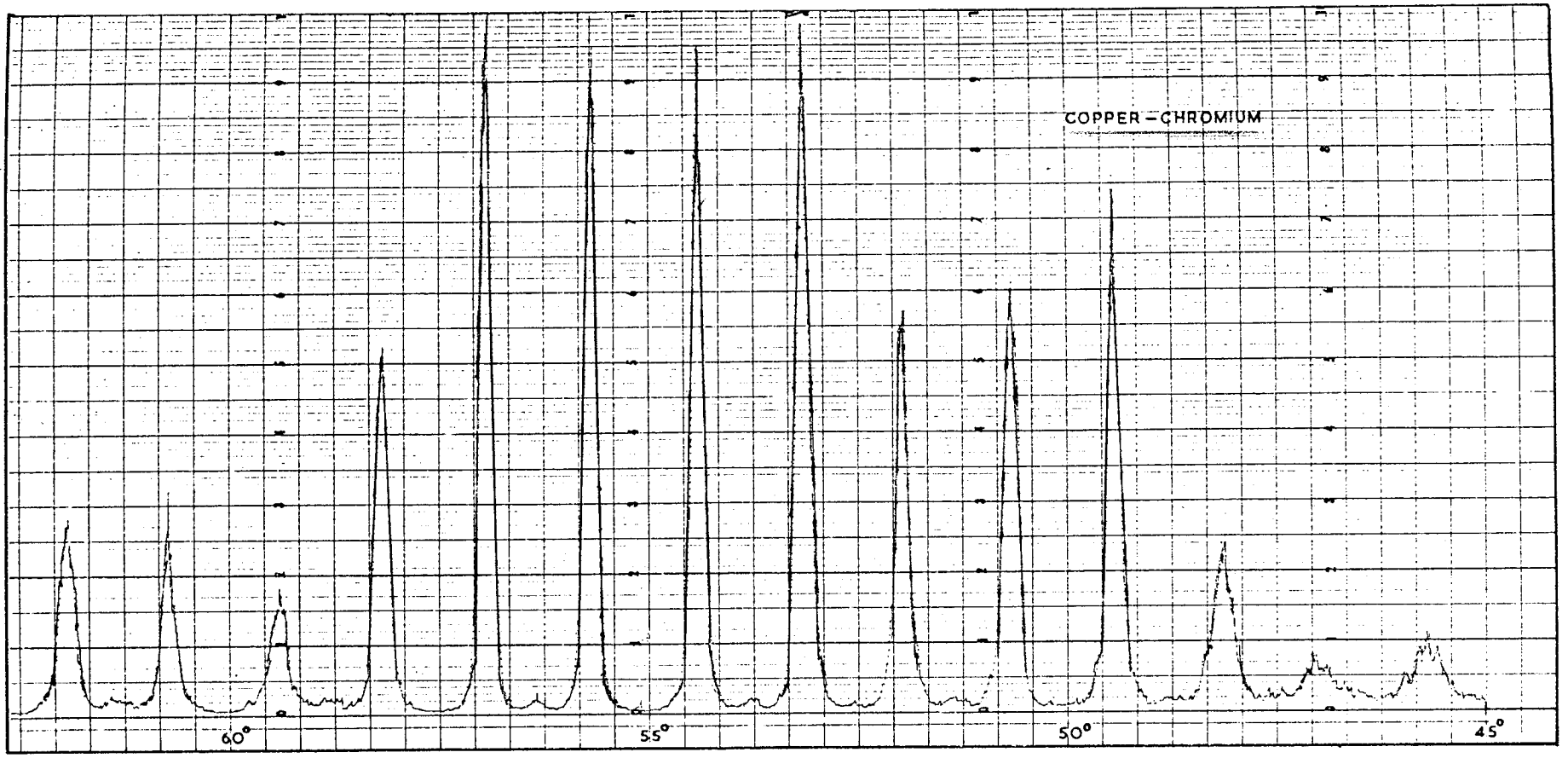

Fig. 7.31

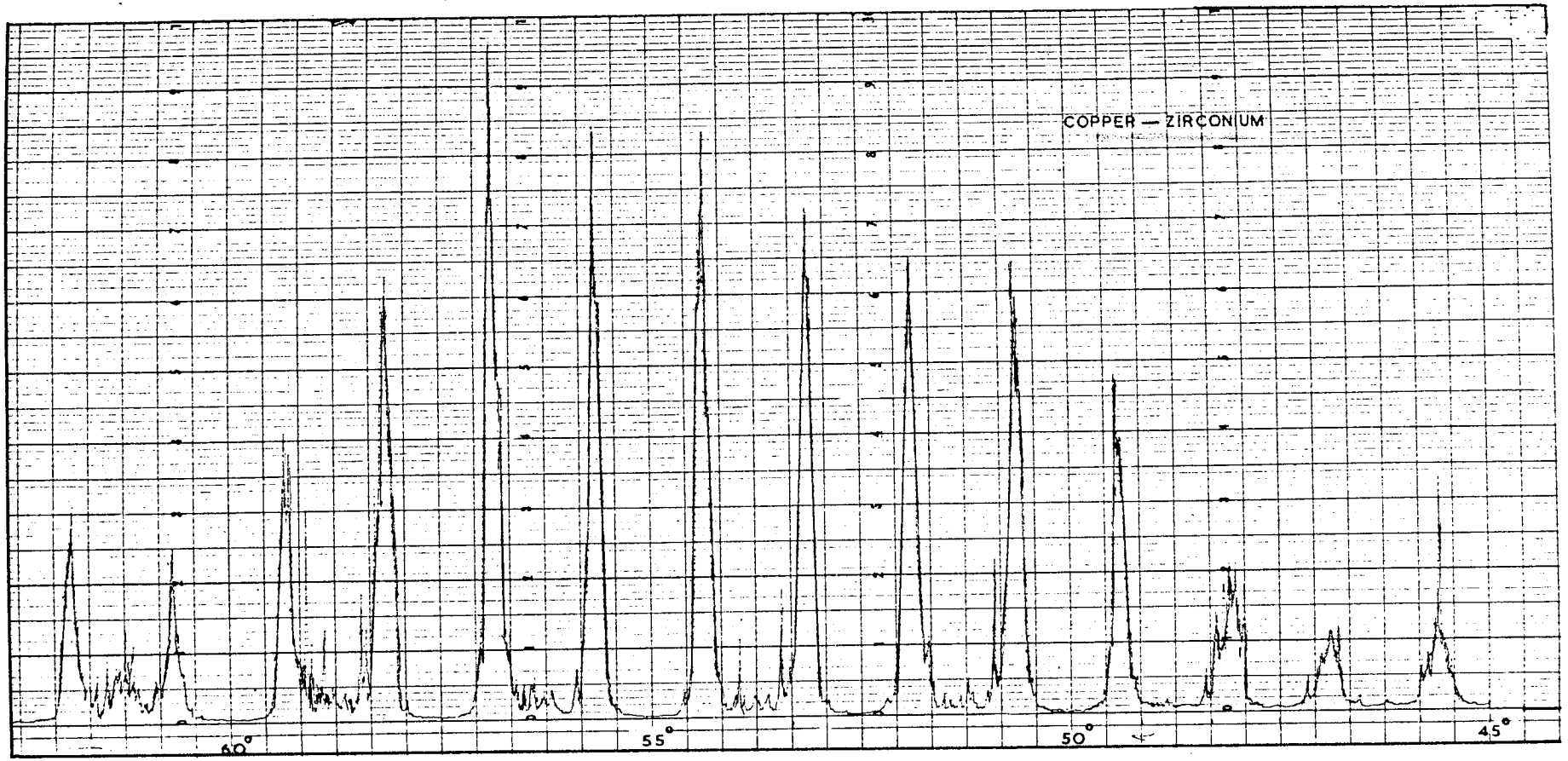

Fig. 7.32

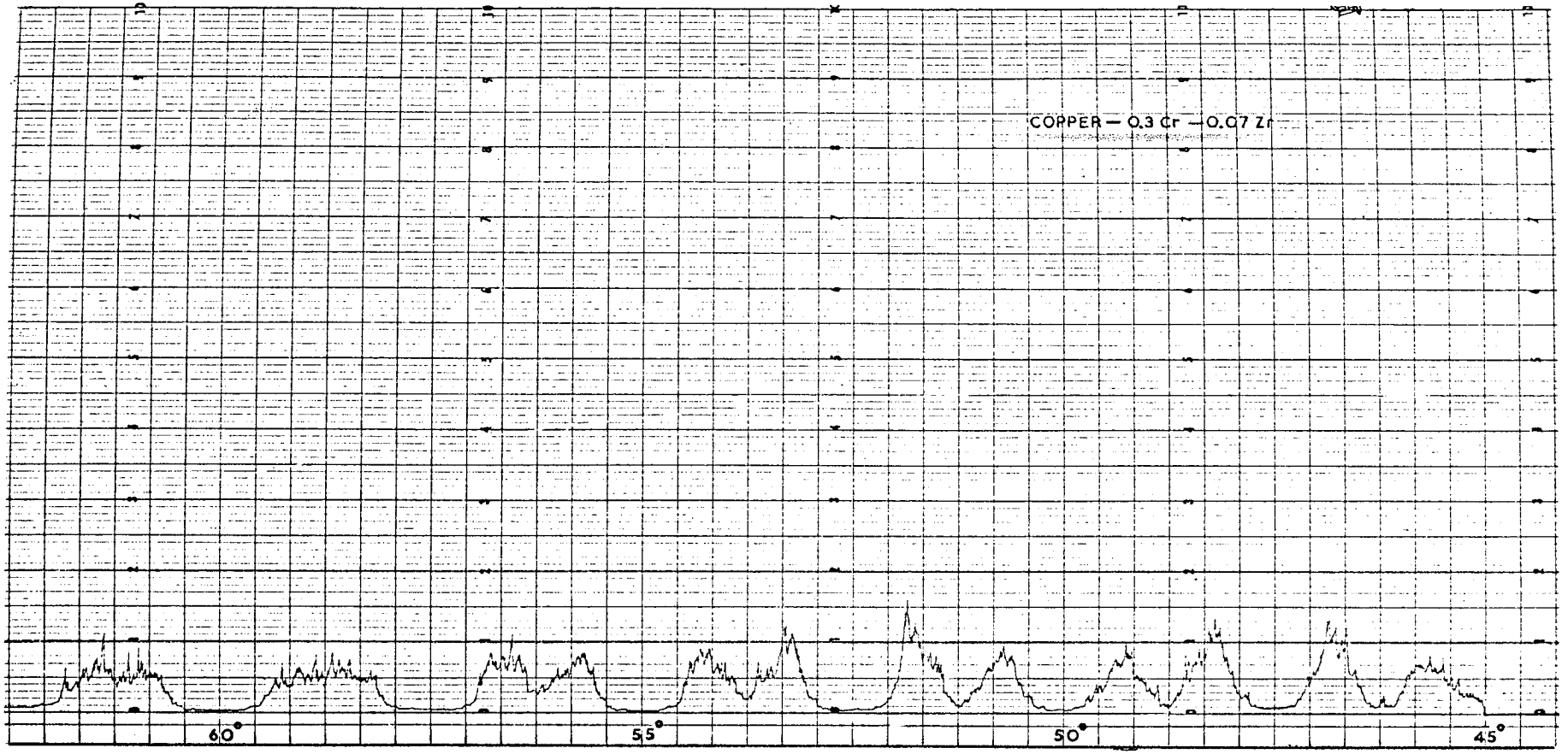

Fig. 7.33

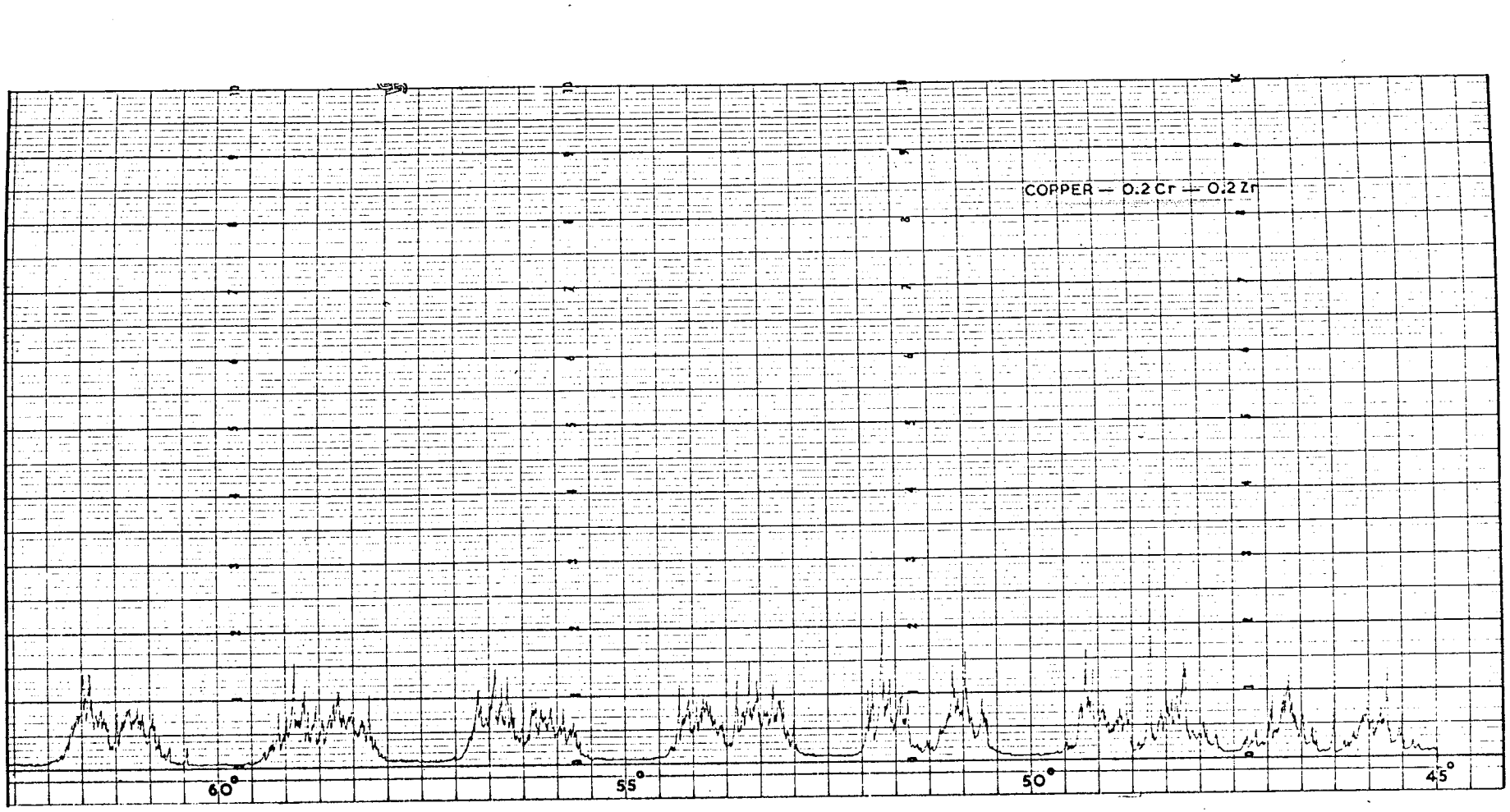

Fig. 7.34

and Cu-Zr, and that of pure copper, appears insignificant and thus the nucleation and subsequent growth of faults in Cu-Zr and not in Cu-Cr during ageing suggests that a low stacking fault energy solid solution is not a necessary pre-requisite for stacking fault growth during ageing of these materials, unlike the case for austenitic stainless steels. A similar analysis can be applied to the two ternary alloys and therefore the formation of stacking faults on ageing zirconium rich alloys can only be readily explained on the basis of the formation of a Cottrell type "atmosphere" of zirconium atoms at dislocations. Such dislocations will be expected to dissociate due to the localised lowering of the stacking fault energy at the dislocation core, thereby creating a layer of C.P.H. crystal in the copper matrix. It follows that zirconium atoms should continue to migrate to these regions as suggested by Suzuki[45] since zirconium has a C.P.H. crystal structure. However, the continued growth of stacking faults in these alloys to the lengths observed, and the observation that a large number of the total dislocations present remain undissociated during ageing indicate that this mechanism may only be important during the very early stages of transformation.

7.5. Mechanical Properties

The mechanical properties obtained from the alloy

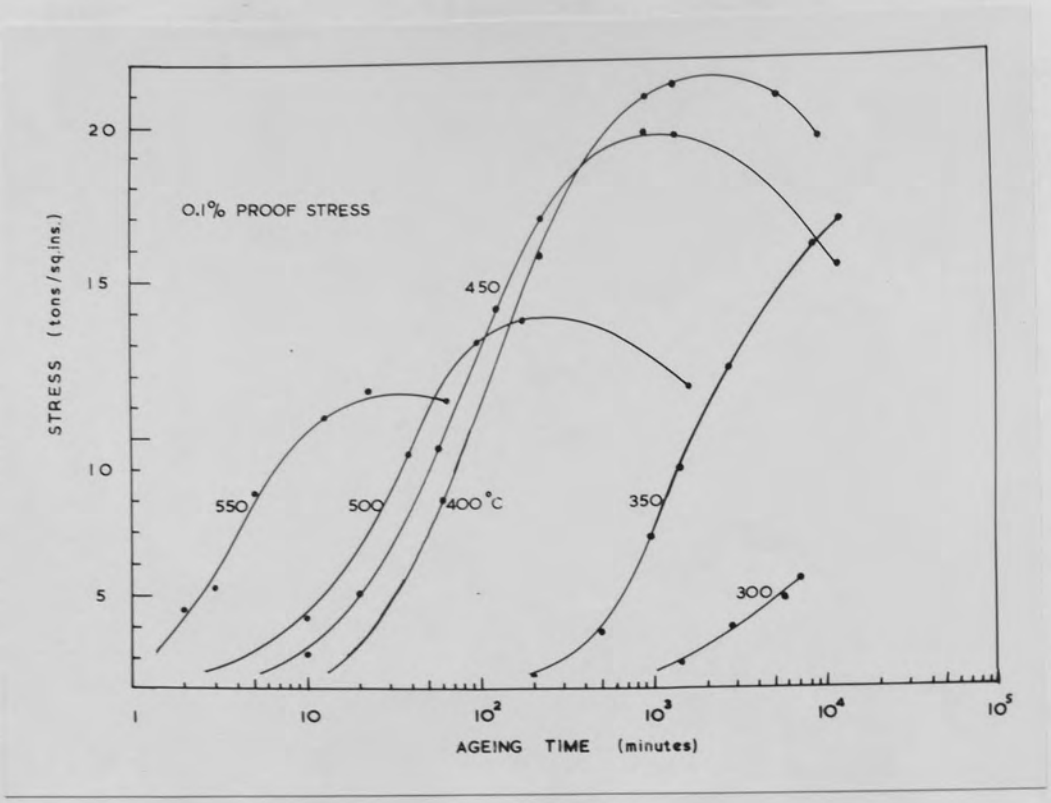

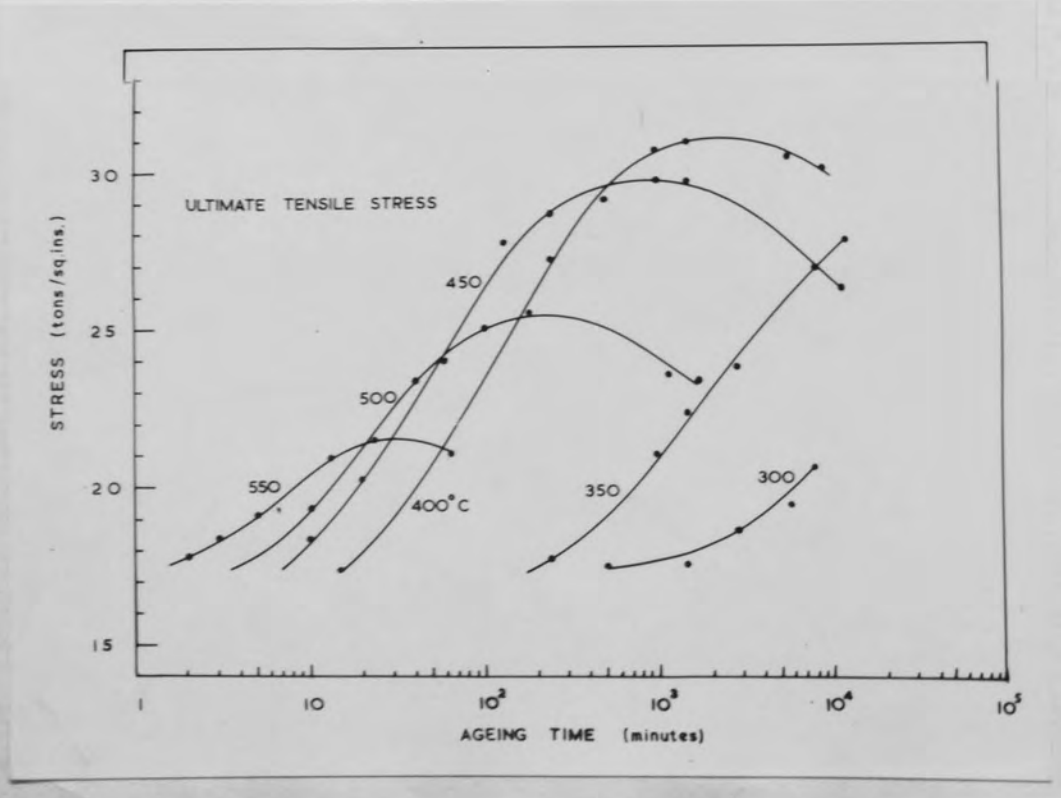

Fig.7.35 Mechanical Test results from isothermally aged materials.

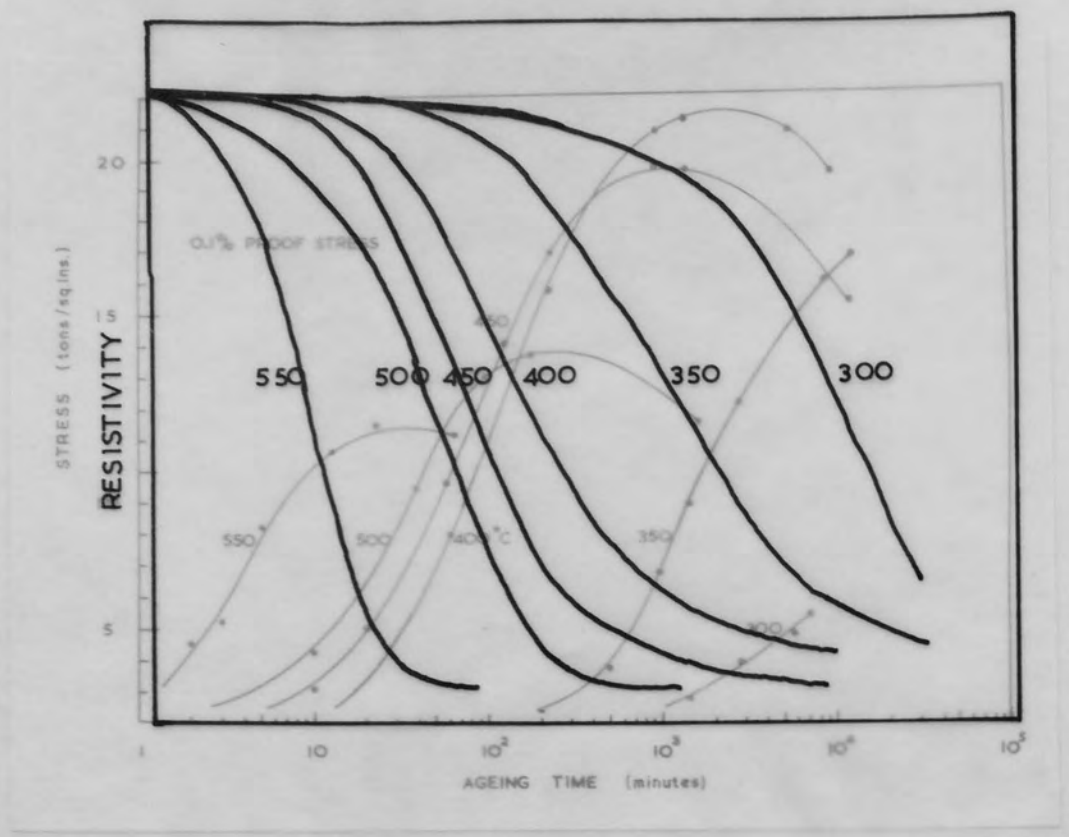

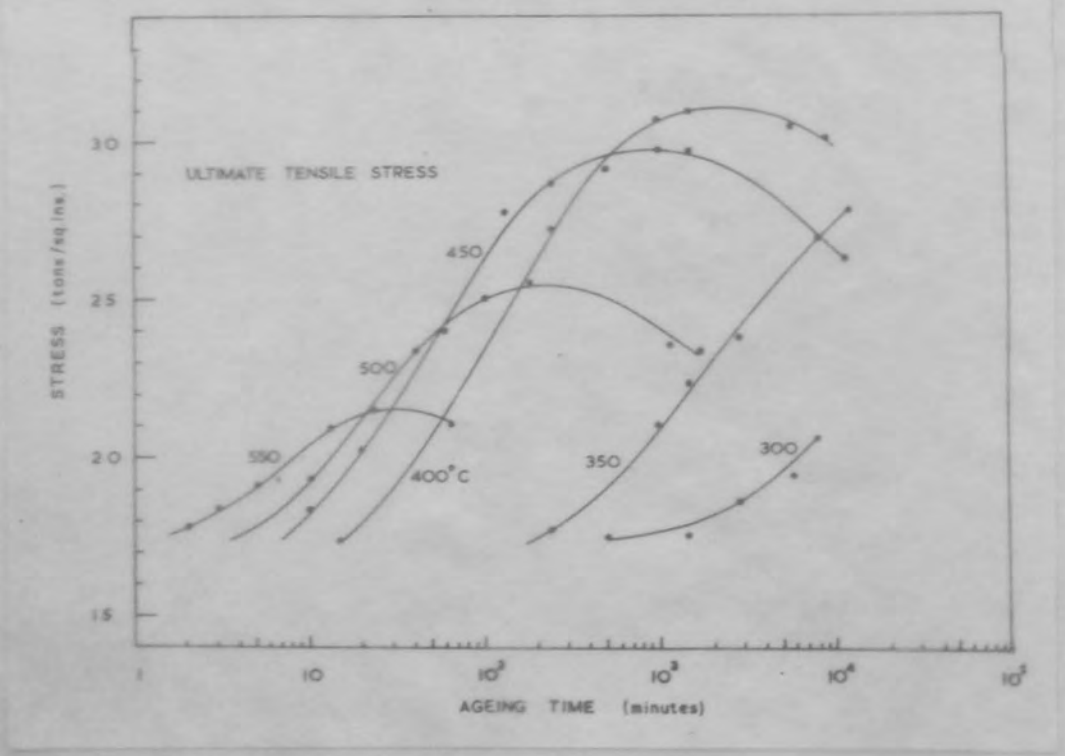

Fig.7.35 Mechanical Test results from isothermally aged materials.

aged within the temperature range 300°-550°C are given in Fig.7.35. The peak values of 0.1% proof stress and U.T.S. were attained on ageing at 450°C for periods in excess of one day, and represent the highest properties developed in the alloys studied. The 0.1% proof stress peak value of 21.4 tons/sq.ins.is equivalent to 7.4×10^{-3}G and is a considerable improvement over copper chromium which for the same alloy content of 0.4% gives a peak 0.1%proof stress of 17.4 tons/sq.ins. When aged to give maximum strength at 450°C, the modulus of elasticity of the alloy was 22×10^{6}lbs/sq.ins.

As with previous alloys, maximum strengthening occurred at a given ageing temperature when the alloy was aged for times which allowed the complete transformation of the supersaturated solid solution, as indicated by resistivity measurements.

7.6 Concluding Summary

The resistivity data has been interpreted in a similar manner to that used for the copper zirconium alloy and is found to faithfully indicate the ageing temperature at which stacking faults become an important nucleation source. The Avrami plot of the data does not allow a rigourous analysis of the controlling mechanisms of transformation occurring in this alloy due to the presence of chromium particles and Cu_3Zr precipitates in the aged alloy.

Below 400°C, the structure of the aged alloy is similar to that expected from the formation of G.P. zones containing zirconium and chromium, whereas stacking faults containing chromium particles are present in alloys aged above 400°C. Detailed analysis of the faults shows that their presence is a function of the zirconium content of the material, and that the extrinsic mode of faulting is preferred. The faults form by the dissociation of a glissile, $\frac{1}{2}a\langle 110\rangle$ type dislocation into two Shockley partial dislocations, and appear to nucleate from intersecting dislocation lines. Direct quenching experiments have been performed and the structures obtained compared with those gained from the Cu-Zr alloy given similar heat treatments, to show that the chromium particles have little influence on the formation of the faulted structure and subsequent fault growth. Direct quenching the alloy also prevents chromium from nucleating homogeneously within the matrix.

X-ray analysis of all four alloys has indicated that in the solution treated condition, the value of stacking fault energy is likely to be similar to that of copper at 70 ergs.cms.$^{-2}$, and therefore, a low stacking fault energy matrix is not a necessary pre-requisite for stacking fault growth during ageing. The early stages of fault formation may, however, be assisted by zirconium segregation to lattice imperfections.

CHAPTER 8.

DISCUSSION

DISCUSSION

8.1 Introduction

In this chapter, an attempt is made to collate the wide variety of data abstracted from the series of alloys investigated and to discuss jointly the prominent features exhibited by the alloys.

8.2 Homogeneous Nucleation of Chromium

The breakdown of the solid solution in the binary system copper chromium has been predicted by resistivity data, and shown experimentally by electron metallography, to proceed via the simple, single stage precipitation of B.C.C. chromium particles in the copper matrix. The maintainance of coherency between particle and matrix at high ageing temperatures and after prolonged ageing times is explained on the basis of the low misfit the particles have with the matrix when arranged in a Kurdjemov-Sachs type crystallographic orientation relationship. Using this data, the retention of high mechanical properties by the alloy over a wide range of ageing temperatures can be explained on the basis that it is geometrically possible for dislocations to be forced to cut through the coherent chromium particles since the close packed planes and directions of the F.C.C. matrix and B.C.C. particle are parallel. The shear modulus of

chromium is 8.8 x 10^{11} dynes.cms^{-2} which is twice that of the soft copper matrix, and since the particles grow along the slip directions in the aged alloy, then the mean free path for dislocation movement between particles is small.

Quenching of the solution treated alloy to room temperature prior to ageing ensures that copious homogeneous nucleation of chromium occurs, whereas direct quenching to the ageing temperature tends to reduce the number of active nuclei for homogeneous nucleation and promotes precipitation on dislocations. Where dislocation networks are present, the chromium is found to decorate only alternate nodes, and it is suggested that these are the extended nodes.

The addition of 0.07% zirconium to copper chromium gives rise to similar microstructures, although the rates at which these structures are attained are slower by a factor of ten. Once underway, however, the precipitation reactions occur with similar values of the empirical activation energy to copper chromium. Direct quenching the ternary Cu-0.3%Cr-0.07%Zr hinders the homogeneous nucleation of chromium in the copper matrix even further and suggests that zirconium atoms have the same effect on the kinetics of chromium precipitation as do vacancies. However, a more detailed analysis of the kinetic data for the ternary alloy suggests that zirconium atoms may also be active in slowing down the growth of the chromium

particles by modifying the precipitate-matrix interface.

When the zirconium content is increased to 0.2% as in the ternary Cu-0.2%Cr-0.2%Zr, the proportion of homogeneously nucleated chromium becomes less, and by direct quenching the alloy to the ageing temperature, all of the chromium present in the alloy is nucleated hetrogeneously at the partial dislocations bounding expanding stacking faults.

Thus, the difficulty of homogeneously nucleating chromium in these three alloys can be related to both zirconium content and to heat treatment variables. Written schematically, the fraction of homogeneously nucleated chromium in the alloy structures decreases in the following order:-

ALLOY	HEAT TREATMENT	CHROMIUM NUCLEATION
Cu-Cr	C.A.	Copious homogeneous nucleation
(Cu-Cr) (Cu-0.3%Cr-0.07%Zr)	D.Q. C.A.	
Cu-0.3%Cr-0.07%Zr	D.Q.	
Cu-0.2%Cr-0.2%Zr	C.A.	
Cu-0.2%Cr-0.2%Zr	D.Q.	Hetrogeneous; only on stacking faults

(C.A.) - Conventially aged.

(D.Q.) - Direct quenched to the ageing temperature.

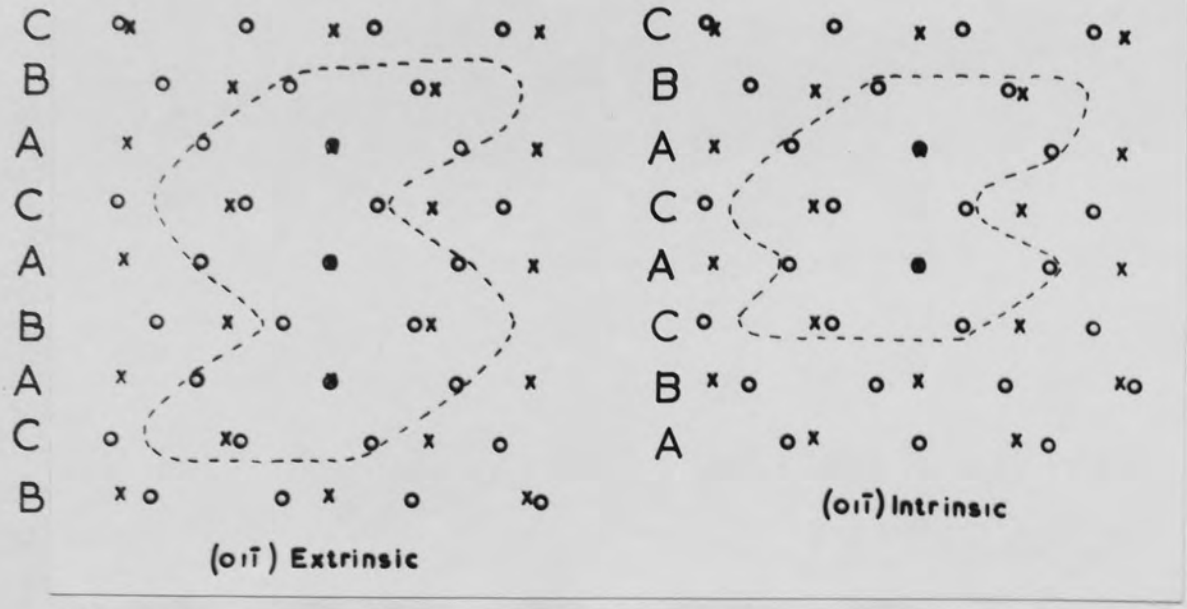

Fig.8.1 Area of "good-fit" between chromium and copper atoms described on the (01$\bar{1}$) plane for a faulted matrix.

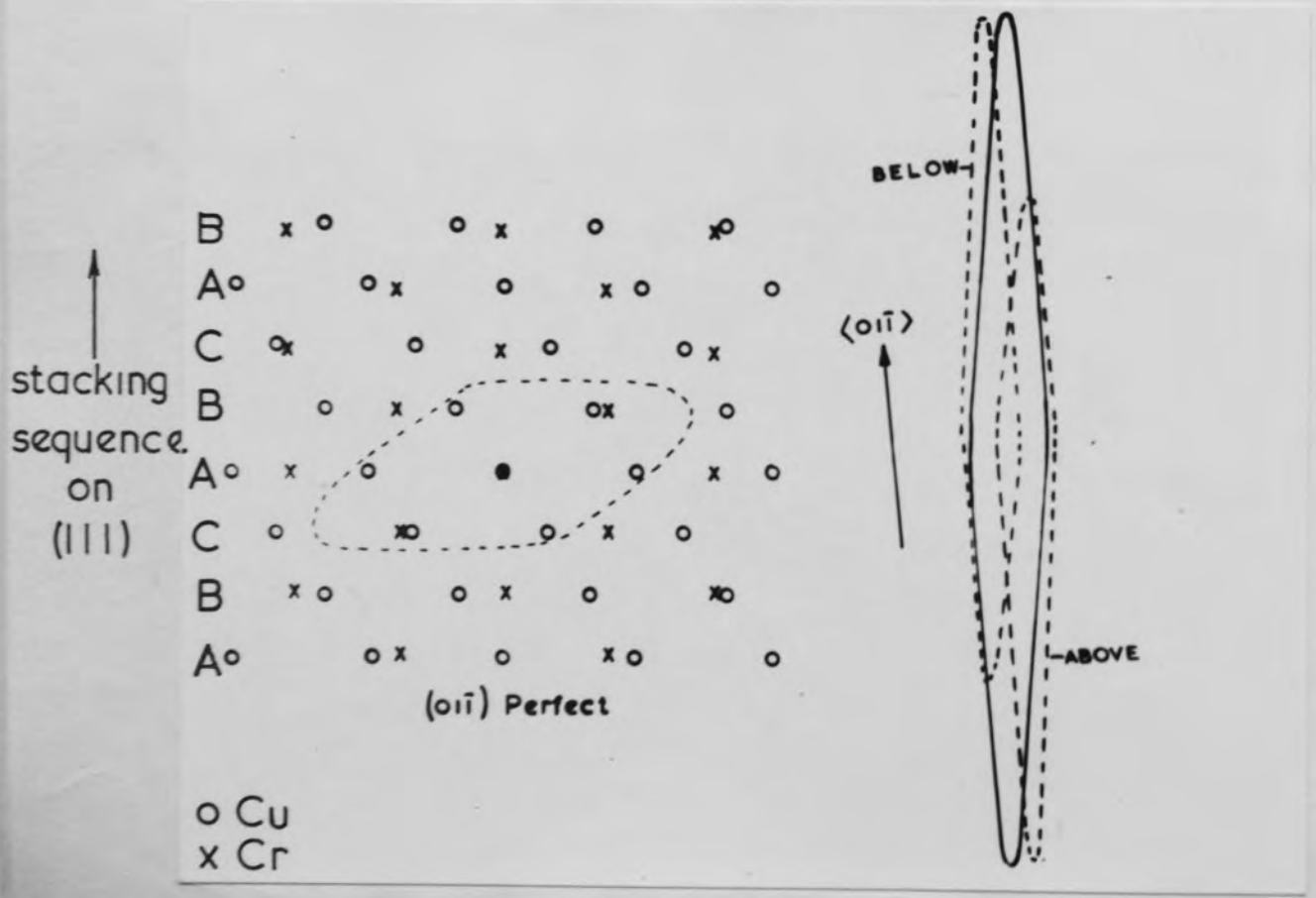

Fig.4.21 (Repeat)

8.3 Hetrogeneous Nucleation of Chromium

Selected area diffraction patterns from faulted regions in the aged ternary alloy Cu--0.2%Cr-0.2%Zr show that the chromium present within the faults maintains a Kurdjemov-Sachs orientation relationship with the matrix. Therefore, a similar analysis to that described in section 4.3.2 where the lattice positions occupied by the copper atoms are noted with respect to those occupied by chromium atoms when this orientation relationship is obeyed, may be performed to explain the presence of chromium in faulted regions of the matrix.

Using the same criterion for delineating the regions of "good fit" on the $(0\bar{1}1)$ plane of the copper lattice, i.e. where the matrix atoms lie within $d/3$ of the corresponding chromium atoms, the numbers of matrix atoms have been computed for the case of the perfect crystal, the crystal containing an intrinsic fault, and when the crystal contains an extrinsic fault. A two-dimensional representation of the increased number of atom sites made available in faulted regions of the copper matrix is shown in Fig.8.1, and Fig.4.21 is reproduced to afford comparison with the unfaulted matrix. Numerically, the atomic lattice sites within the volume of "good fit" are 338, 578 and 818 for perfect, intrinsic faulted and extrinsic faulted crystal respectively. The ratios of these numbers of atoms remained almost constant when the

proximity of the chromium atoms to copper atoms was taken as $d/6$ of the spacing between matrix atoms for "good fit" viz:-

For $d/3$	Extrinsic/Perfect Crystal	2.40/1
For $d/6$	Extrinsic/Perfect Crystal	2.43/1

8.4 Precipitation at Stacking Faults

8.4.1 Formation of Faults

The introduction of stacking faults in the aged structure of Cu-Zr and Cu-0.2%Cr-0.2%Zr is attended by an approximate reduction of 50% in the empirical activation energy for transformation in each system, and consequently the transformation rate is reduced to allow the partial dislocations bounding the faults to grow out into the matrix thereby providing mobile nucleation sources. The partial dislcoations bounding the faults in both alloys are Shockley partial dislocations of the type $1/6\langle 112\rangle$ and form by the dissociation of a glissile dislocation of the type $\frac{1}{2}\langle 110\rangle$ on the $\{111\}$ planes of the copper matrix. The equilibrium width to which the partial dislocations separate in a material is related to the stacking fault energy and for pure copper is approximately 25A°. X-ray analysis suggests that the stacking fault energy of the solution treated alloys is not appreciably different from that of pure copper, and so it is expected that the

dislocations present in these alloys are dissociated to similar widths. On ageing, the dislocation content of the alloys increases, possibly due to the relaxation of quenching strains, and faults are only observed to grow from suitably orientated dislocations. The increased separation of the partial dislocations to form stacking fault ribbons requires the segregation of solute to these regions in the manner suggested by Cottrell[46]. Zirconium may be expected to migrate to such regions and form solute rich atmospheres around dislocations in order to reduce the total elastic strain energy of the system, since it has a large misfit (23%) in the copper matrix. In doing so, a layer of C.P.H. crystal will be formed which should enhance the diffusion of zirconium to such areas since zirconium atoms form in a close packed hexagonal array with an axial ratio $c/a = 1.593$, i.e. close to the theoretical value of 1.63 for a faulted F.C.C. structure. The fact that stacking faults only begin forming rapidly at the ageing temperaturs at which the Cu_3Zr precipitate becomes incoherent suggests that zirconium rich clusters may be present in the early stages of ageing due to the increased critical nucleus size required for the nucleation of incoherent precipitates as opposed to coherent precipitates. The nucleation difficulties can be reduced by the provision of mobile hetrogeneous nucleation centres in the form of expanding stacking faults. A lowering of the

activation energy for transformation is therefore expected when stacking faults begin to grow into the matrix during ageing.

8.4.2 Fault Type

The fact that extrinsic faulting in low stacking fault energy F.C.C. materials is not often observed has been attributed to the difficulty of nucleating the correct partial dislocations necessary to bound such faults. Two Shockley partial dislocations are required on adjoining planes at either end of the fault, and thus four partial dislocations have to be nucleated for extrinsic faults in comparison to two for the formation of the more commonly observed intrinsic stacking faults. Lorretto[73], and more recently Goodhew[70] have shown that the energy of an extrinsic fault is close to that of an intrinsic fault. A typical value of the intrinsic fault energy, γ_{Int}, in copper is given by Goodhew[70] as 75 ergs.cms^{-2} and it is suggested that the extrinsic fault energy, γ_{Ext}, has a value between 75 and 100 ergs.cms^{-2}.

The presence of Cu_3Zr in the faults grown in the copper zirconium alloy cannot be explained in detail until more information regarding the crystal structure and lattice parameters of the compound are know. However, the preferential formation of extrinsic faulting in the aged alloy may indicate that the core of the double Shockley partial bounding such faults is a more effective region

for the pipe diffusion of zirconium along the fault than the single core of the Shockley bounding an intrinsic fault. The presence of chromium in the faults grown in the ternary alloy may be explained in terms of the crystallography of atoms in faulted regions of the matrix as shown in section 8.3. The observed ratio of extrinsic to intrinsic faulting of 7:1 in the ternary alloy is in excellent qualitative agreement with the preferential nucleation site model.

8.4.3. Fault Growth

In the ternary alloy Cu-0.2%Cr-0.2%Zr, the homogeneous nucleation of chromium is difficult, and by direct quenching, all of the chromium can be caused to precipitate hetrogeneously at stacking faults. The presence of chromium in faults has been shown to be favoured due to the closer crystallographic fit between faulted matrix and B.C.C. precipitate when in a Kurdjemov-Sachs orientation relationship and therefore, the driving force for the expansion of the fault can be provided by the energetics of precipitate formation. Thus even though the faults can grow to lengths of up to 20 microns, this does not imply that the alloy would exhibit any of the characteristics normally associated with a low-stacking-fault energy material, and indeed, many undissociated dislocations are found in materials containing high densities of stacking faults. When the alloy is direct quenched to the higher ageing temperatures, the supersaturation of

chromium and vacancies is presumbaly too low to allow the homogeneous nucleation of chromium and therefore the faults must nucleate all of the chromium in the alloy thereby requiring that they grow to the observed lengths. The continued expansion of stacking faults into a matrix which is continuously being depleted of solute and hence is increasing its stacking fault energy apports the favourable nucleation site model for chromium, and explains the prevalence of extrinsic faulting.

Stacking fault growth is not required when the alloys are aged at low temperatures where supersaturation effects due to vacancies and solute are sufficient to allow the majority of the transformation to occur homogeneously, nor is it required at very high ageing temperatures since diffusion rates are high and nuclei form rapidly throughout the matrix even though solute and vacancy supersaturation effects are low. This behaviour is well illustrated by the empirical activation energy plots, where the onset of stacking fault growth is indicated at 400°C for Cu-0.2%Cr-0.2%Zr and 450°C for Cu-Zr. Below these temperatures, the wholly homogeneous nature of the transformations occuring in these alloys is reflected in the increased activation energy for the process.

8.4.4 Critical Ageing Temperatures

The metallographic similarities between niobium stabilized austenitic stainless steel and the two alloys

discussed above can be extended to include considerations of the critical ageing temperatures at which stacking fault precipitation is first observed in each system. Van Aswegan et.al.[48] first report the incidence of stacking fault growth in an 18Cr/10Ni/1Nb steel at 700°C which is equivalent to $0.55T_M$ where T_M is the melting point of the alloy in °K. For Cu-Zr, stacking faults first appear at 450°C $\equiv 0.535T_M$ and for Cu-0.2%Cr-0.2%Zr at $0.505T_M$. Moreover, tempering the steels at 850°C produces structures similar to those observed in the copper alloys when aged at 600°C i.e. precipitation predominantly on undissociated dislocations. These temperatures are also equivalent at $0.635T_M$ and $0.644T_M$ respectively and suggest that the diffusivity of the matrix with respect to the alloying elements required to form the precipitates is similar for both systems.

8.4.5 Removal of Fault Contrast

The removal of stacking fault fringes by the creation of unfaulted crystal occurs when ageing is continued beyond the recovery of maximum electrical conductivity or sometimes earlier when faults are intersected by other faults, dislocations large precipitates, or simply by the thinned foil surface. A characteristic feature of the microstructure at this stage is that islands of perfect crystal are present within the faults indicating that the fault has been cleared by the nucleation

of another partial dislocation and not by the re-association of the original glissile Shockley partials (For example see Figs.5.13, 5.14, 5.15, 7.8, 7.21 and 7.29). It is unlikely that the faults are removed by the re-association of the original partials since their path is effectively blocked by the large numbers of particles nucleated along the slip plane in their wake. The removal of the fault therefore takes place by the growth and coalescence of islands of perfect crystal. It is pertinent to note that large numbers of islands can be created either from dislocation reactions ensuing from the intersection of the fault with the Cu_3Zr precipitate which grows as discs on the $\{111\}$ planes of the copper, and during its growth becomes incoherent, or from the growth of precipitate within the faults. The dislocation reactions are expected to be similar to those used by Smallman and co-workers[74] to explain the removal of stacking fault from quenched in vacancy loops in aluminium. The nucleation of a Shockley partial dislocation at the edge of the vacancy loop grows and converts the faulted loop into a region of perfect crystal bounded by a dislocation loop. The energy changes involved in such reactions have been extensively studied from loop shrinkage experiments, and it is possible using relationships such as those quoted by Goodhew, Dobson and Smallman[70] to calculate the size of the island of perfect crystal which

would need to be formed in order to continue to grow and convert the faults observed in these alloys into perfect crystal. The calculation involves the knowledge that the total energy of a faulted loop, E, equal to the self energy of the dislocation loop bounding the faulted region, E_S, and the energy due to the fault is given by:-

$$E = E_S + \pi r^2 \gamma$$

It follows that when the energy due to the area of the fault increases beyond that of the self energy of the dislocation loop, then the fault will be removed i.e. we wish to calculate the value of r when

$$\pi r^2 \gamma = E_S \quad .. \quad .. \quad (1)$$

According to Goodhew et.al[70], a currently accepted value of γ_{Int} for copper is 75 ergs.cms.$^{-2}$; from this, and measurements made on the shrinkage of single and double faulted loops* he has suggested that the value of γ_{Ext} lies between 75 and 100 ergs.cms.$^{-2}$. The value of E_S is given by:-

$$E_S = \frac{3r\mu b^2}{4}\left[\ln\left(\frac{8r}{b}\right) - \frac{9}{8}\right] \quad .. \quad (2)$$

where r is the radius of the loop, b is the burgers vector of the clearing dislocation, and μ is the shear modulus of the matrix.

---

* An intrinsic fault is equivalent to a single faulted loop, and an extrinsic fault can be considered as a double faulted loop.

Therefore, the minimum radius of the island of perfect crystal that would be stable is given by:-

$$r = \frac{3\mu b^2}{4\pi\gamma} \left[\ln \left(\frac{8r}{b}\right) - \frac{9}{8} \right] \quad \ldots \quad (3)$$

This equation cannot be solved analytically, but requires the application of Newtons Method of Successive Approximations for an accurate solution. The equation gives y as a function of r, i.e. $y = f(r) = r - A \ln r - B$ where A and B are constants, and in order to find the value of r for which y = 0, then the first differential of y must be obtained to give a second function equal to $f'(r)$, i.e.

$\frac{dy}{dr} = 1 - \frac{A}{r} = f'(r)$ which can then be used to give an approximate solution for r by straight forward numerical substitution (r_n). The next best answer ($r_n + 1$) is given by:-

$$r_{n+1} = r_n - \frac{f(r_n)}{f'(r_n)}$$

Therefore, assuming that the partial dislocation responsible for creating the island of perfect crystal within the fault is a Shockley, then $b = \frac{1}{6} a \langle 112 \rangle = 1.4760A^{\circ}$. Taking a value of 4.5×10^{11} dynes.cms^{-2} for the shear modulus of copper then the equation given in (3) may be evaluated for r in an intrinsic fault, using $\gamma_{Int} = 75$ erg s.cms.$^{-2}$, and an extrinsic fault, using $\gamma_{Ext} = 100$ ergs.cms.$^{-2}$ since the removal of the fault occurs in a substanially pure copper matrix.

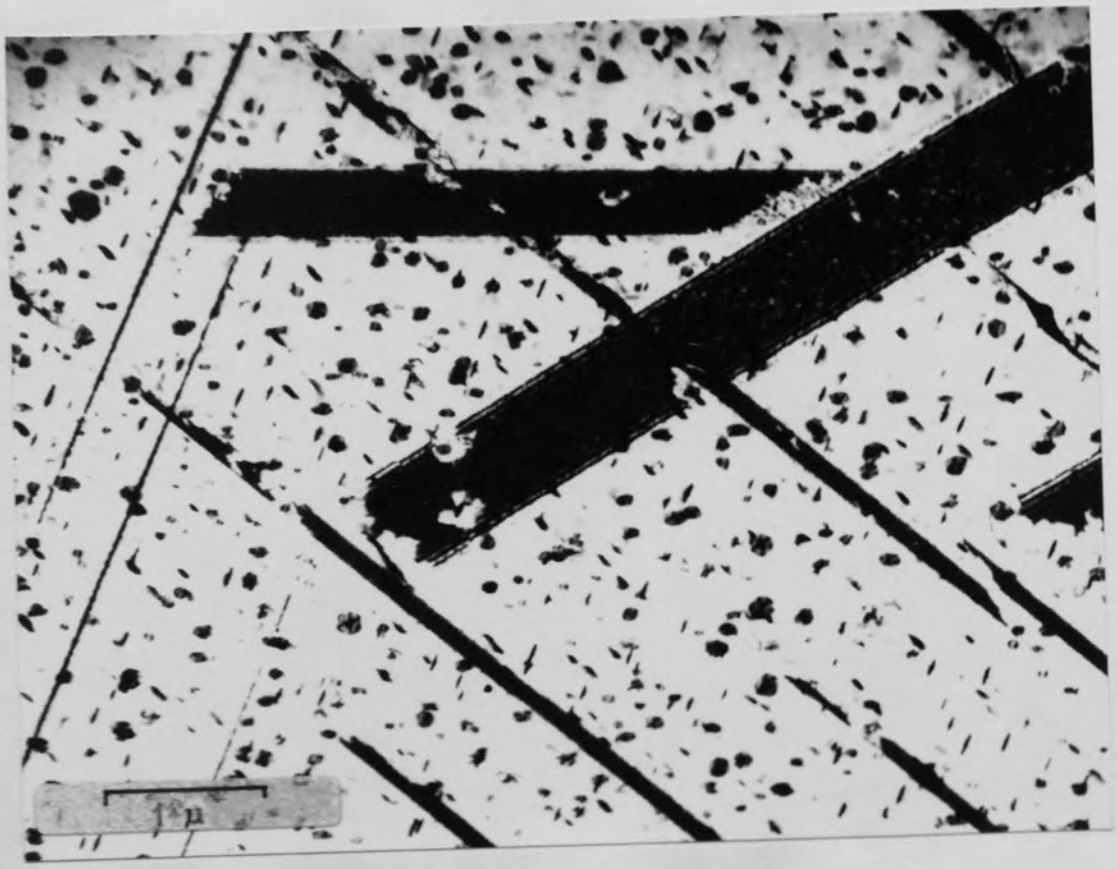

Fig.8.2 Islands of perfect crystal created within stacking faults, the smallest of which are 250A° radius.

For intrinsic faults:-

$$r_{(cms)} \geq \frac{3 \times 4.5 \times 10^{11} \times (1.476 \times 10^{-8})^2}{4\pi \times 75} \left[\ln \frac{8r}{1.476 \times 10^{-8}} - \frac{9}{8} \right]$$

$$\therefore \quad r_{(A^\circ)} \geq 31.182 \left(\ln 5.42r - \frac{9}{8} \right)$$

$$r - 71.743 \log_{10} r - 17.601 \geqslant 0 \text{ , which gives}$$

$$r = \underline{179 A^\circ}$$

For extrinsic faults:-

$$r = \underline{126 A^\circ}$$

These values can be considered as the limiting cases for the faults under investigation since both intrinsic and extrinsic faults are observed. Inspection of Fig.8.2 shows that islands of perfect crystal exist in the faulted regions of the crystal, which range from 250 - 1500Å in radius; similarly, Figs.5.13, 5.14, 5.15, 7.8, 7.21 and 7.29 exhibit islands of perfect crystal within the faults, and the minimum radius observed is of the order of $250 A^\circ$, in excellent agreement with the values predicted above. These islands of perfect crystal within the faults are therefore stable, and will continue to grow until, the fault is removed by the impingement and coalescence of all such regions, as demonstrated by Figs.7.7 and 7.10.

The above treatment does not take into account the problem of nucleation of the partial dislocation

necessary to create perfect crystal within the faults. However, a consideration of the conditions existing in the two alloys containing faults when these reactions occur shows that firstly many hetrogeneous nucleation sources are available in the form of intersecting faults and precipitates on other {111} planes (e.g. Fig.5.13), and second, that the precipitates within the faults are thicker than one lattice spacing and therefore destroy the fault during growth. When the precipitates within the faults reach a size of approximately 125 - 180A° radius then the faults surrounding the precipitate may be expected to become instable. Fig.5.14 for copper zirconium aged at 550°C shows how the rapid growth of precipitate to 250A° radius has removed the fault completely. Having nucleated the dislocations necessary to create regions of perfect crystal, the driving force for the continued growth of such islands which are greater in radius than the values calculated above is readily available.

8.5 Grain Boundary Precipitation

It has been suggested that the stacking faults form in the two zirconium bearing materials due to the segregation of zirconium to dislocations, by a Cottrell and/or Suzuki type of segregation, since zirconium has a large misfit and a C.P.H. structure.

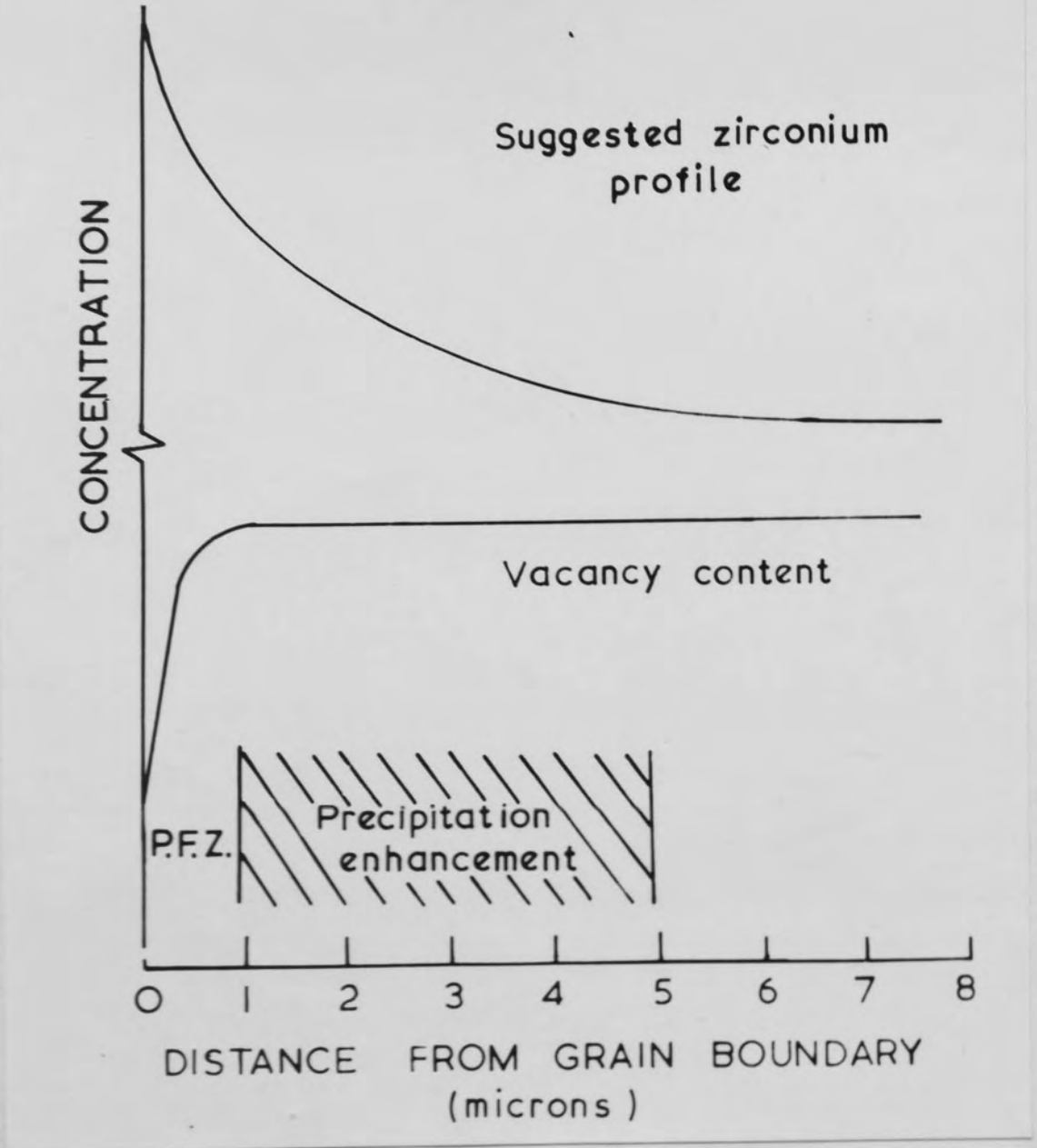

Fig.8.3 Solute and vacancy profiles used to explain the precipitation enhanced regions observed near grain boundaries.

The creation of the precipitate enhanced regions observed in these two alloys can be explained using the assumption that zirconium atoms do migrate to lattice imperfections either during the quench, or in the early stages of ageing. If so, then the grain boundaries are expected to accommodate greater quantities of zirconium than is the matrix, and it is reasonable to predict a solute profile of the type shown in Fig.8.3*. If a grain boundary vacancy profile typical of quenched metals is now superposed on this solute profile, then micrographs such as those shown in Figs.5.22, 5.23, 7.26 and 7.27 of direct quenched material containing both P.F.Z's. and regions of precipitate enhancement can be explained using an argument involving the supply of a critical solute/vacancy supersaturation. Within the grains, the vacancy supersaturation is high but the solute supersaturation low and homogeneous nucleation of Cu_3Zr is prevented unless the vacancy

* The only way in which solute profiles at grain boundaries can be measured is by electron microprobe analysis and until recently the technique was considered unreliable due to the comparitively large volume of material analysed by the finest of electron beams. However, Levine and Rapperport[75] have reported results gained from a study of the grain boundary regions in very dilute copper - tin alloys and have shown that the solute concentration in regions within 3 microns either side of grain boundaries is between 25% and 35% higher than in the matrix. In view of the similarities between zirconium and tin in terms of misfit in the copper matrix, it may be possible at a later date to determine a similar solute profile in copper zirconium alloys.

supersaturation is greatly increased e.g. by room temperature quenching. Similarly, regions very close to the grain boundary suffer from vacancy depletion and it may be considered difficult to nucleate Cu_3Zr homogeneously unless the solute supersaturation is increased. Evidence for segregation of zirconium to the boundaries is given by the presence of large zirconium containing precipitates shown in Fig.7.27 which lie in the grain boundaries of the material. A region approximately 1 micron wide adjacent to the boundary is precipitate free and may originate due to solute depletion by the precipitate in the grain boundary or simply by vacancy depletion.

The behaviour of stacking faults in the regions of precipitate enhancement near grain boundaries in copper zirconium can be explained simply on the basis that the hetrogeneous nucleation source offered by the growing fault is not required to nucleate the Cu_3Zr precipitate in such regions. However, a similar argument cannot be advanced for the behaviour in the ternary alloy and it must be assumed on present knowledge, that the faults are unable to expand into the precipitate enhanced region due to either (a) the matrix is of high stacking fault energy and will not support the fault or (b) that no chromium exists in these regions or that (c) if it does, then it is unable to diffuse to the partial dislocations bounding the fault.

The first suggestion has the advantage that it could be used to explain stacking fault behaviour in both alloy systems Cu-Zr and Cu-0.2%Cr-0.2%Zr. A guide to the validity of (b) and (c) may be possible from electron probe analysis across grain boundary regions in the light of recent improvements in the techniques available for such studies[75].

CONCLUSIONS

As a result of this research programme, it is concluded that:-

1. Resistivity data abstracted from isothermal ageing experiments conducted on four alloys from the system copper-chromium-zirconium has been successfully used to provide information on the kinetics of precipitation processes occurring in these alloys, and to predict the variation of such processes with heat treatment and alloy composition.

2. Precipitation occurs in the alloy copper-0.4% chromium by the rejection of B.C.C. chromium particles which maintain a coherent interface and a Kurdjumov-Sachs crystallographic orientation relationship with the copper matrix over the range of ageing temperatures studied. The interfacial energy existing between precipitated chromium particle and matrix has been calculated from particle coarsening experiments as 200 ergs.cms^{-2} and is indicative of the small misfit existing between precipitated particle and matrix when arranged in the proposed orientation relationship.

3. The precipitation reactions occurring in the alloy copper-.0.24%zirconium vary with ageing

temperature and three stages of transormation have been recognized viz:-

(a) At temperatures below 450°C, the predominant precipitation mechanism is the homogeneous nucleation of coherent disc shaped precipitates which grow on the {111} planes of the copper matrix, and which are thought to be the compound Cu_3Zr.

(b) At, and above 450°C, the Cu_3Zr precipitate is incoherent and stacking faults grow during ageing by the dissociation of glissile whole dislocations into two Shockley partial dislocations. The faults have been found to provide a suitable hetrogeneous nucleation source for the Cu_3Zr precipitate.

(c) Above 500°C, the fraction of homogeneously nucleated precipitate decreases continuously with increasing ageing temperature until at 550°C, precipitation occurs predominantly on undissociated dislocations.

4. When chromium and zirconium are present in copper, the ensuing precipitation reactions are strongly influenced by the zirconium content. The fraction of homogeneously nucleated chromium particles becomes progessively smaller with increasing zirconium content,

and the alloy Cu-0.2%Cr-0.2%Zr can be heat treated to promote the growth of stacking faults during ageing which provide favourable hetrogeneous nucleation sites for all of the chromium present in the alloy.

5. The intrinsic and extrinsic faults present in the high zirconium containing alloys are formed by the dissociation of a glissile dislocation into two Shockley partial dislocations. Nucleation is assisted by the combined effects of zirconium segregation to dislocations and the existence of a coherent ⟶ incoherent transition of the interface between matrix and Cu_3Zr precipitate. The continued dissociation of the glissile dislocation to form large stacking faults is not due to a lowering of the stacking fault energy of the matrix, but to the creation of favourable nucleation sites for the precipitates present in the aged alloys.

ACKNOWLEDGEMENTS

The author wishes to record his gratitude to Dr. J.A. Belk for his continued interest in, and supervision of the research programme.

The author is also indebted to Professor W.O. Alexander for the provision of research facilities within the Department of Metallurgy, and to the Science Research Council for the award of a maintainance grant for the period 1965-1968.

Thanks are also due to Messrs. Johnson Matthey Ltd. for supplying the materials, and to Mr. P. Cox for photographic assistance during the preparation of the manuscript.

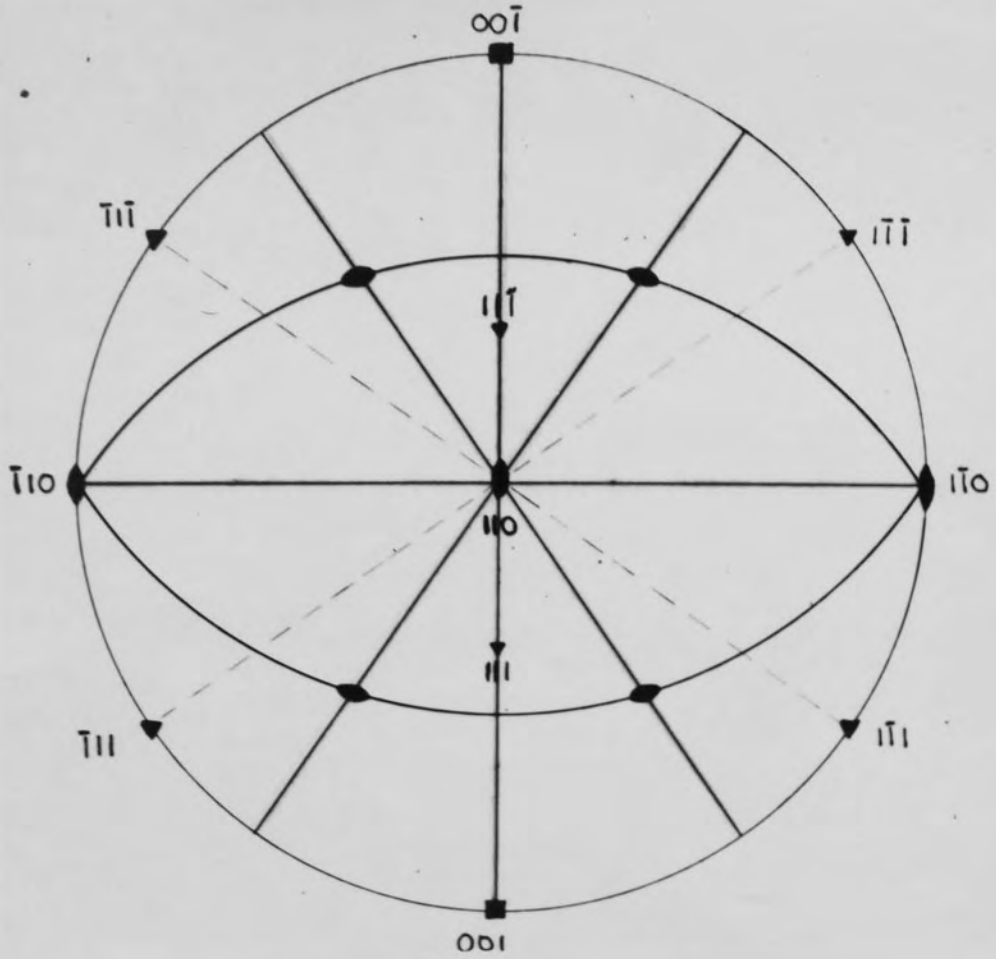

Fig.A1 [110] Projection]

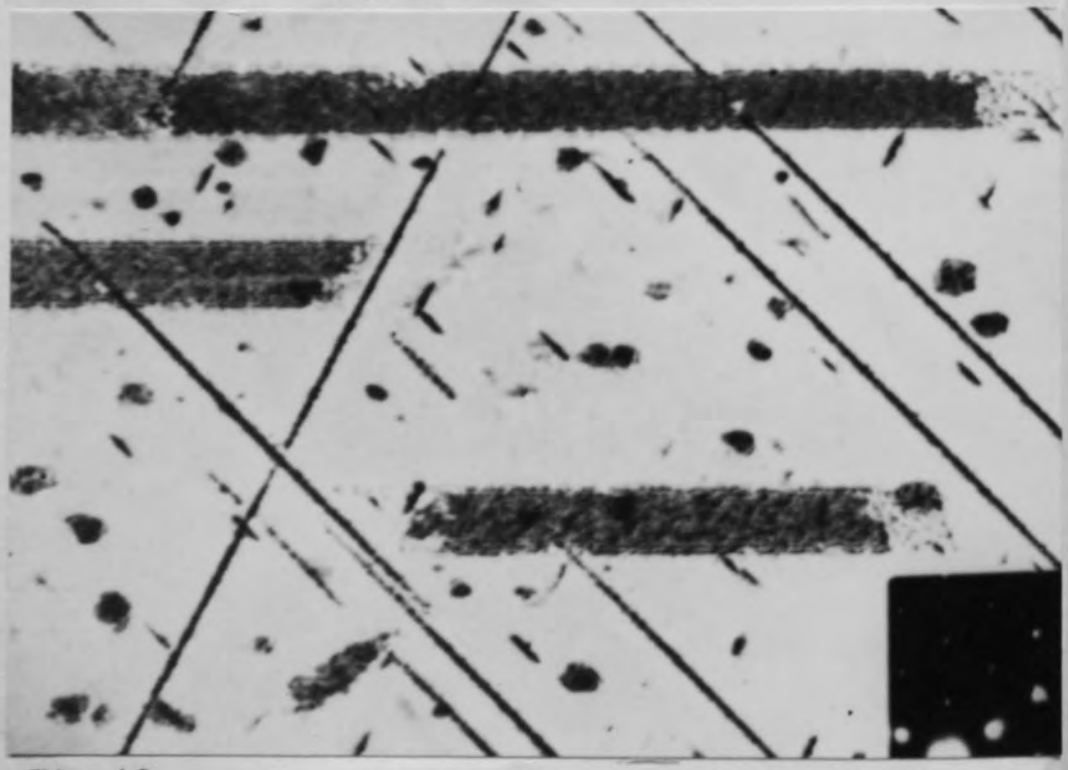

Fig.A2

APPENDIX 1

Foil Orientation & Crystallography

The thermo-mechanical treatment schedule necessary to produce either of the three predominant foil orientations encountered during metallographic examination of the copper-based alloys has been described in Section 3.6.1. The crystallography of such foils may be conveniently represented by the standard stereographic projections [110] ; [211] ; and [001] given in Figs.A1, A3 and A5 respectively. Selected micrographs taken from foils which were orientated such that the foil normal was close to one of these zone axes are displayed in Figs.A2, A4 and A6 together with their respective diffraction patterns. The diffraction patterns may be indexed from an inspection of the poles on the circumference of the relevant stereographic projection.

(110) Foil Orientation

Foils with a [110] direction exactly parallel to the electron beam have the planes $(\bar{1}11)$ and $(1\bar{1}1)$ perpendicular to the foil surface, whilst the planes (111) and $(11\bar{1})$ are inclined to the foil surface at $35^{\circ}16'$. The presence of stacking faults in two of the alloys studied allows the {111} planes in the foil to be readily identified, and Fig.A2 represents a foil which is orientated very closely to an exact (110) plane. The more commonly observed orientations near (110) show a

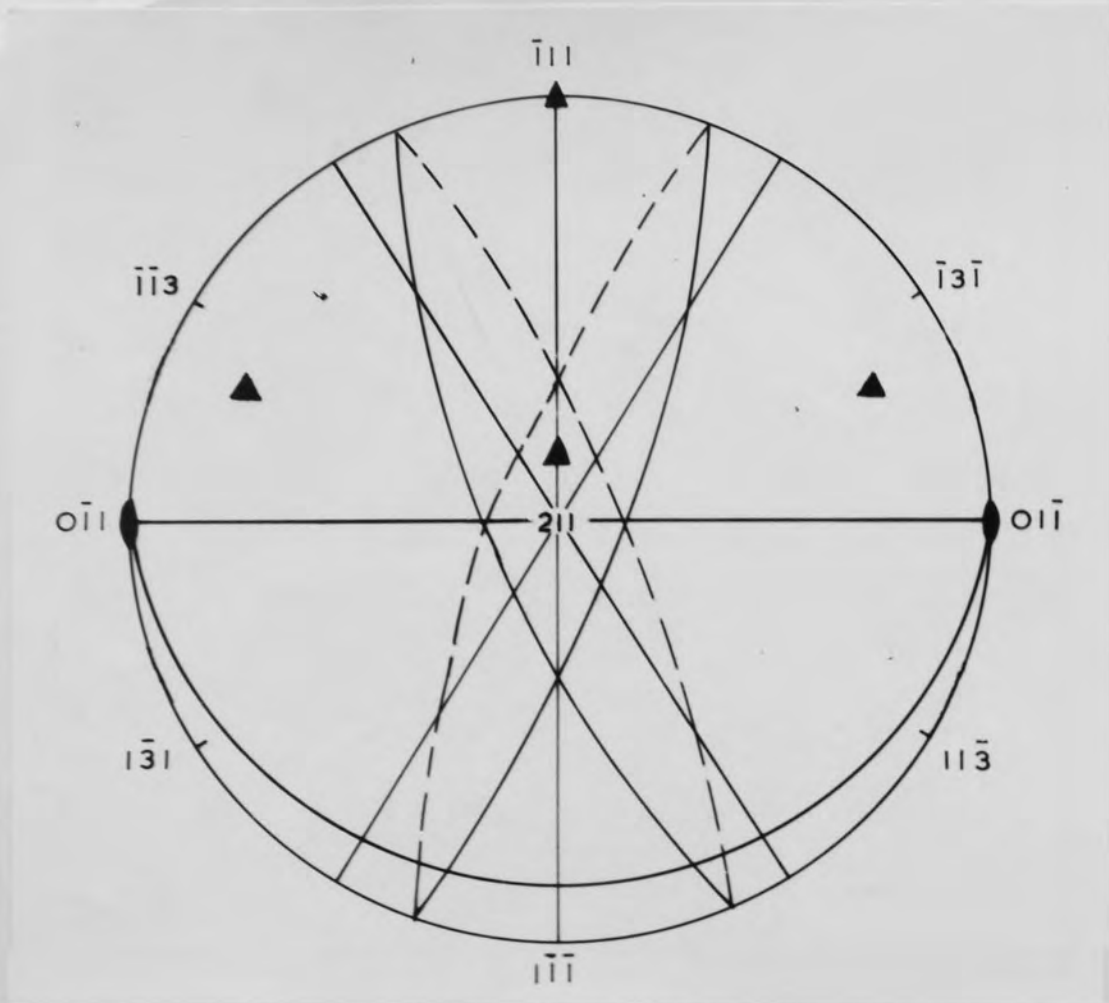

Fig.A3 [211] Projection

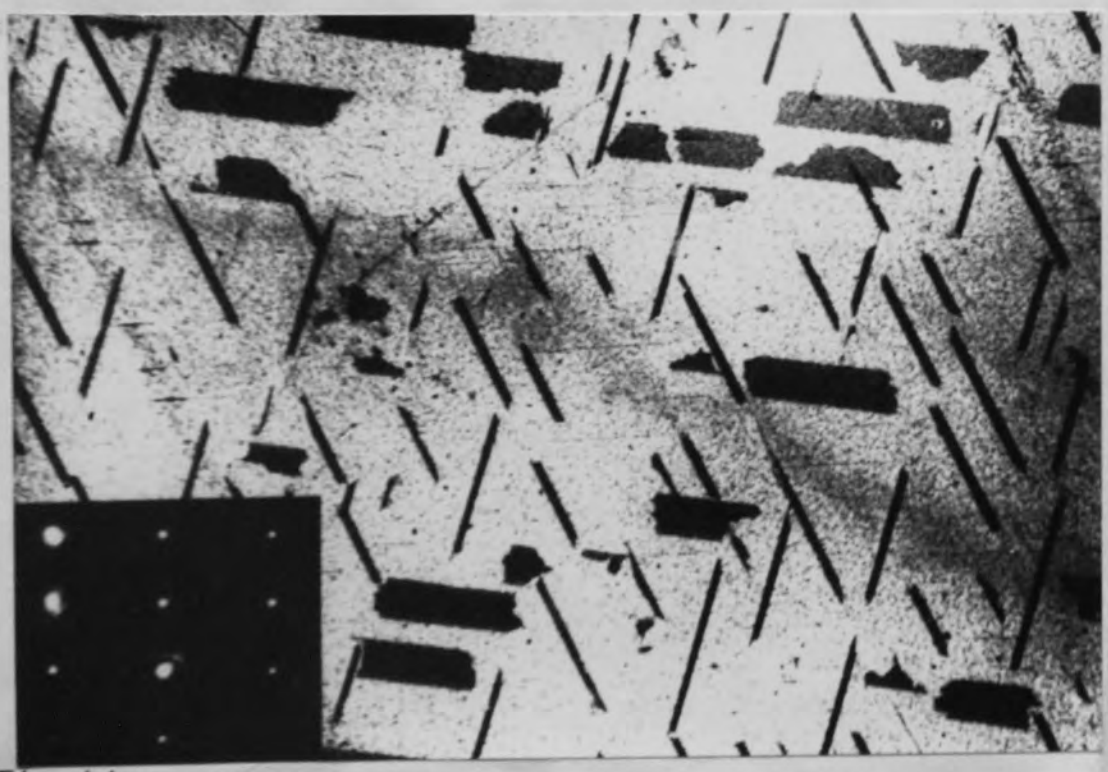

Fig.A4

divergence of the inclined planes (111) and $(11\bar{1})$ about the $[1\bar{1}0]$ direction in the foil, e.g. in Fig.7.24 where the divergence is 24°, and which is equivalent to an 8° rotation of the [110] projection about a [100] axis.

The low indexed reflections available from a (110) foil are [002] , [111] and [220] and thus provide the most useful combination of reflecting conditions for diffraction contrast experiments involving the determinatio of the Burgers vectors of dislocations.

(211) Foil Orientation

Foils with a [211] direction exactly parallel to the electron beam have the planes $(1\bar{1}1)$ and $(11\bar{1})$ inclined at 60°, and the (111) plane inclined at $19^{\circ}28'$ to the foil surface. The plane $(\bar{1}11)$ is again perpendicular to the foil surface. The micrograph illustrated in Fig.A4 illustrates the wider images obtained from stacking faults present on the (111) plane in such foils. Accurate foil thickness measurements are facilitated by the presence of the larger numbers of fault fringes contained within those faults on the (111) plane.

The low indexed reflections available from this foil orientation are [111] ; [220] ; and [113], and consequ observations of stacking faults and measurements of stacking fault density become difficult due to the disappearance of the characteristic fringe contrast which occurs when either

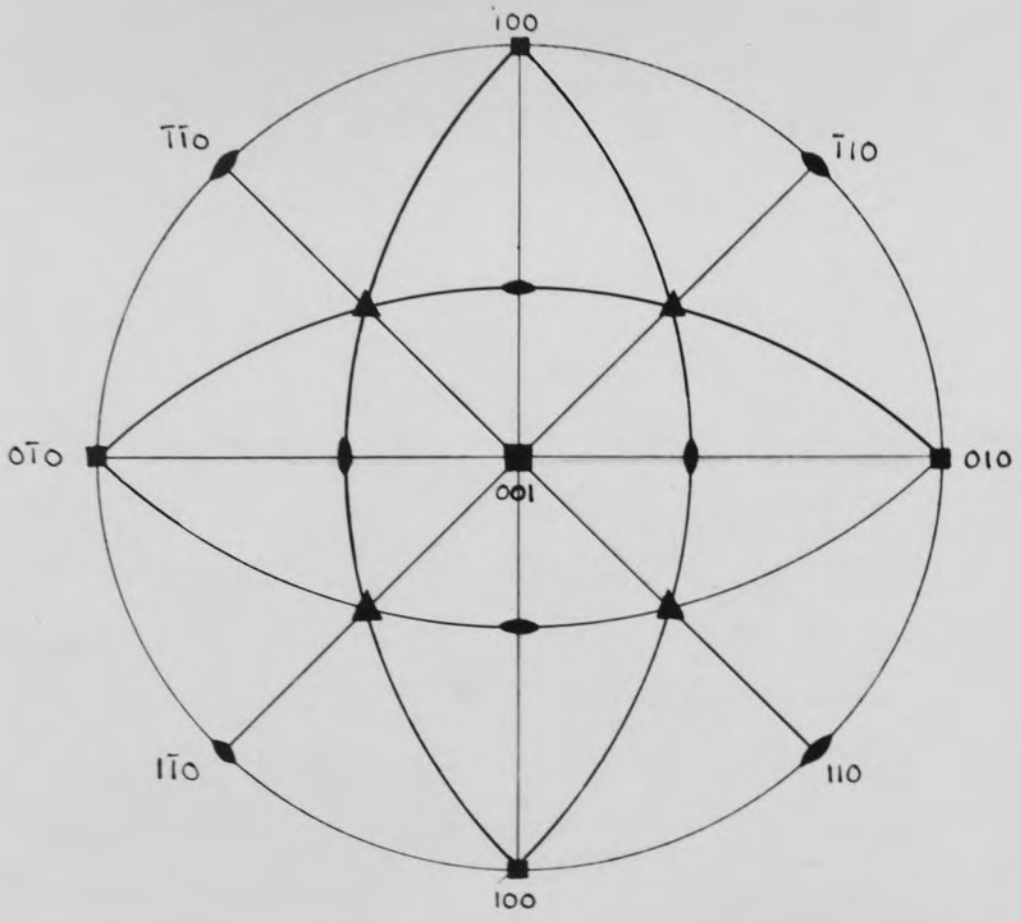

Fig.A5 [001] Projection

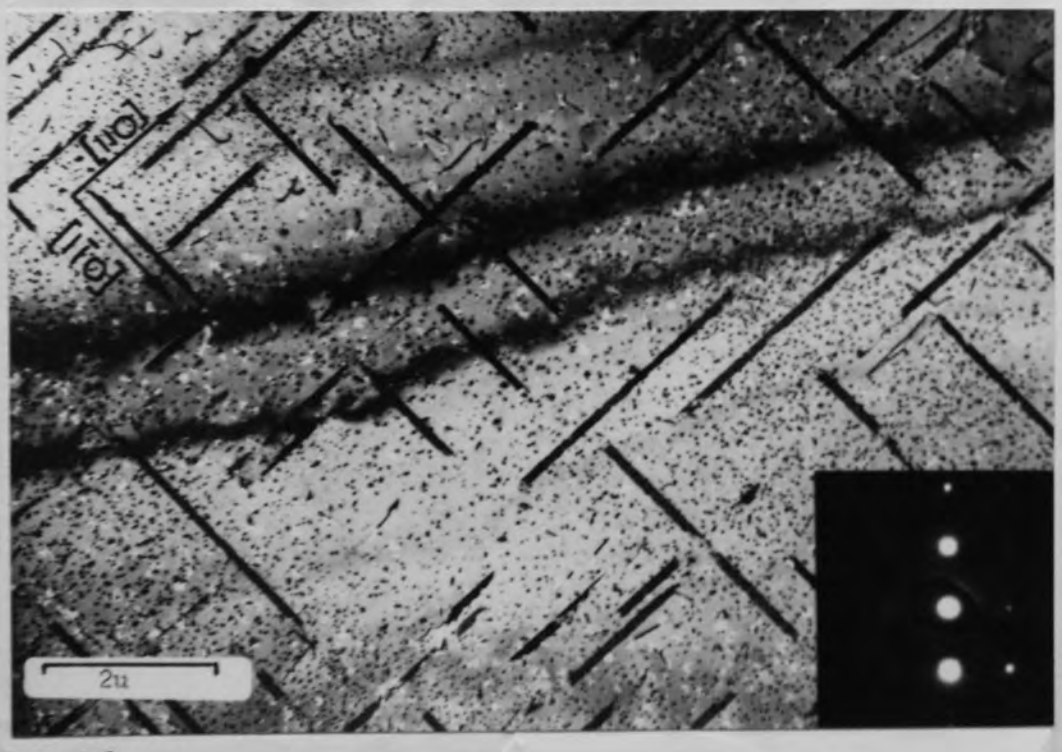

Fig.A6

⟨220⟩ or ⟨113⟩ type diffraction vectors are operating strongly, since g.R = 0 for these reflections.

(001) Foil Orientation

Foils with a [001] direction exactly parallel to the electron beam have all four {111} planes inclined at $54^{o}44'$ to the foil surface, as shown by reference to Fig.A6. The sense of the slope of such planes with respect to the foil surface, and hence the precise plane on which the stacking faults are present can be determined by noting the assymetry of the fault image produced when the foil is viewed in dark field.

The low indexed reflections available for diffraction contrast experiments in this foil orientation are [002] and [220] type.

APPENDIX II

X-ray Determination of the Compound Cu_3Zr.

The Debye-Scherrer film strip obtained from the experimental alloy 3 shown in Fig.3.10 (75wt.%Cu) is illustrated in Fig.A7.

Fig. A7.

A similar film strip has been analysed by Edwards[69] and he has shown that the powder method is unsatisfactory for the structural analysis of the compound Cu_3Zr due to heavy absorption within the sample, and also to fluorescence. By comparing the film strip results with those obtained from a diffractometer analysis, he was able to show that the absorption which occurs in the Debye-Scherrer method produces a "line-shift" —— the magnitude of which varies with Bragg angle, and he suggests that it is this effect which has almost certainly hindered the determination of the compound structure by previous workers.

Of the 54 lines produced on irradiating a specimen of 72wt.%Cu, with CuKα X-rays, only the first 16 were fitted

to a suggested orthorhombic structure of lattice parameters:-

$$a = 7.3061\ A^{o}$$

$$b = 8.0995\ A^{o}$$

$$c = 6.7649\ A^{o}$$

However, no accurate density determinations were performed and it must be concluded that further work is needed in order to assign a crystal structure to the first intermediate compound existing in the Cu-Zr system.

REFERENCES

1. Gregory P., Bangay A.J. and Bird T.L.; Metallurgia 71 (1965) 207.
2. Pawlek F. and Reichel K.; Z.Metallk 47 (1956) 347.
3. Smart J.S. and Smith A.A.; Trans.A.I.M.E. 147 (1942) 4[illegible]
4. Smart J.S. and Smith A.A.; ibid 166 (1945) 144.
5. Warrington D.H.; Thesis, Ph.d. Cambridge University (1961).
6. Seeger A.; "Handbuch der Physik" 7 (2) Springer-Verlag (1958).
7. Honeycombe R.W.K.; Progress in Materials Science 9 (1961) 93.
8. Sargeant R.M.; J.L.M. 96 (1968) 197.
9. Hansen M.; "Constitution of Binary Alloys" McGraw-Hill (1958).
10. Saarivirta M.J.; Trans. A.I.M.E. 218 (1960) 431.
11. Zwicker U.; "Metall" 16th year No.5 (1962) 409.
12. Showak W.; Trans. A.I.M.E. 224 (1962) 1297.
13. Donachie M.J.; J.I.M. 92 (1964) 180.
14. Zakharov M.V., Stepanova M.C. and Glazov V.M.; Metallovedenie I Obrabotka Metallov 3 (1957) 23.
15. Harris A.R.P.; B.Sc (project report) Aston University (1964).
16. Koster W. and Knorr W.; Z. Metallk 45 (1954) 350.
17. Williams R.O.; Trans. A.S.M. 52 (1960) 530.
18. Hibbard R.W. et.al.; Trans. A.I.M.E. 175 (1948) 283.
19. Nishikowa S., Kobayashi S. and Magata K.; Nippon Kinzoku 30 (1966) 760.
20. Saarivirta M.J.; Trans. A.I.M.E. 218 (1960) 935.

21. Hibbard R.W. and Hart E.W.; Trans. A.I.M.E. 203 (1955) 200.

22. Hodge W.; Journal of Metals (1957) 408.

23. Rutherford N.B., Dooley J. and Hewitt D.N.; C.D.A. Symposium on "The effect of Research and Design on the use of copper in the Electrical Industry" October 1962.

24. Lynch J.P.; Wire and Wire Products (1958) 483.

25. Mizumo K.; Sumit Light Metal Technical Reports 3 (1962) 55.

26. Richards T. and Stamford M.; C.D.A. Conference on "Modern Aspects of Copper in Electrical Engineering" May 1968.

27. Nicholson R.B. and Kelly A.; Progress In Materials Science Vol.10 P.148. (Pergamon Press).

28. Volmer M. and Weber A.; Z. Phys.Chem. 119 (1925) 277.

29. Becker R. and Doring W.; Ann.Phys. 24 (1935) 719.

30. Cahn J.W., and Hilliard J.E.; ActaMet. 9 (1961) 795.

31. Burke J.; "The Kinetics of Phase Transformations in Metals" London 1965(Pergamon Press).

32. Nabarro F.R.N.; Proc.Roy.Soc. A175 (1940) 519.

33. Friedel J.; "Les Dislocations" Gauthier Villars 1956.

34. Liftshitz M. and Slyzov V.V.; J.Exp.Theor.Phys.(USSR) 35 (1958) 479.

35. Wagner C.; Z.Electrochem 65 (1961) 581.

36. Oriani R.A.; Acta Met. 12 (1964) 1399.

37. Ardell A.J. and Nicholson R.B.; ibid 14 (1966) 1295.

38. Embury J.D. and Nicholson R.B.; ibid 13 (1965) 403.

39. Federihigi T. and Thomas G.; Phil.Mag. 7 (1962) 127.

40. Lorimer G.W. and Nicholson R.B.; Acta.Met. 14 (1966)

41. Simmons R.O. and Balluffi R.N.; Phys.Rev. 129 (1963) 1533.

42. Horbogen E.; Acta.Met. 10 (1962) 525.

43. Cahn J.W. Ibid 5 (1957) 169.

44. Thompson N. Proc.Phys.Soc. 66 (1953)B 481.

45. Suzuki H.; Sci.Rep.Res.Inst. Tohoku University A1 (1949) 183.

46. Cottrell A.H., Relation of Properties to Microstructure A.S.M. (1954) 131.

47. Nicholson R.B. and Nutting J.; Acta Met. 9 (1961) 332.

48. Van Aswegen J.S.T., Honeycombe R.W.K. and Warrington D.H.; ibid 12 (1964) 1.

49. Silcock J.M. and Tunstall W.J.; Phil.Mag. 10 (1964) 361

50. Dehlinger U.; "The Physical Chemistry of Metallic Solution and Intermetallic Compounds' Pager 4B H.M.S.O (1959).

51. Cottrell A.H. and Bilby B.A.; Proc.Phys.Soc. A.62 (1949) 49.

52. Johnson W.A. and Mehl R.F.; Trans. A.I.M.E. 135 (1939) 416.

53. Avrami M.; J. Chem.Phys. 7 (1939) .1103.

54. Tomlinson H.M.; Phil.Mag. 3 (1958) 867.

55. Ashby M.F. and Brown M. ibid 8 (1963) 1083.

56. Hirsch P.B., Howie A. and Whelan M.J.; Phil.Trans. A252 (1960) 499.

57. Hashimoto H., Howie A. and Whelan M.J.; Phil.Mag. 5 (1960) 967.

58. Gevers R., Art A. and Amelinckx S.; Physica Status Solidi 3 (1963) 1563

59. Belk J.A.; Unpublished work.

60. Cullity B.D.; "Elements of X-ray Diffraction" Reading (U.S.A.) Addison-Wesley (1956).

61. Dillamore I.L., Smallman R.E. and Roberts W.T.; Phil.Mag. 9 (1964) 517.

62. Ham F.S.; J.Appl. Phys. 30 (1959) 1518.

63. Bonar L.G.; Thesis Ph.d. Cambridge University (1962).

64. Lorrimer G.W.; Thesis Ph.d. Manchester University (1967).

65. Whelan M.J.; Proc.Roy.Soc. A249 (1958) 114.

66. Howie A.; Met. Reviews 6 (1961) 467.

67. Brooks H.; "Metal Interfaces" Amer.Soc.Metals (1952) 20.

68. Hirsch P.B., Howie A., Whelan M.J.; Phil.Trans.Roy.Soc. A252 (1960) 499.

69. Edwards D.; Bsc. (Project Report) Aston University. (1960)

70. Goodhew P.J., Dobson P.S. and Smallman R.E.; Met.Sci.Jnl. 1 (1967) 198.

71. Roberts W.T.; (Private Communication).

72. Howie A. and Swann P.R.; Phil.Mag. 6 (1961) 1215.

73. Lorretto M.H.; ibid 10 (1964) 467.

74. Smallman R.E. and Dobson P.S.; ibid 14 (1966) 357.

75. Levine E.D. and Rapperport E.J.; Scripta Metallurgica 2 (1968) 165.